



## Copyright Undertaking

This thesis is protected by copyright, with all rights reserved.

**By reading and using the thesis, the reader understands and agrees to the following terms:**

1. The reader will abide by the rules and legal ordinances governing copyright regarding the use of the thesis.
2. The reader will use the thesis for the purpose of research or private study only and not for distribution or further reproduction or any other purpose.
3. The reader agrees to indemnify and hold the University harmless from and against any loss, damage, cost, liability or expenses arising from copyright infringement or unauthorized usage.

### IMPORTANT

If you have reasons to believe that any materials in this thesis are deemed not suitable to be distributed in this form, or a copyright owner having difficulty with the material being included in our database, please contact [lbsys@polyu.edu.hk](mailto:lbsys@polyu.edu.hk) providing details. The Library will look into your claim and consider taking remedial action upon receipt of the written requests.

**ADVANCED ANODE MATERIALS FOR  
POTASSIUM ION BATTERIES: INSERTION  
CHEMISTRY AND STABILITY  
EXPLORATION**

**DU XIAOQIONG**

**PhD**

**The Hong Kong Polytechnic University**

**2022**

**The Hong Kong Polytechnic University**

**Department of Applied Physics**

**Advanced Anode Materials for Potassium Ion Batteries:  
Insertion Chemistry and Stability Exploration**

**DU Xiaoqiong**

A thesis submitted in partial fulfillment of the requirements for  
the degree of Doctor of Philosophy

**August 2021**

## **Certificate of originality**

I hereby declare that this thesis is my own work and that, to the best of my knowledge and belief, it reproduces no material previously published or written, nor material that has been accepted for the award of any other degree or diploma, except where due acknowledgment has been made in the text.

\_\_\_\_\_ (Signed)

DU Xiaoqiong \_\_\_\_\_ (Name of student)

## Abstract

Potassium ion batteries (PIBs) have emerged as attractive alternatives to the prevailing lithium ion batteries (LIBs) for large-scale energy storage. The natural abundance of potassium sources brings about potential benefits in the cost and sustainability. Several promising cathodes relying on non-toxic Mn and Fe elements are developed, further reducing the cost and increasing environmental benignity. Turning to the anodes, the graphite shows a theoretical capacity of merely 279 mAh g<sup>-1</sup> for K ions storage, which is much lower than that in LIBs. Therefore, this thesis aims to design high-capacity anodes for PIBs through insertion chemistry exploration and electrode/electrolyte interface optimization.

Comparison studies between alkali-metal ion storage are firstly conducted to provide insights into the effects of ionic carriers on the structural evolution of electrodes, which are currently somewhat lacking due to the absence of appropriate host materials. MoS<sub>2</sub>/carbon nanofiber is used as a model material to investigate Li/Na/K ions storage behavior *via in/ex situ* transmission electron microscopy (TEM). It is found the nanofiber shows a more significant volume expansion of 140% toward K ion uptake than Li (103%) and Na (123%) ions insertion. However, the layered MoS<sub>2</sub> structure is largely preserved after K ion insertion, while tiny particles are observed in the cases of Li and Na because of structural collapse. The reason roots in the less electrovalent of K-S bond than Li and Na ones, which is beneficial for maintaining more layered species upon K ion incorporation. The detailed phase transition mechanisms of MoS<sub>2</sub> upon K ion insertion are investigated by *in situ* X-ray diffraction (XRD) and theoretical simulation, confirming the intermediate phases of K<sub>0.5</sub>MoS<sub>2</sub> and K<sub>1.0</sub>MoS<sub>2</sub>. These intercalated compounds effectively preserve the layered structure and maintain original morphology for the stable cycling of micro-sized MoS<sub>2</sub> particles without carbon coating.

Subsequent efforts are dedicated to stabilizing Sb anodes with a superior theoretical capacity of 660 mAh g<sup>-1</sup>. However, the severe particle pulverizations and solid electrolyte interphases (SEIs) fracture lead to poor electrochemical stabilities. With the assistance of newly developed ethylene glycol diethyl ether (EGDDE)-based electrolyte, the commercial Sb microparticles with a high reversible capacity of 573 mAh g<sup>-1</sup> are stabilized over 180 cycles under 0.1 A g<sup>-1</sup> in PIBs. The reason lies in the formation of the elastic SEIs on the particle surface, which effectively wraps the micro-sized Sb particles to accommodate repeated swelling-contracting and prevent copious electrolytes decompositions. Similar enhancement is observed in another ether-based electrolyte based on tetrahydrofuran (THF) solvent. The Sb electrode delivers a

sustainable capacity of  $600 \text{ mA h g}^{-1}$  in 1 M KFSI/THF over 100 cycles under  $0.1 \text{ A g}^{-1}$ . Moreover, such ether-based electrolytes can be extended to stabilize microsized Sn anode for sodium ion batteries (SIBs). Sn microparticles maintain a high capacity of 669 and  $786 \text{ mA h g}^{-1}$  after 100 cycles under  $0.2 \text{ A g}^{-1}$  for EGDEE and THF-based electrolytes, respectively. The atomic force microscopy (AFM) tests are conducted to unravel the mechanical origin of improving electrochemical performance. It reveals that robust SEIs with superb mechanical properties are constructed in ether-based electrolytes, significantly boosting the performance of the alloy anode.

Phosphorus is another high-capacity anode with a theoretical capacity of  $1154 \text{ mA h g}^{-1}$  towards K ion storage. Black phosphorus-graphite (BP/G) composite with a high BP loading of 80 wt.% is synthesized and stabilized via the utilization of a localized high concentration electrolyte (LHCE), *i.e.*, KFSI in trimethyl phosphate (TMP) with a fluorinated ether as the diluent. We reveal the benefits of high concentration electrolytes rely on the formation of inorganic component rich SEI, which effectively passivates the electrode from copious parasite reactions. Furthermore, the diluent increases the electrolyte's ionic conductivity for achieving attractive rate capability and homogenizes the element distribution in the SEI. The latter essentially improves SEI's maximum elastic deformation energy for accommodating the volume change, resulting in excellent cyclic performance. This work promotes the application of advanced PIBs by adopting high-capacity BP anodes, on the one hand. On the other hand, it unravels the beneficial roles of LHCE in building robust SEI for stabilizing alloy anodes.

## List of publications

#Equal contribution first author; \* corresponding author.

1. **Du, X.#**; Huang, J.#; Guo, X; Lin, X; Huang, J.-Q.; Tan, H.; Zhu, Y.; Zhang, B. \*, Preserved layered structure enables stable cyclic performance of MoS<sub>2</sub> upon potassium insertion. *Chem. Mater.* **2019**, *31*, 8801-8809.
2. **Du, X.#**; Guo, X.#; Huang, J.#; Lu, Z.; Tan, H.; Huang, J.-Q.; Zhu, Y.\*; Zhang, B. \*, Exploring the structure evolution of MoS<sub>2</sub> upon Li/Na/K ion insertion and the origin of the unusual stability in potassium ion batteries. *Nanoscale Horiz.* **2020**, *5*, 1618-1627.
3. **Du, X.#**; Gao, Y.#; Zhang, B. \*, Building elastic solid electrolyte interphases for stabilizing micro-sized antimony anodes in potassium ion batteries. *Adv. Funct. Mater.* **2021**, *31*, 2102562.
4. **Du, X.**; Zhang, B. \*, Robust solid electrolyte interphases in localized high concentration electrolytes boosting black phosphorus anode for potassium ion Batteries. *ACS Nano* **2021**, *15*, 16851-16860.
5. Gao, Y.#; **Du, X.#**; Hou, Z.#; Shen, X.; Mai, Y.-W.; Tarascon, J.-M.; Zhang, B. \*, Unraveling the mechanical origin of stable solid electrolyte interphase. *Joule* **2021**, *5*, 1860-1872.
6. **Du, X.#**; Gao, Y.#; Hou, Z.; Guo, X.; Zhu, Y.; Zhang, B. \*, Building mechanically stable solid electrolyte interphases for micro-sized Sn anodes in sodium ion batteries. Under review.
7. Tan, H.; **Du, X.**; Zhou, R.; Hou, Z.; Zhang, B. \*, Rational design of microstructure and interphase enables high-capacity and long-life carbon anodes for potassium ion batteries. *Carbon* **2021**, *176*, 383-389.
8. Tan, H.; **Du, X.**; Huang, J.-Q.; Zhang, B. \*, KVPO<sub>4</sub>F as a novel insertion-type anode for potassium ion batteries. *Chem. Commun.* **2019**, *55*, 11311-11314.
9. Lin, X.; **Du, X.**; Tsui, P. S.; Huang, J.-Q.; Tan, H.; Zhang, B. \*, Exploring room- and low-temperature performance of hard carbon material in half and full Na-ion batteries. *Electrochim. Acta* **2019**, *316*, 60-68.
10. Huang, J.#; Guo, X.#; **Du, X.**; Lin, X.; Huang, J.-Q.; Tan, H.; Zhu, Y.\*; Zhang, B. \*, Nanostructures of solid electrolyte interphases and their consequences for micro-sized Sn anodes in sodium ion batteries. *Energy Environ. Sci.* **2019**, *12*, 1550-1557.

### Conference

1. Poster presentation: **Du, X.#**; Huang, J.#; Guo, X; Lin, X; Huang, J.-Q.; Tan, H.; Zhu, Y.; Zhang, B. \*, Preserved layered structure enables stable cyclic performance of MoS<sub>2</sub> upon potassium insertion. *Hong Kong Symposium of Batteries*, **2018**, Hong Kong.

## Acknowledgments

First and foremost, I would like to express my deepest gratitude and thanks to my supervisor, Dr. ZHANG Biao, for his insightful guidance, invaluable discussion, concrete instruction, helpful suggestions, enthusiastic and timely support during the whole period of my PhD studies. From assembling the coin cell to writing paper, he has taught me too many things. He leads me to the battery field and teaches me the right way of doing and thinking research and makes me be a better person. These will benefit me for the rest of my life. I also would like to thank my co-supervisor Prof. LAU Shu Ping. Meanwhile, I acknowledge the financial support from the general research fund (GRF) scheme of the Hong Kong Research Grants Council and the Hong Kong Polytechnic University.

I sincerely thank my colleagues and friends, Dr. HUANG Jiaqiang, Dr. LIN Xiuyi, Dr. HUANG Jianqiu, Dr. TAN Hong, Dr. GAO Yao, Dr. ZHANG Ruding, Dr. BAI Zhaowen, Dr. LIU Qiang, Dr. YANG Longkun, Mr. HOU Zhen and Ms. MA Menglin for their support and help during these years. In particular, I am really grateful to Dr. HUANG Jiaqiang for spending his precious time training me. I also thank the help from Prof. CHEN Guohua and Dr. ZHU Ye. Especially, I would like to thank Prof. LUO Wei for enlightening me on the research in Wuhan University.

I also wish to acknowledge all other faculties and staff in the department of applied physics (AP) and university research facility in materials characterization and device fabrication (UMF), who have given me valuable instructions and countless help on instrument operations and sample characterizations.

Finally, I sincerely appreciate Dr. GUO Xuyun for encouraging and supporting me to get through the hard time in my PhD studies. Moreover, I would like to thank my family. I am forever indebted to my parents and little sister DU Yufei for the everlasting understanding, love, encouragement and firm support.

DU Xiaoqiong  
PolyU  
August 2021

# Table of contents

Certificate of originality .....	i
Abstract .....	ii
List of publications.....	iv
Acknowledgments .....	v
Table of contents .....	vi
List of figures .....	x
List of tables.....	xix
List of abbreviations.....	xx
<b>Chapter 1 Introduction.....</b>	<b>1</b>
1.1 Potassium ion batteries.....	1
1.2 Cathodes materials for PIBs .....	3
1.2.1 Prussian blue analogs (PBAs).....	3
1.2.2 Layered transition metal oxides .....	5
1.2.3 Polyanionic compounds .....	6
1.2.4 Organic materials and others.....	7
1.3 Electrolytes for PIBs .....	9
1.3.1 Salts.....	10
1.3.2 Ester solvents .....	10
1.3.3 Ether solvents.....	12
1.3.4 Other solvents .....	14
1.4 Anodes materials for PIBs.....	15
1.4.1 Carbonaceous materials .....	15
1.4.2 Alloys.....	16
1.4.3 Metal oxides/sulfides/selenides.....	18
1.4.4 Phosphorus based materials .....	19
1.4.5 Others.....	21
1.5 Objective and outline .....	23

## **Chapter 2 Experimental ..... 24**

2.1 Material syntheses .....	24
2.1.1 MoS <sub>2</sub> /C nanofibers, carbon nanofibers and petal-like neat MoS <sub>2</sub> .....	24
2.1.2 Sb nanoparticles .....	24
2.1.3 Prussian blue K <sub>x</sub> MnFe(CN) <sub>6</sub> .....	25
2.1.4 Neat Sb and Sn on Cu foil.....	25
2.1.5 RP, BP, BP/G, K <sub>4</sub> P <sub>3</sub> .....	25
2.2 Electrodes and electrolytes preparation.....	26
2.2.1 Electrodes.....	26
2.2.2 Electrolytes .....	26
2.3 Electrochemical measurements .....	27
2.4 Sample characterizations.....	27
2.4.1 Structure, morphology, composition characterizations.....	27
2.4.2 <i>In situ</i> characterizations .....	28
2.4.3 Mechanical property characterizations .....	28
2.5 DFT calculations .....	30

## **Chapter 3 Exploring the structure evolution of MoS<sub>2</sub> upon Li/Na/K ion insertion and origin of unusual stability for potassium ion batteries..... 31**

3.1 Introduction .....	32
3.2 Results and discussion.....	33
3.2.1 MoS <sub>2</sub> /C nanofibers characterization .....	33
3.2.2 Comparison of charge storage processes .....	36
3.2.3 Electrochemical performances evaluation .....	43
3.2.4 Theoretical study.....	48
3.3 Summary .....	53

**Chapter 4 Preserved layered structure enables stable cyclic performance of MoS<sub>2</sub> upon potassium insertion..... 55**

4.1 Introduction ..... 55

4.2 Results and discussion..... 56

    4.2.1 Electrochemical performances evaluation ..... 56

    4.2.2 K-MoS<sub>2</sub> phase transition mechanism ..... 60

    4.2.3 Confirmation of layered K<sub>1.0</sub>MoS<sub>2</sub> phase..... 66

    4.2.4 Competition between intercalation and conversion reactions..... 70

4.3 Summary ..... 74

**Chapter 5 Building elastic solid electrolyte interphases for stabilizing micro-sized antimony anodes in potassium ion batteries..... 75**

5.1 Introduction ..... 75

5.2 Results and discussion..... 77

    5.2.1 Electrochemical performances evaluation ..... 77

    5.2.2 K-Sb alloying mechanism ..... 86

    5.2.3 Nanostructure, mechanical properties and chemical compositions of SEIs..... 90

    5.2.4 Full cell demonstration ..... 98

    5.2.5 Extending SEI construction to micro-sized Sn anodes in SIBs..... 99

5.3 Summary ..... 109

**Chapter 6 Robust solid electrolyte interphases in localized high concentration electrolytes boosting black phosphorus anode for potassium ion batteries..... 110**

6.1 Introduction ..... 110

6.2 Results and discussion..... 112

    6.2.1 Physical characterizations ..... 112

    6.2.2 Solvation structures of electrolytes ..... 115

6.2.3 K-P alloying mechanism.....	117
6.2.4 Electrochemical performance evaluation.....	119
6.2.5 Full cell demonstration .....	128
6.2.6 Chemical compositions, nanostructure and mechanical properties of SEIs.....	130
6.3 Summary .....	134
<b>Chapter 7 Conclusions and future work.....</b>	<b>136</b>
7.1 Conclusions .....	136
7.2 Future work .....	138
<b>Reference.....</b>	<b>140</b>

## List of figures

Figure 1.1 (a) The schematic of alkali-metal ion battery under discharging process. (b) Number of publications related to PIBs (until 2021 August). .....	2
Figure 1.2 The crystal structure of $K_xTM_1[TM_2(CN)_6]_{1-y}$ . .....	4
Figure 1.3 The discharge and charge curves of (a) $K_xFe[Fe(CN)_6]$ and (b) $K_xMnFe(CN)_6$ for PIBs under $25\text{ mA g}^{-1}$ . .....	5
Figure 1.4 The structures of P2-type, P3-type and O3-type $K_xTMO_2$ . <sup>24</sup> .....	6
Figure 1.5 The crystal structures of (a) $K_xTM_y(XO_4)_z$ and (b) $K_xTM_y(XO_4)_nF_m$ ; (c) The discharge and charge curves of $K_3V_2(PO_4)_2F_3$ for PIBs under $20\text{ mA g}^{-1}$ . .....	7
Figure 1.6 The chemical structure of (a) cation-type cathode of PTCDA and (b) anion-type cathode of PVK. ....	8
Figure 1.7 A summary of promising cathode materials for PIBs. <sup>18-19, 25, 28-30, 32-49</sup> .....	9
Figure 1.8 The chemical structures of the $KPF_6$ , KFSI and KTFSI salts. ....	10
Figure 1.9 The chemical structures of the ester solvents and FEC additive. ....	11
Figure 1.10 The chemical structures of the glyme-based solvents. ....	12
Figure 1.11 The chemical structures of the cyclic ether solvents and HFE additive. ....	13
Figure 1.12 The chemical structures of the TMP, TEP and TMS solvents. ....	14
Figure 1.13 The correlation between different kinds of anodes and K ion storage mechanisms. ....	15
Figure 1.14 The illustration of graphite, soft carbon and hard carbon toward K ion storage. .	16
Figure 1.15 (a) Theoretical capacities and corresponding average voltages and (b) the volume expansions of various anode materials for PIBs. <sup>73</sup> .....	17
Figure 1.16 The first discharge and charge curves of (a) $MoS_2$ and (b) $Sb_2S_3$ anodes for PIBs under $100\text{ mA g}^{-1}$ . ....	18
Figure 1.17 The chemical structure of WP, RP and BP. ....	20
Figure 1.18 A summary of promising anode materials for PIBs. <sup>52, 58-59, 76, 80-81, 83, 85, 89, 92-111</sup> ..	22
Figure 2.1 The schematic of the AFM tests. ....	29
Figure 3.1 Schematic illustration of electrospinning setup. ....	34
Figure 3.2 $MoS_2/C$ nanofibers. (a) XRD pattern and (b) TG. ....	34
Figure 3.3 XPS spectra of $MoS_2/C$ nanofibers. (a) C1s, (b) O1s, (c) Mo3d and (d) S2p. ....	35

Figure 3.4 MoS <sub>2</sub> /C nanofibers. (a) SEM image; (b, c) TEM images and (b inset) SAED pattern; (d) HRTEM image.....	35
Figure 3.5 Schematic illustration of <i>in situ</i> TEM experiment setup. ....	36
Figure 3.6 <i>In situ</i> TEM images of MoS <sub>2</sub> /C nanofibers for (a) Li, (b) Na and (c) K ions uptake at different reaction stages (insets: magnified images with a scale bar of 2 nm). The statistic scatters diagram of (d) lattice width of MoS <sub>2</sub> crystal and (e) lateral expansion of MoS <sub>2</sub> /C nanofiber in real time <i>in situ</i> TEM observations.....	37
Figure 3.7 HAADF-STEM image and corresponding EELS elemental maps of MoS <sub>2</sub> /C nanofibers before (up) and after (below) lithiation.....	38
Figure 3.8 HAADF-STEM image and corresponding EELS elemental maps of MoS <sub>2</sub> /C nanofibers before (up) and after (below) sodiation. ....	38
Figure 3.9 HAADF-STEM image and corresponding EELS elemental maps of MoS <sub>2</sub> /C nanofibers before (up) and after (below) potassiation. ....	39
Figure 3.10 <i>In situ</i> XRD patterns of MoS <sub>2</sub> /C nanofibers in the first cycle for (a) LIBs and (b) SIBs.....	40
Figure 3.11 <i>In situ</i> XRD and <i>ex situ</i> TEM for MoS <sub>2</sub> /C nanofibers. (a) <i>In situ</i> XRD patterns in PIBs in the first two cycles; The statistic histograms for MoS <sub>2</sub> crystals of (b) layer numbers at different states in PIBs and (c) lateral length in PIBs and SIBs; <i>Ex situ</i> TEM images at first fully discharged state in (d) LIBs; (e) SIBs and (f) PIBs (Conversion reaction products in LIBs are marked by circles and intercalation reaction products in SIBs and PIBs are marked by rectangles). ....	41
Figure 3.12 <i>Ex situ</i> TEM images of MoS <sub>2</sub> /C nanofibers for PIBs on the first cycle. (a, b) OCV state; (c, d) discharge to 1.0 V; (e, f) discharge to 0.5 V; (g, h) discharge to 0 V and (i, j) charge to 3 V. ....	42
Figure 3.13 Electrochemical performance in LIBs, SIBs and PIBs. (a) Discharge and charge profiles of MoS <sub>2</sub> /C nanofibers at first cycle at 50 m A g <sup>-1</sup> ; (b) dQ/dV vs. voltage plots of MoS <sub>2</sub> /C nanofibers at first cycle; (c) Cyclic performance with Coulombic efficiency of MoS <sub>2</sub> /C nanofibers and petal-like neat MoS <sub>2</sub> at 500 m A g <sup>-1</sup> ; (d) Retention percentage of MoS <sub>2</sub> /C nanofibers and neat MoS <sub>2</sub> after 200 cycles.....	44
Figure 3.14 (a) Rate performance and (b) retention of MoS <sub>2</sub> /C nanofibers in LIBs, SIBs and PIBs. (Retention is based on the discharged capacity in the fifth cycle). ....	45
Figure 3.15 Carbon nanofibers. (a) Discharge and charge profiles at first cycle at 50 m A g <sup>-1</sup> (inset: TEM image); (b) cyclic performance at 500 m A g <sup>-1</sup> . ....	45

Figure 3.16 Petal-like neat MoS <sub>2</sub> . (a) XRD pattern; (b, c) TEM images and (b inset) SAED pattern; (d) HRTEM image.....	46
Figure 3.17 <i>Ex situ</i> TEM images and schematics of MoS <sub>2</sub> /C nanofibers in (a, b) LIBs, (c, d) SIBs and (e, f) PIBs after 200 cycles. ....	47
Figure 3.18 The TEM image and SAED pattern of MoS <sub>2</sub> /C nanofibers in LIBs after 200 cycles. ....	48
Figure 3.19 DFT simulations. (a) The calculated structures for LiMoS <sub>2</sub> and KMoS <sub>2</sub> ; (b) charge density difference distributions for KMoS <sub>2</sub> ; (c) two-dimensional charge density difference of LiMoS <sub>2</sub> and KMoS <sub>2</sub> across Li/K and Mo-S; (d) calculated changes in Li/Na/K atoms charges (delta Q) of LiMoS <sub>2</sub> , NaMoS <sub>2</sub> and KMoS <sub>2</sub> , respectively (a positive value of delta Q indicates charges loss).....	50
Figure 3.20 DFT simulations. (a) The calculated structures for NaMoS <sub>2</sub> . (b) charge density difference distributions for LiMoS <sub>2</sub> and NaMoS <sub>2</sub> . ....	51
Figure 3.21 Two-dimensional charge density difference of NaMoS <sub>2</sub> across Na and Mo-S. ...	51
Figure 4.1 (a) SEM image and (b) particle size distribution by Gauss fitting for commercial MoS <sub>2</sub> . ....	57
Figure 4.2 Electrochemical performance of MoS <sub>2</sub> anodes in PIBs. (a)The 1st, 2nd and 5th charge and discharge profiles; (b) the corresponding differential capacity curves (dQ/dV); (c) rate performance, cycling stability and Coulombic efficiency; (d) diffusion coefficients as a function of discharge and charge during the 1st and 2nd cycle. ....	58
Figure 4.3 (a) TEM image and (b) XPS spectra of C 1s and O 1s for MoS <sub>2</sub> electrode at first cycled state.....	58
Figure 4.4 (a) GITT profile of first and second cycle. (b) Current step diagram at 1.24 V vs. K <sup>+</sup> /K of the first potassiation process of MoS <sub>2</sub> electrode for PIBs.....	59
Figure 4.5 The electrochemical performance plot of TMDs anode materials including MoS <sub>2</sub> /N doped-C, <sup>186</sup> MoS <sub>2</sub> @SnO <sub>2</sub> @C, <sup>172</sup> D-MoS <sub>2</sub> NFs, <sup>187</sup> MS-700, <sup>188</sup> NbSe <sub>2</sub> , <sup>189</sup> MoSe <sub>2</sub> /MXene@C <sup>160</sup> and MoSe <sub>2</sub> /N-C. <sup>162</sup> ....	60
Figure 4.6 Phase transitions of MoS <sub>2</sub> . (a) <i>in situ</i> XRD patterns of MoS <sub>2</sub> at different discharge and charge states, the corresponding voltage profiles are given on the right. For clear visualization, enlarged XRD pattern between 10°-14° is put on the left. The letters stand for first discharge (D1), first charge (C1) and second discharge (D2) with the followed numbers showing the capacity in mA h g <sup>-1</sup> . (e.g. C1 167 means	

the capacity is  $167 \text{ mA h g}^{-1}$  of K ions de-intercalation in the first charge.). (b) Density-functional theory (DFT) calculation with Vdw-optPBE corrections of  $\text{MoS}_2$  electrodes. The solid line indicates the thermodynamically stable phases within DFT and temperature errors, while the dashed line refers to the lowest formation enthalpy of each composition. The red dots show the structures in addition to the ones of the lowest enthalpy. (c) The simulated and experimental XRD patterns. Insets are the calculated crystalline structures. .... 61

Figure 4.7 XRD patterns of  $\text{K}_{1.0}\text{MoS}_2$  prepared by high energy ball milling with stoichiometric amount of potassium metal and  $\text{MoS}_2$ . .... 62

Figure 4.8 Simulated structures of  $\text{K}_{1.5}\text{MoS}_2$ . .... 63

Figure 4.9 *In situ* Raman spectra of  $\text{MoS}_2$  electrodes at different states and the corresponding voltage profiles. .... 65

Figure 4.10 Morphology evolution of  $\text{MoS}_2$  electrodes. TEM, corresponding SAED and HRTEM images of (a and b) pristine  $\text{MoS}_2$ ; (c and d) after first discharge to 0 V; (e and f) the first charged to 3V; (g and h) after 100 cycles; Insets: HRTEM image of metallic Mo. (i) HAADF-STEM image and corresponding EDS elemental maps of the first fully discharged  $\text{MoS}_2$  electrode; (j) schematic diagram for phase transition of  $\text{MoS}_2$ . .... 66

Figure 4.11 (a) Schematic of preparing  $\text{MoS}_2$ -Discharge-0V-water electrode. PVDF is used as a binder instead of CMC to avoid the dissolution. (b) XRD pattern of these different samples. (c, d, e) TEM, SAED and HRTEM images of sample  $\text{MoS}_2$ -Discharge-0V-water, indicating the recovery of  $\text{MoS}_2$  phase. .... 68

Figure 4.12 The HAADF-STEM image and corresponding EDS mapping of  $\text{MoS}_2$  anode in the first fully charged state. .... 69

Figure 4.13 The HAADF-STEM image and corresponding EDS mapping of  $\text{MoS}_2$  anode after 100 cycles. .... 70

Figure 4.14 The 1st and 2nd charge and discharge profiles at different rates. .... 71

Figure 4.15 Rate-dependent phase transition. (a) *Ex situ* XRD pattern of first fully discharged (D 0 V) and charged (C 3 V)  $\text{MoS}_2$  electrode with different current density (b) cyclic performance of  $\text{MoS}_2$  electrode at different current density (inset: ratio of the capacities contributed by intercalation and conversion); (c) schematic of phase transition for  $\text{MoS}_2$  upon K ion insertion. Dash line indicates the process

cannot be achieved by electrochemical reaction but is possible through chemical oxidation. ....	72
Figure 4.16 The 1st and 2nd charge/discharge profiles and cyclic performance of MoS <sub>2</sub> electrodes at 5 mA g <sup>-1</sup> .....	73
Figure 4.17 Cyclic performance of MoS <sub>2</sub> electrode at 1000 mA g <sup>-1</sup> .....	74
Figure 5.1 SEM images and histograms of the particle size distributions of (a-b) commercial Sb, (c-d) ball milled Sb. ....	78
Figure 5.2 XRD patterns of commercial Sb (black line) and ball-milled Sb (red line). ....	79
Figure 5.3 Electrochemical performance of Sb electrodes. The galvanostatic discharge-charge profiles in (a) 1 M KFSI/ECPC and (b) 1 M KFSI/EGDEE electrolytes of selected cycles under 0.1 A g <sup>-1</sup> (inset: rate performances). (c) Cyclic performance under 0.1 A g <sup>-1</sup> .....	79
Figure 5.4 Electrochemical performance of Sb electrodes. The galvanostatic discharge-charge profiles in (a) 1 M KFSI/THF electrolytes of selected cycles under 0.1 A g <sup>-1</sup> . (b) Cyclic performance under 0.1 A g <sup>-1</sup> . ....	80
Figure 5.5 (a) Cyclic performance of micro-sized Sb and synthesized Sb electrodes under 0.5 A g <sup>-1</sup> . (b) SEM image of synthesized Sb with an average particle size of about 500 nm. (c) XRD pattern of synthesized Sb. ....	81
Figure 5.6 Cyclic performance of micro-sized Sb in 1M KFSI/DME and 1M KFSI/DGME under 0.1 Ag <sup>-1</sup> with a cut-off voltage of 0-1.5V. ....	83
Figure 5.7 Rate performance of Sb electrodes in 1 M KFSI/EGDEE and 1 M KFSI/ECPC electrolytes (1C= 660 mA g <sup>-1</sup> ). ....	84
Figure 5.8 EIS spectra of Sb electrodes at (a) OCV state and (b) after cycling three times. (inset) The corresponding equivalent circuit for the EIS fitting. ....	85
Figure 5.9 GITT measurements in the first cycle. (a) Voltage curve vs. time. (b) Current step diagram at 0.88 V. (c) The linear behaviour of voltage vs. time at 0.88 V. (d) the average value of diffusion coefficient calculated from (a). ....	86
Figure 5.10 Cyclic voltammogram of Sb collected at a scan rate of 0.05 mV s <sup>-1</sup> and a scan range of 0-1.5 V in 1M KFSI/EGDEE. ....	87
Figure 5.11 (a) Contour map of <i>in situ</i> XRD for micro-sized Sb electrode in 1 M KFSI/EGDEE electrolyte on the first two cycles under 0.05 A g <sup>-1</sup> (peak-shift is marked in rectangle frame). (b) Schematic of the phase transformations, where c-K <sub>3</sub> Sb and h-K <sub>3</sub> Sb represent cubic and hexagonal K <sub>3</sub> Sb, respectively (Dash arrow stands for	

coexistence). Detailed lattice parameters of these phases are listed in Table 5.3. .....	88
Figure 5.12 Illustrations of the $K_1Sb$ structure derived from $Li_1Sb$ (Yellow and violet spheres represent Sb and K atom, respectively). <sup>237</sup> .....	89
Figure 5.13 <i>Ex situ</i> XRD patterns of Sb electrodes in 1 M KFSI/EGDEE electrolyte at different states under current density of $0.03 A g^{-1}$ (C and D stand for charge and discharge, respectively). .....	90
Figure 5.14 Morphologies and EEL spectra of cycled Sb electrodes: STEM/TEM images after 3 cycles in (a-c) 1 M KFSI/ECPC and (d-f) 1 M KFSI/EGDEE; after 50 cycles in (g-h) 1 M KFSI/ECPC and (i-j) 1 M KFSI/EGDEE. (k) EEL spectra after 50 cycles. SEM images after 100 cycles in (l) 1 M KFSI/ECPC, and (m) 1 M KFSI/EGDEE.....	91
Figure 5.15 HAADF-STEM images of the Sb electrode in 1 M KFSI/ECPC electrolyte after 3 cycles. ....	92
Figure 5.16 Illustration of electrode/SEI evolution in ECPC (up) and EGDEE-based (down) electrolytes. ....	92
Figure 5.17 HAADF-STEM and EELS elemental maps of Sb electrode in 1 M KFSI/ECPC electrolyte after 50 times cycling. ....	94
Figure 5.18 HAADF-STEM and EELS elemental maps of Sb electrode in 1 M KFSI/EGDEE electrolyte after 50 times cycling. ....	94
Figure 5.19 XRD pattern of electrodeposited Sb on Cu foil (inset: photograph). ....	95
Figure 5.20 AFM and XPS characterizations. (a) Characteristic force curves obtained from the AFM tests on electrodeposited Sb electrodes. AFM topography images in (b) 1 M KFSI/ECPC and (c) 1 M KFSI/EGDEE. (d) Distributions of Young's modulus and yield strain of SEIs. (e) Histogram with an error bar of yield strain. XPS spectra of Sb electrodes after cycling 3 times in (f) 1 M KFSI/ECPC and (g) 1 M KFSI/EGDEE electrolytes.....	97
Figure 5.21 (a) Illustration of the full cell operation by adopting respectively the first charge and discharge curves of half Sb and $K_xMnFe(CN)_6$ cells (inset: Schematic configuration of the PIBs full cell). (b) rate performance and (c) cyclic performance of $K_xMnFe(CN)_6  Sb$ full cell (d) Ragone plot. (The value is based on the active material mass of anode and cathode). ....	99

Figure 5.22 (a) SEM image and inset) particle size distribution of Sn electrode. (b) The galvanostatic discharge-charge profiles of the first cycle in 1M NaPF <sub>6</sub> /PC-FEC, 1M NaPF <sub>6</sub> /EGDDE and NaPF <sub>6</sub> /THF electrolytes under 0.05 A g <sup>-1</sup> . (c) Cycling performance under 0.2 A g <sup>-1</sup> .....	101
Figure 5.23 Rate performance of Sn electrodes in (a) 1 M NaPF <sub>6</sub> /EGDDE and (b) 1 M NaPF <sub>6</sub> /THF. ....	102
Figure 5.24 SEM images of Sn electrodes: (a-c) in 1 M NaPF <sub>6</sub> /PC-FEC; (d-f) in 1 M NaPF <sub>6</sub> /EGDDE and (g-i) in 1 M NaPF <sub>6</sub> /THF after 100 cycles. ....	103
Figure 5.25 Nyquist plots of the Sn electrodes cycled three times in (a) 1 M NaPF <sub>6</sub> /PC-FEC, (b) 1 M NaPF <sub>6</sub> /EGDDE and (c) 1 M NaPF <sub>6</sub> /THF; d) the fitted impedance in these three electrolytes (d inset: the equivalent circuit used for EIS fitting). ....	104
Figure 5.26 TEM/HRTEM characterization and SEI illustrations of Sn electrodes after 3 cycles in (a-d) 1 M NaPF <sub>6</sub> /PC-FEC, (e-h) 1 M NaPF <sub>6</sub> /EGDDE and (i-l) 1 M NaPF <sub>6</sub> /THF electrolytes. ....	105
Figure 5.27 XPS measurements of (a) C1s, (b) O1s and (c) F1s for cycled Sn electrodes in corresponding electrolytes. ....	107
Figure 5.28 Mechanical properties of SEIs. (a) Characteristic force curves obtained from the AFM tests on magnetron sputtered Sn electrodes; (b) average Young's modulus and yield strain $\epsilon_Y$ and (c) U for SEIs formed in the three electrolytes. Sample size = 108, 91 and 87 for PC-FEC, EGDDE and THF, respectively. ....	108
Figure 6.1 Sample preparation. (a) XRD patterns and (b) Raman spectra of RP, BP, and BP/G composite; TEM images of (c) BP and (d) BP/G composite.....	114
Figure 6.2 The TEM and HRTEM images of purified RP.....	114
Figure 6.3 (a) The EDS mapping of C and P elements and (b) XPS spectra for BP/G composite. ....	115
Figure 6.4 (a) Electrochemistry impedance spectra and (b) the calculated ionic conductivities of NCE, HCE and LHCE. ....	116
Figure 6.5 Electrolyte solvation structures. (a-c) Raman spectra of NCE, HCE, LHCE, KFSI, TMP and HFE. ....	117
Figure 6.6 (a) CV curves of BP/G electrodes in NCE, HCE and LHCE at the scan rate of 0.1 mV s <sup>-1</sup> ; (b) <i>Ex situ</i> Raman characterization of BP/G electrodes under different states in LHCE (note: D1-0.8V represents 0.8 V in the first discharge process). ....	118

Figure 6.7 Raman spectra of BP/G electrode (a) at first fully discharged state (D1-0V) in NCE; (b) at first fully discharged (D1-0V) and first fully charged (C1-2.5V) states in HCE. ....	118
Figure 6.8 Comparison of Raman spectra of HEBM synthesized $K_4P_3$ and first fully discharged (D1-0 V) BP/G electrodes in LHCE. ....	119
Figure 6.9 The selected galvanostatic discharge-charge profiles of BP/G electrodes under $0.1 \text{ A g}^{-1}$ in (a) NCE and (b) HCE. ....	120
Figure 6.10 SEM images of BP/G electrode: (a-b) pristine; cycled three times in (c-d) NCE, (e-f) HCE and (g-h) LHCE. ....	120
Figure 6.11 The electrochemical performances of BP/G. (a) Voltage profiles under $0.1 \text{ A g}^{-1}$ in LHCE; (b) Cyclic performance under $0.1 \text{ A g}^{-1}$ in NCE, HCE, and LHCE; (c) rate capability in HCE and LHCE; d) Diffusion constant values derived from the CV profiles (Figure 6.13); e) Long-term cyclic performances in corresponding electrolytes. ....	122
Figure 6.12 The selected galvanostatic discharge-charge profiles and corresponding cyclic performances of (a-b) ball milled graphite and (c-d) ball milled BP electrodes under $0.1 \text{ A g}^{-1}$ in LHCE. ....	123
Figure 6.13 CV rate curves of BP/G electrodes in (a) HCE and (b) LHCE; Fitting results of peak current $i_p$ (A) vs. the square root of scan rate $v^{1/2} (\text{V s}^{-1})^{1/2}$ for (c) R1, (d) R2, (e) O1 and (f) O2 peaks (R for reduction and O for oxidation). ....	125
Figure 6.14 The Nyquist plots of the BP/G electrodes at OCV state in (a) HCE and (b) LHCE; cycled three times in (c) HCE and (d) LHCE. ....	126
Figure 6.15 The selected galvanostatic discharge-charge profiles and corresponding cyclic performances of (a) and (b) RP/G in PIBs and (c) and (d) BP/G in SIBs. ....	128
Figure 6.16 (a) The XPD pattern of $K_x\text{MnFe}(\text{CN})_6$ (inset: the crystal structure); (b) the selected galvanostatic discharge-charge profiles and (c) cyclic performance for $K_x\text{MnFe}(\text{CN})_6$ half cell in LHCE; (d) and (e) full cell performances of BP/G   $K_x\text{MnFe}(\text{CN})_6$ in LHCE. ....	129
Figure 6.17 XPS Characterizations of BP/G electrodes after three cycles. C1s, P2p, F1s, and S2p spectra (a) in NCE; (b) HCE; c) LHCE and d) the atomic percentage of P and S elements in corresponding electrolytes. ....	131
Figure 6.18 (a-b) The TEM images of BP/G after cycling three times in NCE. ....	132

Figure 6.19 The TEM, STEM images and EDS mapping of BP/G after cycling three times in (a-c) HCE; (d-f) LHCE. ....	132
Figure 6.20 Morphologies and mechanical properties of the SEIs. The TEM, STEM images and EDS mapping after long-term cycling (300 cycles) in (a, b) HCE and (c, d) LHCE; e) Young's modulus ( $E$ ) and elastic strain limit ( $\epsilon_Y$ ), and f) the maximum elastic deformation energy ( $U$ ) of SEIs formed in these two electrolytes. ....	133
Figure 7.1 (a) The first charge and discharge curves for MoS <sub>2</sub> , Sb and BP/G in PIBs. (b) Cyclic performances of micro-sized Sb, Sn, Bi, Si electrodes under 0.1 A g <sup>-1</sup> in 1 M KFSI/EGDDE for PIBs. ....	139

## List of tables

Table 1.1 Physicochemical properties of Li, Na and K. <sup>12, 15</sup> .....	3
Table 1.2 The physical and chemical properties of the commonly used ester solvents (The data are collected from the safety data sheets of Sigma-Aldrich and previous publications <sup>51, 55-56</sup> ). .....	11
Table 1.3 The physical and chemical properties of the commonly used ether solvents (The data are collected from the safety data sheets of Sigma-Aldrich and previous publications <sup>51, 55-56</sup> ). .....	13
Table 1.4 The physical and chemical properties of the TMP, TEP and TMS solvents (The data are collected from the safety data sheets of Sigma-Aldrich and previous publications <sup>62-63</sup> ). .....	14
Table 3.1 Formation energy of conversion reaction calculated by DFT. ....	50
Table 3.2 Bader charges of LiMoS <sub>2</sub> calculated by DFT. ....	51
Table 3.3 Bader charges of NaMoS <sub>2</sub> calculated by DFT. ....	52
Table 3.4 Bader charges of KMoS <sub>2</sub> calculated by DFT. ....	53
Table 4.1 The simulated structures without showing K-S bonding and K atoms, and the lattice parameters of calculated phases. ....	63
Table 4.2 The calculate formation enthalpy of intercalation and conversion reactions by DFT. ....	72
Table 5.1 Electrochemical performance comparison between this work and other Sb-based anode materials in the literature. ....	82
Table 5.2 Cell resistance (R <sub>s</sub> ), charge transfer resistance (R <sub>ct</sub> ) and SEI resistance (R <sub>SEI</sub> ) of Sb electrodes from equivalent circuit fitting of experimental data. ....	85
Table 5.3 Lattice parameters of Sb, K <sub>1</sub> Sb, c-K <sub>3</sub> Sb and h-K <sub>3</sub> Sb phases. ....	88
Table 6.1 The electrochemical performance of reported RP or BP composites in PIBs. ....	123
Table 6.2 Cell resistance (R <sub>s</sub> ) and charge transfer resistance (R <sub>ct</sub> ) resistance of SEI of BP/G electrodes from equivalent circuit fitting of experimental data in Figure 6.14. ....	127

## List of abbreviations

2Me-THF	2-methyltetrahydrofuran
AFM	atomic force microscopy
BP	black phosphorus
CMC	carboxymethyl cellulose
CV	cyclic voltammetry
DEC	diethyl carbonate
DFT	density functional theory
DGME, G2	diglyme electrolyte
DI	deionized
DMC	dimethyl carbonate
DME, G1	dimethoxyethane/ethylene glycol dimethyl ether
DMF	dimethylformamide
EC	ethylene carbonate
EDS	energy dispersive spectrometer
EELS	electron energy loss spectrometry
EIS	electrochemical impedance spectroscopy
EMC	ethyl methyl carbonate
FEC	fluoroethylene carbonate
G1-Bu	ethylene glycol dibutyl ether
G1-Et, EGDEE	ethylene glycol diethyl ether

G2-Bu	diethylene glycol dibutyl ether
G2-Et	diethylene glycol diethyl ether
G3	triethylene glycol dimethyl ether
G4	tetraethylene glycol dimethyl ether
GITT	galvanostatic intermittent titration technique
HAADF	high-angle annular dark field
HEBM	high-energy ball milled
HFE	1,1,2,2-tetrafluoroethyl-2,2,2-trifluoroethyl ether
HRTEM	high-resolution transmission electron microscopy
ICE	initial Coulombic efficiency
KFSI	potassium bis(fluorosulfonyl)imide
KMP	potassium metal polyanionic compound
KTFSI	potassium bis(trifluoromethanesulfonyl)imide
LIB	lithium ion battery
LiFSI	lithium bis(trifluoromethane)sulfonimide
LSV	linear sweep voltammetry
NaFSI	sodium bis(trifluoromethane)sulfonimide
NF	nanofiber
PAN	polyacrylonitrile
PBA	prussian blue analog
PC	propylene carbonate
PIB	potassium ion battery

RP	red phosphorus
SAED	Selected area electron diffraction
SEI	solid electrolyte interphase
SEM	scanning electron microscopy
SIB	sodium ion battery
SP	super P
STEM	scanning transmission electron microscopy
TEP	triethyl phosphate
TGA	thermogravimetric analysis
THF	tetrahydrofuran
TMD	transition metal dichalcogenide
TMO	transition metal oxide
TMP	trimethyl phosphate
TMS	tetramethylene sulfone
VGCF	vapor grown carbon fiber
WP	white phosphorus
XPS	X-ray photoelectron spectroscopy
XRD	X-ray diffraction

# Chapter 1

## Introduction

This chapter summarizes the overall advantages of potassium ion batteries (PIBs) and presents a concise literature review on cathode materials, electrolytes, and anode materials for PIBs.

### 1.1 Potassium ion batteries

The rechargeable batteries rely on the intercalation and deintercalation of cations become indispensable energy storage systems for a wide range of devices from portable electronic devices to electric vehicles.<sup>1-2</sup> The battery mainly consists of a cathode (positive electrode), an anode (negative electrode), and an electrolyte.<sup>3</sup> Upon charging, the cations are released from the cathode and immigrate through the electrolyte to the anode. A reversed process occurs in the discharging process (Figure 1.1a). The most successful representatives are lithium ion batteries (LIBs). They quickly dominant the portable electronic marks after commercialization in 1991 by Sony due to the high energy density. Nevertheless, the fast-growing demands on LIBs in recent years raise concerns about the sustainable supply of scarce lithium resources. On the other hand, the popular cathode of LIBs requires the utilization of toxic Co element, discouraging the application in large-scale energy storage.<sup>4</sup> Therefore, batteries using other cations are developed, including sodium ion batteries (SIBs),<sup>5</sup> potassium ion batteries (PIBs),<sup>6</sup> magnesium ion batteries (MIBs),<sup>7</sup> aluminium ion batteries (AIBs),<sup>8</sup> zinc ion batteries (ZIBs)<sup>9</sup> and calcium ion batteries (CIBs).<sup>10</sup> In particular, PIBs have received more and more attention considering the similarities in the intercalation chemistry with LIBs. As presented in Figure 1.1b, the number of reported papers related to PIBs has been significantly increased since 2015.

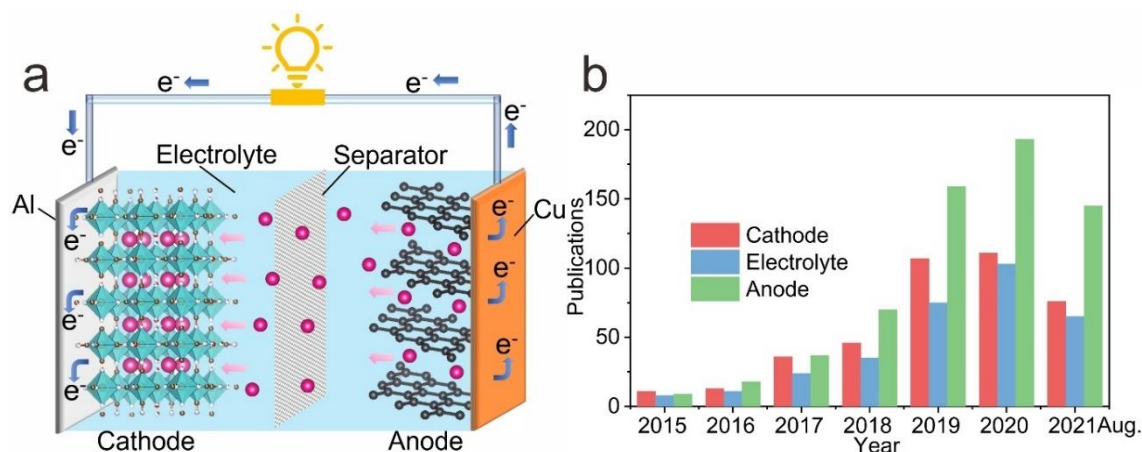


Figure 1.1 (a) The schematic of alkali-metal ion battery under discharging process. (b) Number of publications related to PIBs (until 2021 August).

PIBs hold several advantages over LIBs for large-scale energy storage (Table 1.1). The main merits are as follows:

- i) The K element is much more abundant than the Li element in the earth crust (2.6 wt.% vs. 0.02 wt.%), largely dissipating the concerns of long-term and sustainable lithium supply.<sup>11</sup>
- ii) The electrolyte salts in PIBs, such as potassium hexafluorophosphate ( $\text{KPF}_6$ , 338 USD  $\text{kg}^{-1}$ ), are much cheaper than that in LIBs (for instance, 7113 USD  $\text{kg}^{-1}$  for lithium hexafluorophosphate ( $\text{LiPF}_6$ )).<sup>12</sup>
- iii) The standard redox potential of  $\text{K}^+/\text{K}$  (-2.93 V vs. standard hydrogen electrode (SHE)) is close to  $\text{Li}^+/\text{Li}$  (-3.04 V vs. SHE) and lower than the Na counterpart (-2.71 V vs. SHE).<sup>13</sup> Particularly, the  $\text{K}^+/\text{K}$  presents the lowest standard redox potential of -2.88 V and the smallest Stokes' radius of 3.6 Å in the non-aqueous electrolyte among alkali metals, which promises a high operation voltage for improving the energy density and fast ionic transportation for realizing high-power density.<sup>14</sup> The lower desolvation energies of K ions with organic electrolyte solvent than the Li and Na counterpart further benefit the rate performance.<sup>15</sup>
- iv) Al could be used as the current collector in the anode side since K does not alloy with Al, reducing the manufacturing cost.

Nevertheless, the larger ionic radius of K ion (1.38 Å) poses challenges to the electrode design. Current electrode materials are inherited mainly from the counterparts developed in LIBs.

Table 1.1 Physicochemical properties of Li, Na and K.<sup>12, 15</sup>

Parameter	Li	Na	K
Abundance in the earth crust	0.02 wt. %	2.7 wt. %	2.6 wt. %
Price of APF <sub>6</sub> electrolyte salt <sup>a</sup>	7113 USD kg <sup>-1</sup>	200 USD kg <sup>-1</sup>	338 USD kg <sup>-1</sup>
Standard redox potential in water (vs. SHE)	-3.04 V	-2.71 V	-2.93 V
Standard redox potential in PC (vs. SHE)	-2.79 V	-2.56 V	-2.88 V
Stokes' radius in PC	4.8 Å	4.6 Å	3.6 Å
Desolvation energy in PC	215.8 kJ mol <sup>-1</sup>	158.2 kJ mol <sup>-1</sup>	119.2 kJ mol <sup>-1</sup>
Ionic radius	0.76 Å	1.06 Å	1.38 Å

<sup>a</sup> A represents Li, Na and K, respectively.

## 1.2 Cathodes materials for PIBs

The cathode materials play a critical role in determining the energy density of PIBs. Several types of cathodes are developed in the past several years, including the Prussian blue analogs, layered transition-metal oxides, polyanionic compounds, and organic materials.

### 1.2.1 Prussian blue analogs (PBAs)

PBAs are the most popular cathode candidates. They have the general formula of  $K_x TM1[TM2(CN)_6]_{1-y} \cdot zH_2O$ , where TM1 and TM2 are transition metals, which can be same or different;  $z$  is the number of  $H_2O$ . The PBA has a three-dimensional network structure, which can host K ion in its interspace.<sup>16</sup> In the structure of PBAs, TM1 and TM2 are octahedrally coordinated with six C and N atoms to form TM1-C≡N-TM2 sequences (Figure 1.2). The synthesis methods of PBA have usually utilized coprecipitation procedures in aqueous solutions using potassium ferrocyanide ( $K_4[Fe(CN)_6] \cdot 3H_2O$ ) and transition metals salts as precursors. This method is environmentally benign, low-cost, and easy for mass production.

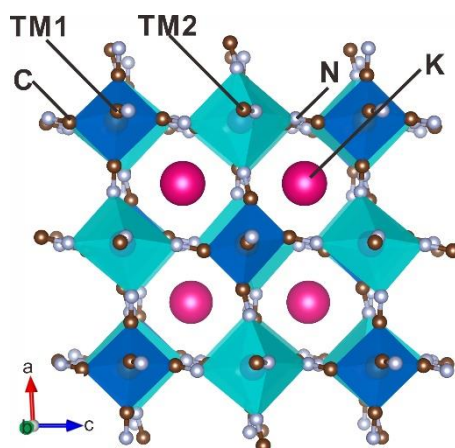


Figure 1.2 The crystal structure of  $K_x TM1 [TM2(CN)_6]_{1-y}$ .

The  $K_x Fe [Fe(CN)_6]$  was first used as cathode in PIBs by A. Eftekhari *et al.* in 2005.<sup>17</sup> It shows an excellent discharge capacity of  $74 \text{ mAh g}^{-1}$  under  $25 \text{ mA g}^{-1}$  with a moderate average voltage of  $2.7 \text{ V}$ , based on the  $Fe^{2+}/Fe^{3+}$  redox couple (Figure 1.3a). To further enhance the capacity, PBAs with multi-metal redox couples are developed. In 2017, J. B. Goodenough and co-workers<sup>18</sup> synthesized a cyanoperovskite  $K_x MnFe(CN)_6$  ( $0 \leq x \leq 2$ ) particles as an advanced cathode for PIBs. The  $K_x MnFe(CN)_6$  shows a monoclinic structure in which  $Mn^{2+}$  and  $Fe^{2+}$  ions occupy the Mn-N and Fe-C octahedra. Two plateaus at  $4.23 \text{ V}$  and  $4.26 \text{ V}$  are observed in the charging process, corresponding to K ions extraction to form  $MnFe(CN)_6$ . Upon discharge, there are two plateaus at about  $3.9$  and  $3.7 \text{ V}$ , which originate from the reverse reactions. It delivers about  $134 \text{ mAh g}^{-1}$  reversible capacity under  $25 \text{ mA g}^{-1}$ , much higher than the counterparts with single-metal redox couples (Figure 1.3b). Although the specific capacity is improved from  $K_x Fe [Fe(CN)_6]$  to  $K_x MnFe(CN)_6$ , the  $K_x MnFe(CN)_6$  structure still exists a small amount of  $Fe(CN)_6$  vacancies and water due to the fast nucleation in aqueous solution, which will reduce the specific capacities of PBA. Furthermore, ethylenediaminetetraacetic acid dipotassium salt is applied to slow down the nucleation growth for obtaining  $5\text{-}200 \text{ nm}$   $K_2 Mn [Fe(CN)_6]$  cubes with negligible content of defects and water.<sup>19</sup> The reversible capacity can be further enhanced to  $154.7 \text{ mAh g}^{-1}$  for  $K_2 Mn [Fe(CN)_6]$  under a current density of  $15 \text{ mA g}^{-1}$  with an average potential of  $3.94 \text{ V}$ . The K ion storage mechanism of  $K_2 Mn [Fe(CN)_6]$  follows the monoclinic-cubic-tetragonal pathways. The  $K_2 Mn [Fe(CN)_6]$  successively releases two K to form  $K Mn^{2+} [Fe^{3+}(CN)_6]$ , and  $Mn^{3+} [Fe^{3+}(CN)_6]$  at the end of charge. The reverse-phase transition of  $Mn^{3+} [Fe^{3+}(CN)_6]$  to  $K_2 Mn [Fe(CN)_6]$  is recovered in discharging process. The

framework structure of  $\text{K}_2\text{Mn}[\text{Fe}(\text{CN})_6]$  can be well maintained toward extraction and insertion of K ions.

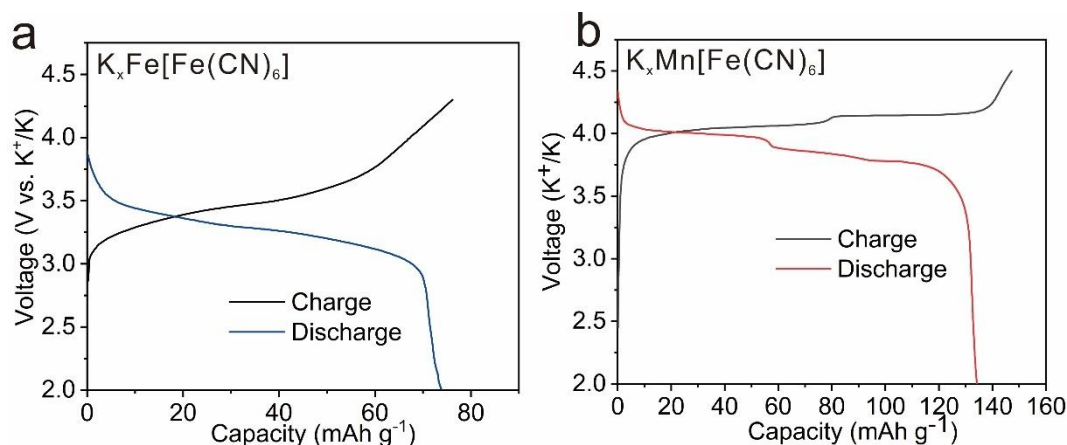


Figure 1.3 The discharge and charge curves of (a)  $\text{K}_x\text{Fe}[\text{Fe}(\text{CN})_6]$  and (b)  $\text{K}_x\text{Mn}[\text{Fe}(\text{CN})_6]$  for PIBs under  $25 \text{ mA g}^{-1}$ .

### 1.2.2 Layered transition metal oxides

The layered transition metal oxides (TMOs) have the general formula of  $\text{K}_x\text{TMO}_2$ , where the TM is the transition metals and can be a mixture of more than one element. The TMOs structure consists of  $\text{TMO}_6$  layers and K ion layers. It has three kinds of stack orders, *i.e.*, P2-type, P3-type, and O3-type (Figure 1.4), where P represents the prismatic sites occupied by K ion and O is for octahedral sites, and the value followed P and O represents the K layers in the unit cell. Encouraged by the  $\text{LiCoO}_2$  cathode in LIBs, the TMOs based on the redox couple of  $\text{Co}^{3+}/\text{Co}^{4+}$  are also studied for PIBs. The P2-type  $\text{K}_{0.6}\text{CoO}_2$  is investigated for highly reversible potassium ion intercalation by Kim *et al.*<sup>20</sup>. It delivers a capacity of about  $80 \text{ mAh g}^{-1}$  with the K varies from 0.33 to 0.68, which shows a redox potential of about 2.7 V vs.  $\text{K}^+/\text{K}$ . The TMOs based on Mn redox couples of  $\text{Mn}^{3+}/\text{Mn}^{4+}$  are represented as the  $\text{K}_x\text{MnO}_2$  ( $0.3 \leq x \leq 0.6$ ). In 2016, S. Passerini and co-workers<sup>21</sup> first studied the cathode  $\text{K}_{0.3}\text{MnO}_2$ , a layered birnessite material with a P2-type structure. It possesses a capacity of  $136 \text{ mAh g}^{-1}$  between 4.0 V and 1.5 V but shows a fast capacity degradation after 50 cycles. Kim *et al.* proposed P3-type  $\text{K}_{0.5}\text{MnO}_2$  as a potential cathode material for PIBs. It exhibits a higher capacity of  $100 \text{ mAh g}^{-1}$  than the P2-type  $\text{K}_{0.3}\text{MnO}_2$  and shows a good cycling performance over 100 cycles.<sup>22</sup> In 2018, Kim *et al.*

successfully synthesized O3-type  $\text{KCrO}_2$  material, demonstrating a reversible capacity of  $92 \text{ mAh g}^{-1}$  with an average voltage of about  $2.73 \text{ V}$ .<sup>23</sup>

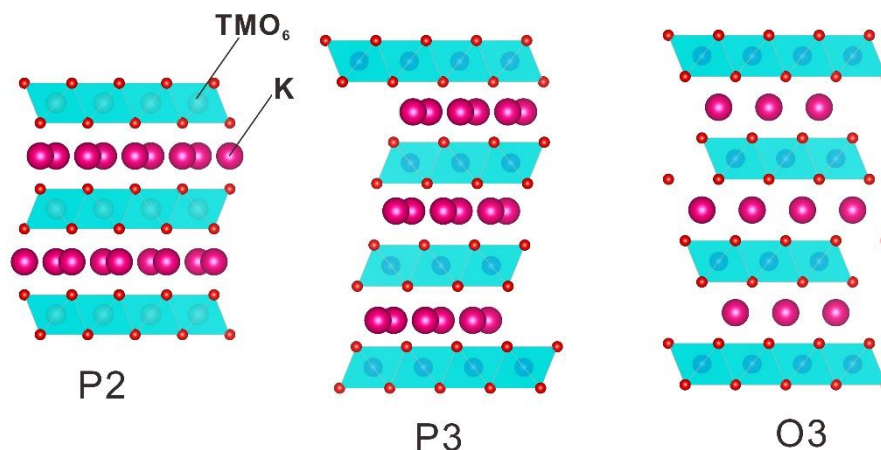


Figure 1.4 The structures of P2-type, P3-type and O3-type  $\text{K}_x\text{TMO}_2$ .<sup>24</sup>

### 1.2.3 Polyanionic compounds

The polyanionic compounds (KMPs) have a large family, including fluorophosphates, pyrophosphates, phosphates, and sulfates. The KMPs have a general formula of  $\text{K}_x\text{TM}_y(\text{XO}_4)_z$ , where the TM is transition metals that can be more than one elements, and X is usually P or S elements. The anion unit  $\text{XO}_4$  possesses the tetrahedron sites, TM-O is octahedral, and K ions are hosted in interstitial sites (Figure 1.5a). Among these KMPs, the vanadium (V)-based polyanionic compounds are the most popular due to their high voltage and capacities in PIBs, corresponding to the high redox couples of  $\text{V}^{5+}/\text{V}^{4+}$  and  $\text{V}^{4+}/\text{V}^{3+}$ .  $\text{K}_x\text{V}_y(\text{PO}_4)_z$  composites have been extensively investigated as cathode materials in PIBs. Han *et al.* prepared  $\text{K}_3\text{V}_2(\text{PO}_4)_3/\text{C}$  nanocomposites *via* solid-state reaction under a high temperature. The  $\text{K}_3\text{V}_2(\text{PO}_4)_3/\text{C}$  shows a discharge capacity of  $54 \text{ mAh g}^{-1}$  with an average voltage of about  $3.0 \text{ V}$ .<sup>25</sup> Furthermore, the F anion with the highest electronegativity is introduced into the polyanionic to forming a  $\text{K}_x\text{TM}_y(\text{XO}_4)_n\text{F}_m$  structure (Figure 1.5b), which can highly improve the operating voltages and energy densities. This is because the inductive effect decreases the strength of TM-O covalent bond, resulting in higher redox potentials.<sup>26</sup> Lin *et al.*<sup>27</sup> used  $\text{Na}_3\text{V}_2(\text{PO}_4)_2\text{F}_3$  as a precursor to prepare  $\text{K}_3\text{V}_2(\text{PO}_4)_2\text{F}_3$  by *in situ* exchanging Na with K during the discharging/charging processes. Such a new fluorophosphate cathode  $\text{K}_3\text{V}_2(\text{PO}_4)_2\text{F}_3$  shows a high reversible capacity of about  $100 \text{ mAh g}^{-1}$  with two obvious plateaus at  $4.0$  and  $3.2 \text{ V}$  (Figure 1.5c). The K insertion

process is highly reversible, maintaining excellent cyclic performance. Moreover, Chihara *et al.* successfully synthesized  $\text{KVPO}_4\text{F}$  material, which shows a relatively high discharging potential of 4.0 V and decent reversible capacity of  $92 \text{ mAh g}^{-1}$  in PIBs.<sup>28</sup>

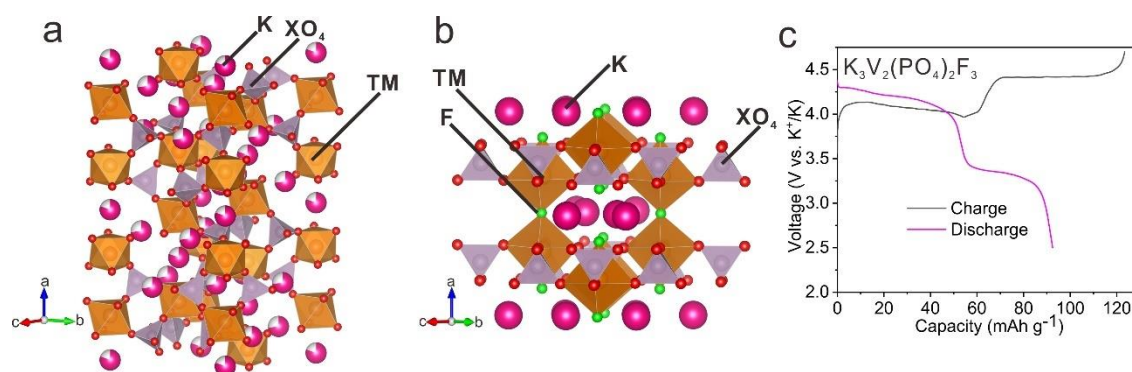


Figure 1.5 The crystal structures of (a)  $\text{K}_x\text{TMy}(\text{XO}_4)_z$  and (b)  $\text{K}_x\text{TMy}(\text{XO}_4)_n\text{F}_m$ ; (c) The discharge and charge curves of  $\text{K}_3\text{V}_2(\text{PO}_4)_2\text{F}_3$  for PIBs under  $20 \text{ mA g}^{-1}$ .

#### 1.2.4 Organic materials and others

Compared to the inorganic cathode materials, the studies of organic cathode materials are still in infancy. More importantly, the organic cathodes need to be potassiated to incorporate K ions in their hosts due to the absence of K source in the original structure. According to the insertion and extraction mechanisms, the organic cathode can be divided into cation-type and anion-type. The cation-type organic materials mainly use  $\text{C}=\text{O}$  bonds to capture K ions, as presented in Figure 1.6a. This kind of material is represented by 3,4,9,10-perylene-tetracarboxylic acid dianhydride (PTCDA), which can deliver a high reversible capacity of  $131 \text{ mAh g}^{-1}$  with an average operating voltage of about 2.5 V.<sup>29</sup> The anion-type cathodes use the N atoms with a positive charge to attract the  $\text{FSI}^-$  or  $\text{PF}_6^-$  anions (Figure 1.6b). For instance, the Poly(N-vinylcarbazole) (PVK) is a good candidate for the anion-type organic cathode. It can deliver a decent specific capacity of  $138 \text{ mAh g}^{-1}$  with a high average potential of 4.05 V in PIBs, ascribed to the unique redox pair and the low molecular weight.<sup>30</sup>

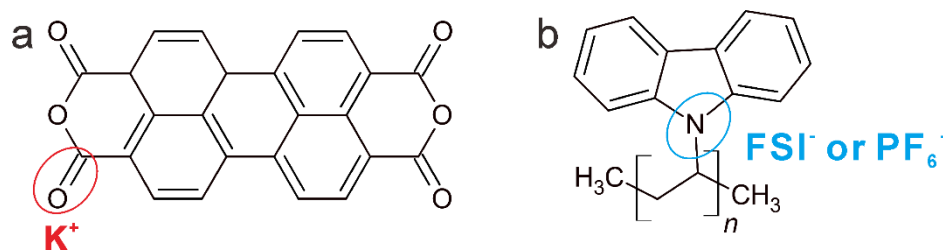


Figure 1.6 The chemical structure of (a) cation-type cathode of PTCDA and (b) anion-type cathode of PVK.

Some other cathodes based on graphitic carbon are also researched these years. For example, Tan *et al.* investigated free standing graphite cathode for PIBs by the venture of dual-anion intercalation of  $\text{FSI}^-$  and  $\text{PF}_6^-$ . It shows a high average potential of 4.65 V and an attractive capacity of  $94 \text{ mAh g}^{-1}$ , which can be stabilized for more than 100 cycles.<sup>31</sup>

The cathodes mentioned above materials are compared in Figure 1.7. It can be found that:

- i) The Prussian blue analogs have the highest specific capacities and decent operating voltages among all the cathodes, presenting great potentials for application in PIBs.
- ii) The layered transition metal oxides exhibit low capacities and moderate voltages because of the heavy transition metal and low K content.
- iii) The vanadium-based polyanionic compounds possess high operating voltages corresponding to the redox couples of  $\text{V}^{5+}/\text{V}^{4+}$  and  $\text{V}^{4+}/\text{V}^{3+}$ .
- iv) Cation-type organic materials have much higher capacities and voltages than anion-type, comparable to the Prussian blue analogs.

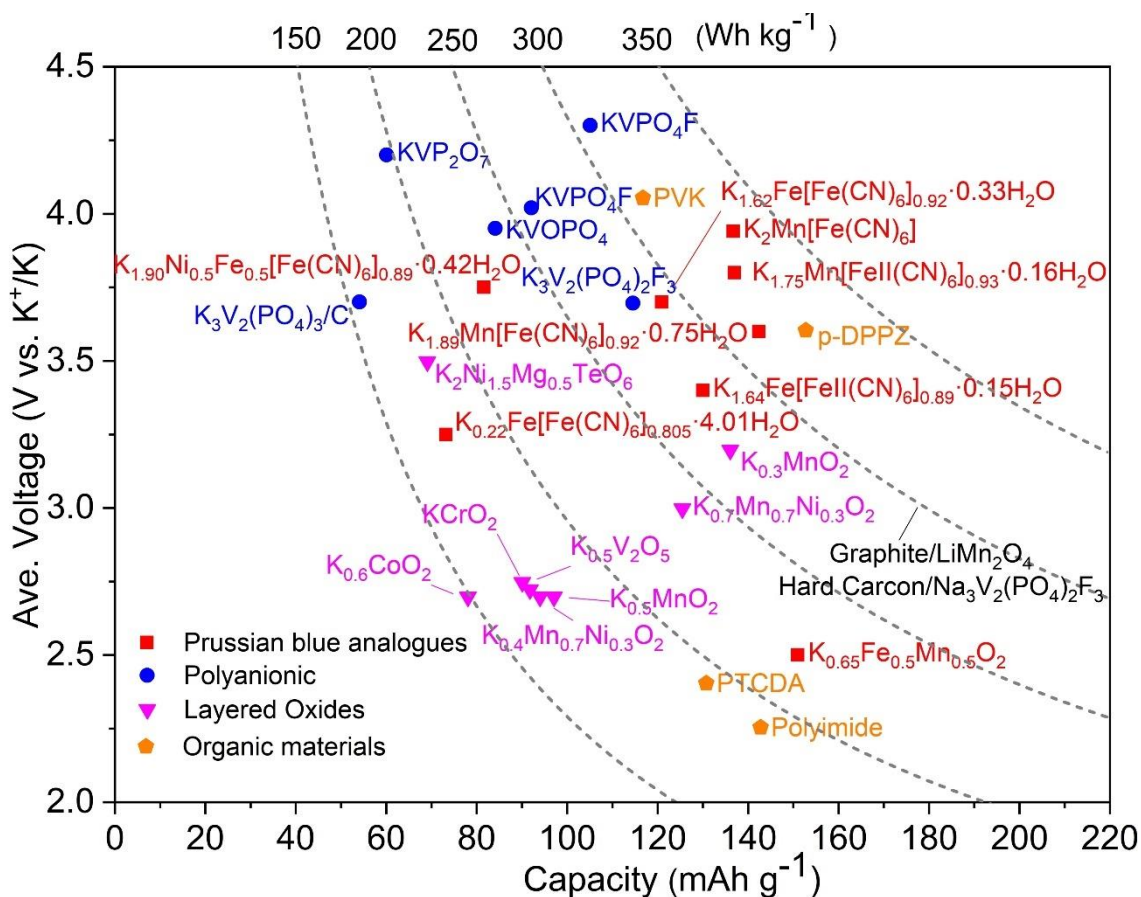


Figure 1.7 A summary of promising cathode materials for PIBs.<sup>18-19, 25, 28-30, 32-49</sup>

### 1.3 Electrolytes for PIBs

Electrolytes are made of salts and solvents with/without additives, playing pivotal roles in electrochemical performances. Two main parameters need to be considered for the electrolyte design, *i.e.*, ionic conductivity and electrochemical stability.<sup>50</sup> The electrolyte ion conductivity determines the reaction kinetics, which is affected by the dissociation and viscosity of the electrolyte.<sup>51</sup> The electrochemical stability, on the one hand, dictates the operation voltage. On the other hand, it controls the electrode/electrolyte interfaces on both the cathode and anode sides. Functional additives are developed to help build robust interfaces. Other parameters, like flashing point and flammability, should also be taken into account for electrolyte design.

### 1.3.1 Salts

The commonly used electrolyte salts in the PIBs include potassium hexafluorophosphate ( $\text{KPF}_6$ ), potassium bis(fluorosulfonyl)imide (KFSI) and potassium bis(trifluoromethanesulfonyl)imide (KTFSI) (Figure 1.8) due to their high solubilities in both ester and ether solvents. In 2017, Xiao *et al.* firstly used KFSI as an electrolyte salt in PIBs. It is found that the KFSI salt leads to high reversibility in the K plating and stripping owing to the formation of uniform solid electrolyte interphase (SEI) on the K metal anode. Later, Zheng *et al.* in 2018 investigated the electrochemical cyclic performances of Bi anode can be remarkably improved when replacing  $\text{KPF}_6$  with KFSI salt.<sup>52</sup> After that, the KFSI and KTFSI become the popular choices, in which KTFSI has a similar structure with KFSI (Figure 1.8)

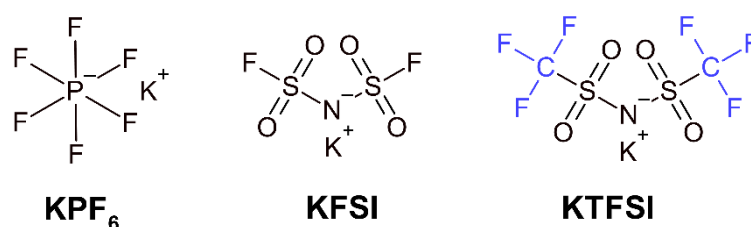


Figure 1.8 The chemical structures of the  $\text{KPF}_6$ , KFSI and KTFSI salts.

### 1.3.2 Ester solvents

The ester solvents can divide into cyclic carbonates and linear carbonates. As presented in Figure 1.9, ethylene carbonate (EC) and propylene carbonate (PC) belong to cyclic carbonates. The linear carbonates include dimethyl carbonate (DMC), ethyl methyl carbonate (EMC) and diethyl carbonate (DEC). It has been reported the cyclic carbonates are much more stable than linear ones at low potentials.<sup>53</sup> In contrast, linear carbonate has a low viscosity, the reason why a mixture of cyclic and linear carbonate is adopted in most studies. The physical and chemical properties of these solvents are compared in Table 1.2. The cyclic esters, EC and PC, have a larger dielectric constant than the linear esters, suggesting the high capabilities of EC and PC to dissolve salts. More importantly, EC and PC have a high flash point over  $100\text{ }^\circ\text{C}$ , which is much safer than DMC, EMC and DEC with a flashpoint below  $25\text{ }^\circ\text{C}$ . However, the high melting point of EC ( $36.4\text{ }^\circ\text{C}$ ) makes it a solid state at room temperature. Therefore, EC is usually mixed with other linear carbonates, forming the EC/DMC (1:1 vol.%), EC/EMC

(1:1 vol.% or 3:7 vol.%) or EC/DEC (1:1 vol.%) electrolyte solvents. Moreover, the fluoroethylene carbonate (FEC), a fluoride cyclic carbonate, is usually added to the electrolyte as an additive (2-5 vol.%) to boost the electrochemical performance on account of its ring-opening polymerization.<sup>54</sup>

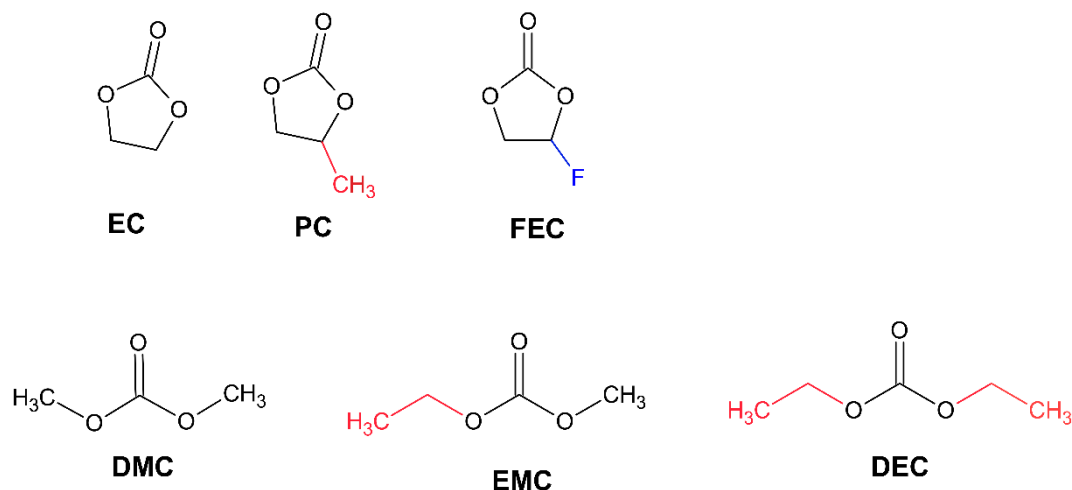


Figure 1.9 The chemical structures of the ester solvents and FEC additive.

Table 1.2 The physical and chemical properties of the commonly used ester solvents (The data are collected from the safety data sheets of Sigma-Aldrich and previous publications<sup>51, 55-56</sup>).

Solvent	CAS No.	Melting point $T_m/^\circ\text{C}$	Boiling point $T_b/^\circ\text{C}$	Flash point $T_f/^\circ\text{C}$	Dielectric constant $\epsilon$ (25 °C)	Viscosity $\eta$ /cp
EC	96-49-1	36.4	243	143	89.78	1.9 (40 °C)
PC	108-32-7	-55	240	116	64.92	2.53 (25 °C)
DMC	616-38-6	4.6	90	16	3.107	0.59 (20 °C)
DEC	105-58-8	-43	126	25	2.805	0.75 (25 °C)
EMC	623-53-0	-55	101	23.9	2.958	0.89 (25 °C)
FEC	114435-02-8	20	212	102.2	110	4.1 (40 °C)

## 1.3.3 Ether solvents

Ether-based electrolytes in batteries were first used in 1972 by Whittingham at a low operation voltage of 3 V. However, it was abandoned later due to the unstable reactions beyond 4 V, which is required for most intercalation cathode such as  $\text{LiCoO}_2$ .<sup>57</sup> Similar to ester solvents, the ether solvents also consist of linear and cyclic ethers. The linear ethers used in PIBs are usually glycol diethers, *i.e.* glymes, which are saturated polyethers containing only C, H and O elements. As presented in Figure 1.10, glymes with different chain lengths can be divide into ethylene glycol dimethyl ether (G1 or DME), diethylene glycol dimethyl ether (G2 or DGME), triethylene glycol dimethyl ether (G3), tetraethylene glycol dimethyl ether (G4), and their derivatives with different terminal groups. When the terminal methyl groups are replaced by ethyl, they will turn to ethylene glycol diethyl ether (G1-Et or EGDEE) and diethylene glycol diethyl ether (G2-Et). Similarly, they will become ethylene glycol dibutyl ether (G1-Bu) and diethylene glycol dibutyl ether (G2-Bu) when the terminal group is butyl. From Table 1.3, it can be seen that the melting, boiling and flash points of glymes increase with the chain length, and they have a dielectric constant of 5-7. Up to now, the development of ether-based electrolytes is still in infancy; only several kinds of ether solvents (G<sub>1</sub>, G<sub>2</sub>) are adopted.<sup>58-59</sup>

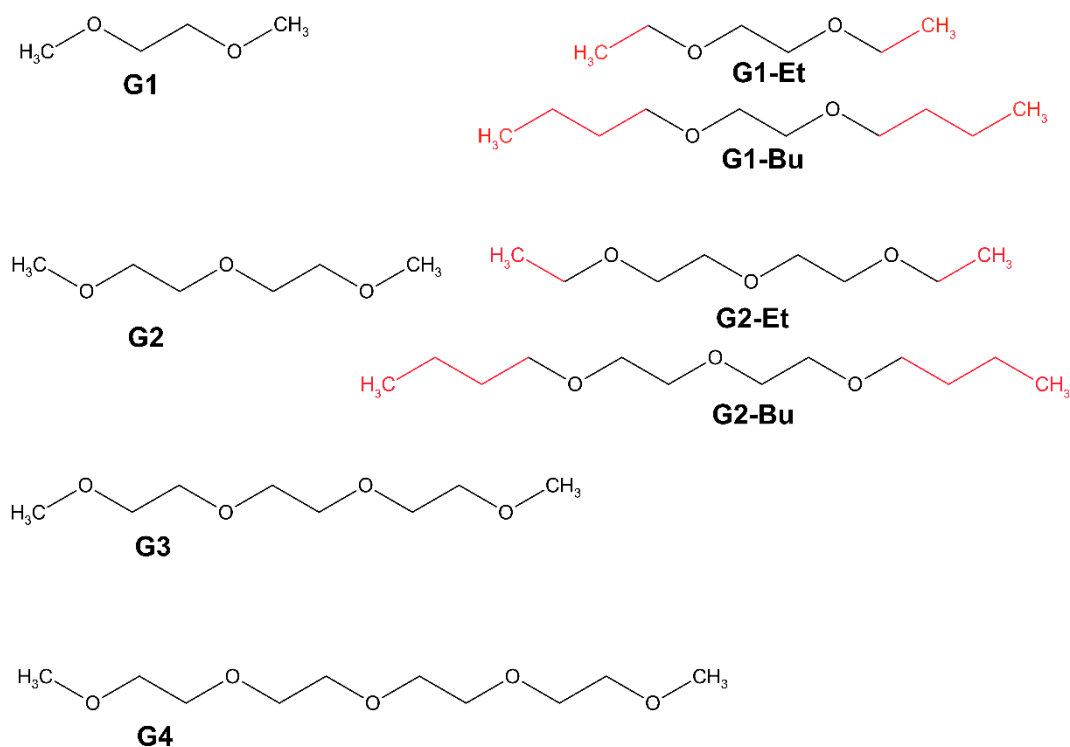


Figure 1.10 The chemical structures of the glyme-based solvents.

The cyclic ethers include mainly tetrahydrofuran (THF) and 2-methyltetrahydrofuran (2Me-THF) (Figure 1.11). The THF and 2Me-THF solvents are rarely explored in PIBs but have been systematically explored in LIBs. In 2019, a LiF-rich SEI was constructed by Chen *et al.* via the utilization of 2.0 M LiPF<sub>6</sub>/THF+2Me-THF (1:1 vol.%) electrolyte,<sup>55</sup> realizing stable cycling of micro-sized Si, Bi, and Al anodes in LIBs. However, the low flash point of THF and 2Me-THF makes it hard to be applied in real cells due to safety issues (Table 1.3). Besides, 1,1,2,2-tetrafluoroethyl-2,2,2-trifluoroethyl ether (HFE) can be used as F-containing additive and diluent in the electrolyte (Figure 1.11).

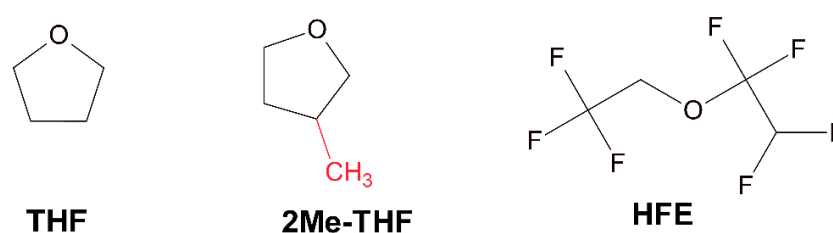


Figure 1.11 The chemical structures of the cyclic ether solvents and HFE additive.

Table 1.3 The physical and chemical properties of the commonly used ether solvents (The data are collected from the safety data sheets of Sigma-Aldrich and previous publications<sup>51, 55-56</sup>).

Solvent	CAS No.	Melting	Boiling	Flash	Dielectric	Viscosity $\eta$ /cp
		point	point	point	constant	
		$T_m/^\circ\text{C}$	$T_b/^\circ\text{C}$	$T_f/^\circ\text{C}$	$\epsilon$ (25 $^\circ\text{C}$ )	
G1	110-71-4	-58	85	5	7.2	0.46 (25 $^\circ\text{C}$ )
G1-Et	629-14-1	-74	121	22		0.7 (20 $^\circ\text{C}$ )
G1-Bu	112-48-1	-69	202	85		
G2	111-96-6	-64	162	57	7.3	2 (20 $^\circ\text{C}$ )
G2-Et	112-36-7	-44	188	67	5.7	1.4 (20 $^\circ\text{C}$ )
G2-Bu	112-73-2	-60	256	118		2.39 (20 $^\circ\text{C}$ )
G3	112-49-2	-45	216	113	7.5	2.5 (20 $^\circ\text{C}$ )
G4	143-24-8	-30	275	136	7.8	4.1 (20 $^\circ\text{C}$ )
THF	109-99-9	-108.4	65	-21.2	7.52	0.46 (25 $^\circ\text{C}$ )
2Me-THF	96-47-9	-20	78	-10	6.2	0.47 (25 $^\circ\text{C}$ )

HFE	406-78-0	-94	56.7	-	-	-
-----	----------	-----	------	---	---	---

### 1.3.4 Other solvents

Some other P- and S-based solvents are also investigated in PIBs due to their merit of non-flammability, as represented by trimethyl phosphate (TMP), triethyl phosphate (TEP) and tetramethylene sulfone (TMS) (Figure 1.12). In PIBs, TMP has been widely researched due to its low melting point, high boiling point, and non-flammable property (Table 1.4).<sup>60</sup> Furthermore, a higher dielectric constant of TMP compared to TEP (21.6 vs. 13), allows the preparation of highly concentrated electrolytes.<sup>61</sup> It also possesses excellent oxidative stability to be compatible with high-voltage cathodes for practical applications. TMS has large viscosity, which is detrimental for the fast K ion diffusions.

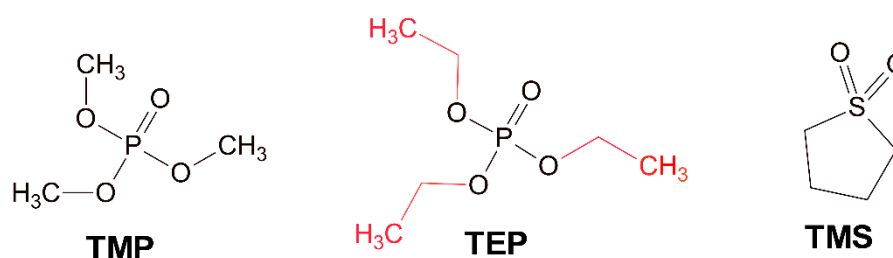


Figure 1.12 The chemical structures of the TMP, TEP and TMS solvents.

Table 1.4 The physical and chemical properties of the TMP, TEP and TMS solvents (The data are collected from the safety data sheets of Sigma-Aldrich and previous publications<sup>62-63</sup>).

Solvent	CAS No.	Melting point $T_m/^\circ\text{C}$	Boiling point $T_b/^\circ\text{C}$	Flash point $T_f/^\circ\text{C}$	Dielectric constant $\epsilon$ (25 °C)	Viscosity $\eta$ /cp
TMP	512-56-1	-46	197	150	21.6	1.3 (25 °C)
TEP	78-40-0	-56.5	215	130	13	1.6 (20 °C)
TMS	126-33-0	27	285	177	60 (20 °C)	10.34 (20 °C)

## 1.4 Anodes materials for PIBs

From the material aspects, the anode materials in PIBs can be divided into four catalogs, including carbonaceous materials, alloys, metal oxides/sulfides/selenides, and phosphorus-based materials. There are three main types of K ion storage mechanisms, *i.e.*, intercalation, conversion and alloying reaction. Some anodes may have more than one K ion storage mechanism, such as the hybrid of intercalation and conversion reactions or conversion plus alloying reactions, as presented in Figure 1.13.

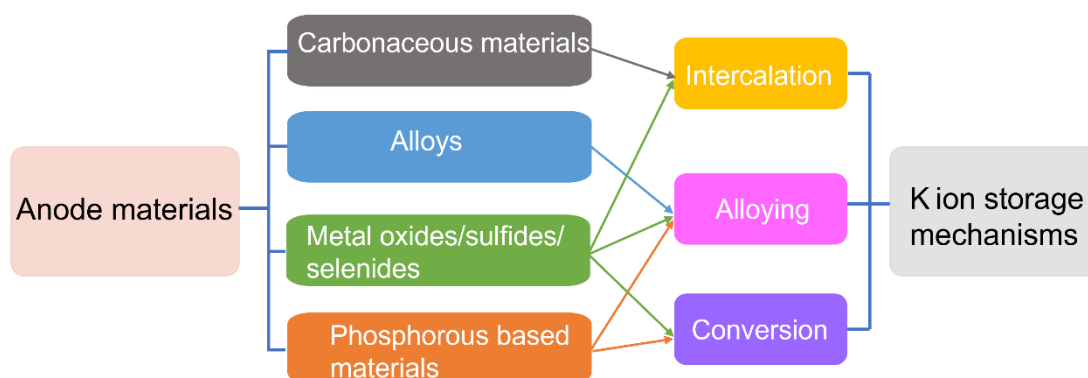


Figure 1.13 The correlation between different kinds of anodes and K ion storage mechanisms.

### 1.4.1 Carbonaceous materials

Graphite has a well-defined layered structure with a d-spacing of about 3.3 Å, which has a theoretical capacity of 279 mAh g<sup>-1</sup> for forming KC<sub>8</sub> in PIBs (Figure 1.14a). In 2015, Jian *et al.* first reported the graphite anode in PIBs,<sup>64</sup> which exhibits a reversible capacity of 273 mAh g<sup>-1</sup> in an ester-based electrolyte. However, the capacity fast fades to 100 mAh g<sup>-1</sup> after 50 cycles due to the large volume expansions for forming intercalation compounds: KC<sub>36</sub>→KC<sub>24</sub>→KC<sub>8</sub>. Later, Fan *et al.* reported that the graphite anode could be stabilized over 2000 cycles by using high concentration electrolytes.<sup>65</sup> Another two disordered carbon materials, soft carbon and hard carbon, are also applied in PIBs. The soft carbon has a turbostratic structure with considerable defects, and hard carbon has a “house of cards” structure with more nanopores and O-containing functional groups. The soft and hard carbon has a larger interlayer distance than graphite, corresponding to 3.4-3.6 and 3.7-4.0 Å, respectively. They can storage K ions *via* adsorption and insertion mechanisms (Figure 1.14b and c).<sup>66</sup> Lin *et al.* investigated the various

carbons with different disorder degree in PIBs, which show the similar reversible capacity of around  $280 \text{ mAh g}^{-1}$  but distinct voltage profiles.<sup>66</sup> Apart from those, many novel carbon materials, like heteroatom doped carbon and porous carbon, are also explored for the application in PIBs.<sup>67</sup>

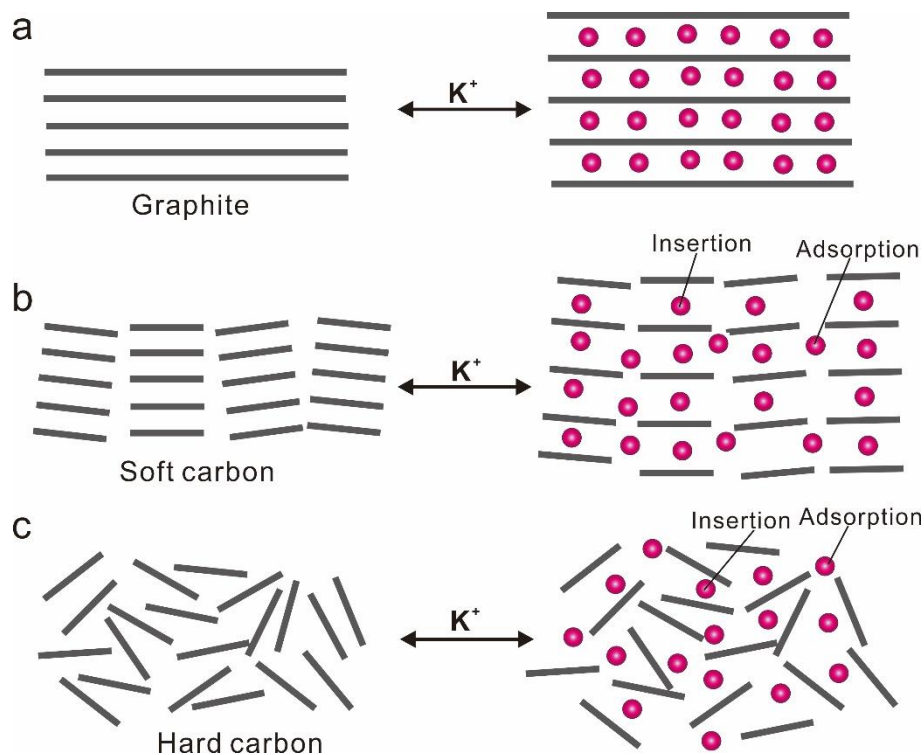


Figure 1.14 The illustration of graphite, soft carbon and hard carbon toward K ion storage.

#### 1.4.2 Alloys

Alloy anodes such as Si, Sb, Bi, Ge and Sn have long been considered promising alternatives to carbonaceous materials for high-energy PIBs.<sup>68-70</sup> These anodes could uptake several K ions per atom through alloying reactions ( $M + nK \leftrightarrow K_nM$ , M represents the Si, Sb, Bi, Ge, Sn, etc.), delivering exceptional specific capacities at appropriate potentials (Figure 1.15a). Specifically, the Sb anode shows a high theoretical capacity of about  $660 \text{ mAh g}^{-1}$  by forming the  $K_3\text{Sb}$  phase. Except for the Si anode, which has a negligible activity toward K ion storage,<sup>71</sup> the other alloy anodes are extensively investigated in PIBs.<sup>72</sup> However, accompanying the high specific capacity, these anodes suffer from a significant volume expansion higher than 200% (Figure

1.15b). Such severe structural change leads to particle fracture and fast capacity degradation during cycling.

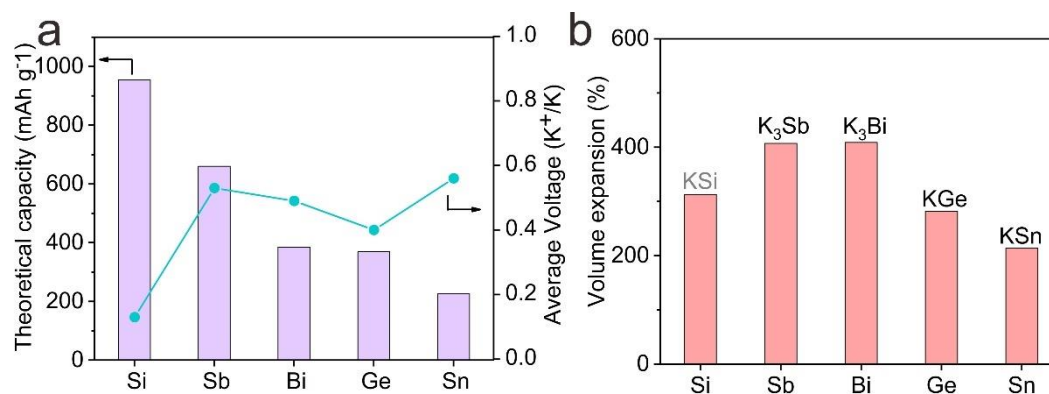


Figure 1.15 (a) Theoretical capacities and corresponding average voltages and (b) the volume expansions of various anode materials for PIBs.<sup>73</sup>

Many works have been devoted to fabricating nanostructures and optimizing electrolytes to improve the cyclic performances of alloy anodes. Ge *et al.* prepared ultra-small Sb nanocrystals within nanochannel-containing carbon nanofibers (uSb@CNF) *via* electrospinning method, which presents unprecedented cyclic stabilities with a reversible capacity of 225 mAh g<sup>-1</sup> over 2000 cycles under 1 A g<sup>-1</sup>.<sup>72</sup> Moreover, the Sb nanoparticles with an average size of 14.0 nm embedded carbon nanosheet (Sb/CNS) were prepared by Han *et al.* It can maintain a considerable capacity of 247 mAh g<sup>-1</sup> after 600 cycles under 0.2 A g<sup>-1</sup>.<sup>74</sup> Turn to the electrolyte modification, Lei *et al.* in 2018 reported that microsized Bi particles could be stabilized in 1.0 M KPF<sub>6</sub>/G1 electrolytes due to the construction of polyether-like SEI and the formation of three-dimensional porous networks.<sup>75</sup> Huang *et al.* also found the excellent cyclic stabilities of Bi microparticles with a high capacity of 394 mAh g<sup>-1</sup> over 100 cycles under 0.4 A g<sup>-1</sup> in PIBs when employing 1M KPF<sub>6</sub>/G2 as the electrolyte.<sup>59</sup> Recently, Lin *et al.* reported the micro-sized Sb can be stabilized readily by using high concentration electrolytes (4 M KFSI/G1), showing 628 mAh g<sup>-1</sup> capacities over 100 cycles under 0.1 A g<sup>-1</sup>.<sup>76</sup> In addition, some binary alloys such as SbBi and SnSb are fabricated to improve K ion storage performances by stepwise alloying.<sup>77-</sup>

### 1.4.3 Metal oxides/sulfides/selenides

The metal oxides/sulfides/selenides ( $\text{MX}_n$ , M is metal, like Co, Ni, Cu, Fe, Sb, Bi, Sn, etc.; X represents O, S or Se element) anodes have been widely studied in PIBs. Such material can storage K ions through multiple intercalations, conversion or alloying reactions and deliver remarkable capacities. More importantly, these materials do not have significant volume expansion as much as alloys. The drawback is they have a large voltage hysteresis between discharging and charging (Figure 1.16), leading to low energy efficiency.<sup>79</sup>

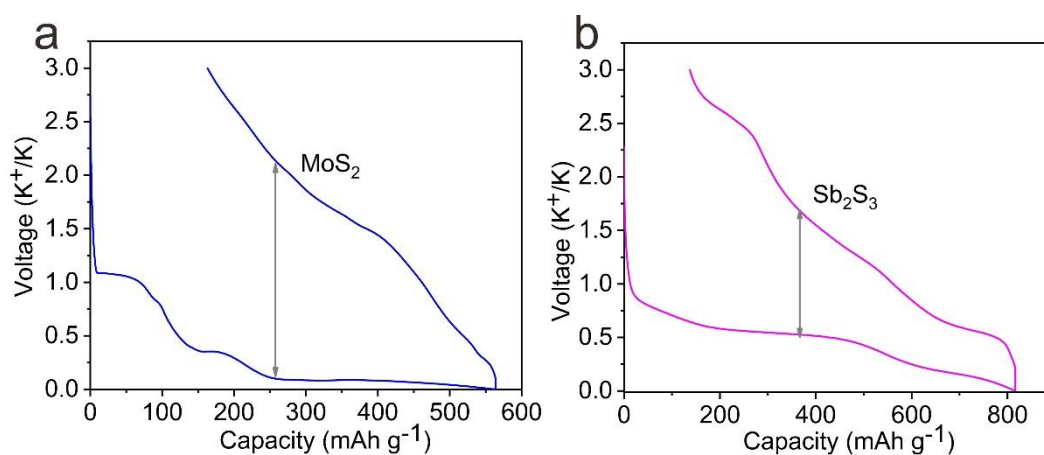


Figure 1.16 The first discharge and charge curves of (a)  $\text{MoS}_2$  and (b)  $\text{Sb}_2\text{S}_3$  anodes for PIBs under  $100 \text{ mA g}^{-1}$ .

#### i) Metal oxides

Metal oxides receive particular interest due to their excellent K ion storage performance. Adekoya *et al.* designed  $\text{Co}_3\text{O}_4$ @N-doped carbon composite as an advanced anode for PIBs, which shows a superior capacity of  $448.7 \text{ mAh g}^{-1}$  at  $50 \text{ mA g}^{-1}$  after 40 cycles. The K ion storage mechanism within the  $\text{Co}_3\text{O}_4$  electrode is based on the conversion reaction ( $\text{Co}_3\text{O}_4 + 8\text{K} \rightarrow 3\text{Co} + 4\text{K}_2\text{O}$ ).<sup>80</sup> Li *et al.* prepared  $\text{Sb}_2\text{O}_3$ -based anode ( $\text{Sb}_2\text{O}_3$ -RGO) by anchoring  $\text{Sb}_2\text{O}_3$  onto reduced graphene oxide. The  $\text{Sb}_2\text{O}_3$ -RGO composite exhibits a reversible specific capacity of  $309 \text{ mAh g}^{-1}$  after 100 cycles at  $100 \text{ mA g}^{-1}$  using an ether-based electrolyte. The electrochemical reaction process of  $\text{Sb}_2\text{O}_3$ -RGO in PIBs is firstly to form  $\text{K}_x\text{Sb}_2\text{O}_3$  via intercalation reaction ( $\text{Sb}_2\text{O}_3 + x\text{K} \rightarrow \text{K}_x\text{Sb}_2\text{O}_3$ ) and then the  $\text{K}_x\text{Sb}_2\text{O}_3$  transfers to  $\text{K}_2\text{O}$  and Sb

through conversion reaction ( $K_xSb_2O_3 \rightarrow K_xO + Sb$ ). Lastly, the generated Sb turns to  $K_3Sb$  by alloying reactions ( $Sb + 3K \rightarrow K_3Sb$ ).<sup>81</sup>

## ii) Metal sulfides

Metal sulfides have layered crystal structures with large interlayer distances.  $MoS_2$ ,  $SnS_2$  and  $Sb_2S_3$  are the typical representatives with a d-spacing of 6.3 Å, 5.9 Å and 5.7 Å, respectively. Such a large layer distance is readily for the intercalation reaction of large K ions. For instance, Yao *et al.* synthesized densified metallic  $MoS_2$  on graphene (1T- $MoS_2/G$ ) as a high-rate anode for PIBs. It shows a high capacity of 511 and 327 mAh  $g^{-1}$  under 0.1 and 1.0 A  $g^{-1}$  through intercalation ( $MoS_2 + xK \rightarrow K_xMoS_2$ ) and following conversion reactions ( $K_xMoS_2 \rightarrow Mo + K_xS$ ).<sup>82</sup> Moreover, few-layered  $Sb_2S_3$  can deliver stable capacity of 404 mAh  $g^{-1}$  after 200 cycles under 0.5 A  $g^{-1}$ .<sup>83</sup> The reaction pathways of  $Sb_2S_3$  and K include intercalation reaction ( $Sb_2S_3 + xK \rightarrow K_xSb_2S_3$ ), conversion reaction ( $K_xSb_2S_3 \rightarrow K_xS + Sb$ ) and alloying reaction ( $Sb + 3K \rightarrow K_3Sb$ ).<sup>84</sup>

## iii) Metal selenides

Compared to metal sulfides, the metal selenides have a weaker M-Se bond than M-S bond, which is favorable for fast conversion reactions. Due to the good electrical conductivity and high specific capacity, CoSe had been reported by Liu *et al.* in PIBs. The CoSe nanoparticles are embedded in an N-doped carbon nanotube (CoSe@NCNTs), exhibiting a high capacity of 435 mAh  $g^{-1}$  under 0.1 A  $g^{-1}$ . The K ion storage mechanism of CoSe is involved with interaction ( $CoSe + xK \rightarrow K_xCoSe$ ) and conversion reactions ( $K_xCoSe \rightarrow K_xSe + Co$ ).<sup>85</sup> Moreover, replacing nonactive Co with Sb can further improve the capacity of metal selenides. For example, Wang *et al.* prepared  $Sb_2Se_3$  with N-doped carbon and RGO sheet ( $Sb_2Se_3@NC@rGO$ ), which presents a high charge capacity of about 590 mAh  $g^{-1}$  under 50 mA  $g^{-1}$  and excellent cyclic stability in PIBs.<sup>86</sup>

## 1.4.4 Phosphorus based materials

### i) P anode

Phosphorus (P) shows a high capacity of  $1154 \text{ mAh g}^{-1}$  with a large volume change (301%) for forming  $\text{K}_4\text{P}_3$  through alloying reaction ( $3\text{P} + 4\text{K} \rightarrow \text{K}_4\text{P}_3$ ). P has three types of allotropes in nature, which are red phosphorus (RP), white phosphorus (WP), and black phosphorus (BP). RP is amorphous and non-toxic, while WP with  $\text{P}_4$  structure is highly flammable and pyrophoric, and BP is a stable two-dimensional layered structure material (Figure 1.17). BP and RP are widely adopted for anodes in PIBs. However, the poor electronic conductivity of P leads to sluggish kinetics toward K ion storage. Therefore, the P is usually incorporated into the conductive carbon to improve its electronic conductivity and enhance electrochemical performances.

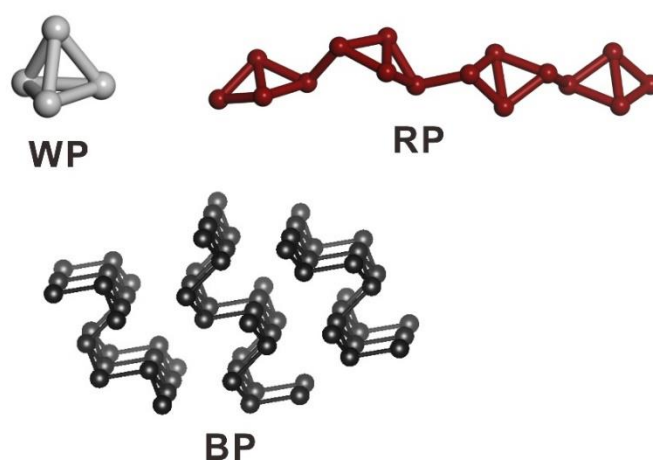


Figure 1.17 The chemical structure of WP, RP and BP.

In 2017, Sultana *et al.* synthesized BP-carbon (7:3 wt.%) nanocomposite *via* the ball milling method. It exhibits a first charge capacity of  $617 \text{ mAh g}^{-1}$  upon K ion insertion at  $50 \text{ mA g}^{-1}$  but shows fast decay in 50 cycles.<sup>87</sup> To improve the stability, Wu *et al.* used the vaporization condensation conversion method to fabricate RP nanoparticles enclosed in a free-standing carbon nanofiber with P loading of 66 wt.% (RP@N-PHCNFs). It can be maintained for 800 cycles with a capacity of  $465 \text{ mAh g}^{-1}$  under  $2 \text{ A g}^{-1}$  owing to sturdy contact between P and carbon matrix. However, it suffers from a low initial Coulombic efficiency of about 35% because of the severe electrolyte decomposition on the carbon host with large specific area. Recently, Jin *et al.* designed a layered BP-Graphite (BP-G) composite through liquid-phase exfoliation and high-energy mechanical ball milling method. The BP-G can reach  $1300 \text{ mAh g}^{-1}$

<sup>1</sup>, forming the undesired  $K_3P$  under  $250 \text{ mAh g}^{-1}$  but having fast capacity decay within 50 cycles. The reason lies in that  $K_3P$  hinders the potassiation of BP and slows down the ion diffusion rate.<sup>88</sup>

## ii) Metal phosphides

Some metal phosphides, including  $Sn_4P_3$ , FeP and  $CuP_2$  are also synthesized for the investigations in PIBs. Zhang *et al.* first reported the  $Sn_4P_3/C$  anode toward K ion storage in 2017, which shows a first reversible capacity of  $358.2 \text{ mAh g}^{-1}$  with retention of 85.7% after 50 cycles under  $50 \text{ mA g}^{-1}$ . The K ion storage processes of  $Sn_4P_3$  involve conversion reaction ( $Sn_4P_3 + (9-3x)K \rightarrow 4Sn + 3K_{3-x}P$ ) and alloying reaction ( $Sn + K \rightarrow KSn$ ).<sup>89</sup> A yolk-shell structured FeP with carbon nanoboxs (FeP@CNBs) were synthesized by Yang *et al.*, delivering a stable capacity of  $205 \text{ mAh g}^{-1}$  over 300 cycles under  $200 \text{ mA g}^{-1}$ . Moreover, the  $CuP_2$  on carbon nanosphere ( $CuP_2@CNSs$ ) was also reported by the same group.<sup>90</sup>  $CuP_2@CNSs$  harvests a high reversible capacity of  $400 \text{ mAh g}^{-1}$  under  $200 \text{ mA g}^{-1}$  by utilization of high concentration electrolyte (4 M KFSI/G1).<sup>91</sup>

### 1.4.5 Others

Some other novel anodes are also explored for PIBs. Tan *et al.* reported an insertion-type anode  $KVPO_4F$  that can deliver a capacity of  $100 \text{ mAh g}^{-1}$  between 0-3 V and excellent stability. Although polyanionic compounds are commonly used as the cathode,  $KVPO_4F$  can be employed as an anode to accept more K ion insertion because the K ion sites are not fully occupied in the original structure.<sup>92</sup> Moreover, Wang *et al.* synthesized Bi and Sb-based oxychloride ( $Bi_{0.51}Sb_{0.49}OCl/rGO$ ) on reduced graphene oxide substrate and explored it as an anode in PIBs. It shows a discharge capacity of  $319 \text{ mAh g}^{-1}$  under  $1 \text{ A g}^{-1}$ . The reaction mechanism of  $Bi_{0.51}Sb_{0.49}OCl/rGO$  in the first cycle is different from the subsequent cycles. In the first discharge, the  $Bi_{0.51}Sb_{0.49}OCl/rGO$  is converted to (Bi,Sb) alloy by the electrochemical reduction, and then the (Bi,Sb) alloy reacts with K through alloying reaction ( $(Bi,Sb) + xK \rightarrow K_x(Bi,Sb)$ ). In the subsequent cycles, the K ion storage mechanism turns to reversible alloying and dealloying reactions of (Bi,Sb) alloy.<sup>93</sup>

The anodes mentioned above materials are summarized in Figure 1.18. We can conclude that:

- i) Graphite shows excellent stability for K ion storage but suffers from low capacity. The capacity could be increased by introducing the defects and decreasing the crystallinity, albeit at the cost of high average potential.
- ii) Alloys have high capacities of around 400-600 mAh g<sup>-1</sup> and appropriate operation potentials. They are among the most promising anodes to realize high energy density PIBs, but the long-term cyclic performances remain a grand challenge.
- iii) The metal oxides/sulfides/selenides present considerable capacities in PIBs. The large voltage hysteresis restricts the practical application.
- iv) P based anodes deliver the highest theoretical capacity among all the candidates. The practical application is still afflicted by the poor electronic conductivity and fast capacity fading.

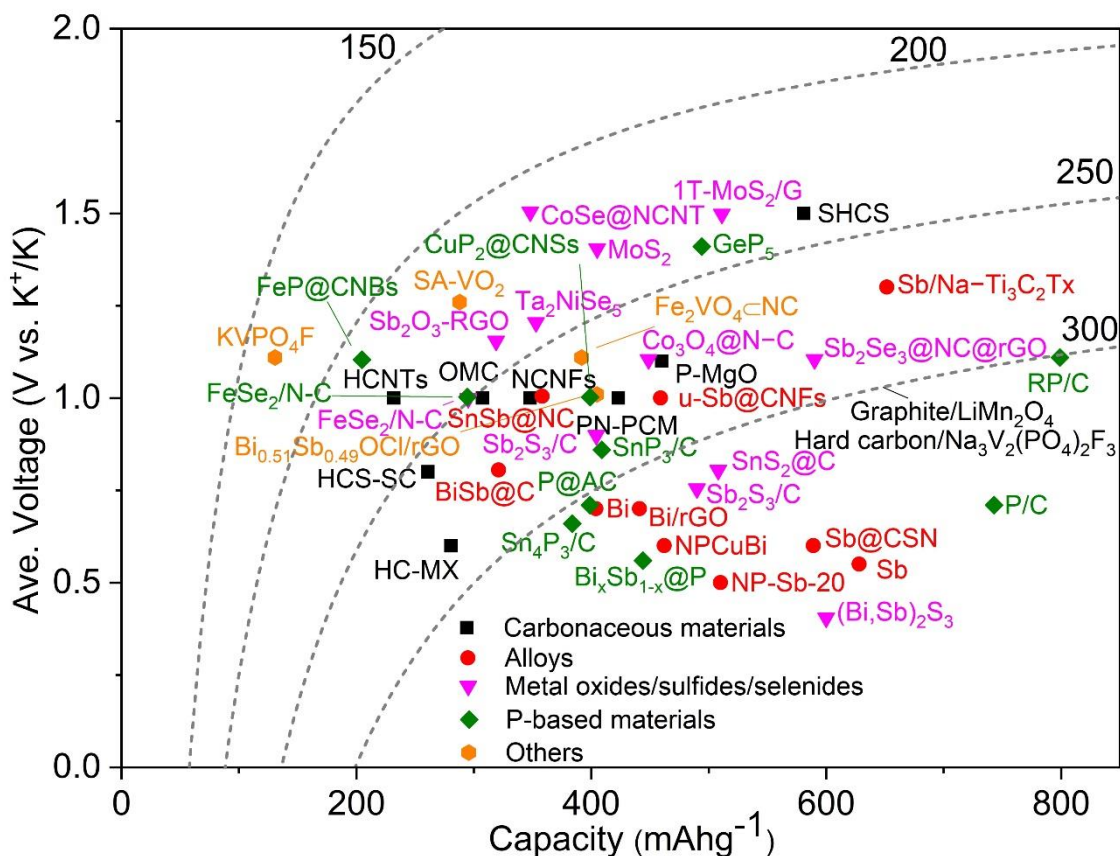


Figure 1.18 A summary of promising anode materials for PIBs.<sup>52, 58-59, 76, 80-81, 83, 85, 89, 92-111</sup>

## 1.5 Objective and outline

Advanced anodes are essential to realizing high-energy-density PIBs for potential application in large-scale energy storage. The development of high-capacity and long lifespan anodes remains a grand challenge due to the unclear insertion chemistry and large structural deformation upon K ion uptake. Currently, most of the anodes are directly inherited from the Li and Na ion technologies, and a similar mechanism is adopted for explaining the electrochemical behavior without detailed evidence. The reaction pathway and phase transformation process are critical to the fundamental understanding of K ion storage and the design of appropriate approaches to address stability issues. After disclosing the insertion chemistry, subsequent efforts are devoted to improving the cyclic stability through microstructure design and electrode/electrolyte interface optimization. The main objectives of this thesis are as follows:

- (1) To explore the K ion insertion chemistry for understanding structural evolution and compare it with Li and Na ion storage.
- (2) To design high-capacity Sb and P anodes with long-term cyclic stability through building robust SEIs.

Accordingly, the thesis is organized as follows. The progress of previous work on PIBs is summarized in **Chapter 1**. **Chapter 2** gives the experimental details of this work. The insertion chemistry comparison between Li, Na, and K ions is explored in **Chapter 3**, based on which micro-sized MoS<sub>2</sub> anode is developed in **Chapter 4**. **Chapter 5** focuses on the phase transformation of Sb anodes and the stabilization through building elastic SEIs in two new ether-based electrolytes. The concept is readily extended to Sn anodes in SIBs to generalize the approaches. **Chapter 6** centers on P anode, which is stabilized by synthesizing BP/graphite composite and building a mechanically stable SEI. The major outputs are summarized in **Chapter 7**, and the remaining issues for future studies are also presented.

## Chapter 2

### Experimental

This chapter gives detailed experimental about material syntheses, electrode and electrolyte preparations, electrochemical measurements, sample characterizations and density functional theory (DFT) calculations.

#### 2.1 Material syntheses

##### 2.1.1 MoS<sub>2</sub>/C nanofibers, carbon nanofibers and petal-like neat MoS<sub>2</sub>

MoS<sub>2</sub>/C nanofibers were prepared by electrospinning. Typically, polyacrylonitrile (PAN, 0.5 g) was dissolved in dimethylformamide (DMF, 10 mL). Ammonium tetra-thiomolybdate ((NH<sub>4</sub>)<sub>2</sub>MoS<sub>4</sub>, 0.8 g) was added under continuous stirring to get a uniform solution. Electrospinning was conducted under a high voltage of 18 kV with a feed rate of 30 μL min<sup>-1</sup> to obtain a film on Al foils. The film precursor was first stabilized at 250 °C for 4 hours in a Muffle furnace before annealing at 900 °C for 2 hours under Ar atmosphere. After the annealing, (NH<sub>4</sub>)<sub>2</sub>MoS<sub>4</sub> decomposed to MoS<sub>2</sub>, and PAN turns into carbon. The pure carbon nanofibers were prepared by the same method without adding (NH<sub>4</sub>)<sub>2</sub>MoS<sub>4</sub>. In comparison, petal-like neat MoS<sub>2</sub> was synthesized by a hydrothermal method.<sup>112</sup> Ammonium heptamolybdate tetrahydrate ((NH<sub>4</sub>)<sub>6</sub>Mo<sub>7</sub>O<sub>24</sub>·4H<sub>2</sub>O, 0.5 mmol) and thiourea (NH<sub>2</sub>CSNH<sub>2</sub>, 7 mmol) were dissolved in 35 mL deionized (DI) water. The solution was kept in a 50 mL Teflon-lined stainless steel autoclave at 220 °C for 18 hours. The final product was washed by DI water and ethanol before drying at 80 °C overnight.

##### 2.1.2 Sb nanoparticles

The Sb particles were synthesized by the chemical reduction method.<sup>113</sup> The citric acid (C<sub>6</sub>H<sub>8</sub>O<sub>7</sub>, 2.5 g) was first dissolved into 50 mL DI water and antimony trichloride (SbCl<sub>3</sub>, 570 mg) was

added under ultrasonic. The solution was diluted to 300 mL by adding DI water. The diluted solution was further put in the ultrasonic bath for 20 minutes to get a clear solution A. Sodium borohydride ( $\text{NaBH}_4$ , 600 mg) was dissolved in 60 mL DI water under ultrasonic to get solution B. Solution B was dropwise added into solution A under magnetic stirring. The mixture solution was further put in the ultrasonic bath for 3 hours for complete reaction. The black powder was collected by centrifugation and dried at 60 °C under vacuum.

### 2.1.3 Prussian blue $\text{K}_x\text{MnFe}(\text{CN})_6$

The  $\text{K}_x\text{MnFe}(\text{CN})_6$  cathode was prepared by precipitation method in an aqueous solution.<sup>18</sup> 50 wt.% manganese(II) nitrate solution ( $\text{Mn}(\text{NO}_3)_2$  solution, 2.3 g) was added into 50 mL DI water to get solution A. Potassium ferrocyanide ( $\text{K}_4[\text{Fe}(\text{CN})_6] \cdot 3\text{H}_2\text{O}$ , 1.27 g) and potassium chloride (KCl, 17.8 g) were dissolved into 100 mL DI water to form solution B. Solution A were dropwise added into solution B under magnetic stirring. After 2 hours of aging, the precipitates were collected by centrifugation and dried at 60 °C under vacuum.

### 2.1.4 Neat Sb and Sn on Cu foil

Neat Sb electrodes were prepared by the electrodeposition based on the previously reported method.<sup>114</sup> The solution consists of 0.02 M antimony trichloride, 0.1 M citric acid and 0.05 M trisodium citrate. The pH was adjusted to 2 by adding 5 M sulfuric acid. Pulsed electrodeposition was performed on Biologic SP150 electrochemical workstation using a three-electrode electrochemical cell, where Ag/AgCl was used as the reference electrode, Pt as the counter electrode and a Cu foil was pinched on the working electrode. A potential of -980 mV was applied. The pulse was 400  $\mu\text{s}$  and the time between the pulse was 800  $\mu\text{s}$ . The deposited Sb on Cu foil was washed by deionized water and dried under 60 °C. The neat Sn electrodes were prepared by magnetron sputtering on Cu foil. The distance between the Sn target and Cu foil was 10 cm, and the time for sputtering was 5 minutes at 50 W.

### 2.1.5 RP, BP, BP/G, $\text{K}_4\text{P}_3$

The amorphous red phosphorus (RP) powder (Alfa Aesar, 98%) was purified before use. RP (2 g) was washed by 200 mL boiling deionized water under the string and rinsed several times until the pH value turned neutral.<sup>115</sup> The purified RP powder was collected by centrifugation and dried at 70 °C under vacuum. RP (1 g) was sealed in the 100 mL jar under Ar atmosphere and high-energy ball milled (HEBM, SPEX 8000) for 1 hour to synthesize black phosphorus (BP). Afterward, BP (400 mg, 80 wt.%) and graphite (100 mg, 20 wt.%, KS6, MTI) were mixed by mechanical ball milling (QM-3SP2 planetary ball mill) for 48 hours under 360 rpm to

prepare BP/G composite. The ball-milled BP, RP/G or graphite preparation were similar to BP/G composite, except without adding graphite or BP. All samples were sealed under Ar atmosphere before ball milling, and the jar was open in the glovebox after the treatment. The  $K_4P_3$  was synthesized by high-energy ball milling K metal (47 mg) and BP (28 mg) powder for 30 minutes under Ar atmosphere. To avoid oxidation, all the samples were stocked in the glovebox ( $O_2 < 0.1$  ppm,  $H_2O < 0.1$  ppm).

## 2.2 Electrodes and electrolytes preparation

### 2.2.1 Electrodes

The  $MoS_2/C$  nanofibers were directly used as freestanding electrodes. Microsized  $MoS_2$  (powder,  $< 2$   $\mu m$ , 99%, Sigma Aldrich) were prepared by ball milling  $MoS_2$  powder, vapor grown carbon fibers (VGCF), super P and carboxymethyl cellulose (CMC) with a mass ratio of 7: 1: 1: 1 for 2 hours. The microsized Sb and Sn were prepared as the same weight ration but ball milling for 4 hours for Sb and 2 hours for Sn. After obtaining the powders by ball milling, a uniform slurry was prepared by dispersed the mixture in deionized water. Then the as-prepared slurry was coated on Cu foil to make a tape. After being dried  $80^\circ C$  for 12 hours, the electrodes with a diameter of 12 mm were used to assemble coin cell and Swagelok type cells. The  $K_xMnFe(CN)_6$  cathode was mixed with 30 wt.% super P and 10 wt.% CMC to make a tap on Al foil. The tapes were dried at  $80^\circ C$  under vacuum and punched into 12 mm electrodes for assembling coin cells. The BP/G electrode was prepared in the glovebox, a slurry was first prepared by hand grinding BP/G (75 wt.%), super P (15 wt.%), polyacrylic acid (PAA, 10 wt.%) with N-methyl-2-pyrrolidone (NMP) in the glovebox. The slurry was cast on Cu foil and dried at  $100^\circ C$  for 12 hours under vacuum in Buchi glass oven (B-585 Drying). All the electrodes were directly transferred into the glovebox in the Buchi glass after drying. The BP/G tapes were chopped into  $\frac{1}{2}$  inch diameter electrodes with active mass loading of about  $1\text{ mg cm}^{-2}$ . The cathode for matching BP/G anode was prepared by mixing 70 wt.%  $K_xMnFe(CN)_6$  and 30 wt.% super P, which is directly used in powder form electrode.

### 2.2.2 Electrolytes

Ethylene carbonate (EC), propylene carbonate (PC), dimethoxyethane (G1, DME), diglyme electrolyte (G2, DGME), dimethyl carbonate (DMC), lithium bis(trifluoromethane)sulfonimide (LiFSI), sodium bis(trifluoromethane)sulfonimide (NaFSI), lithium hexafluorophosphate ( $LiPF_6$ ) and trimethyl phosphate (TMP) were purchased from DoDo Chem; ethylene glycol

diethyl ether (EGDEE), 1,1,2,2-tetrafluoroethyl 2,2,2-trifluoroethyl ether (HFE,  $\geq 97\%$ ) and fluoroethylene carbonate (FEC) were provided by Macklin. Tetrahydrofuran (THF) was provided by Alfa Aesar. Potassium bis(fluorosulfonyl)imide (KFSI) was purchased from Energy Chemical. The sodium hexafluorophosphate ( $\text{NaPF}_6$ ) was purchased from Kishida Chemical co., ltd, Japan. 1 M LiFSI/EGDEE, 1 M  $\text{LiPF}_6$ /ECDEC ( $v(\text{EC})/v(\text{DEC}) = 1:1$ ), 1 M  $\text{NaPF}_6$ /EGDEE, 1 M  $\text{NaPF}_6$ /PC-3% vol. FEC (1 M  $\text{NaPF}_6$ /PC-FEC), 1 M NaFSI/EGDEE, 1 M KFSI/EGDEE, 1 M KFSI/DME, 1 M KFSI/DGME, 1 M KFSI/ECPC ( $v(\text{EC})/v(\text{PC}) = 1:1$ ), 5 M KFSI/ECPC, 1 M KFSI/TMP (NCE), 5 M KFSI/TMP (HCE) and KFSI/TMP/HFE with the molar ratio of 1:1.7:2 (LHCE) were prepared as electrolytes. All electrolyte salt and solvents were used without any purification. Na-LHCE was prepared by the same formulation as the K counterpart but replacing the KFSI by NaFSI. To prepare LHCE, the KFSI salt was first dissolved in TMP solvent under the string to form a transparent and clear solution, and then HFE was added and continuously stirred until the solution turned clear again.

### 2.3 Electrochemical measurements

Two-electrode coin cells were assembled in the glove box with K/Na/Li metal as the counter/reference electrode. One piece of glass fiber (Whatman, CF/D) was used as the separator. Galvanostatic discharge and charge and long-term cycling performances of batteries were tested on LAND battery testing system. The conductive carbons including super P and VGCF in the electrodes have a low capacity of about  $100 \text{ mAh g}^{-1}$  in tested electrolytes. The calculation of capacities is based on the mass of  $\text{MoS}_2/\text{C}$  nanofiber, neat  $\text{MoS}_2$ , microsized  $\text{MoS}_2$ , nanosized Sb, microsized Sb, microsized Sn and BP/G composite in the corresponded chapters. The electrochemical impedance spectroscopy (EIS) spectra were conducted on the electrochemical workstation (Biologic SP150) between 100 kHz and 0.1 Hz with an amplitude of 5 mV. Cyclic voltammetry (CV) data were collected on an electrochemical Solartron Analytical 1400 workstation. The galvanostatic intermittent titration technique (GITT) tests were collected on Arbin battery systems.

### 2.4 Sample characterizations

#### 2.4.1 Structure, morphology, composition characterizations

The X-ray powder diffraction (XRD) patterns were collected by Rigaku Smartlab with  $\text{Cu-K}\alpha$  radiation source at 45 kV and 200 mA condition. *Ex situ* XRD measurements were conducted with Swagelok type cells that sample was coated on Cu current collector at different discharge

and charge states. Scanning electron microscope (SEM) images were acquired from Tescan VEGA3 with a tungsten thermionic emission system. Thermogravimetric analysis (TGA) was conducted using TGA/DSC3+ (Mettler Toledo) from 50 to 650 °C with a heating rate of 15 °C·min<sup>-1</sup> in air. Transmission electron microscopy (TEM) and scanning TEM (STEM) images were performed on JEOL JEM-2100F, operated under 200 kV. X-ray photoelectron spectroscopy (XPS) was conducted on Thermo Scientific Nexsa and the samples were sealed in a vacuum transfer holder to avoid air exposure.

#### 2.4.2 *In situ* characterizations

For *in situ* XRD measurements, an XRD cell with a Be window was employed and the sample was coated on Be window. *In situ* Raman spectra were obtained by WITec alpha 300 confocal Raman microscope (532 nm laser excitation) with EL CELL type cell. For the *in situ* TEM study, the MoS<sub>2</sub>/C nanofibers were loaded onto electrochemical etched microsized tungsten tip and fixed with conductive silver epoxy. Another tungsten tip with submicron size at the top was used to scratch fresh alkaline metal (Li, Na, or K) surface in an Ar-filled glove box and attached to a piezo-driven biasing probe built the Nanofactory TEM scanning tunneling microscopy (TEM-STM) holder. Once the sealed holder was taken out from the glove box, it was inserted into the TEM column as quickly as possible for immediate *in situ* study by TEM. The native A<sub>2</sub>O (A represents Li, Na or K) on the alkaline metal surface was severed as a solid electrolyte. The voltage bias between alkaline metal tip and MoS<sub>2</sub> tip was applied to -5 V, which was higher than those applied in coin cells.

#### 2.4.3 Mechanical property characterizations

Mechanical testing for the electrodes was performed in the glove box using a Bruker Dimension Icon AFM (Figure 2.1). The adopted probe was an ACTA-20 (APPNANO) and the spring constant was calibrated using the Sader method. The deflection sensitivity of the AFM cantilever was calibrated on a clean sapphire sample before each test. The tip radius (R) was calibrated using a reference sample with a known modulus of elasticity (polystyrene, Bruker PeakForce QNM sample).

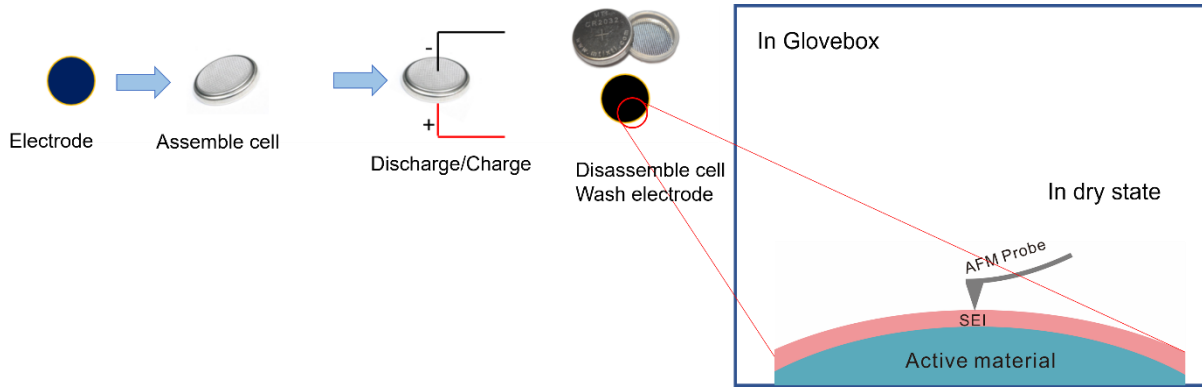


Figure 2.1 The schematic of the AFM tests.

The limit of elastic strain can be obtained following the below equation<sup>116-117</sup>:

Equation 2-1

$$\varepsilon_Y = \frac{1}{1.6\pi} \left( \frac{6F_Y E_r^2}{R^2} \right)^{\frac{1}{3}}$$

Equation 2-2

$$E_r = \left( \frac{1 - \nu^2}{E} + \frac{1 - \nu_{tip}^2}{E_{tip}} \right)^{-1}$$

where  $F_Y$  is the force corresponding to point a' in Figure 5.20a,  $R$  is the radius of the AFM probe,  $E$  is Young's modulus of the SEI,  $\nu$  is the Poisson's ratio of the SEI ( $\nu$  is set as 0.3 for all cases),  $E_{tip}$  is Young's modulus of the AFM probe and  $\nu_{tip}$  is the Poisson's ratio of the AFM probe. We first indent the SEI within the elastic deformation region before conducting the test in Figure 5.20a to obtain  $\varepsilon_Y$ .

The maximum elastic deformation energy ( $U$ ) is used to determine the mechanical stability, which is calculated as follows:

Equation 2-3

$$U = \frac{8}{15} \left( \frac{4}{5} \pi \right)^5 \cdot r^3 \cdot (1 - \nu^2)^4 \cdot E \cdot (\varepsilon_Y)^5$$

where  $r$  is the radius of the rigid indenter (assumed as  $1 \mu\text{m}$ ), the  $\nu$  is the SEI Poisson's ratio, and a typical value of 0.3 is used. To increase the accuracy, the  $E$  and  $\epsilon_Y$  for calculating  $U$  are corrected by eliminating the substrate's interference base on a most recent study.<sup>118</sup>

## 2.5 DFT calculations

Density functional theory (DFT) calculations were carried out with generalized gradient approximation parameterized by Perdew-Burke-Ernzerhof performed in the Vienna Ab initio Simulation Package<sup>119-121</sup>. The optimized Perdew, Burke, and Ernzerhof functional (opt-PBE) were utilized for van der Waals interactions.<sup>122</sup> An energy cut-off of 500 eV was adopted, and the k-point was sampled limiting the spacings  $<0.05 \text{ \AA}^{-1}$ . The energy and force convergence criteria were  $10^{-6}$  eV and  $0.02 \text{ eV \AA}^{-1}$ , respectively. Spin polarization was considered. When the energies of phases are  $<10 \text{ meV}$  per atom above the convex hull or just on the hull, they were regarded as the thermodynamically stable structures within DFT and temperature errors.<sup>123</sup> The equilibrium potentials were calculated according to the following equation:

Equation 2-4



Equation 2-5

$$U = \frac{\Delta G}{-ne} = \frac{E(\text{K}_n\text{MoS}_2) - nE(\text{K}) - E(\text{MoS}_2)}{-ne}$$

where  $n$  is the number of electrons involved in the reaction,  $U$  is the equilibrium potential of the reaction,  $E(\text{K}_n\text{MoS}_2)$ ,  $E(\text{K})$ , and  $E(\text{MoS}_2)$  represent the computed total energies of  $\text{K}_n\text{MoS}_2$ ,  $\text{K}$ , and  $\text{MoS}_2$  at 0 K by DFT, respectively.

## Chapter 3

# Exploring the structure evolution of MoS<sub>2</sub> upon Li/Na/K ion insertion and origin of unusual stability for potassium ion batteries

The recent revival of the research on sodium and potassium ion batteries (SIBs and PIBs) have twofold benefits. It not only provides alternative energy storage technologies to lithium ion batteries (LIBs) with potential advantages on the cost but also enhances our understanding of charge storage through systematic studies on alkali-metal ion batteries with increasing insertion ion sizes. Using MoS<sub>2</sub> as a model material, the structure evolution upon Li, Na, and K ions uptake are compared through *in situ* TEM. Despite the larger size, K ions insertion shows better both electrochemical and structural stability. To understand this paradoxical and counter-intuitive phenomenon, *in situ* XRD are carried out to examine the phase transitions of MoS<sub>2</sub> upon the ion insertion, while *ex situ* TEM are further applied to have a close look at the structures at the nanoscale. Complementary DFT calculations are performed to understand the kinetic/thermodynamic origins of the analogous stability. It reveals that the less electrovalent K-S bond favors the intercalation process, resulting in the preservation of layered structure for stable cycling. This study provides structural insight to design stable electrodes for PIBs.

### 3.1 Introduction

Similarities between alkali-metal ions are expected to smooth the development as the knowledge on lithium ion batteries (LIBs) that accumulated in the past three decades can be largely applied to the emerging sodium ion batteries (SIBs) and potassium ion batteries (PIBs).<sup>124-125</sup> Indeed, analogous systems from the electrolytes to electrode materials are adopted in the alkali-metal ion batteries. For instance, carbonate-based solvents, including ethylene carbonate (EC), dimethyl carbonate (DMC) and diethyl carbonate (DEC) inherited from LIBs remain the most popular choices for the electrolytes in SIBs and PIBs.<sup>58, 105, 126-128</sup> Many materials are capable of storing all the Li, Na and K ion, with hard carbon anode and  $A_3V_2(PO_4)_2F_3$  (A represents Li, Na or K) cathode being the representatives.<sup>27, 66, 129-132</sup> Nevertheless, a simple extrapolation from Li to Na, K system is undoubtedly not enough. This is clearly reflected in the case of  $LiCoO_2$ , the most successful cathode in LIBs, whose  $Na_xCoO_2$  and  $K_xCoO_2$  counterparts fail to deliver attractive capacity and stability.<sup>133-134</sup> While the reasons for the varieties are complex, the large ionic size of Na (1.02 Å) and K (1.38 Å) ion is considered partly responsible. Uptake of ions with a large radius would lead to enormous volume expansion and bring about potential structural damage to the electrode materials. An example is the alloy anodes, which can accept several A ions to form  $A_xM$  (M denotes alloy anodes such as Bi and Sb); much more significant volume expansion is induced in the formation of  $K_xM$  than  $Li_xM$  and  $Na_xM$ .<sup>135-136</sup> Consequently, stabilizing electrodes in PIBs is considered more challenging, necessitating the efforts on both microstructure design and solid electrolyte interphase engineering.<sup>52, 59, 137</sup>

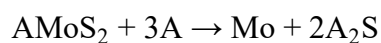
Comparison studies between alkali-metal ion storage are expected to shed insights into the effect of ionic carriers on the structural evolution of electrodes, which are somewhat lacking due likely to the absence of appropriate host materials.  $MoS_2$  has a large layered distance of 6.3 Å, making it an ideal material to accommodate alkali-metal ions with different sizes. It shows promising theoretical capacities of about  $670 \text{ mA h g}^{-1}$  *via* a four-electrons-transfer reaction when serving as the anode in LIBs, SIBs and PIBs.<sup>138-144</sup> Similar charge storage mechanisms are reported, including the intercalation at a high voltage to form layered  $AMoS_2$  (Equation 3-1) compounds and the following conversion reaction to precipitate molybdenum metal and  $A_2S$  (Equation 3-2).<sup>145-147</sup> Herein, we fabricated  $MoS_2/C$  nanofibers as a model

material considering the advantages of one-dimensional morphology for *in situ* experimental and statistics gathering. It reveals that MoS<sub>2</sub>/C nanofibers in PIBs shows the largest volume expansion up to 140%, whereas the volume changes in LIBs and SIBs are only about 103% and 123%, respectively. Counter-intuitively, better structural stabilities and more stable cyclic performance during K ion insertion are observed. Complementary *in/ex situ* transmission electron microscopy (TEM) and theoretical calculations were conducted to study the origin of the difference in structural transformations during Li, Na, and K ions insertion.

Equation 3-1



Equation 3-2



where A represents Li, Na or K.

## 3.2 Results and discussion

### 3.2.1 MoS<sub>2</sub>/C nanofibers characterization

MoS<sub>2</sub>/C nanofibers were prepared by electrospinning as presented in Figure 3.1. The crystalline phase of the nanofibers is identified by X-ray powder diffraction (XRD, Figure 3.2a), which is consistent with 2H-MoS<sub>2</sub> (PDF#37-1492). A sharp peak at around 14.1° can be indexed to (002) plane of MoS<sub>2</sub> and one broad peak at about 21.2° belongs to carbon that originated from carbonization of polyacrylonitrile (PAN). The thermogravimetry (TG, Figure 3.2b) is performed to analyze carbon content in the sample, which is estimated to be ~25%. The chemical state of Mo is examined by X-ray photoelectron spectroscopy (XPS, Figure 3.3), which present two pairs of peaks at 229.0 eV and 232.3 eV in Mo3d spectrum, corresponding to Mo(IV) and Mo(VI) respectively.<sup>148</sup> The small amount of Mo(VI) species in Mo3d spectrum may originate from the oxide layer of the MoS<sub>2</sub>/C nanofiber.<sup>149</sup> The morphologies of MoS<sub>2</sub>/C nanofibers are investigated by scanning electron microscopy (SEM) and TEM. In Figure 3.4a, the MoS<sub>2</sub>/C nanofibers with an average diameter of about 100 nm present uniform thread morphologies after high-temperature treatment. TEM images (Figure 3.4b and c) indicate that layered MoS<sub>2</sub> crystals are homogeneously dispersed in the carbon nanofibers and the selected

area electron diffraction (SAED) pattern (Figure 3.4b inset) clearly shows the multi-crystalline feature of MoS<sub>2</sub>. In the high-resolution (HRTEM) images (Figure 3.4d), MoS<sub>2</sub> crystals consist of 3-5 layers with an interlayer distance of 6.3 Å.

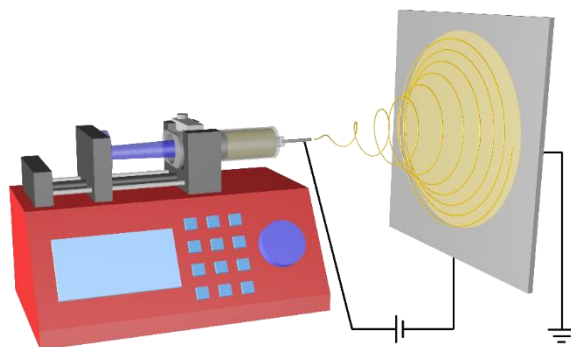


Figure 3.1 Schematic illustration of electrospinning setup.

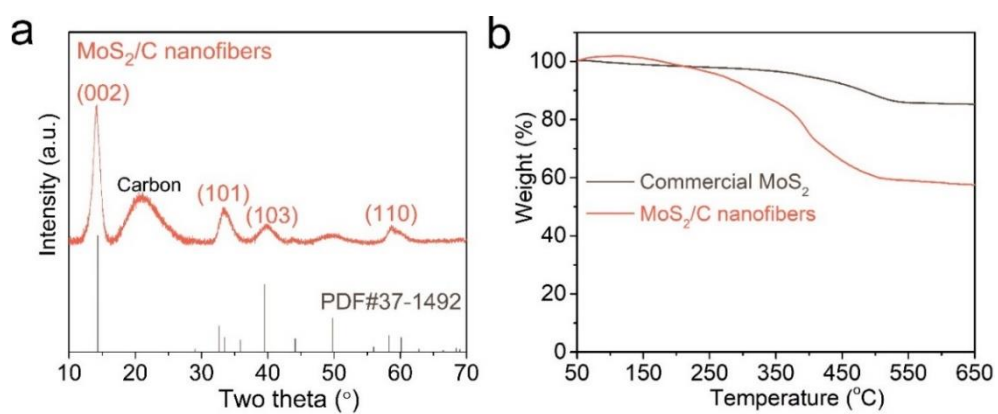


Figure 3.2 MoS<sub>2</sub>/C nanofibers. (a) XRD pattern and (b) TG.

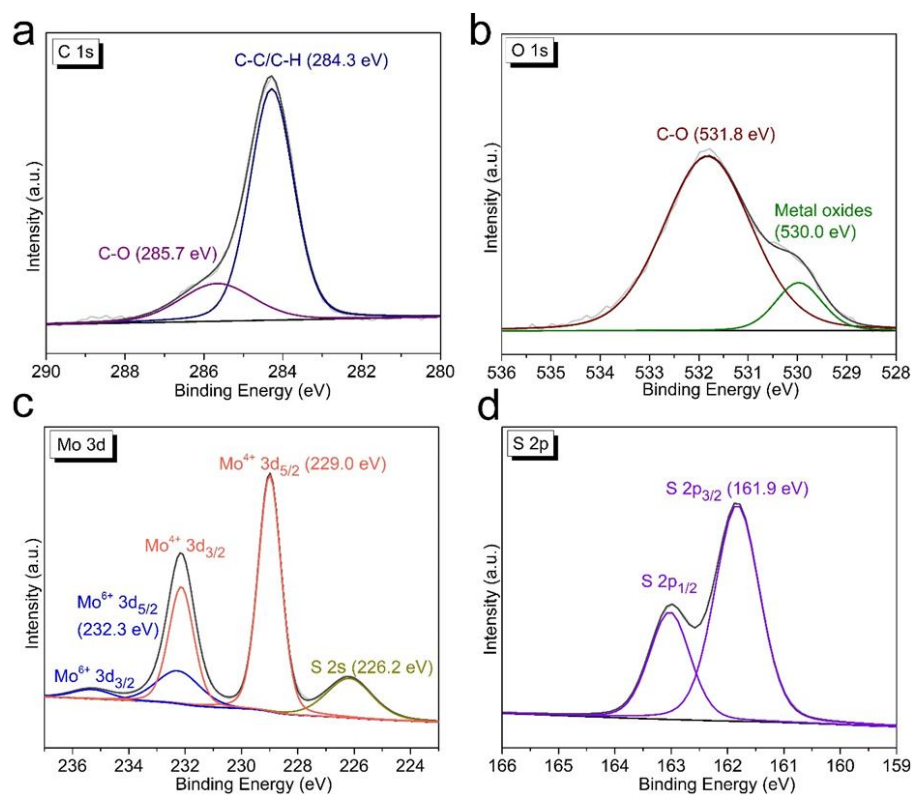


Figure 3.3 XPS spectra of MoS<sub>2</sub>/C nanofibers. (a) C1s, (b) O1s, (c) Mo3d and (d) S2p.

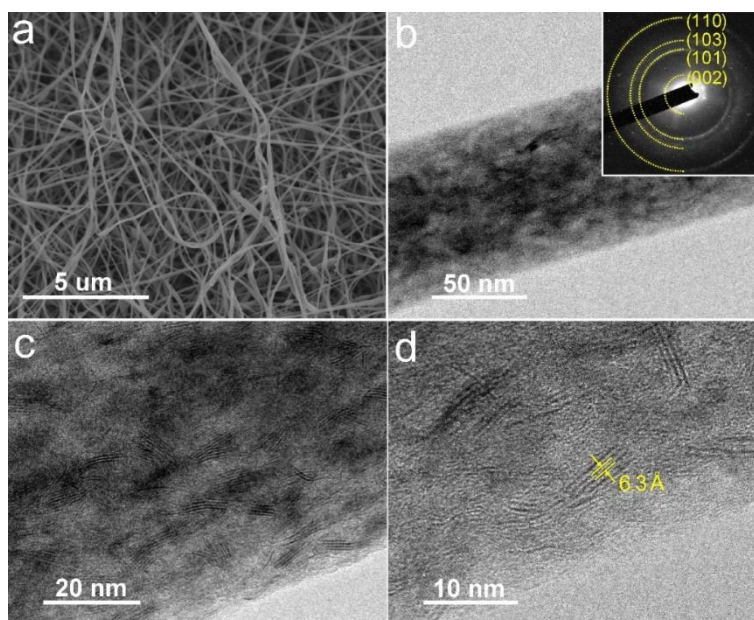


Figure 3.4 MoS<sub>2</sub>/C nanofibers. (a) SEM image; (b, c) TEM images and (b inset) SAED pattern; (d) HRTEM image.

### 3.2.2 Comparison of charge storage processes

*In situ* TEM examinations were carried out to explore the charge storage processes of MoS<sub>2</sub>/C nanofibers uptake of different alkali-metal size ions with alkaline oxides on the surfaces as solid electrolytes and the alkaline metal as the reference/counter electrodes (Figure 3.5). As shown in Figure 3.6a and b, after the first 10 seconds of lithiation and sodiation, the interlayer spacing of MoS<sub>2</sub> increases from 6.3 Å to about 6.4 Å and 7.0 Å, respectively. While for the potassiation process, the interlayer spacing is enlarged to a striking 7.9 Å (Figure 3.6c). Despite the expansions of layers distance by the alkaline atom invasion, the lamellar structure can be retained well in three types of batteries. These processes are mainly involved with the intercalation reaction that alkaline ions are inserted into MoS<sub>2</sub> to form layered AMoS<sub>2</sub> compounds, namely, LiMoS<sub>2</sub>, NaMoS<sub>2</sub>, and KMoS<sub>2</sub>, respectively.<sup>150-153</sup> As for a deep reaction in the following 12 seconds, the layered crystals have almost entirely disappeared in the cases of lithiation because of the conversion of LiMoS<sub>2</sub> to metallic Mo and Li<sub>2</sub>S. Some of the layered crystals are preserved during Na insertion, but the MoS<sub>2</sub> crystals are broken into small pieces. In comparison, the deep potassiation process of MoS<sub>2</sub> displays a different phenomenon from the Li and the Na counterparts that the layered crystals are unabridged with an enlarged interlayer spacing of 7.9 Å. Electron energy loss spectroscopy (EELS) maps (Figure 3.7, Figure 3.8 and Figure 3.9) confirm that Li, Na and K are successfully inserted into MoS<sub>2</sub>/C nanofibers. The lattice width of MoS<sub>2</sub> crystals and the lateral length of MoS<sub>2</sub>/C nanofibers are measured in real time and the detailed statistics are given in Figure 3.6d and e. The expansion of interlayer distance becomes more severe with the increase of intercalant size from Li to Na and K ions. Correspondingly, the lateral expansion of nanofibers after taking Li and Na ions is roughly calculated to be 103% and 123%, respectively, while it reaches nearly 140% for K ions uptake.

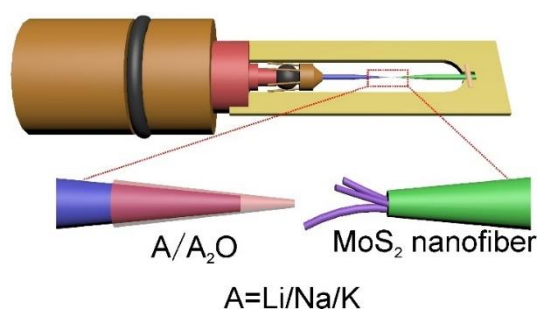


Figure 3.5 Schematic illustration of *in situ* TEM experiment setup.

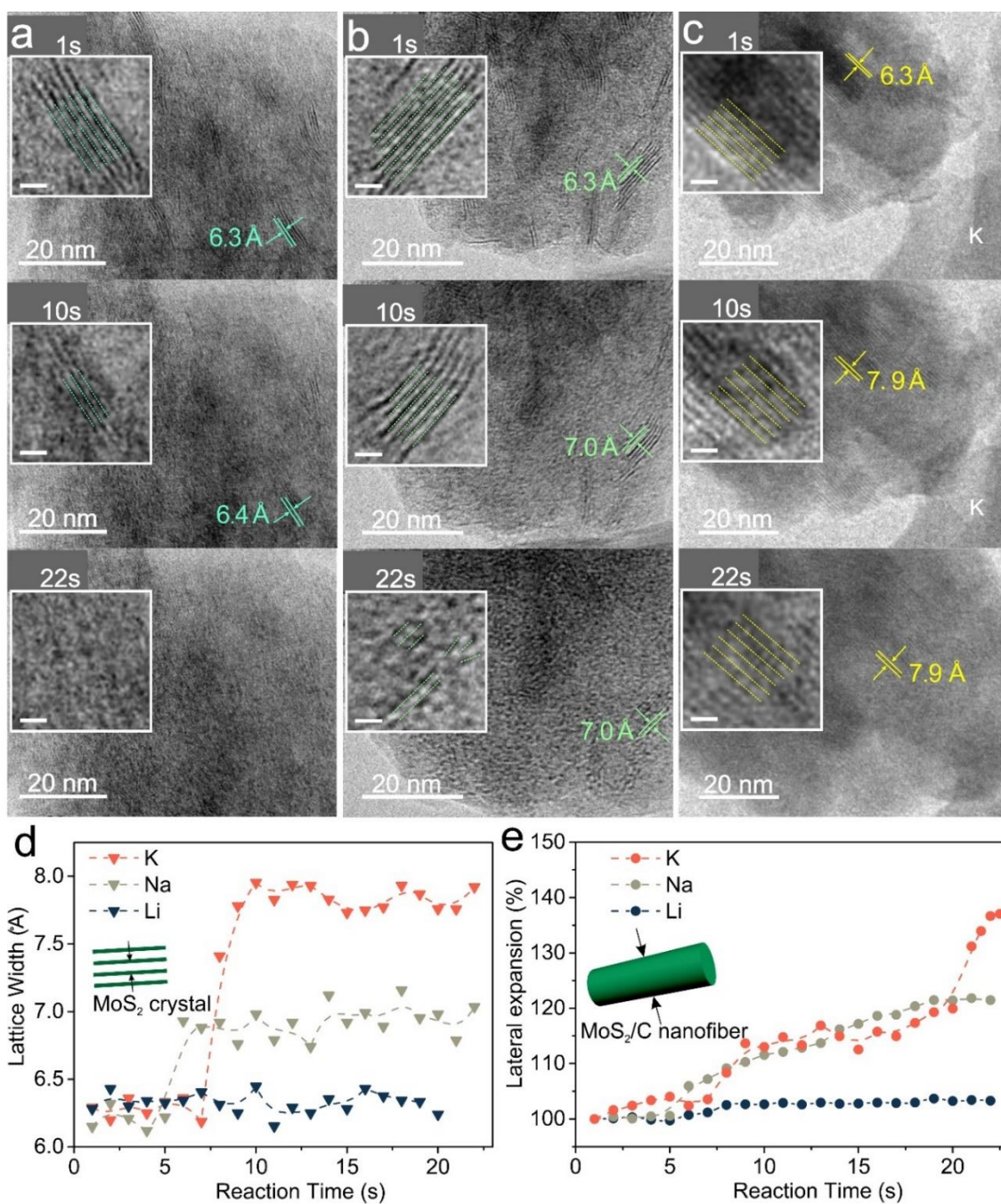


Figure 3.6 *In situ* TEM images of MoS<sub>2</sub>/C nanofibers for (a) Li, (b) Na and (c) K ions uptake at different reaction stages (insets: magnified images with a scale bar of 2 nm). The statistic scatters diagram of (d) lattice width of MoS<sub>2</sub> crystal and (e) lateral expansion of MoS<sub>2</sub>/C nanofiber in real time *in situ* TEM observations.

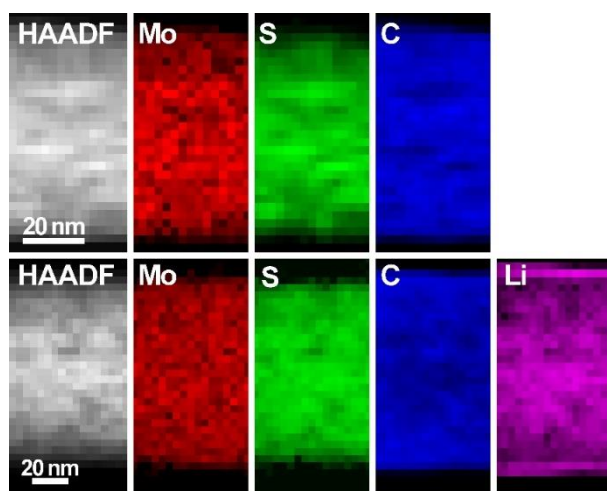


Figure 3.7 HAADF-STEM image and corresponding EELS elemental maps of MoS<sub>2</sub>/C nanofibers before (up) and after (below) lithiation.

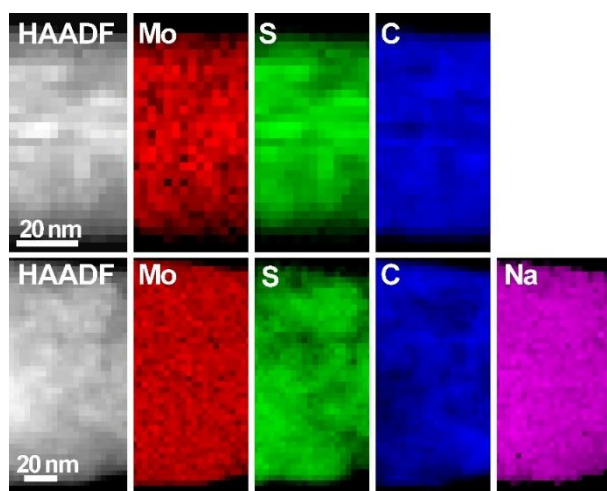


Figure 3.8 HAADF-STEM image and corresponding EELS elemental maps of MoS<sub>2</sub>/C nanofibers before (up) and after (below) sodiation.

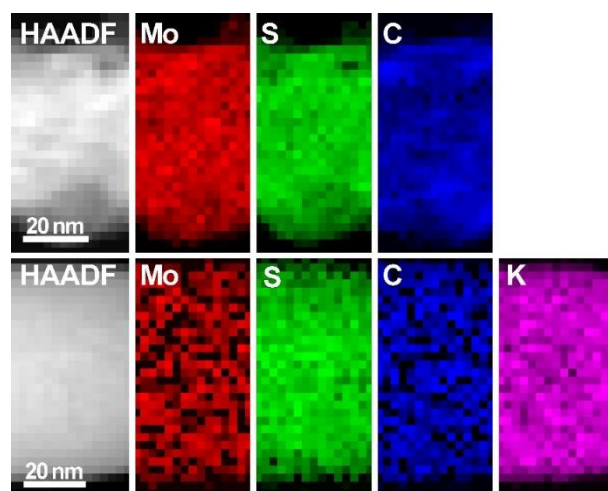


Figure 3.9 HAADF-STEM image and corresponding EELS elemental maps of MoS<sub>2</sub>/C nanofibers before (up) and after (below) potassiation.

To exclude potential artifacts from *in situ* TEM setup, such as the use of A<sub>2</sub>O solid electrolytes, we further performed *in situ* XRD and *ex situ* TEM on real LIBs, SIBs and PIBs, to investigate the unexpected structural stability of MoS<sub>2</sub> at various Li/Na/K ions insertion/extraction stages. In the case of LIBs (Figure 3.10a), the peak of (002) facet gradually shifts to 13.7° after Li ion insertion, which can be attributed to the intercalated product of LiMoS<sub>2</sub>.<sup>154</sup> When discharging to 0 V, no obvious peaks can be recognized, indicating the MoS<sub>2</sub> is transformed to small sized/amorphous Mo and Li<sub>2</sub>S.<sup>155</sup> When charging back to 3 V, no MoS<sub>2</sub> peaks are founded, which means the layered structures of MoS<sub>2</sub> are largely vanished and cannot be recovered after Li ion insertion/extraction. In the first discharging process of SIBs (Figure 3.10b), two new peaks at 11.7° and 12.5° are observed, corresponding to Na<sub>0.5</sub>MoS<sub>2</sub> and NaMoS<sub>2</sub>, respectively.<sup>147</sup> After fully discharge to 0 V, most of the layered NaMoS<sub>2</sub> are decomposed suggested by the low intensity of the peak at 12.5°. It shows a similar phenomenon with Li case that no peaks can be found at fully charged 3 V, implying amorphous or negligible crystallized MoS<sub>2</sub> are dominated after Na ion insertion/extraction. The *in situ* XRD patterns of MoS<sub>2</sub>/C nanofibers for K ion storage in the first and second cycles are presented in Figure 3.11a. During the first discharging process, the intensity of the MoS<sub>2</sub> peak located at 14.1° gradually decreases and a new peak at about 10.6° becomes more prominent, which can be assigned to K<sub>0.4</sub>MoS<sub>2</sub> compound (PDF#27-0421). Then K<sub>0.4</sub>MoS<sub>2</sub> peak shifts to 11.1° after continuous K ions interpolation, where the formed compound is defined as K<sub>x</sub>MoS<sub>2</sub> (x>0.4). Further insertion of

K ions leads to the fully potassiated phase  $\text{KMoS}_2$  pertaining to a broad peak at  $11.3^\circ$ , which agrees well with the  $7.9 \text{ \AA}$  interlayer spacing observed in TEM. Turning to the charging processes, the wide peak of  $11.3^\circ$  shifts back to  $11.1^\circ$  and no obvious  $\text{MoS}_2$  peaks emerge, indicating that  $\text{KMoS}_2$  can only return to  $\text{K}_x\text{MoS}_2$  instead of pristine  $\text{MoS}_2$ . For the following discharging and charging processes, only  $\text{KMoS}_2$  and  $\text{K}_x\text{MoS}_2$  appear on the stage and the corresponding XRD peaks show a periodic right and left shift. The K ions shuttle between  $\text{K}_x\text{MoS}_2$  and  $\text{KMoS}_2$  assures that the phase transition is completely reversible in cycles. It should be noted that the interlayer spacing of  $\text{K}_x\text{MoS}_2$  shrinks during K ion insertion, while it extends when K ion extraction. This inverse relationship between the interlayer spacing and K ion insertion/extraction can be explained by the 2H-1T phase transformation.<sup>154, 156-157</sup>

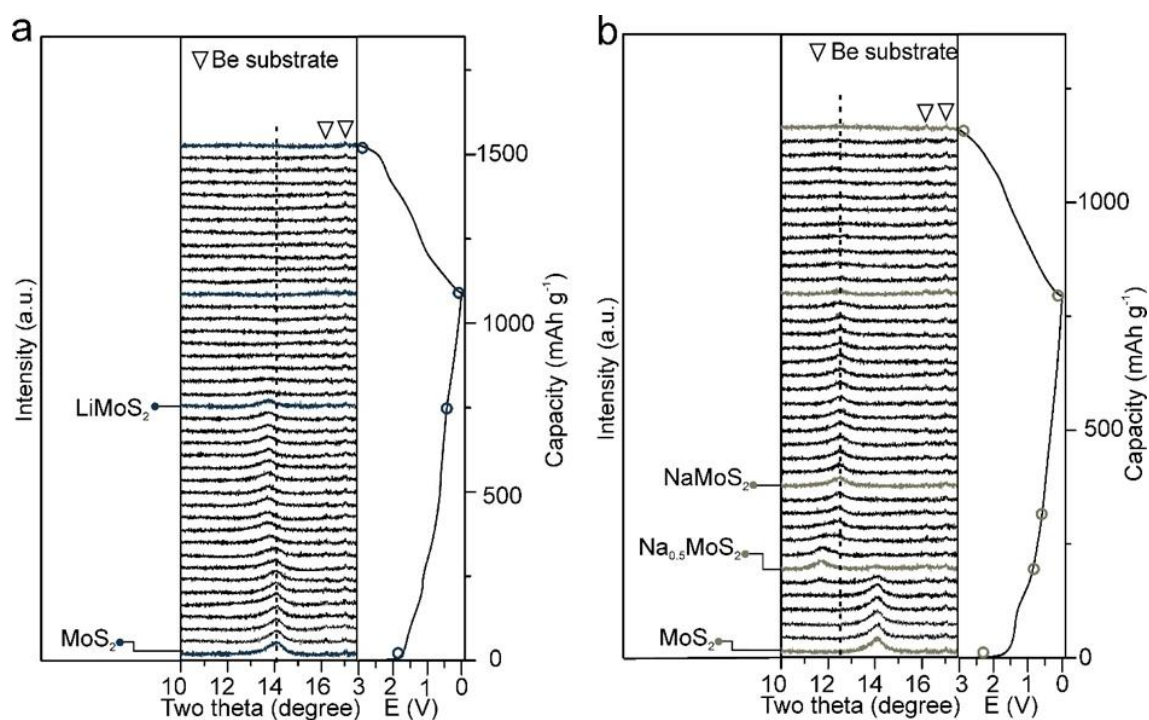


Figure 3.10 *In situ* XRD patterns of  $\text{MoS}_2/\text{C}$  nanofibers in the first cycle for (a) LIBs and (b) SIBs.

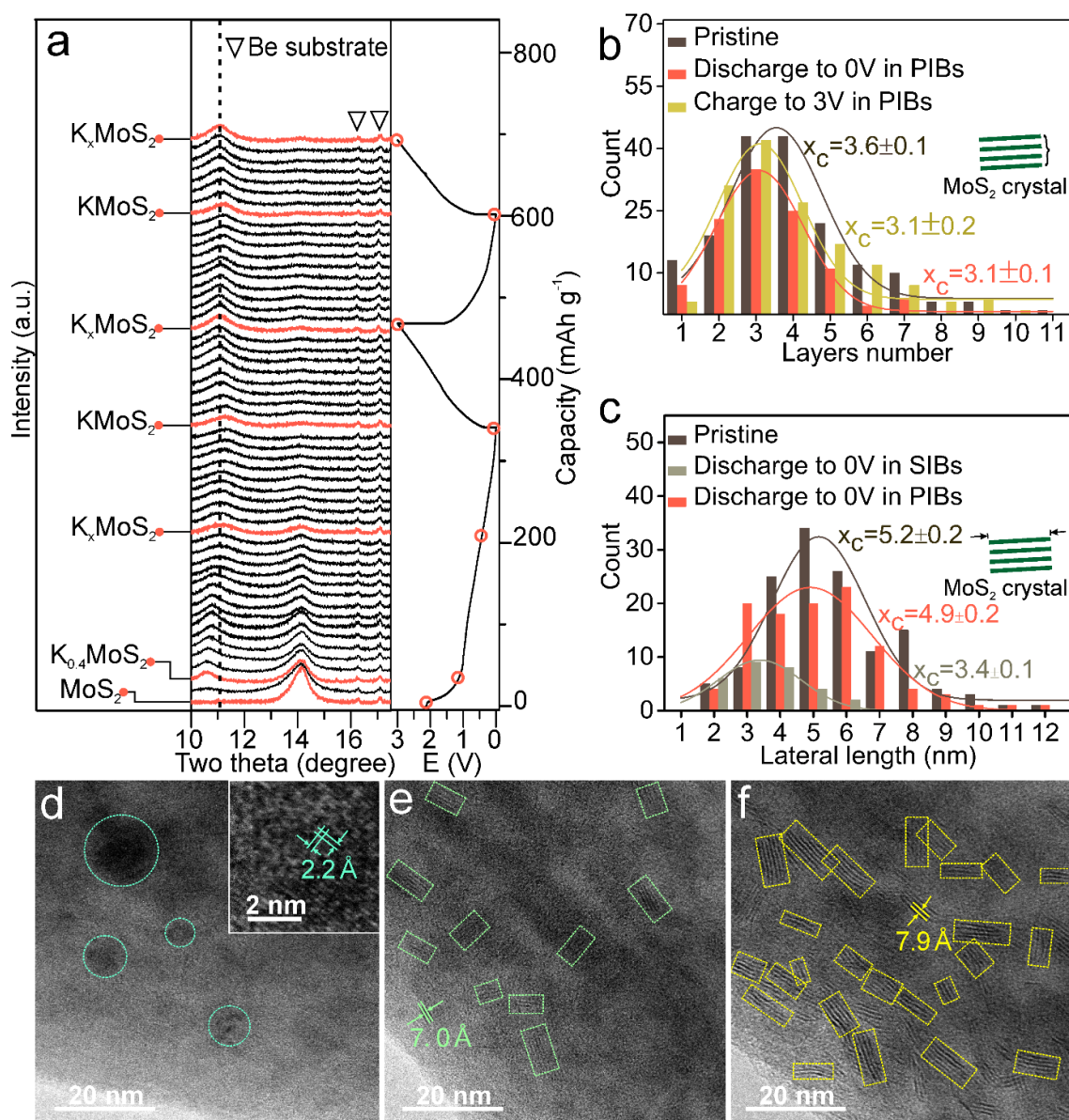


Figure 3.11 *In situ* XRD and *ex situ* TEM for MoS<sub>2</sub>/C nanofibers. (a) *In situ* XRD patterns in PIBs in the first two cycles; The statistic histograms for MoS<sub>2</sub> crystals of (b) layer numbers at different states in PIBs and (c) lateral length in PIBs and SIBs; *Ex situ* TEM images at first fully discharged state in (d) LIBs; (e) SIBs and (f) PIBs (Conversion reaction products in LIBs are marked by circles and intercalation reaction products in SIBs and PIBs are marked by rectangles).

The above *in situ* observations are fully consistent with *ex situ* TEM characterizations on the first cycle of real PIBs. The pristine MoS<sub>2</sub> crystals in the nanofiber are shown in Figure 3.12a and b. When discharging to 1.0 V, a large interlayer spacing of 8.3 Å associated with K<sub>0.4</sub>MoS<sub>2</sub>

is observed (Figure 3.12c and d), corresponding to the  $10.6^\circ$  peak in *in situ* XRD. However, it is not probed by *in situ* TEM probably due to the low-resolution limitation in real time observation and fast reaction process of  $\text{K}_{0.4}\text{MoS}_2$ .<sup>158</sup> After discharging to 0.5 V (Figure 3.12e and f), a slightly shrunken layer distance of  $8.0 \text{ \AA}$  can be found arising from 2H-1T phase transformation, which is related to the  $11.1^\circ$  peak from  $\text{K}_x\text{MoS}_2$  according to *in situ* XRD results. Some unreacted  $\text{MoS}_2$  can be seen with the original interlayer distance of  $6.3 \text{ \AA}$ . For the fully discharged state (Figure 3.12g and h), most of  $\text{MoS}_2$  are converted to  $\text{KMoS}_2$  with a contractive distance of  $7.9 \text{ \AA}$ , as observed by both *in situ* TEM and XRD. Back to 3 V (Figure 3.12i and j), the interlayer distance is extended again to  $8.0 \text{ \AA}$ , indicating that  $\text{KMoS}_2$  backtrack to  $\text{K}_x\text{MoS}_2$  species. Thanks to statistic advantage of nanofiber composite that the  $\text{MoS}_2$  crystals are scattered in nanofibers independently, the layer numbers and lateral length can be readily measured. As shown in Figure 3.11b, the layer numbers of  $\text{MoS}_2$  crystal in nanofibers at different states are counted. The original  $\text{MoS}_2$  presents 3-5 layers, which almost does not change upon charge/discharge, confirming the stability of the layered crystals and the reversible reaction between  $\text{KMoS}_2$  and  $\text{K}_x\text{MoS}_2$ .

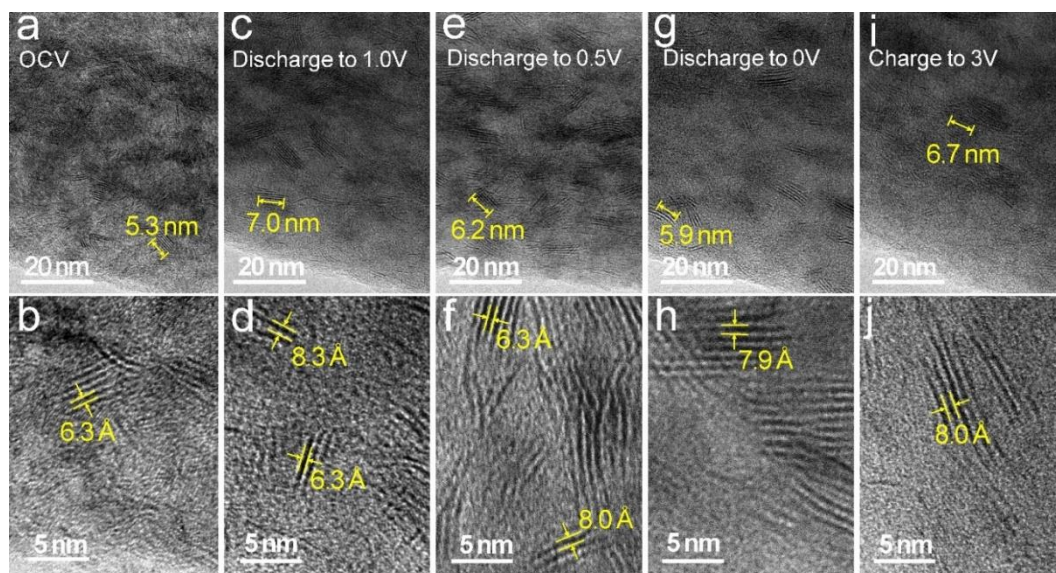


Figure 3.12 *Ex situ* TEM images of  $\text{MoS}_2/\text{C}$  nanofibers for PIBs on the first cycle. (a, b) OCV state; (c, d) discharge to 1.0 V; (e, f) discharge to 0.5 V; (g, h) discharge to 0 V and (i, j) charge to 3 V.

*Ex situ* TEM characterizations were also carried out on LIBs and SIBs at the fully discharged state, to be compared with PIBs. As shown in Figure 3.11d and inset, only dense Mo particles with the lattice-plane spacing of 2.2 Å (PDF#42-1120) are discovered in discharged LIBs, with no trace of layered phases, implying that deep conversion dominates. The small sized metallic Mo may be nondetectable in *in situ* XRD. A small number of layered crystals are presented in discharged SIBs (Figure 3.11e), which are smaller and contain fewer layers with an expanded interlayer spacing of 7.0 Å, in agreement with the *in situ* TEM and *in situ* XRD observation in Figure 3.6b and Figure 3.10b. In contrast, many broad layered crystals with a large interlayer spacing of 7.9 Å are preserved in discharged PIBs (Figure 3.11f). The lateral lengths of layered crystals in both SIBs and PIBs are counted at fully discharged state (Figure 3.11c). The average lateral length of pristine MoS<sub>2</sub> crystals in nanofibers is about 5.2 nm. This value in SIBs dramatically decreases to ca 3.4 nm after sodiation. Those layered crystals vanished in LIBs and SIBs have been presumably converted to Mo and Li<sub>2</sub>S/Na<sub>2</sub>S species through conversion reactions. On the other hand, the lateral length (4.9 nm) in PIBs does not show significant change after discharging to 0 V, further proving the better stability of the layered crystals during K ion storage.

### 3.2.3 Electrochemical performances evaluation

The electrochemical performances of MoS<sub>2</sub>/C nanofibers were tested in LIBs, SIBs, and PIBs for exploring the consequences of structural transformation on the cyclic stability. The first discharge and charge profiles of MoS<sub>2</sub>/C nanofibers in LIBs, SIBs, and PIBs are compared in Figure 3.13a. Much longer plateaus are observed in LIBs and SIBs, indicative of the distinct reaction paths. It can be seen more clearly in dQ/dV plots where sharp peaks are presented during Li and Na insertion (Figure 3.13b). The high initial capacities observed in Li and Na cases are the evidence for conversion reaction since the intercalation reaction can only delivery 167 mAh g<sup>-1</sup> capacity based on the compounds of LiMoS<sub>2</sub> and NaMoS<sub>2</sub>. Consistent with the observed structural stability, MoS<sub>2</sub>/C nanofibers demonstrate the most stable behavior in PIBs, with a capacity retention of about 99.4% after 200 cycles (Figure 3.13c and d). MoS<sub>2</sub>/C nanofibers present a good rate performance for PIBs (Figure 3.14), which is not affected by the larger radius of K ion, showing reversible capacities of 212, 196.2, 186.4, 175.2 mA h g<sup>-1</sup> under increasing current density of 50, 100, 200 and 400 mA h g<sup>-1</sup>, respectively. Note that the pure carbon nanofibers have a capacity of mere 100 mA h g<sup>-1</sup> (Figure 3.15). Considering the 75 wt.%

mass loading of MoS<sub>2</sub> in the composite, the MoS<sub>2</sub> alone in the composite delivers a capacity of about 200 mA h g<sup>-1</sup> at the high current density of 500 mA g<sup>-1</sup>. In contrast, relatively rapid capacity decreases are observed in LIBs and SIBs, retaining only 80.1% and 70.1% of the initial capacity, respectively.

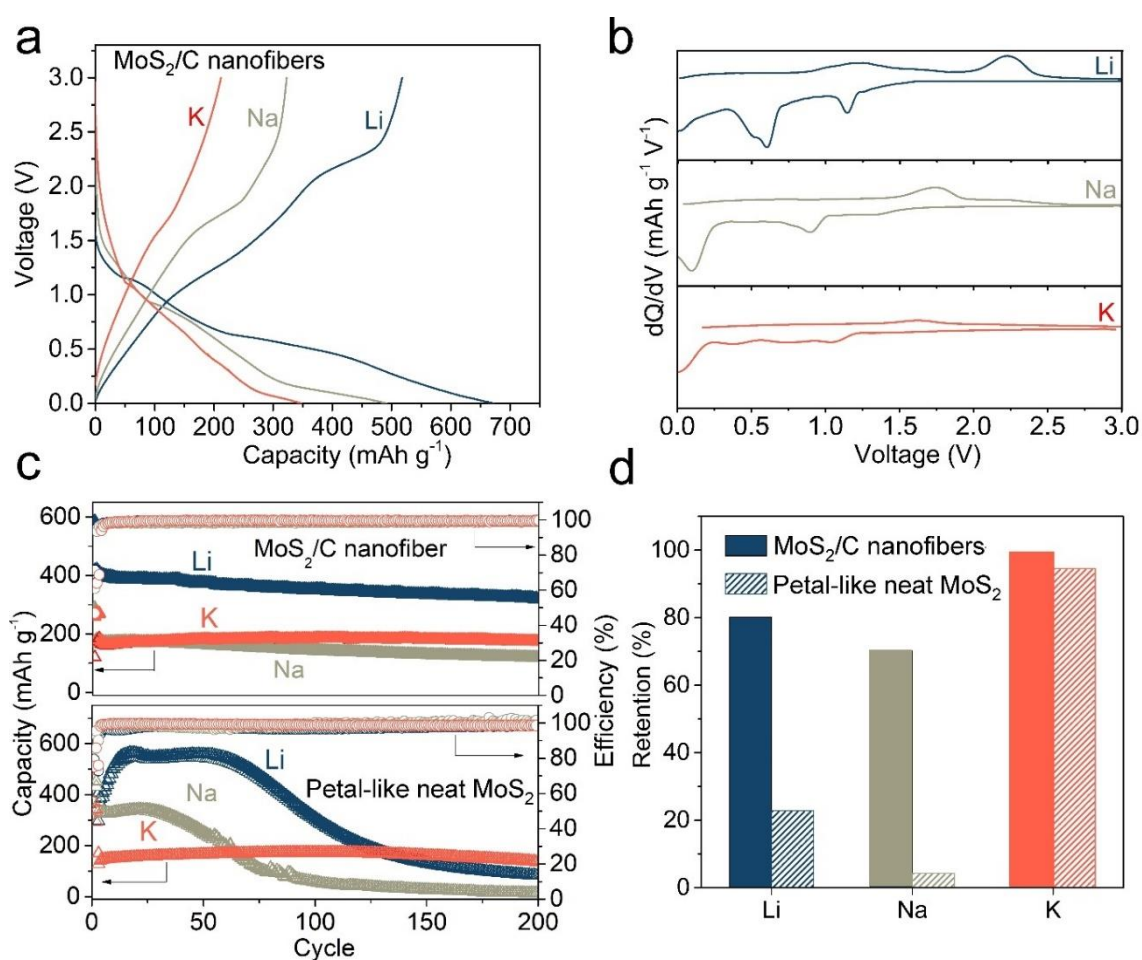


Figure 3.13 Electrochemical performance in LIBs, SIBs and PIBs. (a) Discharge and charge profiles of MoS<sub>2</sub>/C nanofibers at first cycle at 50 mA g<sup>-1</sup>; (b) dQ/dV vs. voltage plots of MoS<sub>2</sub>/C nanofibers at first cycle; (c) Cyclic performance with Coulombic efficiency of MoS<sub>2</sub>/C nanofibers and petal-like neat MoS<sub>2</sub> at 500 mA g<sup>-1</sup>; (d) Retention percentage of MoS<sub>2</sub>/C nanofibers and neat MoS<sub>2</sub> after 200 cycles.

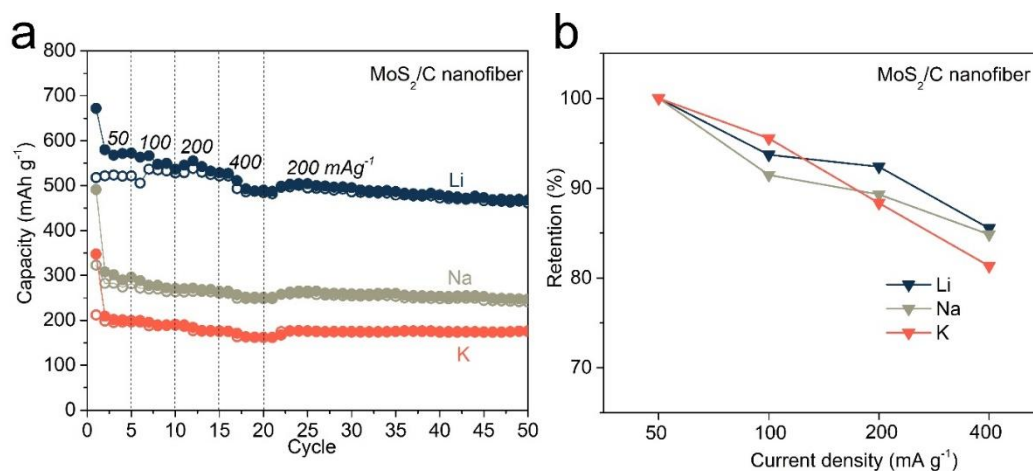


Figure 3.14 (a) Rate performance and (b) retention of MoS<sub>2</sub>/C nanofibers in LIBs, SIBs and PIBs. (Retention is based on the discharged capacity in the fifth cycle).

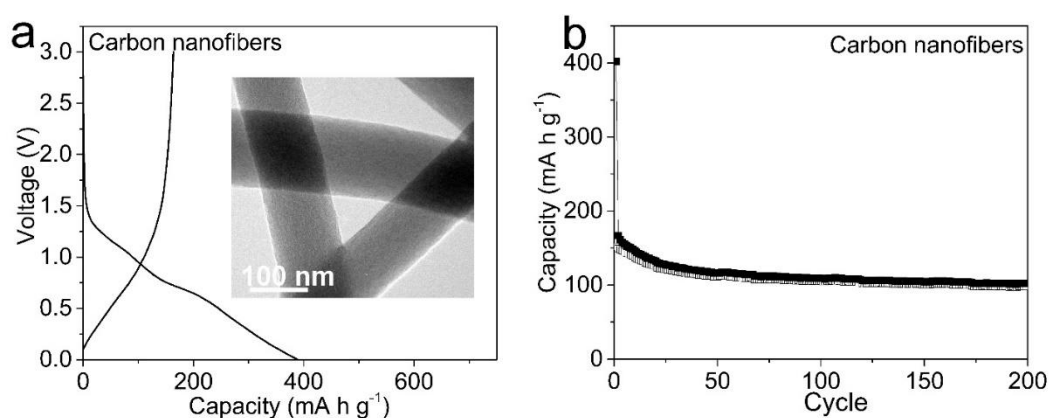


Figure 3.15 Carbon nanofibers. (a) Discharge and charge profiles at first cycle at 50 mA g<sup>-1</sup> (inset: TEM image); (b) cyclic performance at 500 mA g<sup>-1</sup>.

As is well-known, the carbon host in the nanofibers would conduce to better cycling performance for active materials.<sup>77, 159-160</sup> To exclude the interference of carbon, petal-like neat MoS<sub>2</sub> was synthesized by the hydrothermal method.<sup>112</sup> As shown in Figure 3.16a, the prepared neat MoS<sub>2</sub> presents a pure 2H-MoS<sub>2</sub> phase (PDF#37-1492) without any carbon signal. In TEM images (Figure 3.16b, c and b inset), neat MoS<sub>2</sub> present petal-like morphologies with a diameter of ca. 200 nm and are polycrystalline, as revealed by SAED. The HRTEM image (Figure 3.16d) clearly displays a layered structure with an interlayer spacing of 6.3 Å, which is the same as the MoS<sub>2</sub>/C nanofibers. The cyclic performances of neat MoS<sub>2</sub> in LIBs, SIBs and PIBs are given

in Figure 3.13c. Apparent capacity degradation in LIBs and SIBs is observed. In contrast, the neat MoS<sub>2</sub> in PIBs realizes the most stable capacity of 170 mAh g<sup>-1</sup> after 200 cycles with retention of 94.5% (Figure 3.13d). Without protection from the carbon nanofibers, the electrochemical stabilities of MoS<sub>2</sub> show a more striking contrast between the three types of batteries. It is reliable to conclude that MoS<sub>2</sub> intrinsically shows a more stable cyclic performance in PIBs than in LIBs and SIBs.

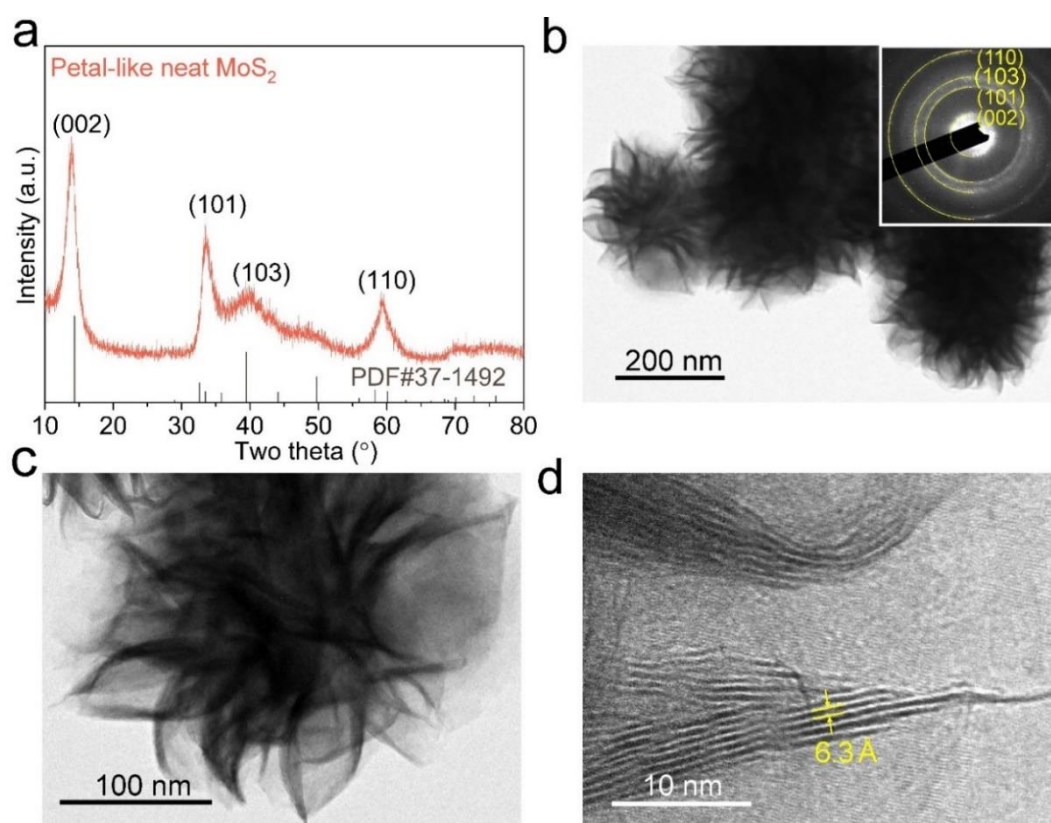


Figure 3.16 Petal-like neat MoS<sub>2</sub>. (a) XRD pattern; (b, c) TEM images and (b inset) SAED pattern; (d) HRTEM image.

We further performed *ex situ* TEM to examine the morphologies of MoS<sub>2</sub>/C nanofibers cycled 200 times. As shown in Figure 3.17a and inset, all the lamellar structural MoS<sub>2</sub> are disappeared and turned into dense nanoparticles after cycling in LIBs. Those particles can be indexed to the Mo phase with a lattice plane spacing of 2.2 Å (PDF#42-1120), which is one of the conversion products. Moreover, the Li<sub>2</sub>S phase can be found in the SAED patterns as another conversion products (Figure 3.18). The layered crystals could no longer be found in SIBs after 200 cycles,

and the materials are changed to loose particles with low contrast (Figure 3.17c). The SAED pattern (Figure 3.17c inset) suggests an amorphous phase without prominent diffraction spots or rings, which is possibly amorphous Mo species by inferring from the Li case. Interestingly, many layered crystals with a layer distance of about  $7.6 \text{ \AA}$  are observed in PIBs (Figure 3.17e and inset). There are fewer layered crystals than the first fully discharged one (Figure 3.11f), possibly because part of the layered  $\text{MoS}_2$  may be consumed through deep conversion reaction. The reaction schematics are described in Figure 3.17b, d and f: the layered crystals in LIBs/SIBs are easily converted to dense/loose particle structures after long cycles, whereas they are the most stable in PIBs explaining the best cyclic stability in electrochemical tests.

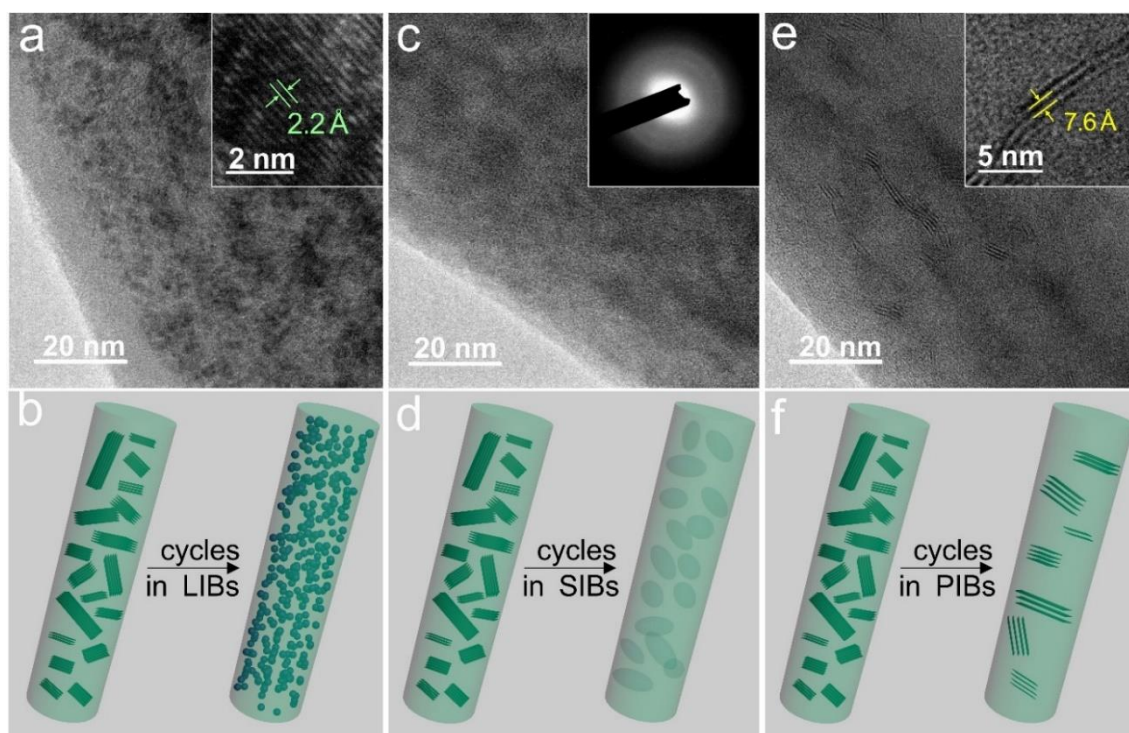


Figure 3.17 *Ex situ* TEM images and schematics of  $\text{MoS}_2/\text{C}$  nanofibers in (a, b) LIBs, (c, d) SIBs and (e, f) PIBs after 200 cycles.

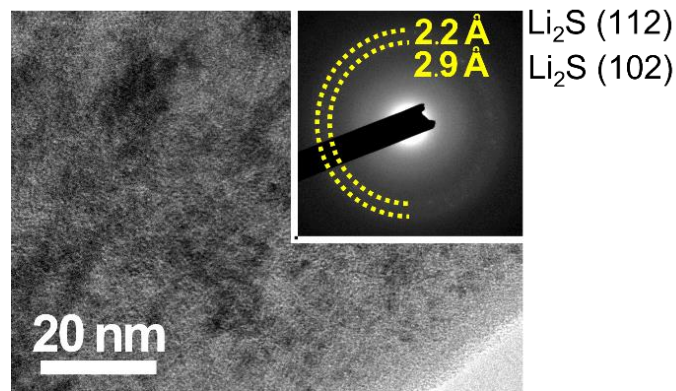


Figure 3.18 The TEM image and SAED pattern of  $\text{MoS}_2/\text{C}$  nanofibers in LIBs after 200 cycles.

### 3.2.4 Theoretical study

The exceptional stability upon large K ion insertion suggests different thermodynamic/kinetic processes governing the intercalation and conversion. DFT computations were carried out to study the mechanisms. We first calculated the reaction enthalpy of conversion from the intercalated compounds  $\text{AMoS}_2$  (A represents Li, Na, and K) to  $\text{A}_2\text{S}$  and Mo. Such values could serve as the descriptor of the thermodynamic driving forces for the conversion reactions. We specifically choose the intermediate intercalated compounds as the reference for our calculation because they are the last intercalated compounds before the conversion reaction actually happens in these three systems. The results are shown in Figure 3.19a, Table 3.1, and Figure 3.20a. The decomposition enthalpies of  $\text{AMoS}_2$  intercalated compounds into Mo and  $\text{A}_2\text{S}$  are -4.46 eV/f.u., -3.16 eV/f.u., and -3.30 eV/f.u. for A=Li, Na, and K, respectively. This indicates a smaller thermodynamic driving force in the case of K for the conversion to take place, leading to the preservation of a large quantity of the lamellar structures. It is also interesting to note that, within the accuracy of DFT framework (as well as neglecting the temperature effect), all the computed reaction enthalpies are negative, meaning the conversion reactions are energetically favorable to take place even at a pretty low degree of alkalization. Therefore, we speculate that the kinetic factor may play a critical role in the conversion reaction as well since such intercalated compounds are observed in experiments. Due to the lack of reliable methods to directly compute the energy barrier for the complicated phase transition, we analyzed the bond characteristics of  $\text{AMoS}_2$ , which may reflect their easiness of conversion reaction. The charge distributions of  $\text{LiMoS}_2$ ,  $\text{NaMoS}_2$ , and  $\text{KMoS}_2$  are investigated by the charge density difference (Figure 3.19b and Figure 3.20b), which is defined by subtracting the electron densities of

Li/Na/K and MoS<sub>2</sub> from the electron density of LiMoS<sub>2</sub>/NaMoS<sub>2</sub>/KMoS<sub>2</sub>. Taking KMoS<sub>2</sub> as an example, it is clear in Figure 3.19b that some charges are accumulated between K and S atoms, suggesting their interaction or bonding. To have a better-quantified view, Figure 3.19c and Figure 3.21 demonstrate the two-dimensional charge density differences along the planes through Li/Na/K and Mo-S atoms. Interestingly, the charge depletion of Li atom (down to -0.07 e bohr<sup>-3</sup>) is more severe than the one of K atom (down to -0.03 e bohr<sup>-3</sup>). The more polar feature of the charge distribution between Li and S suggests the Li-S bond is more electrovalent than the K-S bond.<sup>161</sup> The polarity is further supported by the Bader analysis (Figure 3.19d, Table 3.2, Table 3.3 and Table 3.4) that the Bader charges of alkaline atoms in LiMoS<sub>2</sub>, NaMoS<sub>2</sub>, and KMoS<sub>2</sub> are +0.87, +0.83 and +0.74 e, respectively. The different polarity between Li/K-S bonds may come from the more dispersed electron cloud of K due to the larger number of electrons. When it comes to the conversion reaction, it is conjectured that the more polar bonds between Li and S atoms may kinetically facilitate the formation of Li<sub>2</sub>S by reducing the charge transfer barrier. Shortly, the conversion reaction in the K-MoS<sub>2</sub> system is suppressed thermodynamically (by the lower formation energy) and kinetically (by the less electrovalent K-S bond).

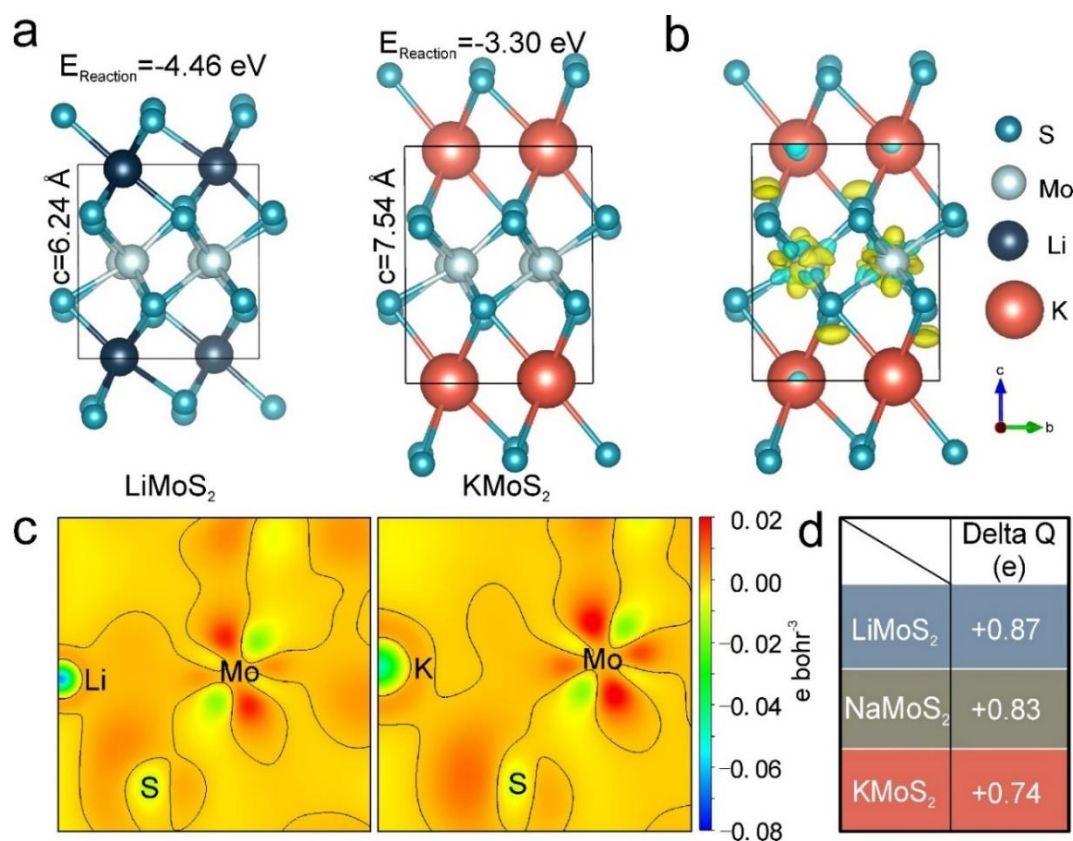


Figure 3.19 DFT simulations. (a) The calculated structures for  $\text{LiMoS}_2$  and  $\text{KMoS}_2$ ; (b) charge density difference distributions for  $\text{KMoS}_2$ ; (c) two-dimensional charge density difference of  $\text{LiMoS}_2$  and  $\text{KMoS}_2$  across Li/K and Mo-S; (d) calculated changes in Li/Na/K atoms charges (delta Q) of  $\text{LiMoS}_2$ ,  $\text{NaMoS}_2$  and  $\text{KMoS}_2$ , respectively (a positive value of delta Q indicates charges loss).

Table 3.1 Formation energy of conversion reaction calculated by DFT.

Reaction formula	Formation energy per equation, eV
$\text{LiMoS}_2 + 3\text{Li} \rightarrow 2\text{Li}_2\text{S} + \text{Mo}$	-4.46
$\text{NaMoS}_2 + 3\text{Na} \rightarrow 2\text{Na}_2\text{S} + \text{Mo}$	-3.16
$\text{KMoS}_2 + 3\text{K} \rightarrow 2\text{K}_2\text{S} + \text{Mo}$	-3.30

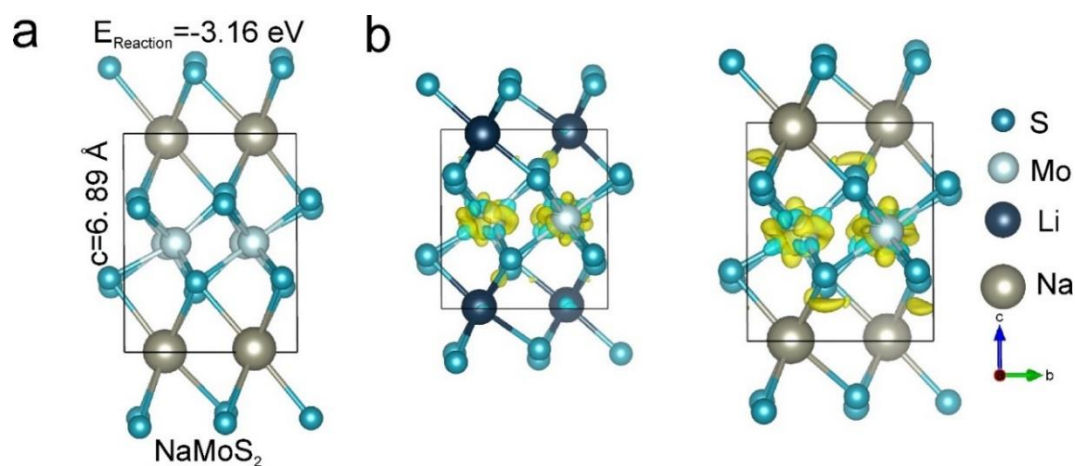


Figure 3.20 DFT simulations. (a) The calculated structures for NaMoS<sub>2</sub>. (b) charge density difference distributions for LiMoS<sub>2</sub> and NaMoS<sub>2</sub>.

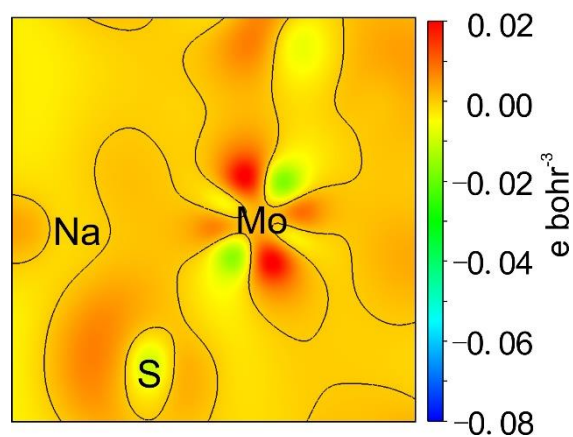


Figure 3.21 Two-dimensional charge density difference of NaMoS<sub>2</sub> across Na and Mo-S.

Table 3.2 Bader charges of LiMoS<sub>2</sub> calculated by DFT.

LiMoS <sub>2</sub>						
#	X	Y	Z	Charge	Oxidation State	Element
1	-2.59625	4.351794	0.134735	2.131359	+0.87	Li
2	5.868415	1.429404	6.100381	2.131359	+0.87	Li
3	0.517746	4.465521	6.175856	2.132736	+0.87	Li
4	2.754427	1.315677	0.05926	2.132736	+0.87	Li

5	2.391099	3.387824	4.840575	6.962424	-0.96	S
6	0.881067	2.393374	1.394541	6.962349	-0.96	S
7	0.955075	0.435462	4.67217	6.9866	-0.99	S
8	2.317091	5.345736	1.562946	6.986556	-0.99	S
9	4.311079	0.493176	4.373794	7.053876	-1.05	S
10	-1.03891	5.288022	1.861322	7.053828	-1.05	S
11	-1.03702	3.367625	4.500062	7.007187	-1.01	S
12	4.309182	2.413573	1.735054	7.007164	-1.01	S
13	3.778862	4.345525	3.142108	12.8646	+1.14	Mo
14	-0.5067	1.435673	3.093008	12.86467	+1.14	Mo
15	0.865863	4.060564	3.116212	12.86171	+1.14	Mo
16	2.406303	1.720634	3.118904	12.86085	+1.14	Mo

Table 3.3 Bader charges of NaMoS<sub>2</sub> calculated by DFT.

NaMoS <sub>2</sub>						
#	X	Y	Z	Charge	Oxidation State	Element
1	-2.68713	4.411477	0.115238	6.165944	+0.83	Na
2	6.011861	1.441757	6.780476	6.165944	+0.83	Na
3	0.557591	4.486844	6.851725	6.167469	+0.83	Na
4	2.76714	1.36639	0.043989	6.167469	+0.83	Na
5	2.406841	3.428325	5.153568	6.978188	-0.98	S
6	0.91789	2.424909	1.742146	6.978148	-0.98	S
7	0.981562	0.439282	4.975082	6.985821	-0.99	S
8	2.343169	5.413952	1.920632	6.985813	-0.99	S
9	4.381836	0.495296	4.688035	7.011752	-1.01	S
10	-1.05711	5.357938	2.207672	7.011705	-1.01	S
11	-1.04972	3.408524	4.80387	6.983182	-0.98	S
12	4.374454	2.44471	2.091837	6.983133	-0.98	S
13	3.824744	4.393717	3.476137	12.85711	+1.14	Mo
14	-0.50001	1.459517	3.419577	12.85718	+1.14	Mo

15	0.875727	4.111541	3.444425	12.85082	+1.15	Mo
16	2.449004	1.741693	3.451289	12.85032	+1.15	Mo

Table 3.4 Bader charges of  $\text{KMoS}_2$  calculated by DFT.

$\text{KMoS}_2$						
#	X	Y	Z	Charge	Oxidation State	Element
1	4.270296	4.479503	0.136914	8.259457	+0.74	K
2	-0.89309	1.455631	7.408322	8.259471	+0.74	K
3	0.563109	4.541108	7.502254	8.258091	+0.74	K
4	2.814099	1.394026	0.042982	8.258051	+0.74	K
5	2.426208	3.475775	5.457142	6.965643	-0.97	S
6	0.951	2.459359	2.088094	6.965636	-0.97	S
7	1.001139	0.447763	5.276035	6.957248	-0.96	S
8	2.376069	5.487371	2.269201	6.957248	-0.96	S
9	4.462263	0.497803	4.986754	6.954054	-0.95	S
10	-1.08506	5.437331	2.558482	6.95402	-0.95	S
11	-1.06381	3.449415	5.101707	6.93455	-0.93	S
12	4.441016	2.485719	2.443521	6.934514	-0.93	S
13	3.878334	4.454059	3.806855	12.83436	+1.17	Mo
14	-0.50113	1.481075	3.738381	12.83442	+1.17	Mo
15	0.88392	4.170707	3.766507	12.83674	+1.16	Mo
16	2.493288	1.764427	3.778729	12.8365	+1.16	Mo

### 3.3 Summary

The alkali-metal ion storage mechanisms from Li, Na to K case are studied by complementary *in situ* experimental and calculation approaches. We articulate that a massive volume expansion of about 140% occurs in K ion incorporation, but unexpected stability is observed. *In situ* TEM is used to examine the structural evolution of layered  $\text{MoS}_2$  upon Li, Na and K ions insertions, indicating that most of the layered crystals are preserved in PIBs. Detailed reaction paths are elucidated by *in situ* XRD and *ex situ* TEM. It is revealed that a large ratio of intercalation

reaction occurs during K ions uptake, giving rise to better structural and electrochemical stability than Li and Na ions insertion. Layered MoS<sub>2</sub> tends to be transformed into tiny particles by deep conversion reaction in the cases of LIBs and SIBs. Assisted by the DFT calculations, we unveil the thermodynamic and kinetic origins of the anomalous stability in the insertion of K ions, where relies on the less electrovalent of K-S bond arising from the larger dispersed electron clouds of K atom than Li and Na ones.

## Chapter 4

### Preserved layered structure enables stable cyclic performance of MoS<sub>2</sub> upon potassium insertion

Transitional metal dichalcogenides represent one important type of anodes for emerging potassium ion batteries (PIBs). K ions are stored through both intercalation and conversion reactions, but the detailed phase transition is not clear. Utilizing commercial MoS<sub>2</sub> as a model material, the competition between intercalation and conversion is revealed, which shows a rate-dependent behavior. The crystal structure of several newly discovered intermediate phases including K<sub>0.5</sub>MoS<sub>2</sub> and K<sub>1.0</sub>MoS<sub>2</sub> is disclosed by complementary experimental and calculational approaches. It shows that intercalation takes place even discharge down to 0 V, differing from the cases in lithium ion (LIBs) and sodium ion batteries (SIBs). The intercalated compound preserves the layered structure of MoS<sub>2</sub>, which avoids the structural collapse and maintains the integrity of the electrode for stable cyclic performance. This finding opens up a new opportunity in the exploration of high-capacity anode among layered transitional metal dichalcogenide families.

#### 4.1 Introduction

Transitional metal dichalcogenides (TMDs) like MoS<sub>2</sub>, MoSe<sub>2</sub>, TiS<sub>2</sub>, VSe<sub>2</sub> and ReS<sub>2</sub>, store the K ions making use of conversion reactions to a large extent.<sup>159, 162-167</sup> Up to four K ions could be uptake, giving rise to a theoretical capacity of over two times as that of a graphite anode, but also cause the capacity degradation arising from enormous strains in the electrode.<sup>168</sup> To alleviate the large volume change during K ion insertion, nanostructured electrodes are widely fabricated, in particular, with nanocarbon materials incorporation.<sup>169-172</sup> Thanks to these efforts, the capacity retention is significantly improved, but some issues associated with nanomaterials,

including the low tap density and large irreversible capacity, remain challenging. Parallel studies on engineering the solid electrolyte interphase (SEI) are conducted to build elastic SEIs for accommodating the volume expansion and maintaining the integrity of the electrode.<sup>173-175</sup> The strategy has been proven effective in stabilizing the anodes of both sodium ion batteries (SIBs) and potassium ion batteries (PIBs) with the utilization of glyme-based electrolyte<sup>75, 176</sup>, although their practical application is restricted by the narrow electrochemical window of glyme solvent compared to carbonates.<sup>177-179</sup>

In addition to the electrode morphology and interphase structure, the cyclic stability also relies largely on the insertion chemistry. In last chapter, it is revealed the best structural integrity of MoS<sub>2</sub> could be maintained during K ion insertion among all the alkali-metal ions. Understanding on the phase transition of metal dichalcogenides during K ions insertion is mainly deduced from their lithiation and sodiation processes.<sup>180-181</sup> In general, both intercalation and conversion take place during potassiation<sup>163-164, 182</sup>, but the detailed process is still a mystery, which also brings about the difficulty in analyzing the corresponding electrode stability. An interesting work by Wu's group is to utilize only the K ion intercalation but avoid the conversion of MoS<sub>2</sub> through shallow discharge to 0.5 V vs. K<sup>+</sup>/K, where an intercalated compound K<sub>0.4</sub>MoS<sub>2</sub> is formed.<sup>183</sup> It shows super-stable cyclic performance because of intercalation-only behavior. Nevertheless, the capacity is limited to 67 mAh g<sup>-1</sup> due to a merely 0.4 K ion intercalation. The detailed phase transition beyond x>0.4 in K<sub>x</sub>MoS<sub>2</sub> is not clear. It is believed that deep discharge will trigger the fully conversion of MoS<sub>2</sub> into Mo and K<sub>2</sub>S, leading to the collapse of layered structure with associated rapid capacity fading. In the current study, using the micro-sized MoS<sub>2</sub> as a model material, we unveil the detailed phase transition pathways and phase competition between the intercalation and conversion, which shows a rate-dependent reaction path and has significant implications on the cyclic stability.

## 4.2 Results and discussion

### 4.2.1 Electrochemical performances evaluation

Commercial MoS<sub>2</sub> were directly used as active materials. The micro-sized MoS<sub>2</sub> is not only beneficial to achieving high Coulombic efficiency and tap density in batteries but has better crystallinity for higher-quality structural examination than nanosized counterpart. SEM images

in Figure 4.1a show the average particle size is around 1.43  $\mu\text{m}$ . They were mixed with 10% carbon super P, 10% vapor grown carbon fibres (VGCF) and 10% carboxymethyl cellulose (CMC) binder to prepare the electrode. 1 M KFSI in EC/PC were adopted as an electrolyte since KFSI salt has been proven beneficial in forming SEI.<sup>52, 184</sup> The voltage profiles of the cell cycled at 50  $\text{mA g}^{-1}$  are given in Figure 4.2a. Three plateaus located at 1.06, 0.36 and 0.09 V are observed in the first discharge, as seen from the  $dQ/dV$  curve (Figure 4.2b), with accumulative capacity of 537  $\text{mA h g}^{-1}$ . In comparison, the charge profile consists of a sloping curve below 1.2 V and a plateau at around 1.56 V with a total capacity of 405  $\text{mA h g}^{-1}$ , corresponding to an initial Coulombic efficiency of 75%. The large capacity loss is mainly ascribed to the formation of SEI. A dense SEI layer with a thickness of around 25 nm is coated on the  $\text{MoS}_2$  particles as shown in Figure 4.3a. It is composed of several organic species plus inorganic components as deduced from XPS Figure 4.3b.

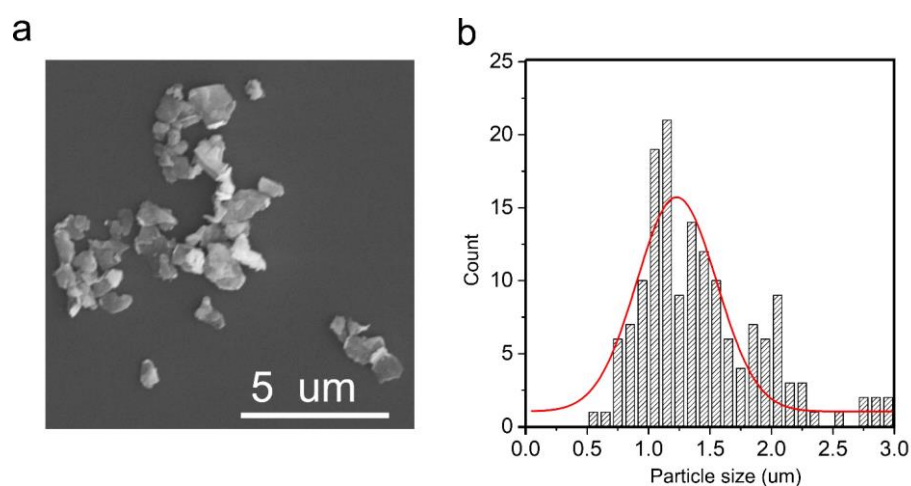


Figure 4.1 (a) SEM image and (b) particle size distribution by Gauss fitting for commercial  $\text{MoS}_2$ .

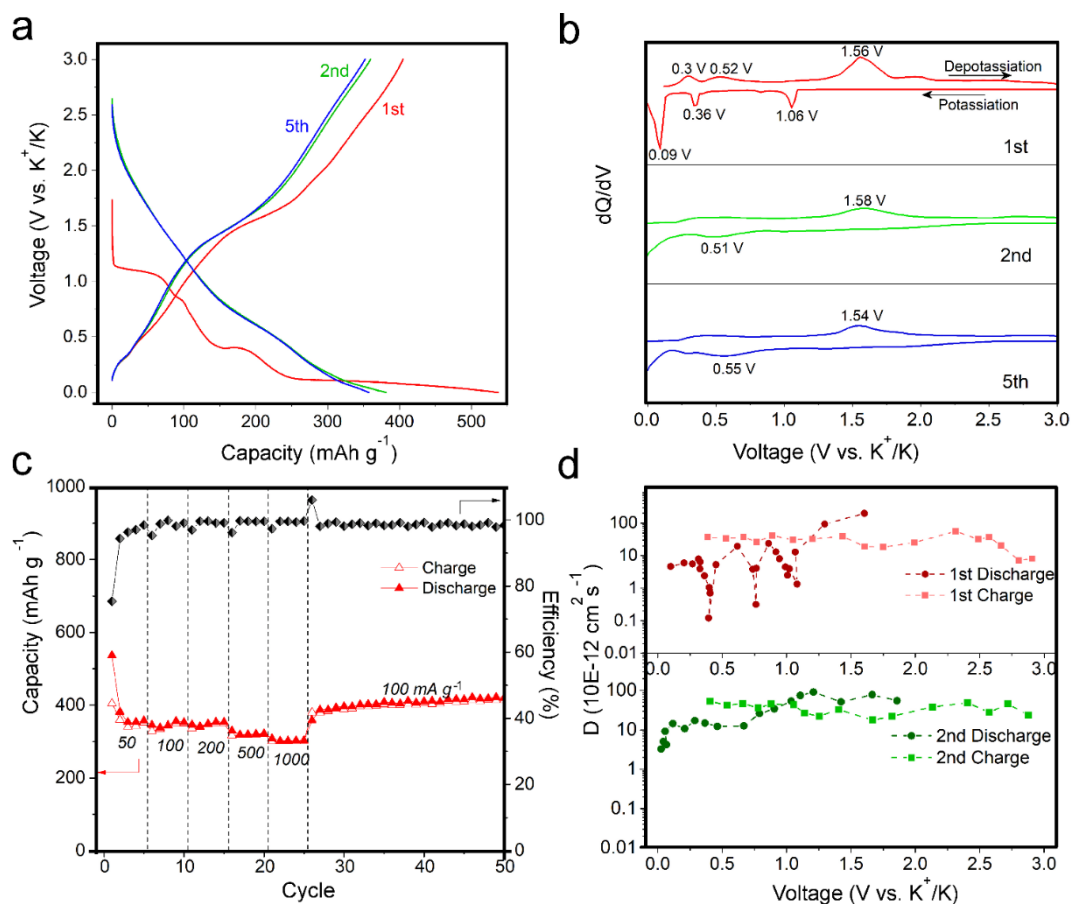


Figure 4.2 Electrochemical performance of MoS<sub>2</sub> anodes in PIBs. (a) The 1st, 2nd and 5th charge and discharge profiles; (b) the corresponding differential capacity curves (dQ/dV); (c) rate performance, cycling stability and Coulombic efficiency; (d) diffusion coefficients as a function of discharge and charge during the 1st and 2nd cycle.

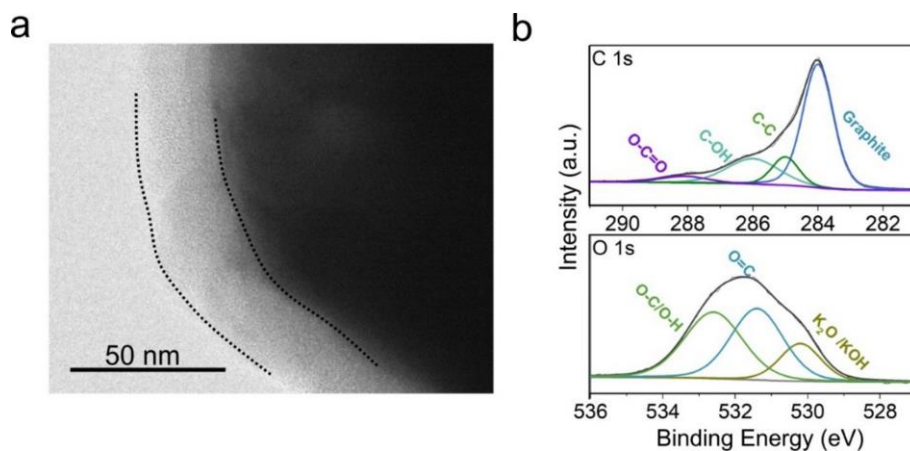


Figure 4.3 (a) TEM image and (b) XPS spectra of C 1s and O 1s for MoS<sub>2</sub> electrode at first cycled state.

The subsequent discharge curve differs a lot from the initial one, which is absent from any clear plateaus and only displays a sloping feature. It indicates a different K ion storage mechanism after initial potassiation. The profiles of the following cycles have identical shapes with the 1st charge and 2nd discharge ones. The capacity becomes stable starting from the 3rd cycle as can be seen in Figure 4.2c. It is a surprise that the capacity does not decrease much when the current density increases from  $50 \text{ mA g}^{-1}$  to  $1000 \text{ mA g}^{-1}$ . The low-rate cycling enables the enlargement of d-spacing, facilitating the K ion transfer under high-current rates. A capacity of  $302 \text{ mA h g}^{-1}$  is maintained when cycled at  $1000 \text{ mA g}^{-1}$ . It suggests a fast K ion diffusion in  $\text{MoS}_2$ , which is confirmed in the galvanostatic intermittent titration technique (GITT) results (Figure 4.2d and Figure 4.4). Despite the varied diffusion coefficient in the first potassiation, which may be due to the complex phase transitions as will be discussed later, the following K ions insertion/extraction delivers a stable and high value in the order of  $10^{-11} \text{ cm}^2 \text{ s}^{-1}$ . This value is comparable to that in Na ion batteries, although K ion has a larger radius than Na one.<sup>185</sup> Lastly, the capacity is recovered to  $380 \text{ mA h g}^{-1}$  when the current density reduces to  $100 \text{ mA g}^{-1}$ , demonstrating superior reversibility. The obtained performance of microsized  $\text{MoS}_2$  is among the best in TMDs anode materials (Figure 4.5), even comparable to the nanostructured composites. The excellent cyclic stability in the microsized particles is out of our expectation, which may imply a distinct reaction path and deserve further investigation.

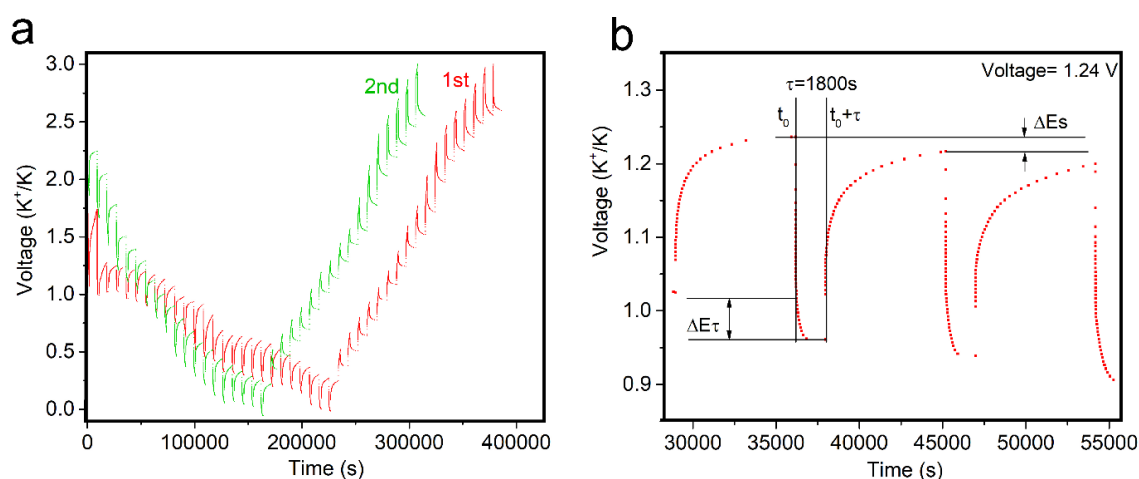


Figure 4.4 (a) GITT profile of first and second cycle. (b) Current step diagram at 1.24 V vs.  $\text{K}^+/\text{K}$  of the first potassiation process of  $\text{MoS}_2$  electrode for PIBs.

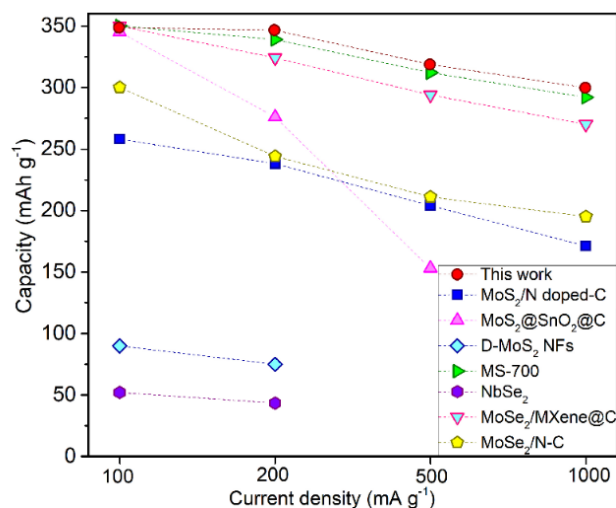


Figure 4.5 The electrochemical performance plot of TMDs anode materials including MoS<sub>2</sub>/N doped-C,<sup>186</sup> MoS<sub>2</sub>@SnO<sub>2</sub>@C,<sup>172</sup> D-MoS<sub>2</sub> NFs,<sup>187</sup> MS-700,<sup>188</sup> NbSe<sub>2</sub>,<sup>189</sup> MoSe<sub>2</sub>/MXene@C<sup>160</sup> and MoSe<sub>2</sub>/N-C.<sup>162</sup>

#### 4.2.2 K-MoS<sub>2</sub> phase transition mechanism

*In situ* X-ray diffraction (XRD) was carried out to investigate the phase transition of microsized MoS<sub>2</sub> anodes. A Swagelok-type cell equipped with a Beryllium window was adopted for the test. The cell was cycled between 0 and 3 V at a low current density of 10 mA g<sup>-1</sup> for fully reacting. Based on the electrochemical curves in Figure 4.2a, the XRD patterns under different charge/discharge depths during first discharge (D1), first charge (C1) and second discharge (D2) were selected and presented in Figure 4.6a. The pattern at open circuit voltage (OCV) state agrees well with 2H-MoS<sub>2</sub> (PDF#37-1492). Several peaks contributed by conductive carbon and Be window are also observed. 2H-MoS<sub>2</sub> has a layered structure consisting of covalently bonded S-Mo-S layers. The (002) peak of pristine MoS<sub>2</sub> is located at 14.5°, corresponding to a d-spacing of 6.1 Å. Upon discharging to 0.9 V, the (002) peak downshifts to 10.8° together with the appearance of new peaks at 21.6°, which could be assigned to the hexagonal K<sub>0.4</sub>MoS<sub>2</sub> compound. This newly formed compound has an expanded d-spacing of 8.3 Å. The peaks from residual MoS<sub>2</sub> are also observed as an indication of incomplete transition at this stage. With further intercalation of K ions, a slight right shift of (002) peak from 10.8° to 11.0° is found, which suggests a small shrinkage of the unit cell. The small contraction may result from a distortion of the initial 2H structure, leading to the formation of K<sub>y</sub>MoS<sub>2</sub>. The peak intensity of this phase gradually decreases with continuously discharging, accompanied by the appearance

of a broad peak at  $11.5^\circ$  implying the formation of another phase  $K_z\text{MoS}_2$  ( $z > y$ ) at 0.1 V. It is counterintuitive to find that the d-spacing of  $K_z\text{MoS}_2$  tends to be reduced with the intercalation of more K ions. Based on previous studies the obvious constriction may attribute to the phase transition from distorted 2H structure to more stable 1T phase, similar to the Li, Na intercalated  $\text{MoS}_2$ <sup>145, 152, 190-191</sup>. When the cell reaches 0V, the  $K_y\text{MoS}_2$  disappears and only the  $K_z\text{MoS}_2$  is maintained. Here the accurate value of  $y$  and  $z$  is difficult to be determined from the capacity due to the possible involvement of conversion reaction and concomitant electrolyte decomposition, hence discouraging ones to reveal the detailed crystal structure of the two phases based solely on the XRD patterns.

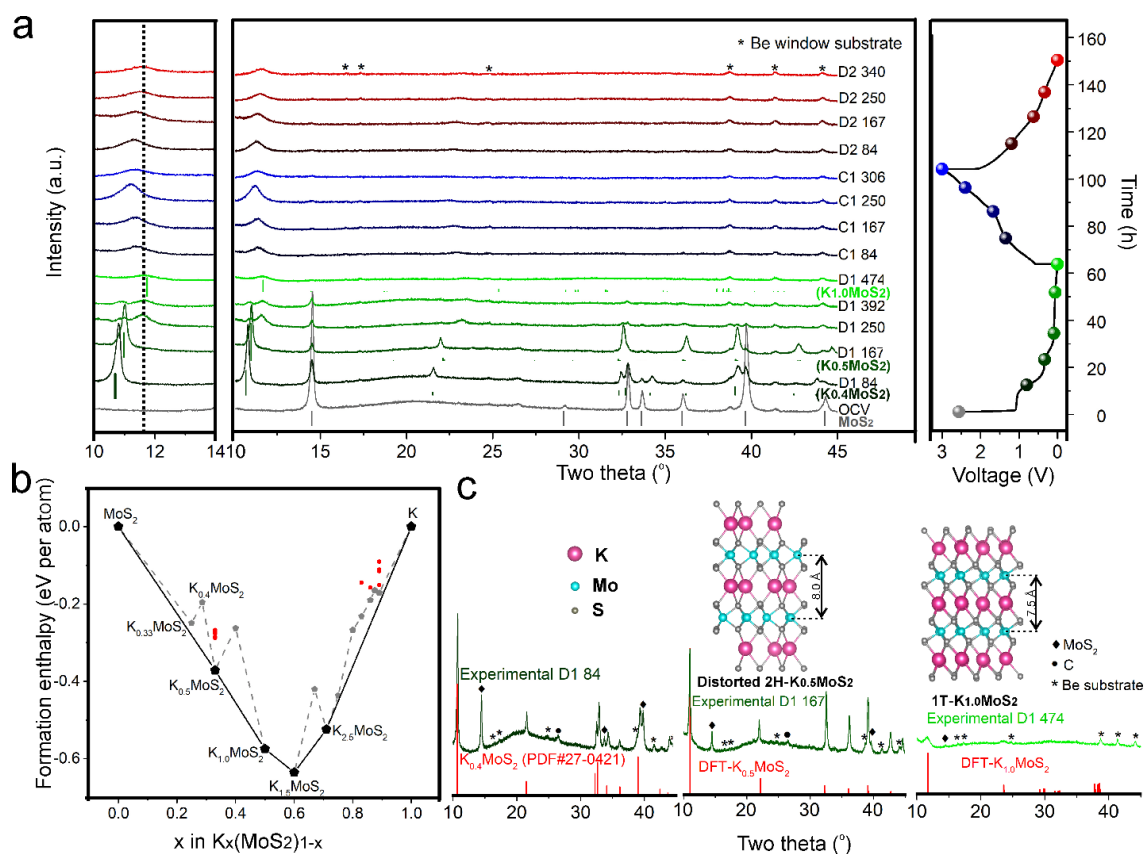


Figure 4.6 Phase transitions of  $\text{MoS}_2$ . (a) *in situ* XRD patterns of  $\text{MoS}_2$  at different discharge and charge states, the corresponding voltage profiles are given on the right. For clear visualization, enlarged XRD pattern between  $10^\circ$ - $14^\circ$  is put on the left. The letters stand for first discharge (D1), first charge (C1) and second discharge (D2) with the followed numbers showing the capacity in  $\text{mA h g}^{-1}$ . (e.g. C1 167 means the capacity is  $167 \text{ mA h g}^{-1}$  of K ions de-intercalation in the first charge.). (b) Density-functional theory (DFT) calculation with Vdw-optPBE corrections of  $\text{MoS}_2$  electrodes. The solid line indicates the thermodynamically stable

phases within DFT and temperature errors, while the dashed line refers to the lowest formation enthalpy of each composition. The red dots show the structures in addition to the ones of the lowest enthalpy. (c) The simulated and experimental XRD patterns. Insets are the calculated crystalline structures.

To address the above issue, theoretical calculations were conducted to figure out the compounds during the K ion insertion. Figure 2b shows the formation enthalpy of all the feasible potassium intercalated MoS<sub>2</sub> phases from the database and Li analogs.<sup>153, 192</sup> It suggests a reaction path of MoS<sub>2</sub>-K<sub>0.5</sub>MoS<sub>2</sub>-K<sub>1.0</sub>MoS<sub>2</sub>-K<sub>1.5</sub>MoS<sub>2</sub> upon potassiation. Apart from the reported K<sub>0.4</sub>MoS<sub>2</sub> phase, the simulated XRD patterns of K<sub>0.5</sub>MoS<sub>2</sub> and K<sub>1.0</sub>MoS<sub>2</sub> agree well with the K<sub>y</sub>MoS<sub>2</sub> and K<sub>z</sub>MoS<sub>2</sub> phases that observed in the *in situ* XRD tests (Figure 4.6c). It reveals that the value of y and z equals to 0.5 and 1, respectively. The K<sub>1</sub>MoS<sub>2</sub> is also confirmed by chemical synthesis through high energy ball milling of stoichiometric amount of potassium and MoS<sub>2</sub> (Figure 4.7). K<sub>0.5</sub>MoS<sub>2</sub> and K<sub>1.0</sub>MoS<sub>2</sub> belong to two different phases of 2H and 1T, but with a distortion in the structure. The parameters of the crystal lattice are given in Table 4.1. Lastly, the calculation indicates the presence of K<sub>1.5</sub>MoS<sub>2</sub>, which is absent in the experimental results due possibly to its unfavourable kinetics. K<sub>1.5</sub>MoS<sub>2</sub> is not a layered structure anymore (Figure 4.8), which may possess a higher energy barrier to break/form the bonds.

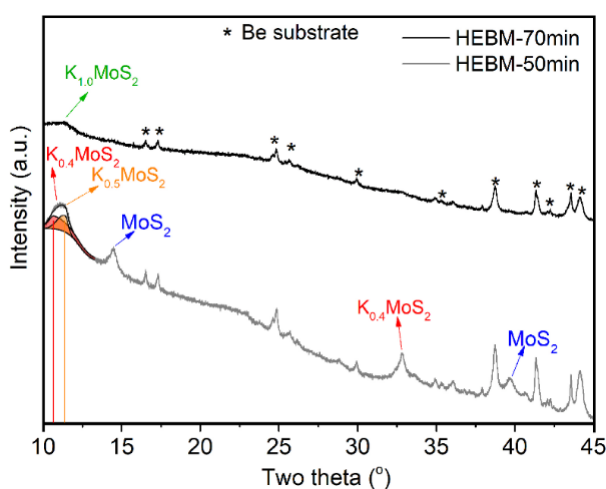
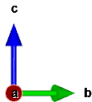
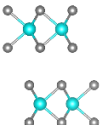
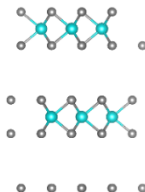
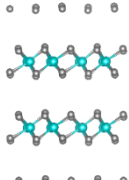
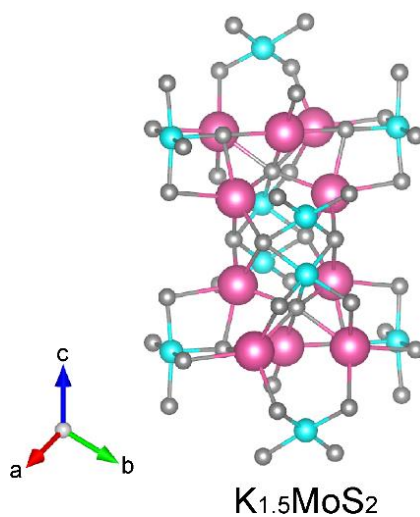


Figure 4.7 XRD patterns of K<sub>1.0</sub>MoS<sub>2</sub> prepared by high energy ball milling with stoichiometric amount of potassium metal and MoS<sub>2</sub>.

Table 4.1 The simulated structures without showing K-S bonding and K atoms, and the lattice parameters of calculated phases.

Simulated structures	2H-MoS <sub>2</sub>	Distorted 2H-K <sub>0.5</sub> MoS <sub>2</sub>	Distorted 1T-K <sub>1.0</sub> MoS <sub>2</sub>	1T- MoS <sub>2</sub>	
					
<b>Lattice parameters</b>	<b>a / Å</b>	3.14	6.50	7.02	3.25
	<b>b / Å</b>	3.14	6.50	6.98	3.25
	<b>c / Å</b>	12.53	16.06	7.54	6.14
	<b>Alpha / °</b>	90	90	90.29	90
	<b>Beta / °</b>	90	90	89.86	90
	<b>Gamma / °</b>	120	120	121.38	120

Figure 4.8 Simulated structures of K<sub>1.5</sub>MoS<sub>2</sub>.

Upon charging, the K ions are removed from  $K_{1.0}MoS_2$ . Interestingly, the main peak at  $11.5^\circ$  degree gradually shifts to the left as a reflection of d-spacing enlargement. The end-phase when charging to 3 V, denoted as  $K_xMoS_2$  ( $x < 1$ ), recovers to neither initial intercalated compound  $K_{0.4}MoS_2$  nor pristine  $MoS_2$ . In the following K ion intercalation (2nd discharge), the peak shifts back and finally restore to  $K_{1.0}MoS_2$  at 0 V, suggesting the reversibility of the insertion/extraction process between  $K_xMoS_2$  and  $K_{1.0}MoS_2$  after 1st discharge. It is worth noting that a small peak at  $14.5^\circ$  associated with unreacted  $MoS_2$  exists at all the states, due to the incomplete reaction arising from the relatively large particle size of the active materials.

The phase transition is further investigated by *in situ* Raman. As shown in Figure 4.9, the pristine  $MoS_2$  at OCV condition shows three peaks which can be assigned to  $E_{1g}$  ( $281.3\text{ cm}^{-1}$ ),  $E_{12g}^1$  ( $378.2\text{ cm}^{-1}$ ) and  $A_{1g}$  ( $404.6\text{ cm}^{-1}$ ) vibration model of typical 2H structures. The intensities of  $E_{12g}^1$  and  $A_{1g}$  peaks decrease with K ion insertion as observed in the D1 84 sample, and finally disappear in the D1 167 sample. Meanwhile, new peaks located at  $147\text{ cm}^{-1}$ ,  $239.2\text{ cm}^{-1}$ ,  $281.3\text{ cm}^{-1}$  and  $326.1\text{ cm}^{-1}$ , corresponding to the  $J_1$ ,  $J_2$ ,  $E_{1g}$  and  $J_3$  of 1T structure, show up and grow along with subsequent K ions insertion. This mainly because 2H- $MoS_2$  with trigonal phase has been gradually replaced by octahedral 1T- $K_{1.0}MoS_2$  structure, which is consistent with XRD results.<sup>145, 154</sup> At 0 V, the initial 2H phase completely vanishes and only the 1T phase is detected. This 1T phase dominates the whole process without recovering to the pristine 2H structure in the following cycles, agrees well with the phase transition between  $K_xMoS_2$  and  $K_{1.0}MoS_2$  after first discharge as demonstrated before in XRD tests. The 1T phase, which has different vibration modes with pristine 2H phase, provides high metallic conductivity and ion mobility, low energy unoccupied states for excellent electrochemical performance.<sup>193-196</sup>

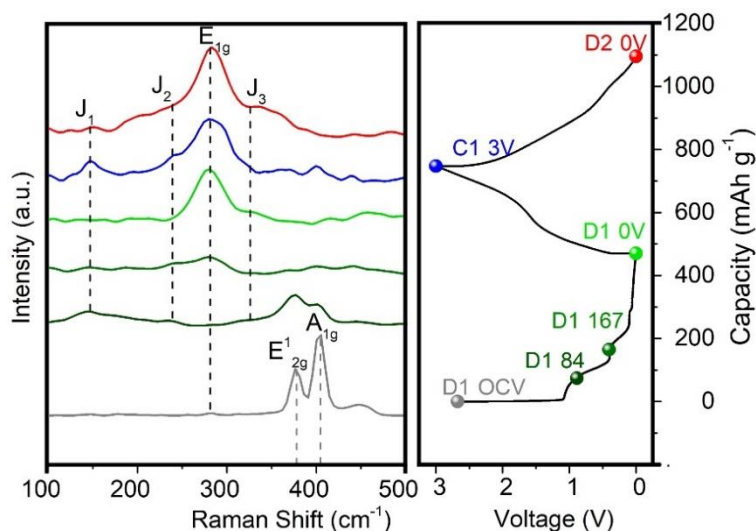


Figure 4.9 *In situ* Raman spectra of MoS<sub>2</sub> electrodes at different states and the corresponding voltage profiles.

The combined calculational and experimental results demonstrate that as high as one K ion per MoS<sub>2</sub> could be intercalated instead of 0.4 K ions. Nevertheless, the intercalation behavior could only contribute a capacity of 167 mA h g<sup>-1</sup>, which is much less than the reversible capacity of 353 mA h g<sup>-1</sup>. It signifies that conversion reaction must have taken place although the XRD does not show clear traces. We speculate that the conversion products, *i.e.*, Mo and K<sub>2</sub>S, have very tiny sizes and probably stay in amorphous states. Therefore, TEM images after different cycles were collected to examine the assumption and probe the morphology evolution of the active materials, as shown in Figure 4.10. The selected area electron diffraction (SAED) and high-resolution transmission electron microscopy (HRTEM) of micro-sized pristine MoS<sub>2</sub> indicate typical 2H phase and layered structure with d-spacing of 6.1 Å (Figure 4.10a and b). After discharging to 0 V (Figure 4.10c and d), the particles remain in microsize instead of breaking up. HRTEM shows that it preserves the layered structure but with an enlarged d-spacing of 7.9 Å, which resembles the K<sub>1.0</sub>MoS<sub>2</sub> phase revealed in XRD. Assisted by the SAED pattern and HRTEM images (insets of Figure 4.10d, f, and h), metallic Mo (PDF#42-1120) species with the d-spacing of 2.2 Å is discovered with poor crystallinity.<sup>186</sup> The observations prove that accompanying with intercalation process the conversion reaction  $4\text{K} + \text{MoS}_2 \rightarrow \text{Mo} + 2\text{K}_2\text{S}$  also occurs, enabling the detection of metallic Mo. When charging to 3 V, the layered structure is maintained which has similar d-spacing with K<sub>1.0</sub>MoS<sub>2</sub>. It does not return to pristine MoS<sub>2</sub>

phase, agrees well with *in situ* XRD tests. The metallic Mo species could still be captured in a charged and cycled sample, reflecting the conversion reaction is not fully reversible (Figure 4.10e and g). The new ring of 3.5 Å in discharged, charged and cycled samples may be ascribed to  $K_xS$ .<sup>197</sup>

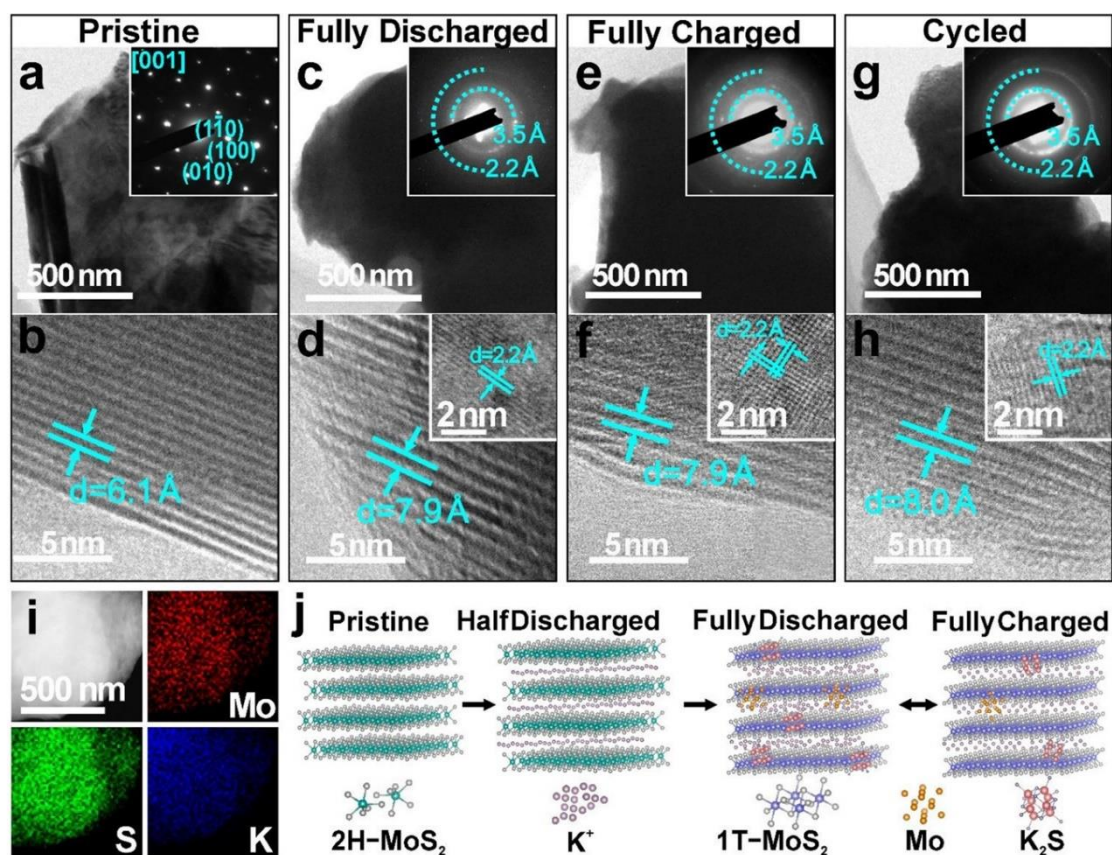


Figure 4.10 Morphology evolution of  $MoS_2$  electrodes. TEM, corresponding SAED and HRTEM images of (a and b) pristine  $MoS_2$ ; (c and d) after first discharge to 0 V; (e and f) the first charged to 3V; (g and h) after 100 cycles; Insets: HRTEM image of metallic Mo. (i) HAADF-STEM image and corresponding EDS elemental maps of the first fully discharged  $MoS_2$  electrode; (j) schematic diagram for phase transition of  $MoS_2$ .

#### 4.2.3 Confirmation of layered $K_{1.0}MoS_2$ phase

Co-occurrence of intercalation and conversion at 0 V is unusual. It differs a lot from previous observations during lithiation and sodiation of  $MoS_2$  in LIBs and SIBs, where all the intercalated compounds will be converted into Mo and  $Li_2S/Na_xS$  at a low voltage.<sup>147, 198</sup> To

---

further confirm the presence of  $K_{1.0}MoS_2$  phase, the fully discharge electrode at 0 V was disassembled and immersed in DI water for one day to remove K ions, which is enlightened by Morrison and co-workers who use forced hydration method to exfoliate  $MoS_2$  from  $Li_xMoS_2$ .<sup>199</sup> Interestingly, the phase is recovered to  $MoS_2$  with a clear layered structure, as demonstrated by XRD and TEM in Figure 4.11. Note that it is impossible to restore the  $MoS_2$  phase through oxidation in water if the final reaction products were only Mo and  $K_2S$ . Therefore, the intercalated phase  $K_{1.0}MoS_2$  must be one of the reaction products at 0 V. Moreover, it is found that only  $K_xMoS_2$  could be obtained during electrochemical oxidation, but a fully de-potassiated  $MoS_2$  is acquired when sinking into the water. We suspect that the last de-potassiation step from  $K_xMoS_2$  to  $MoS_2$  has very slow kinetics, deterring the complete extraction of K ions through an electrochemical process. It is partly supported by the fact that short-time rinse with water cannot fully remove K ions. Instead, continuous oxidation as long as one day in the water is required.

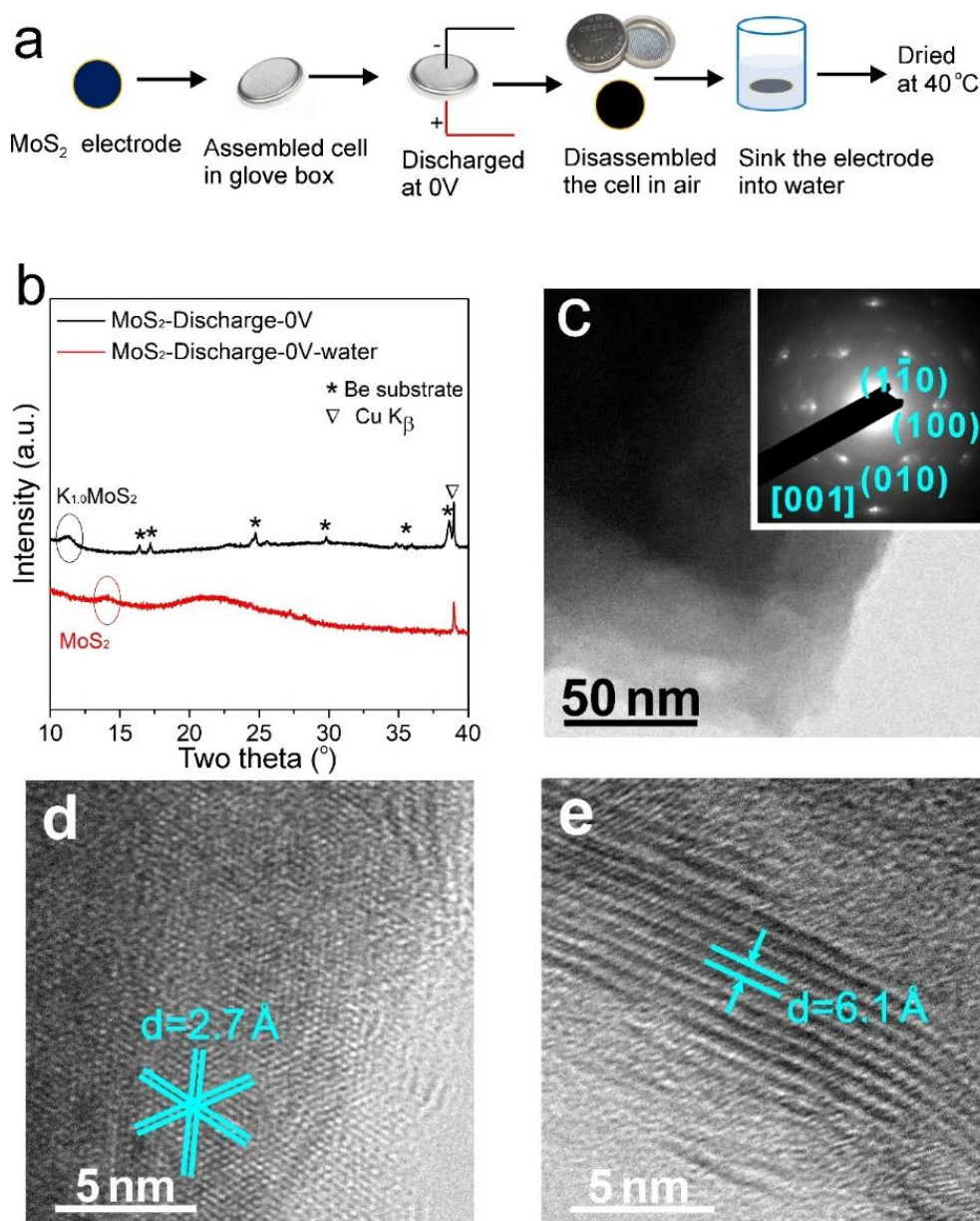


Figure 4.11 (a) Schematic of preparing MoS<sub>2</sub>-Discharge-0V-water electrode. PVDF is used as a binder instead of CMC to avoid the dissolution. (b) XRD pattern of these different samples. (c, d, e) TEM, SAED and HRTEM images of sample MoS<sub>2</sub>-Discharge-0V-water, indicating the recovery of MoS<sub>2</sub> phase.

Preserve of the layered structure is essential to the integrity of the electrode. To examine the long-term stability, TEM images after 100 cycles are given in Figure 4.10g and h. It is noted after repeated insertion/extraction, both integrity of the particle and the layered structure are well kept. This is surprising as the volume change arising from conversion and alloy anodes always lead to pulverization of the particles, which is one of the major reasons for their capacity

degradation. The unity of the electrode is ascribed to the intercalation behavior of  $K_x\text{MoS}_2$ , which is intact in the whole process and serves as a framework to avoid the isolation of the particles. To examine the distribution of the intercalation compounds and conversion products, the high-angle annular dark field image (HAADF) in scanning transmission electron microscopy (STEM) and corresponding elemental mapping of the samples at first fully discharged, charged and cycled states are shown in Figure 4.10i, Figure 4.12 and Figure 4.13. Mo, S and K elements are uniformly distributed in these samples, signifying the reaction products of intercalation and conversion are interlocking with each other. The schematic of the discharge and charge process is shown in Figure 4.10j. During the first discharge process,  $2\text{H-MoS}_2$  transfers to  $1\text{T-K}_{1.0}\text{MoS}_2$  with enlarged interlayer spacing. This broad, rigid construction avoids the huge volume expansion during the K ion intercalation reaction and maintains the structural stability.

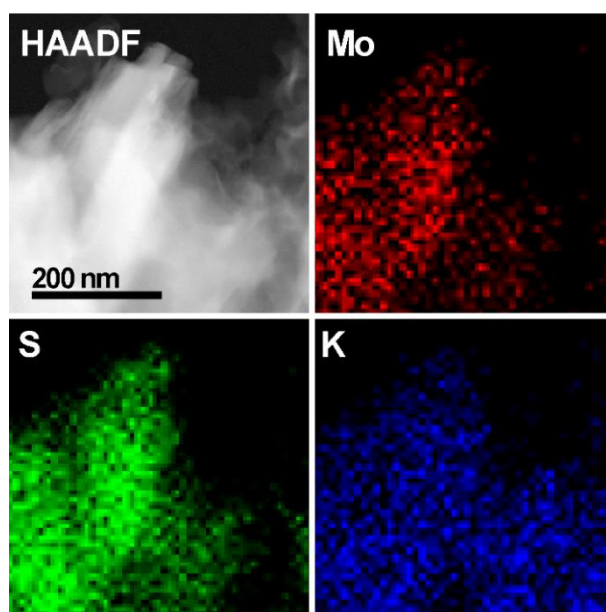


Figure 4.12 The HAADF-STEM image and corresponding EDS mapping of  $\text{MoS}_2$  anode in the first fully charged state.

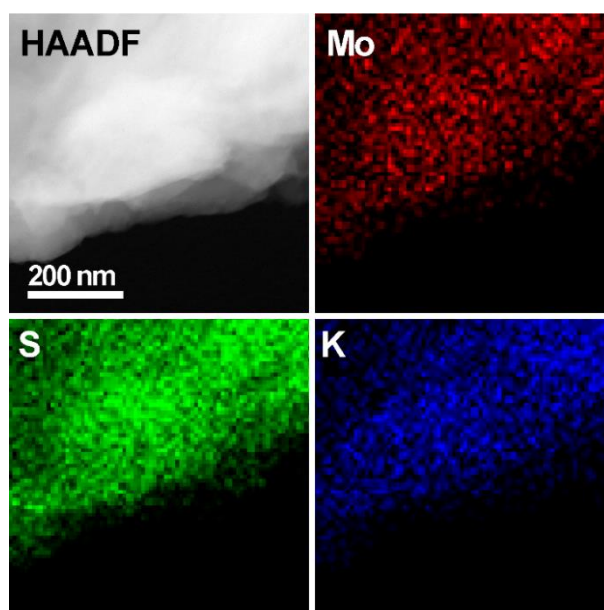


Figure 4.13 The HAADF-STEM image and corresponding EDS mapping of MoS<sub>2</sub> anode after 100 cycles.

#### 4.2.4 Competition between intercalation and conversion reactions

It is found that the capacity decreases with increasing current densities (Figure 4.14). An intriguing question is how the phase transition is dependent on the current rates. Thus, we collected the *ex situ* XRD patterns for the electrodes charge/discharged at different current densities, and the results are compared in Figure 4.15a. When cycling at 50 mA g<sup>-1</sup>, the phase transition process is similar to those observed previously in the *in situ* tests, where the K ions shuttle between K<sub>1.0</sub>MoS<sub>2</sub> and K<sub>x</sub>MoS<sub>2</sub>. Once the current density increases to 500 mA g<sup>-1</sup>, the MoS<sub>2</sub> cannot be fully intercalated but mixed phases of K<sub>0.4</sub>MoS<sub>2</sub> and K<sub>0.5</sub>MoS<sub>2</sub> are observed. It could be partly recovered to pristine MoS<sub>2</sub> phase in the following charge. With further increasing on the current density to 1000 mA g<sup>-1</sup>, an even shallower intercalated compound K<sub>0.4</sub>MoS<sub>2</sub> is found at 0 V. The phase is almost fully recovered to MoS<sub>2</sub> in the subsequent charge. The above findings signify a rate dependent phase transition phenomenon in MoS<sub>2</sub>. It should be mentioned that the conversion reaction still occurs under all the current rates. Although more conversion is involved under slow rate, the integrity of electrode is also maintained due to the presence of intercalation for stable cycling. The capacity contribution from intercalation and conversion is roughly calculated from the reversible capacities of the electrode and the theoretical capacities of each potassiation path. We suppose all the MoS<sub>2</sub> participated in the

reactions. The results are given in the inset of Figure 4.15b. It can be seen that 63.8% of the total capacity comes from intercalation at a high current rate of  $1000 \text{ mA g}^{-1}$ , while the value is only 27.5% for the cell tested at  $50 \text{ mA g}^{-1}$ . The reason lies in the faster kinetics of intercalation than conversion reaction. Moreover, the thermodynamic also plays important roles. The formation enthalpies of these two reactions are calculated, it is found that a smaller formation energy for intercalation reaction than conversion counterpart (Table 4.2), indicating the larger thermodynamically force for the intercalation than conversion reaction.

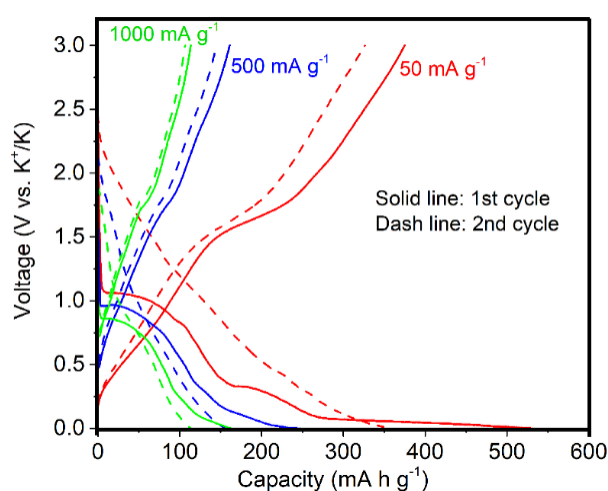


Figure 4.14 The 1st and 2nd charge and discharge profiles at different rates.

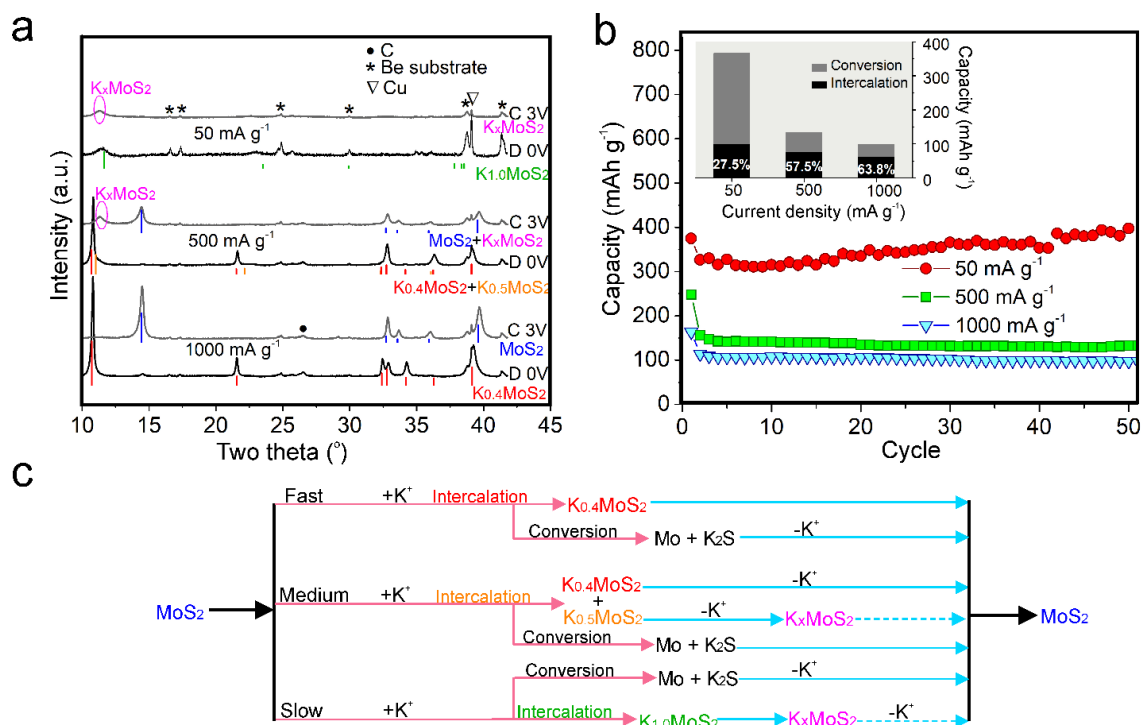


Figure 4.15 Rate-dependent phase transition. (a) *Ex situ* XRD pattern of first fully discharged (D 0 V) and charged (C 3 V) MoS<sub>2</sub> electrode with different current density (b) cyclic performance of MoS<sub>2</sub> electrode at different current density (inset: ratio of the capacities contributed by intercalation and conversion); (c) schematic of phase transition for MoS<sub>2</sub> upon K ion insertion. Dash line indicates the process cannot be achieved by electrochemical reaction but is possible through chemical oxidation.

Table 4.2 The calculate formation enthalpy of intercalation and conversion reactions by DFT.

Reaction formula	Formation energy per formula, eV
MoS <sub>2</sub> +K→KMoS <sub>2</sub> (Intercalation reaction)	-9.04
KMoS <sub>2</sub> +3K→Mo+K <sub>2</sub> S (Conversion reaction)	-3.30

Based on the above discussions, the phase transition of MoS<sub>2</sub> upon potassiation is summarized in Figure 4.15c. Series intermediate phases are unveiled during K ion intercalation. As many as one K ion could be inserted into MoS<sub>2</sub>, differing from 0.4 K ion that reported previously. Nevertheless, the fully potassiated phase only appears when discharging at a low current density. Otherwise, a shallow intercalated phase will be observed under a fast discharge. Among the intercalated compounds, only K<sub>0.4</sub>MoS<sub>2</sub> could return to pristine MoS<sub>2</sub> during charge, while

the recovery of MoS<sub>2</sub> from K-rich K<sub>0.5</sub>MoS<sub>2</sub> and K<sub>1.0</sub>MoS<sub>2</sub> phases is only possible with chemical oxidation due to slow kinetics. Turning to the conversion reaction, it occurs only after the formation of K<sub>0.4</sub>MoS<sub>2</sub> phase as it is absent when cut-off at 0.5 V in the previous work.<sup>183</sup> The conversion reaction cannot be avoided when discharging to 0 V, no matter at a fast or slow cyclic rate, but its contribution to the capacity will be largely reduced with increasing current density. Similarly, intercalation reaction could also take place even cycled at a very slow current density, which is evidenced by obtaining a reversible capacity of around 470 mAh g<sup>-1</sup> under very small current density of 5 mA g<sup>-1</sup> (Figure 4.16). It is still lower than 668 mAh g<sup>-1</sup> for a fully conversion reaction, indicating a fraction of intercalation reaction. The conversion reaction should be reversible based on the capacity obtained since single intercalation process would not lead to such a high capacity. The cells deliver stable cyclic performance at both high and low rates (Figure 4.15b), thanks to the presence of intercalation behaviour, which preserves the layered framework. To make an analogy, the intercalated compounds such as K<sub>1.0</sub>MoS<sub>2</sub> serves as pillars in a house. As long as the pillar stands, the house will not collapse although the inner structure may be destroyed. It explains that a stable capacity of about 360 mA h g<sup>-1</sup> is obtained under 50 mA g<sup>-1</sup>, although conversion reaction is involved. The long-term cyclic performance at 1000 mA g<sup>-1</sup> is presented in Figure 4.17, showing excellent stability with capacity retention of 83% after 300 cycles.

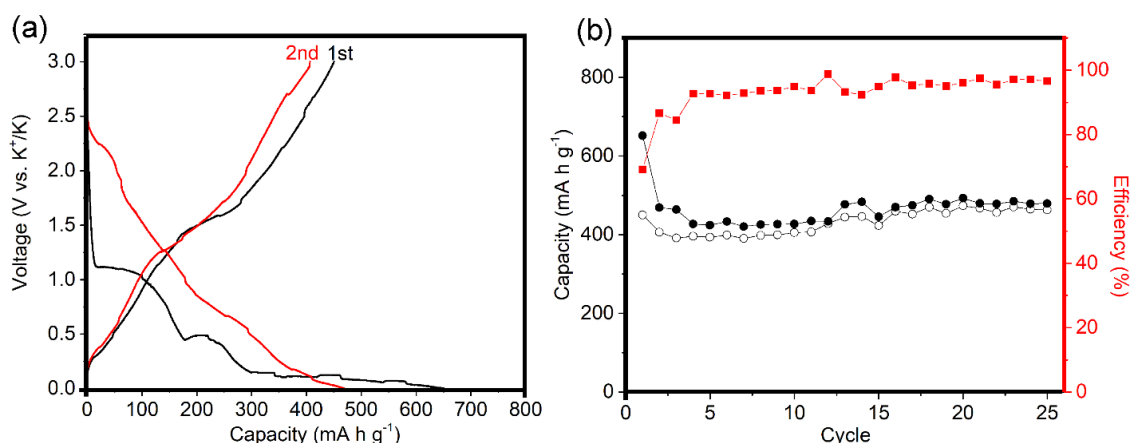


Figure 4.16 The 1st and 2nd charge/discharge profiles and cyclic performance of MoS<sub>2</sub> electrodes at 5 mA g<sup>-1</sup>.

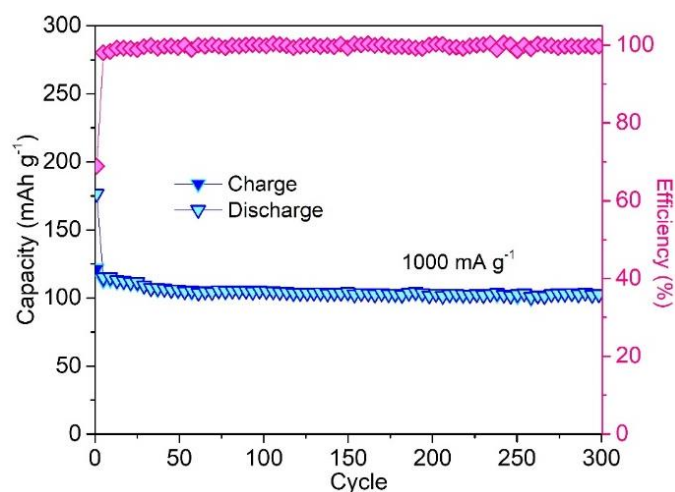


Figure 4.17 Cyclic performance of MoS<sub>2</sub> electrode at 1000 mA g<sup>-1</sup>.

### 4.3 Summary

In summary, using complementary calculational and experimental methods, we unambiguously reveal the phase transition process of MoS<sub>2</sub> during K ion insertion. Several novel potassium intercalated phases including K<sub>0.5</sub>MoS<sub>2</sub> and K<sub>1.0</sub>MoS<sub>2</sub> are discovered and their detailed crystal structures are unveiled. Instead of fully conversion, which would destroy the layered crystalline structure, the intercalation reaction occurs even being discharged to 0 V. The intercalation compounds inherit the original morphology and play a vital role in maintaining the structural integrity, which prevents the collapse of the particles and results in excellent cyclic stability of microsized MoS<sub>2</sub>.

## Chapter 5

### **Building elastic solid electrolyte interphases for stabilizing micro-sized antimony anodes in potassium ion batteries**

**A**lloy anodes composed of micro-sized particles receive increasing attention recently, which outperform the nanostructured counterparts in both the manufacturing cost and volumetric energy density. However, the pulverization of particles and fracture of solid electrolyte interphases (SEIs) during cycling brings about fast capacity degradation. Herein, we show the normally considered fragile SEI could become highly elastic through electrolyte chemistry regulation. Compared to the SEI constructed in classic carbonate electrolyte, the atomic force microscopy (AFM) tests reveal that the one built in ether-based electrolyte doubles the maximum elastic strain to accommodate the repeated swelling-contracting. Such an SEI effectively encapsulates the micro-sized alloy anodes to prevent the capacity loss from particle isolation. This work emphasizes the significance of building robust SEI, which offers the opportunity to enable stable micro-sized alloy anodes.

#### **5.1 Introduction**

Alloy anodes such as Si, Sn, and Sb could uptake several ions per atom through alloy reactions, delivering exceptional capacities at appropriate potentials.<sup>200</sup> Accompanying with the alloying process, the electrode undergoes severe volume expansion, which triggers the pulverization of active particles and the breakage of solid electrolyte interphase (SEI), leading to rapid capacity degradation.<sup>201</sup> The SEI is formed on the anode surface in the first discharge as a result of

electrolyte decomposition.<sup>202</sup> Successful application of modern lithium ion batteries (LIBs) relies largely on the ion conductive and electron insulated SEI, enabling a high Coulombic efficiency by preventing the further reduction of electrolyte in the following cycles. The massive volume expansion of alloy anodes poses a great challenge in maintaining an intact SEI. Owing to the fracture of particles, the newly exposed surface will continuously react with electrolyte once SEI is broken, which decreases the energy density due to excessive consumption of the charges from the cathodes. Meanwhile, the thick and sporadic SEI may isolate the fragmented particles from active alloy/de-alloy.<sup>203</sup>

Considerable amounts of works have been devoted to protecting SEI in alloy anodes through fabricating delicate nanostructures.<sup>137, 204-209</sup> The core-shelled structure is widely prepared, where an inactive or less-expanded material during cycling is coated on the surface of alloy anodes.<sup>90, 106, 210-213</sup> Abundant voids are left in the core part to trigger the inward expansion, while the out layer shields the alloy from exposing the fresh surface to the electrolytes.<sup>101, 214</sup> The synthesis of alloy/carbon nanocomposites is another strategy that has been extensively explored.<sup>77, 80, 109, 215-217</sup> The approach has demonstrated superiority in prolonging the cyclic life of alloy anodes but brought about other adverse effects on the battery performance. A large initial irreversible capacity is spotted due to the copious SEI formation on the high-surface-area nanomaterials. Moreover, the presence of pores/voids and large portions of carbon inevitably decreases the volumetric energy density of batteries.

Rather than passively protecting the weak SEI, most recent works have shown the benefits of reinforcing its mechanical properties. Our previous works also reveal unusual stability of Sn microparticles upon sodiation/de-sodiation with the assistance of glyme electrolyte-derived SEI, which could be readily applied to Bi anodes.<sup>59, 176-177</sup> These exciting results suggest that we could turn the problematic SEI into a treasure to help stabilize alloy anodes if well designed. The direct utilization of microparticles not only reduces the manufacturing cost but also significantly increases the energy density of batteries. The extension of such approaches into potassium ion batteries (PIBs) is not straightforward, considering the more severe volume expansion during potassiation than that in Li and Na ion counterparts.<sup>136</sup> It has been reported

that microsized Bi particles could be stabilized in glyme-based electrolytes due to the construction of robust SEI and the formation of a unique porous structure that partly relieves the stress.<sup>75</sup> However, the same strategy fails to work in neat Sb anodes which present much higher theoretical capacity than Bi. The reason is likely ascribed to the absence of pore formation during cycling, thus requiring optimization of both electrode composition and binder as well as utilization of high-concentration electrolytes.<sup>58, 76, 109, 218-220</sup>

Until now, most of the works focus on the ethylene glycol dimethyl ether (DME, or G1), which has a low viscosity for realizing high-rate performance.<sup>221-223</sup> The application of DME-based electrolyte could be traced back to the 1970s when the first generation Li batteries was developed, but it was abandoned later due to oxidative decomposition on the cathode side and low boiling point of 85 °C.<sup>57</sup> There is a large group of candidates in the ether family. Exploring other ether solvents would open up new avenues in designing robust SEI for alloy anodes. Moreover, a detailed relationship between the mechanical properties and electrochemical stability remains unclear. Herein, we report two new ether-based electrolytes rooted in the linear (ethylene glycol diethyl ether, EGDEE) and cyclic ether (tetrahydrofuran, THF), both of which enable the stable cycling of microsized Sb anodes in PIBs. To explore the underlying mechanism for the unusual stability, atomic force microscopy (AFM) is adopted to characterize the mechanical properties of the SEI. It reveals the highly elastic nature of the SEI in ether-derived electrolyte, which is beneficial to accommodate the volume change of the electrode. Such SEI construction can be readily extended to Sn anodes in SIBs. This work offers an alternative SEI-derived approach to design advanced alloy anodes.

## 5.2 Results and discussion

### 5.2.1 Electrochemical performances evaluation

Commercial Sb with an average particle size of 5.9  $\mu\text{m}$  is used as active materials (Figure 5.1a and b). The powder is mixed with conductive carbon and carboxymethylcellulose sodium (CMC) binder by low-energy planetary ball milling for four hours to make the electrode. X-ray powder diffraction (XRD) patterns show that the (003) and (006) planes of Sb become negligible after ball milling compared with the untreated ones (Figure 5.2). The shear force during mechanical ball milling partly exfoliates the Sb along the c-axis and reduces its thickness,

which has also been observed in previous studies.<sup>224</sup> Consequently, the average particle size of Sb is reduced to approximately 1.1  $\mu\text{m}$  (Figure 5.1c and d). Nevertheless, the crystallinity of Sb is well preserved, as indicated by the prominent (012), (104), and (110) peaks. We first evaluate the electrochemical performance in classic carbonate electrolytes (ECPC) with the potassium bis(fluorosulfonyl)imide (KFSI) as the salt, which has been reported beneficial in SEI formation.<sup>52, 184</sup> In Figure 5.3a, the cell shows a reversible capacity of 517.8  $\text{mAh g}^{-1}$  in the first cycle with a low initial Coulombic efficiency (ICE) of 56.5% due to the severe electrolyte decomposition.

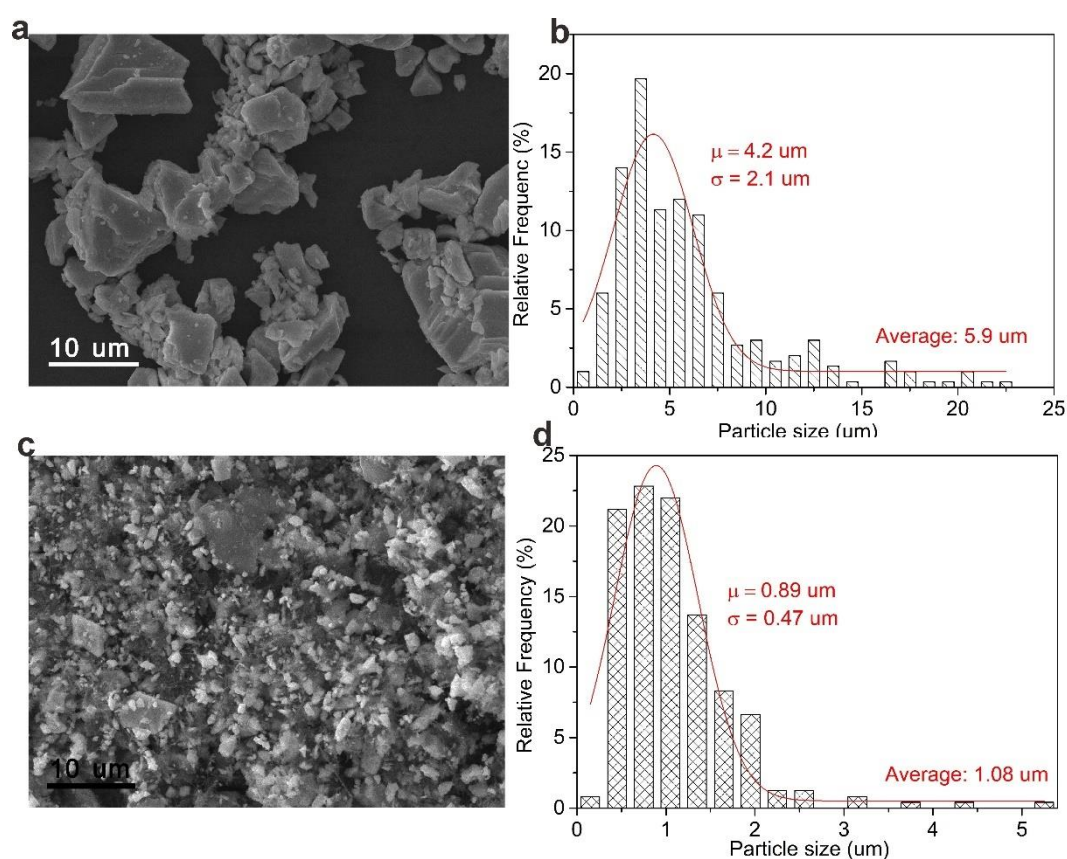


Figure 5.1 SEM images and histograms of the particle size distributions of (a-b) commercial Sb, (c-d) ball milled Sb.

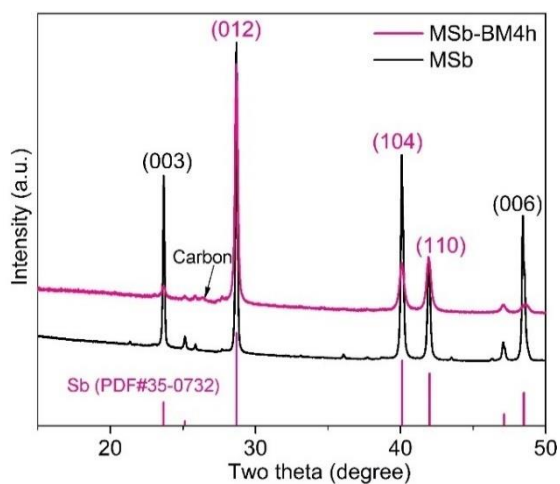


Figure 5.2 XRD patterns of commercial Sb (black line) and ball-milled Sb (red line).

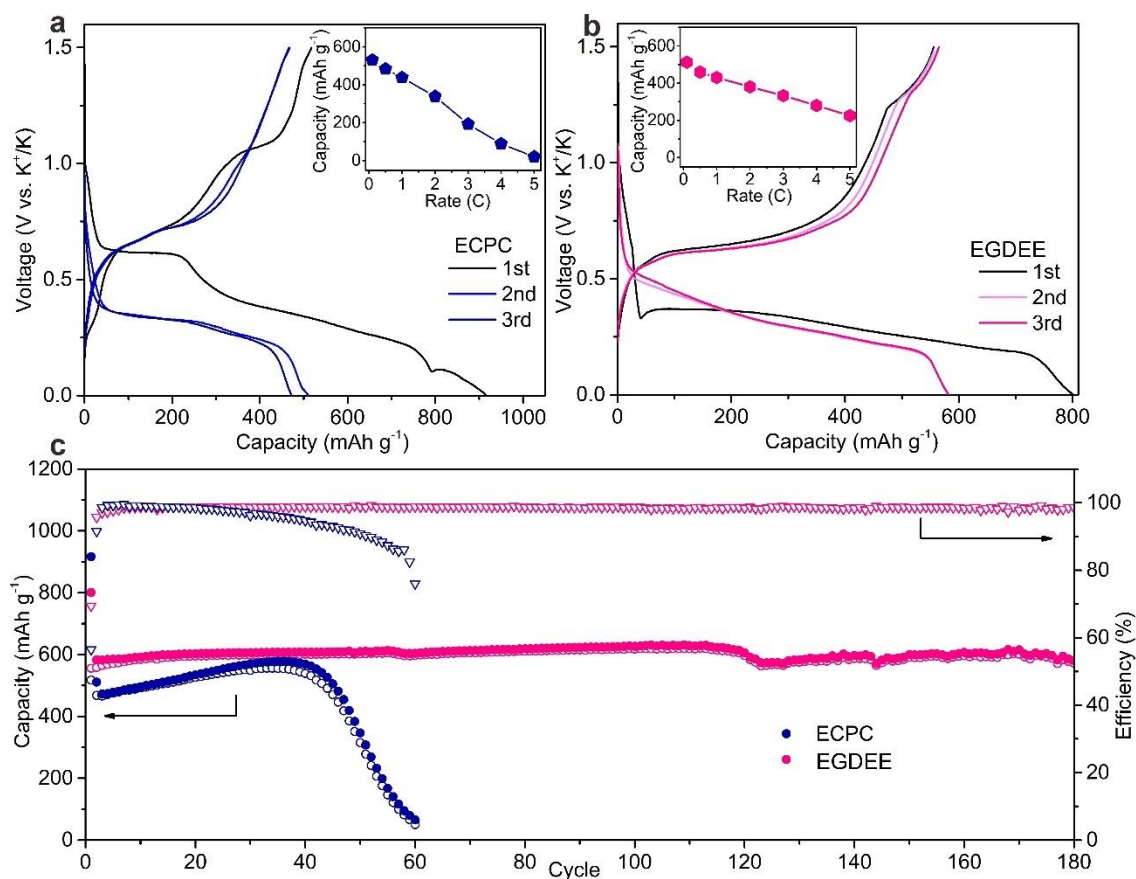


Figure 5.3 Electrochemical performance of Sb electrodes. The galvanostatic discharge-charge profiles in (a) 1 M KFSI/ECPC and (b) 1 M KFSI/EGDEE electrolytes of selected cycles under  $0.1 \text{ A g}^{-1}$  (inset: rate performances). (c) Cyclic performance under  $0.1 \text{ A g}^{-1}$ .

In contrast, the Sb electrode cycled in ethylene glycol diethyl ether (EGDEE) based electrolyte presents a capacity of 800.8 and 555.7 mAh g<sup>-1</sup> in the first discharge and charge, respectively, corresponding to a remarkable ICE of 69.4% (Figure 5.3b). The electrolyte formulation plays a critical role in determining the ICE, where EGDEE solvent outperforms the ECPC counterpart. It implies a stable SEI is formed in EGDEE-based electrolyte, effectively preventing the exposure of new Sb surface as will be discussed later. The cyclic stability is examined under 0.1 A g<sup>-1</sup> (Figure 5.3c). The capacity slightly increases due to the gradual activation of the bulk material.<sup>225-226</sup> A reversible capacity of 573 mAh g<sup>-1</sup> is obtained in EGDEE-based electrolyte after the 180 cycles, corresponding to the insertion of 2.60 K ions per Sb atom, which is close to the value predicted by theoretical calculation.<sup>136</sup> The capacity retention of nearly 100% (compare to the first reversible capacity) is achieved after 180 cycles, whereas the cell cycled in ECPC-based electrolyte completely loses the activity in 60 cycles. Similar improvements are obtained in another cyclic ether (tetrahydrofuran, THF)-based electrolyte. As shown in Figure 5.4a, Sb electrode presents an initial charge capacity of 412.5 mAh g<sup>-1</sup> with ICE of 63.4% in THF-based electrolyte. After gradual activation, a high reversible capacity of 600 mAh g<sup>-1</sup> is obtained over 100 cycles.

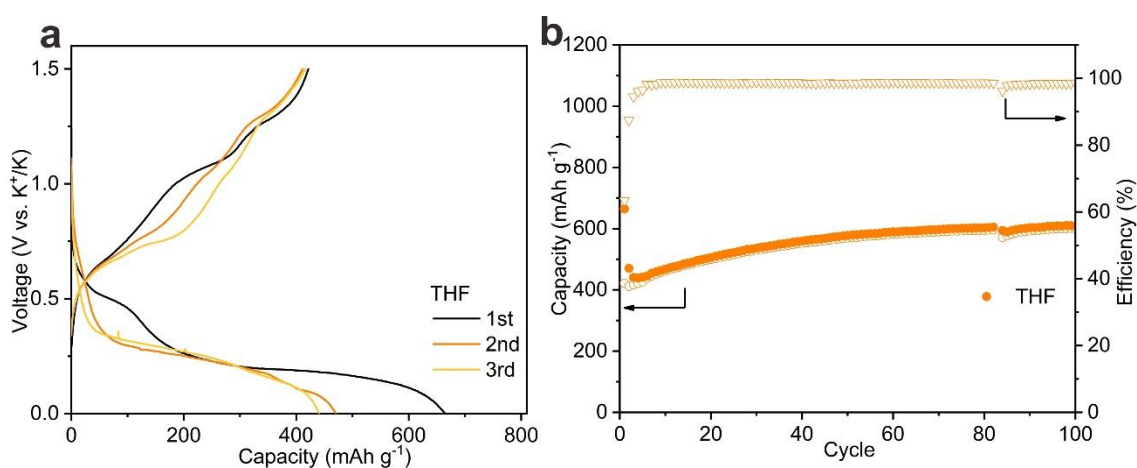


Figure 5.4 Electrochemical performance of Sb electrodes. The galvanostatic discharge-charge profiles in (a) 1 M KFSI/THF electrolytes of selected cycles under 0.1 A g<sup>-1</sup>. (b) Cyclic performance under 0.1 A g<sup>-1</sup>.

We also evaluate the long-term cyclic performance at a high current density of  $0.5 \text{ A g}^{-1}$ . Sb electrodes show a capacity of  $443 \text{ mAh g}^{-1}$  after 150 cycles in 1 M KFSI/EGDDE and  $413.6 \text{ mAh g}^{-1}$  after 100 cycles in 1 M KFSI/THF. The performance could be further improved by either limiting the cut-off voltage to 0-1.0 V or through the synthesis of Sb particles with reduced particle size ( $\sim 500 \text{ nm}$ ) (Figure 5.5). The reversible capacity and superior ICE obtained in ether-based electrolytes offer a very competitive performance among the Sb-based electrodes for PIBs, without resorting to nanostructure design and high concentration electrolyte (Table 5.1). Note that the stable cyclic performance cannot be achieved in the classic ether-based electrolytes, such as 1 M KFSI/DME and 1 M KFSI/DGME (Figure 5.6).

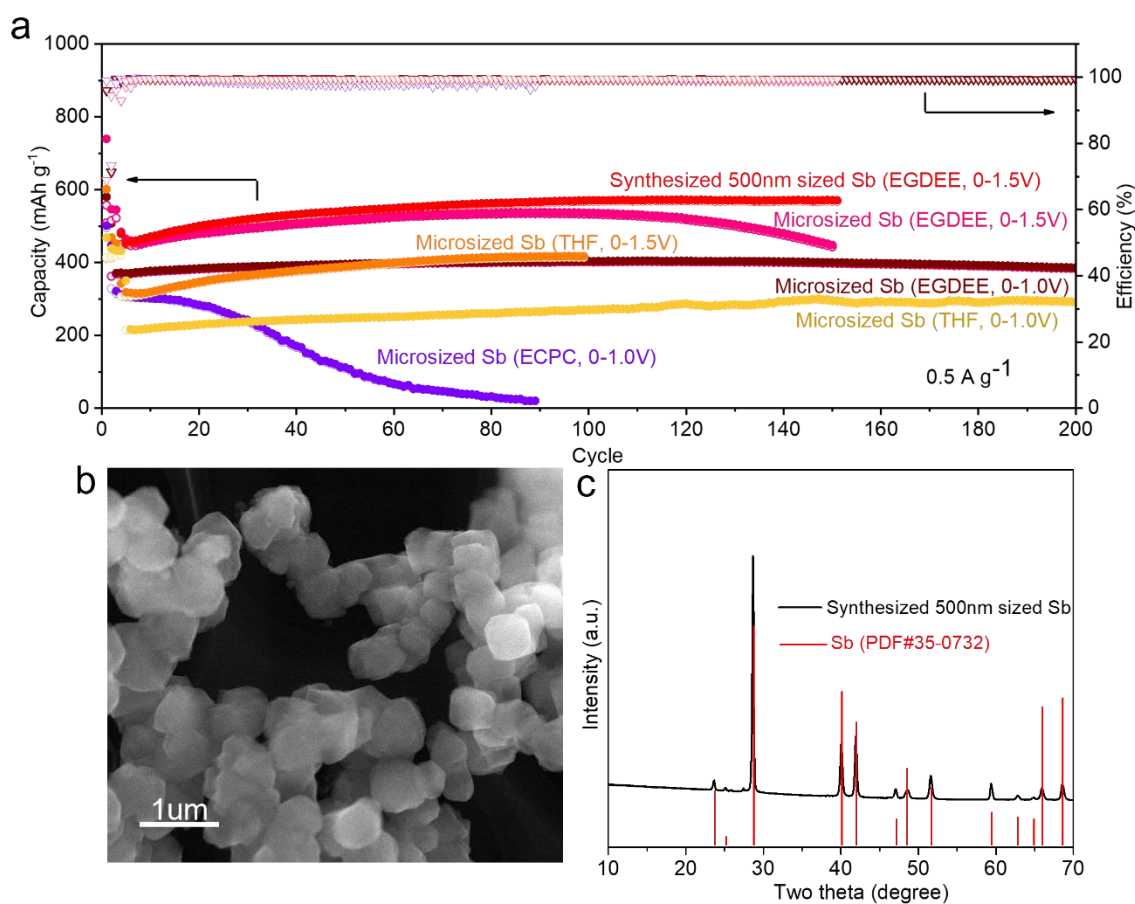


Figure 5.5 (a) Cyclic performance of microsized Sb and synthesized Sb electrodes under  $0.5 \text{ A g}^{-1}$ . (b) SEM image of synthesized Sb with an average particle size of about 500 nm. (c) XRD pattern of synthesized Sb.

Table 5.1 Electrochemical performance comparison between this work and other Sb-based anode materials in the literature.

No.	Anode material (Active material content)	Electrolytes	Current density (A g <sup>-1</sup> )	Reversible Capacity , mAh g <sup>-1</sup> (Cycle number)	ICE	Reference
0	Microsized Sb (70%)	1M KFSI/EGDDEE	0.1	573 (180)	69.4%	This work
			0.5	443 (150)		
		1M KFSI/THF	0.1	599.2 (100)	63.4%	
			0.5	413.6 (100)		
1	Sb/CNS (60%)	1M KPF <sub>6</sub> /EC-DMC	0.05	288.2 (50)	~48%	74
2	Sb <sub>2</sub> S <sub>3</sub> @C (80%)	1MKFSI/DME	0.05	293 (50)	58.40%	84
3	Sb <sub>2</sub> O <sub>3</sub> -RGO (80%)	7M KFSI/DME	0.1	309 (100)	~50%	81
4	Sb <sub>2</sub> Se <sub>3</sub> @C (60%)	0.8M KPF <sub>6</sub> /ECPC	0.1	321.8 (40)	72.30%	227
5	BiSb@C (70%)	5M KFSI/DME	0.2	387 (600)	70.20%	77
6	3D SnSb@NC (80%)	0.5M KPF <sub>6</sub> /DME	0.5	185.8 (200)	90.1%	78
7	MoS <sub>2</sub> /Sb@C (70%)	1MKFSI/DGME	0.5	296.7 (200)	59.30%	228
8	Bi <sub>0.51</sub> Sb <sub>0.49</sub> OCl/rGO (80%)	3M KFSI/DME	0.1	360 (1000)	55.90%	93
9	Sb-C-rGO (70%)	0.8M KFSI/EC-DEC	0.5	245 (100)	46%	229
10	Sb/Na-Ti <sub>3</sub> C <sub>2</sub> T <sub>x</sub> (70%)	4M KTFSI/EC-DEC	0.1	392.2 (450)	65.60%	99
11	u-Sb@CNFs (freestanding)	3M KFSI/DME	0.2	393 (100)	48.30%	109

12	Bi <sub>0.5</sub> Sb <sub>0.5</sub> @P (60%)	4M KFSI/DME	0.5	393.6 (50)	~60%	100
13	Sb@C PNFs (freestanding)	1M KFSI/EC- DEC	0.1	421.4 (100)	~70%	230
14	Bi <sub>1.11</sub> Sb <sub>0.89</sub> S <sub>3</sub> nanotube (70%)	3M KFSI/DME	0.2	432 (100)	59.80 %	206
15	Sb <sub>2</sub> Se <sub>3</sub> @NC@rGO (80%)	5M KFSI/ECDMC	0.05	450 (50)	77.30 %	86
16	SnSb/C (80%)	3M KFSI/DME	0.05	419 (600)	67%	218
17	Sb@HCT (70%)	1M KFSI/EC- DMC	0.5	453.4 (80)	70%	231
18	Sn-Sb LSM (80%)	4M KFSI/EMC	0.5	296 (150)	~67%	232
19	Sb <sub>0.5</sub> Bi <sub>0.5</sub> @C (70%)	5M KFSI/DME	0.5	226 (400)	80.90 %	233
20	Sb@CSN (80%)	4M KTFSI/EC- DEC	0.05	551 (100)	61%	58

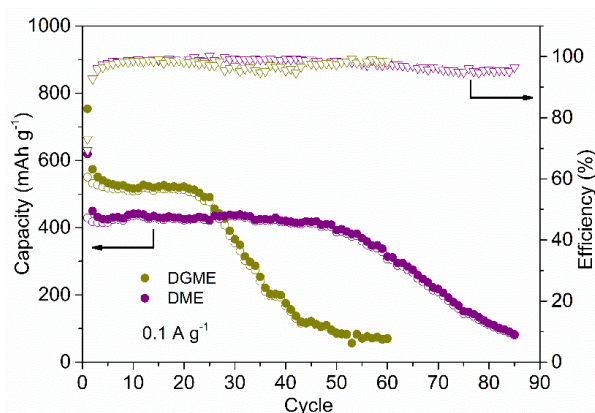


Figure 5.6 Cyclic performance of micro-sized Sb in 1M KFSI/DME and 1M KFSI/DGME under  $0.1 \text{ Ag}^{-1}$  with a cut-off voltage of 0-1.5V.

Apart from the stability, the voltage profiles of EGDEE-based electrolyte show a much lower polarization, suggesting faster kinetics. Therefore, we evaluate the rate capabilities of cells in EGDEE and ECPC-based electrolytes and explore the charge transfer at the interface. In EGDEE-based electrolyte, the Sb electrode delivers decent performance at increasing current

densities, *i.e.*, 430 and 225 mAh g<sup>-1</sup> at 1C and 5C (1C=660 mA g<sup>-1</sup>), respectively (Figure 5.3b inset and Figure 5.7). In contrast to this, the electrode shows negligible capacity in ECPC-based electrolyte when the current density increases to 5C (Figure 5.3a inset and Figure 5.7). The reason lies in the slow kinetics at the electrode/electrolyte interface, as demonstrated in electrochemical impedance spectroscopy (EIS) spectra of the electrodes at open circuit voltage state (OCV) and after three cycles. The fitted data using an equivalent circuit (Figure 5.8 and Table 5.2) show that both the charge transfer ( $R_{ct}$ ) and SEI resistance ( $R_{SEI}$ ) in EGDEE-based electrolyte is much smaller than those in ECPC-based electrolyte. The galvanostatic intermittent titration technique (GITT) is conducted for comparing the diffusion coefficient in ECPC and EGDEE-based electrolytes, which does not show an obvious difference due to the similar phase transformation process (Figure 5.9).

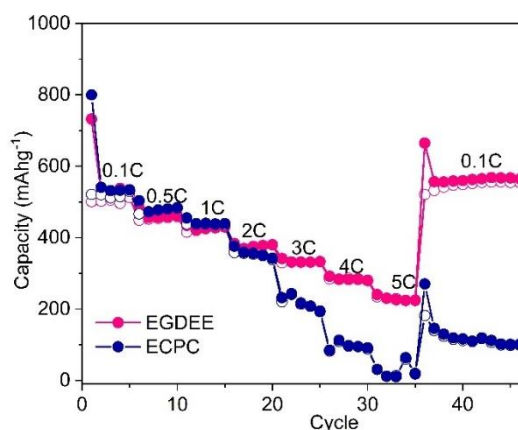


Figure 5.7 Rate performance of Sb electrodes in 1 M KFSI/EGDEE and 1 M KFSI/ECPC electrolytes (1C= 660 mA g<sup>-1</sup>).

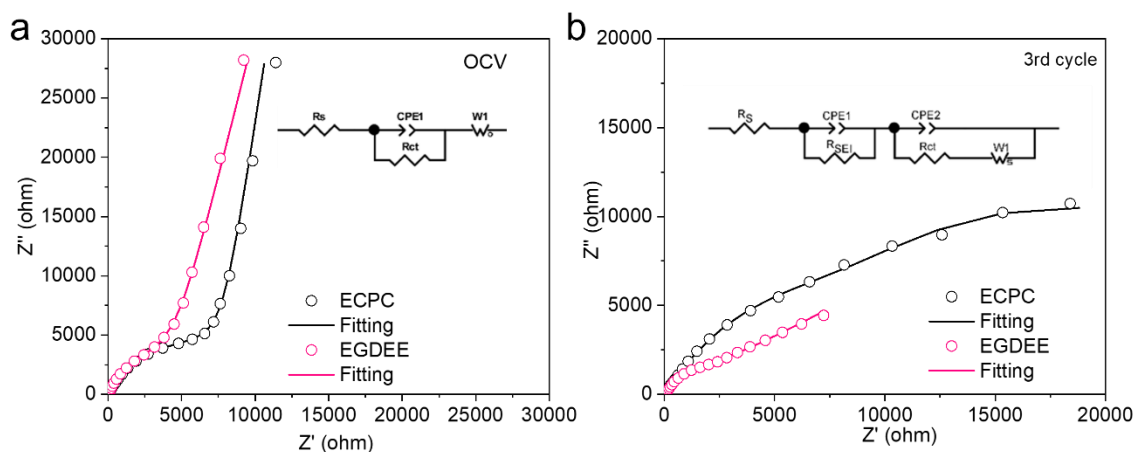


Figure 5.8 EIS spectra of Sb electrodes at (a) OCV state and (b) after cycling three times. (inset) The corresponding equivalent circuit for the EIS fitting.

Table 5.2 Cell resistance ( $R_s$ ), charge transfer resistance ( $R_{ct}$ ) and SEI resistance ( $R_{SEI}$ ) of Sb electrodes from equivalent circuit fitting of experimental data.

State	Electrolytes	$R_s$ ( $\Omega$ )	$R_{ct}$ ( $\Omega$ )	$R_{SEI}$ ( $\Omega$ )
OCV	ECPC	12.51	7341	-
	EGDEE	20.63	3997	-
3rd	ECPC	10.23	2302	4986
	EGDEE	12.79	387.4	340.6

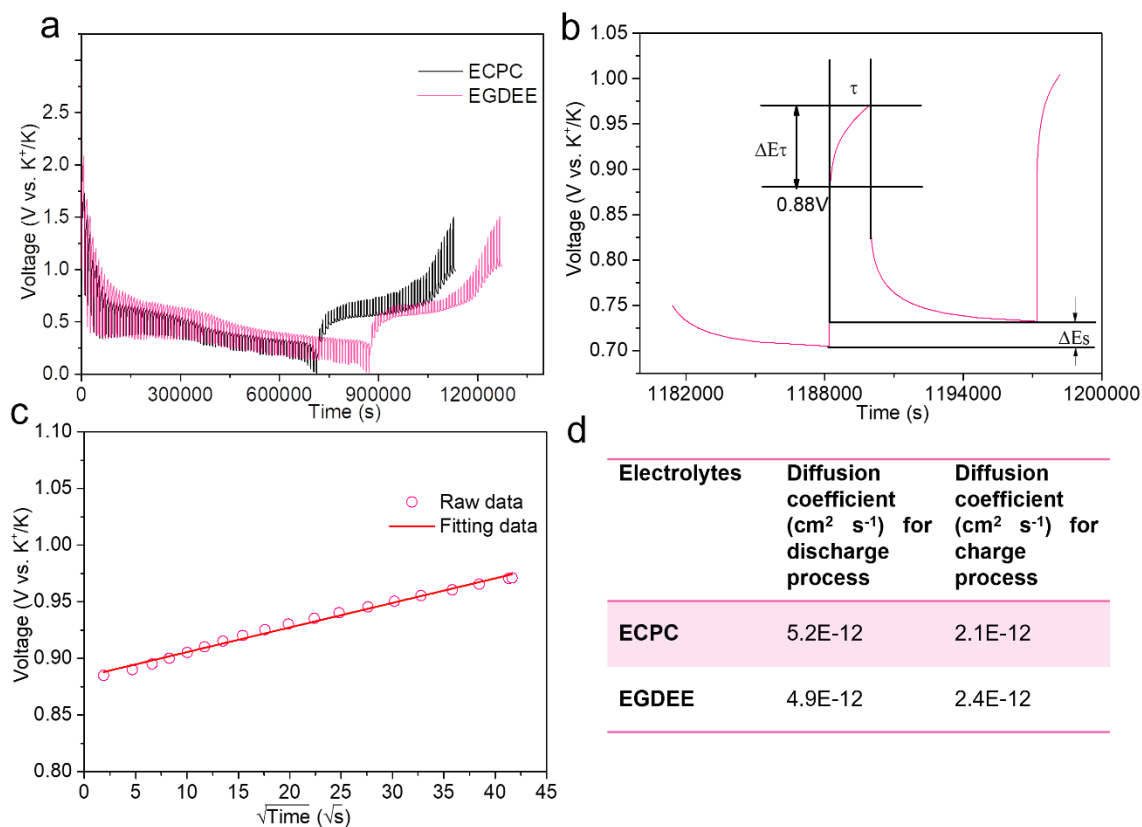


Figure 5.9 GITT measurements in the first cycle. (a) Voltage curve vs. time. (b) Current step diagram at 0.88 V. (c) The linear behaviour of voltage vs.  $\sqrt{time}$  at 0.88 V. (d) the average value of diffusion coefficient calculated from (a).

### 5.2.2 K-Sb alloying mechanism

The cyclic voltammetry (CV) curve (Figure 5.10) presents three peaks located at around 0.48, 0.21 and 0.14 V upon potassiation, indicating a multi-step phase transformation. The K-Sb phase diagram has been extensively studied by computational approaches,<sup>234-235</sup> but the experimental results suggest a distinct reaction path. A final agreement is yet to be achieved due to the complexity of the electrochemical processes. The phase transformation during K-Sb alloy/de-alloy is systematically studied by *in situ* XRD (Figure 5.11a). The XRD pattern at OCV state shows three pronounced peaks at 28.5°, 39.8°, and 41.7° corresponding to (012), (104), and (110) facets of Sb (PDF#35-0732), respectively. The intensities of these peaks gradually decrease during discharge. A new phase emerges at around 0.4 V with three characteristic peaks at 19.5°, 22.6°, and 32.3°. By excluding SEI formation related capacity,

the discharge capacity indicates approximately 0.5 K ions have been alloyed with per Sb atom at this potential. It agrees well with the theoretical prediction where  $K_{0.5}Sb$  would be the first alloy phase in K-Sb phase diagram,<sup>236</sup> but the detailed crystal structure could not be resolved here due to the poor crystallinity. The next phase appears when discharges to 0.25 V, which could be indexed as  $K_1Sb$  having a layered structure that belongs P4/mmm space group.  $K_1Sb$  phase consists of an Sb layer with intercalated K in-between (Figure 5.12), deriving from  $Li_1Sb$  structure.<sup>237</sup> Surprisingly, further discharge does not lead to the formation of any new phase before reaching nearly 0 V, although density functional theory (DFT) calculation suggests the existence of  $K_5Sb_4$ .<sup>234</sup> The major observation between 0.25 V and 0 V is the leftward shift of the peaks related to the  $K_1Sb$  phase. It reflects the broadening of the interlayer distance arising from the intercalation of K ions into the lamellar  $K_1Sb$  to form  $K_{1+x}Sb$ . This phenomenon is unusual in the alloy-type anodes, where staging-like behaviour normally takes place due to the phase transformation between intermediate alloy phases.<sup>72</sup> The cubic  $K_3Sb$  phase appears at the end of discharge (0 V). The minor amount of  $K_1Sb$  and  $K_{0.5}Sb$  remains due possibly to the incomplete reaction stemming from the imperfect contact of the *in situ* cell.

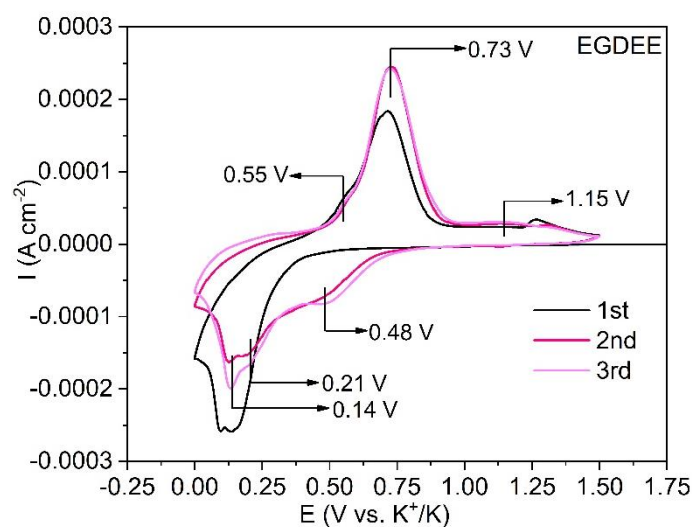


Figure 5.10 Cyclic voltammogram of Sb collected at a scan rate of  $0.05 \text{ mV s}^{-1}$  and a scan range of 0-1.5 V in 1M KFSI/EGDEE.

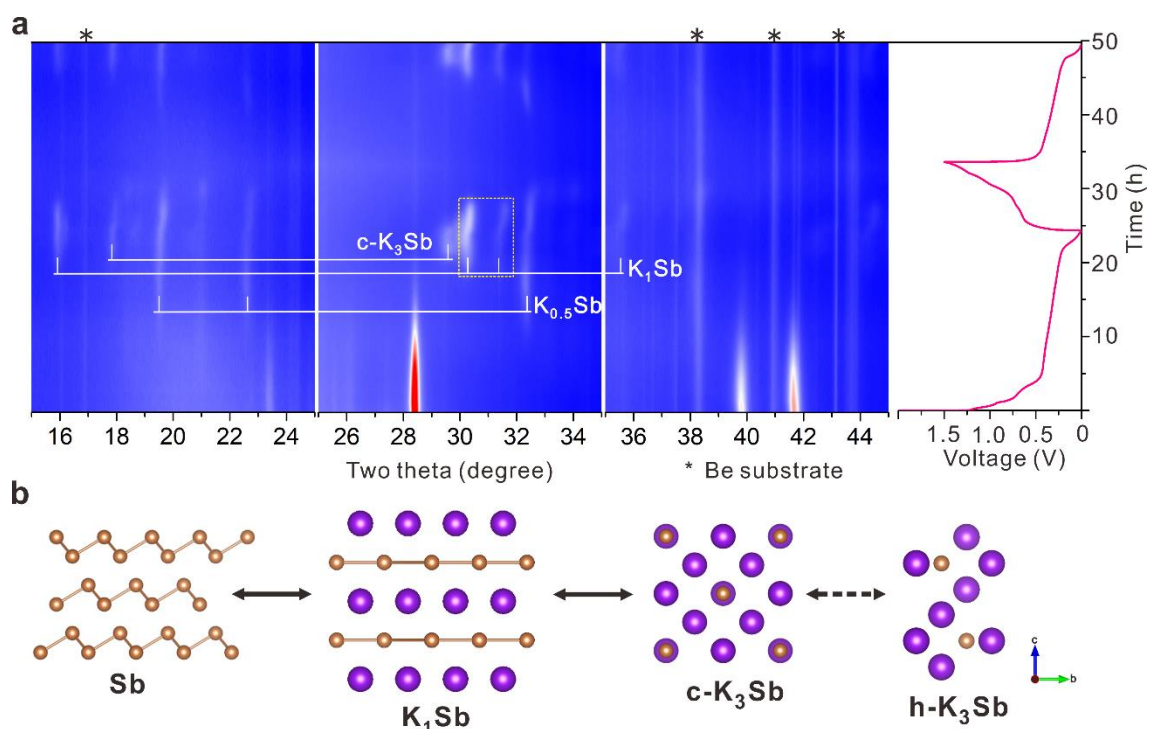


Figure 5.11 (a) Contour map of *in situ* XRD for micro-sized Sb electrode in 1 M KFSI/EGDEE electrolyte on the first two cycles under  $0.05 \text{ A g}^{-1}$  (peak-shift is marked in rectangle frame). (b) Schematic of the phase transformations, where c- $\text{K}_3\text{Sb}$  and h- $\text{K}_3\text{Sb}$  represent cubic and hexagonal  $\text{K}_3\text{Sb}$ , respectively (Dash arrow stands for coexistence). Detailed lattice parameters of these phases are listed in Table 5.3.

Table 5.3 Lattice parameters of Sb,  $\text{K}_1\text{Sb}$ , c- $\text{K}_3\text{Sb}$  and h- $\text{K}_3\text{Sb}$  phases.

Phase	Space group	Lattice parameters	
Sb	R-3m [166]	$a=b=4.30, c=11.22$	$\alpha=\beta=90^\circ, \gamma=120^\circ$
$\text{K}_1\text{Sb}$	P4/mmm [123]	$a=b=3.46, c=5.65$	$\alpha=\beta=\gamma=90^\circ$
c- $\text{K}_3\text{Sb}$	Fm-3m [225]	$a=b=c=8.56$	$\alpha=\beta=\gamma=90^\circ$
h- $\text{K}_3\text{Sb}$	P63/mmc [194]	$a=b=6.13, c=10.88$	$\alpha=\beta=60^\circ, \gamma=120^\circ$

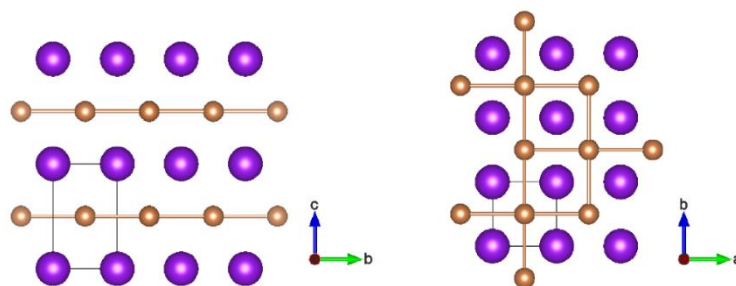


Figure 5.12 Illustrations of the  $K_1Sb$  structure derived from  $Li_1Sb$  (Yellow and violet spheres represent Sb and K atom, respectively).<sup>237</sup>

To avoid any artefact, we also conduct the *ex situ* XRD to allow a full reaction (Figure 5.13). All the intermediate phases are transferred to  $K_3Sb$  in the electrode *ex situ* discharged to 0 V; beside the cubic  $K_3Sb$  phase that captured in the *in situ* test, hexagonal  $K_3Sb$  is also detected. Part of the cubic  $K_3Sb$  phase is transferred into the hexagonal one, suggesting the latter is more thermodynamically stable.<sup>238</sup> Upon charging, the potassiated  $K_3Sb$  phase returns to Sb following the reversed reaction path. A de-intercalation from  $K_{1+x}Sb$  is observed as reflected by the rightward shift of the XRD peak starting from 0.37 V. It confirms the presence of intercalation/de-intercalation behaviour in  $K_1Sb$  phase, owing to the layered structure nature. A similar phenomenon has been reported in antimonene upon Li/Na insertion but has not been clearly spotted in K-Sb system.<sup>239-240</sup> Compared to the alloying process, the intercalation induces less structural deterioration to the electrodes.<sup>79</sup> The presence of the intercalation process enables the gradual volume change to prevent the structural collapse from sudden expansion. Once charging to 1.5 V, the Sb phase reappears although with reduced crystallinity, evidencing the reversibility of K-Sb alloy/de-alloy reactions (Figure 5.13). The phase transformation process is summarized in Figure 5.11b. An intercalation phase  $K_1Sb$  presents before reaching the end cubic  $K_3Sb$  alloy. The latter could be partly transmitted into hexagonal allotropy as indicated by the dashed line.

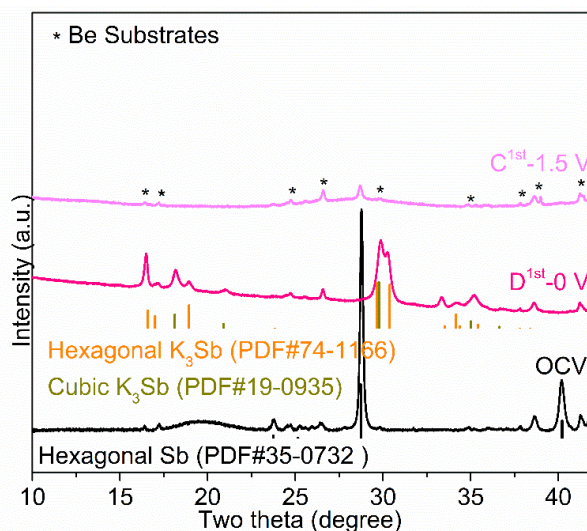


Figure 5.13 *Ex situ* XRD patterns of Sb electrodes in 1 M KFSI/EGDEE electrolyte at different states under current density of  $0.03 \text{ A g}^{-1}$  (C and D stand for charge and discharge, respectively).

### 5.2.3 Nanostructure, mechanical properties and chemical compositions of SEIs

A large relative volume expansion of 407% is induced when the Sb is transformed into  $\text{K}_3\text{Sb}$ ,<sup>238</sup> which may cause the fracture of both active particles and SEI. Due to the high vapour pressure of THF, the SEIs studies focus on the comparison of ECPC and EGDEE-based electrolytes. The integrity of Sb electrodes cycled in EGDEE and ECPC-based electrolytes are investigated by transmission electron microscopy (TEM) and scanning TEM (STEM). Apparent cracks in the Sb microparticles are observed after cycling in ECPC-based electrolytes (Figure 5.14a). Meanwhile, numerous tiny particles present on the edge of the pristine material (Figure 5.14b and c), which can be indexed as (110) lattice of cubic Sb (ICSD#9013008) with d-spacing of  $2.2 \text{ \AA}$  and intersection angle of  $90^\circ$ . It can be inferred that those small cubic Sb particles are originated from the pulverization of Sb host. Surprisingly, there is no clear boundary between the SEI layer and the active material. SEI is expected to form in the first discharge as a result of electrolyte decomposition. Ideally, the SEI would encapsulate the particles and isolate them from the electrolyte. We speculate that the SEI breaks in traditional carbonate electrolytes during the K-Sb alloy process owing to the enormous volume expansion. Consequently, the newly exposed surface from the fragmented particles contacts again with the electrolyte, leading to the re-decomposition of the electrolyte to form additional SEI, which wrapped the tiny particles. The repeated particle fracture and SEI reconstruction result in a super thick SEI

with tiny Sb enclosed. As demonstrated in STEM image (Figure 5.15), the thickness of SEI could reach around 50 nm with variation in localized positions. Such a process, as illustrated in Figure 5.16, brings about electrode deterioration in several aspects. Firstly, the SEI fracture-formation continuously consume the K ions, giving rise to low Coulombic efficiency. Meanwhile, the resulted thick SEI layer increases the charge transfer resistance, as shown in EIS measurement, which severely decreases the rate capability. Furthermore, the fragmented particles may completely lose the electrical contact to become inactive for K ions uptake, resulting in the capacity degradation that has been observed in the cyclic test.

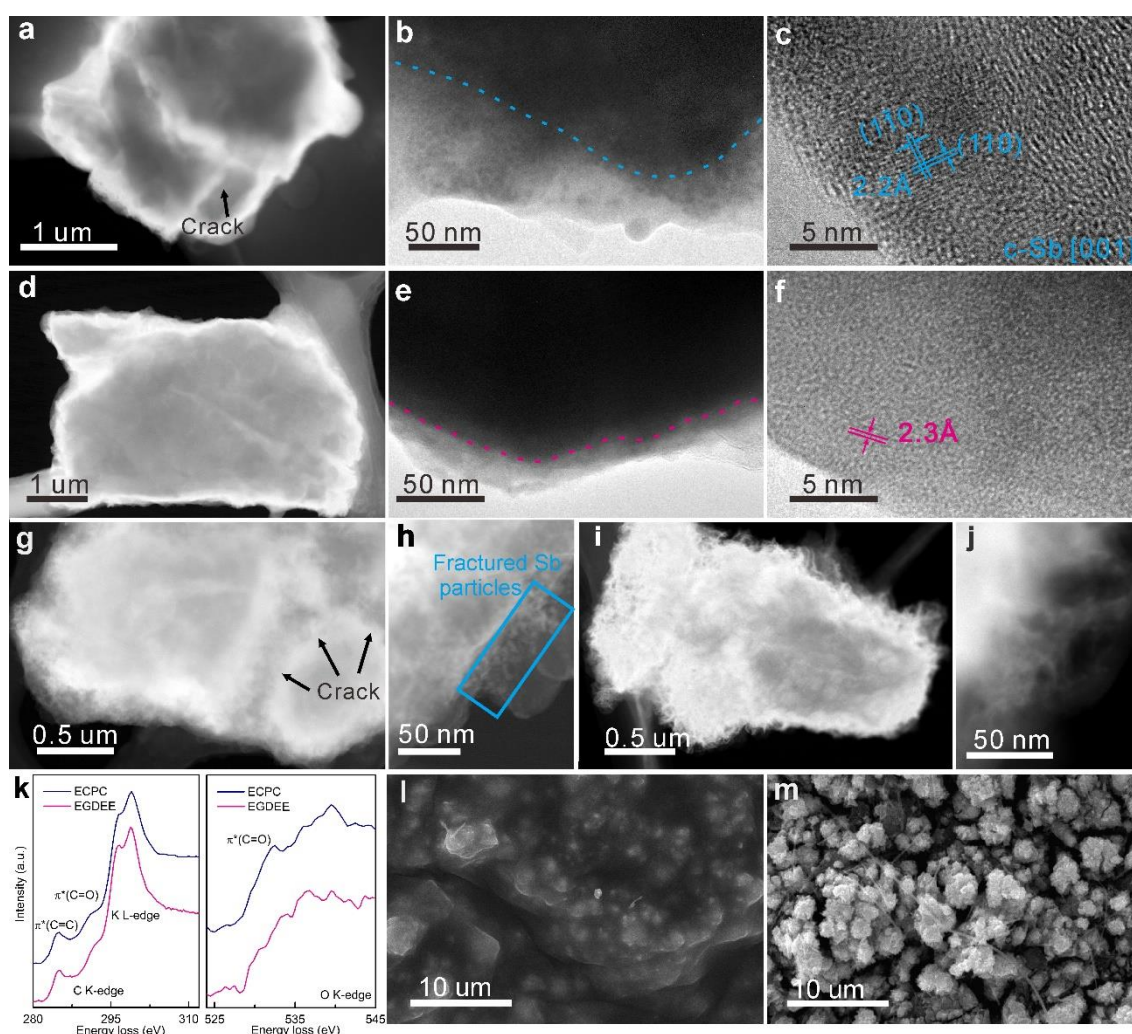


Figure 5.14 Morphologies and EEL spectra of cycled Sb electrodes: STEM/TEM images after 3 cycles in (a-c) 1 M KFSI/ECPC and (d-f) 1 M KFSI/EGDDE; after 50 cycles in (g-h) 1 M

KFSI/ECPC and (i-j) 1 M KFSI/EGDEE. (k) EEL spectra after 50 cycles. SEM images after 100 cycles in (l) 1 M KFSI/ECPC, and (m) 1 M KFSI/EGDEE.

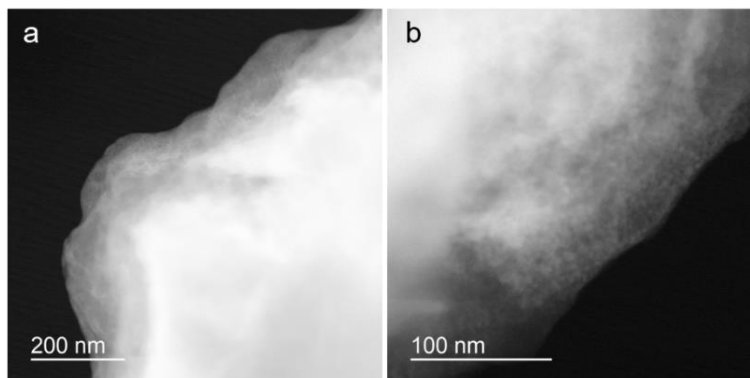


Figure 5.15 HAADF-STEM images of the Sb electrode in 1 M KFSI/ECPC electrolyte after 3 cycles.

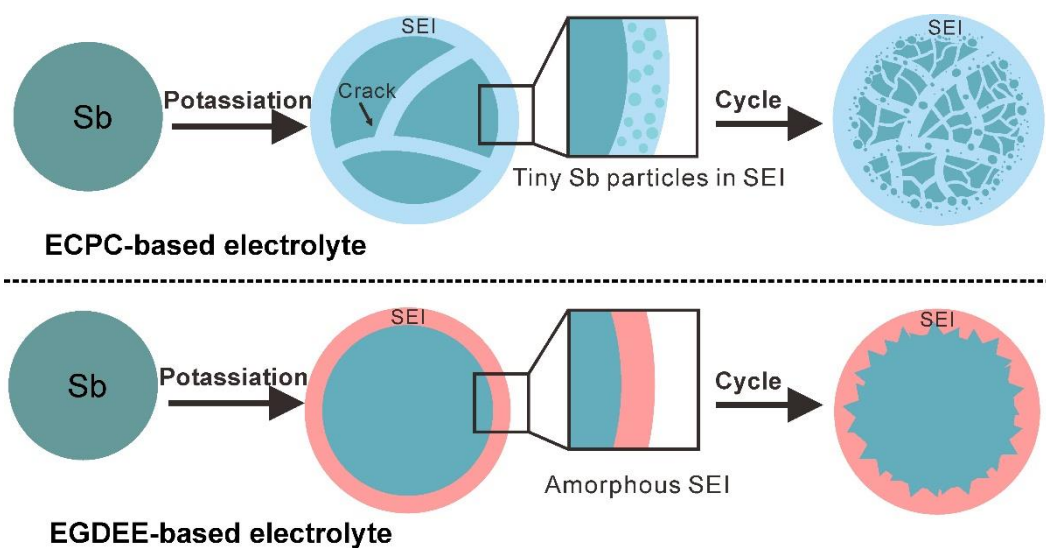


Figure 5.16 Illustration of electrode/SEI evolution in ECPC (up) and EGDEE-based (down) electrolytes.

Compared to the electrode cycled in ECPC-based electrolyte, the one prepared in EGDEE counterpart possesses an intact morphology after three cycles (Figure 5.14d). Although small cracks arising from internal stress is discerned, the integrity of microsized particles is well

preserved. The enlarged image (Figure 5.14e) shows a sharp discrepancy, where none of the fragmented particles are detected. A thinner SEI with a thickness of around 20 nm is covered on the Sb. The SEI formed here has an almost amorphous structure. Only minor amounts of crystals with an extremely small size of about 3 nm is detected (Figure 5.14f). They could be indexed as the (220) lattice of  $K_2O$  (PDF#47-1701) based on the d-spacing of 2.3 Å, which is a common component of SEI in PIBs.<sup>241</sup> The morphologies of the electrodes after long-term cycling are further investigated in ECPC (Figure 5.14g and h) and EGDEE-based electrolyte (Figure 5.14i and j). Severe cracks and broken particles are found in the centre and edges of the electrode tested in ECPC based electrolyte, while the integrity of Sb particles is largely maintained after cycling in EGDEE counterpart. Only slight structural change occurs on edge due to the repeated alloy/de-alloy, where many flakes present but without separating from the host particle. Electron energy loss (EEL) spectra analysis is conducted to deduce the components in SEI (Figure 5.14k). Obvious  $\pi^*(C=O)$  vibration is detected in both C and O spectra for the SEI formed in ECPC-based electrolyte, due possibly to the presence of carbonate species as will be further discussed by X-ray photoelectron spectroscopy (XPS). Electron energy loss spectroscopy (EELS) elemental maps in Figure 5.17 and Figure 5.18 clearly show the distribution of Sb, C, O, and K, where the last three elements are mainly from SEI. The observations indicate that the SEI built in EGDEE-based electrolyte is able to accommodate the tremendous volume expansion, which not only constrains the particles from pulverization but also prevents the repeated SEI formation, as illustrated in Figure 5.16. The overall morphologies of the electrodes further substantiate the above conjecture. Scanning electron microscope (SEM) images (Figure 5.14l and m) show that the microsize nature of the particles is remained in EGDEE-based electrolyte, whereas particles are fragmented for those tested in ECPC equivalent. Moreover, the particles are covered by a thick SEI layer due to the continuous formation of SEI in the latter electrolyte.

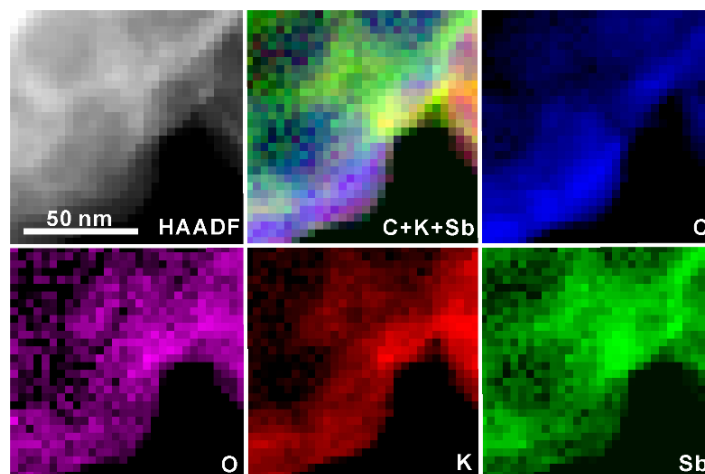


Figure 5.17 HAADF-STEM and EELS elemental maps of Sb electrode in 1 M KFSI/ECPC electrolyte after 50 times cycling.

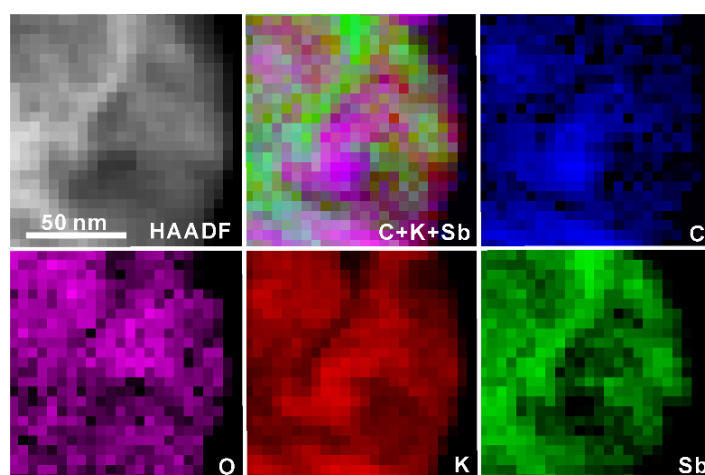


Figure 5.18 HAADF-STEM and EELS elemental maps of Sb electrode in 1 M KFSI/EGDDE electrolyte after 50 times cycling.

The capability of SEI in buffering the volume expansion comes as a surprise, as it is considered the most fragile part, which requires prudent protection in previous reports.<sup>242</sup> Therefore, we evaluate the mechanical properties of SEI by the atomic force microscopy (AFM) technique in the Ar filled glovebox. To exclude the interference from binder and carbon additives, a neat Sb film is coated on Cu foil through electrodeposition. The Sb has the same crystal structure as the one used in the conventional electrode (Figure 5.19). The electrode is charged/discharged for

three cycles to build the SEI layer on the particles. Typical force-displacement curves obtained from the AFM-based nanoindentation tests of SEI are shown in Figure 5.20a. At point a, the AFM probe starts to contact the SEI surface with zero external force. As the AFM probe continues to move downward, the SEI begins to deform elastically. With increasing force, the SEI reaches the limit of elastic deformation, corresponding to the first discontinuity point on the force-displacement curve (point a'). We can obtain the value of Young's modulus ( $E$ ) of the SEI based on the Hertz contact model.<sup>243,176</sup> Adopting the von Mises' shear strain-energy criterion or the Tresca's maximum shear stress criterion, the maximum elastic strain ( $\varepsilon_Y$ ) of SEI can be obtained (Equation 2-1 and Equation 2-2).<sup>116-117</sup> Figure 5.20b and c show the AFM topography images of the electrodeposited Sb electrodes cycled in ECPC and EGDEE-based electrolytes, respectively. The surface roughness factor  $R_a$  (the arithmetic mean deviation of the assessed profile) of the electrode surface is generated from topography images. After three cycles in ECPC-based electrolyte,  $R_a$  can be calculated as  $30.52 \pm 12.16$  nm, while the value is  $65.83 \pm 9.77$  nm in EGDEE counterpart. Besides the surface roughness, another noticeable appearance is the cracks. We statistically count the fracture pattern density (the total fracture length/area) of the two electrodes and find that the value of the electrode cycled in ECPC-based electrolyte is almost 3.06 times higher than the electrode tested in EGDEE equivalent.

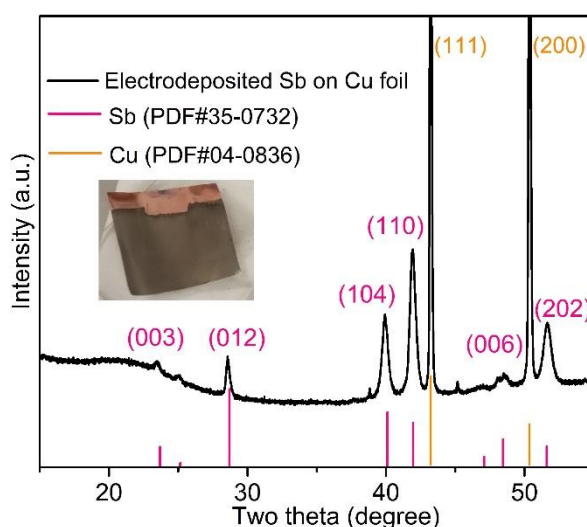


Figure 5.19 XRD pattern of electrodeposited Sb on Cu foil (inset: photograph).

Figure 5.20d summarizes the obtained  $E$  and  $\varepsilon_Y$  values of the SEI formed in these two types of electrolytes. Compared to the SEI formed in ECPC-based electrolyte ( $E$ :  $1134.97 \pm 624.16$  MPa,  $\varepsilon_Y$ :  $0.44 \pm 0.14$ ), the one in EGDEE has a smaller  $E$  value ( $578.05 \pm 339.87$  MPa) but a larger  $\varepsilon_Y$  ( $0.92 \pm 0.42$ ) (Figure 5.20e). The value of  $\varepsilon_Y$  determines the upper limit of the reversible deformation that the SEI can bear. Large  $\varepsilon_Y$  will be highly advantageous for the electrode with a large volume change. The ECPC-derived SEI has a high Young's modulus and poor deformation capability, which may originate from the various hard Sb ( $E$ : 55 GPa) particles encapsulated in the SEI layer, as observed in the TEM images (Figure 5.14b and Figure 5.15). The topographic features discussed above are in good accordance with the measured mechanical properties of SEI. The smaller Young's modulus of the SEI formed in EGDEE-based electrolyte makes it less resistant to local deformation, which leads to an increase in surface roughness. The larger  $\varepsilon_Y$  makes it less likely to yield or fracture during the drastic volume change of the electrode, and results in a much lower fracture density compared to the case in ECPC. The results attest to the significance of large  $\varepsilon_Y$  of SEI in maintaining the solidity of an electrode during expansion and contraction.

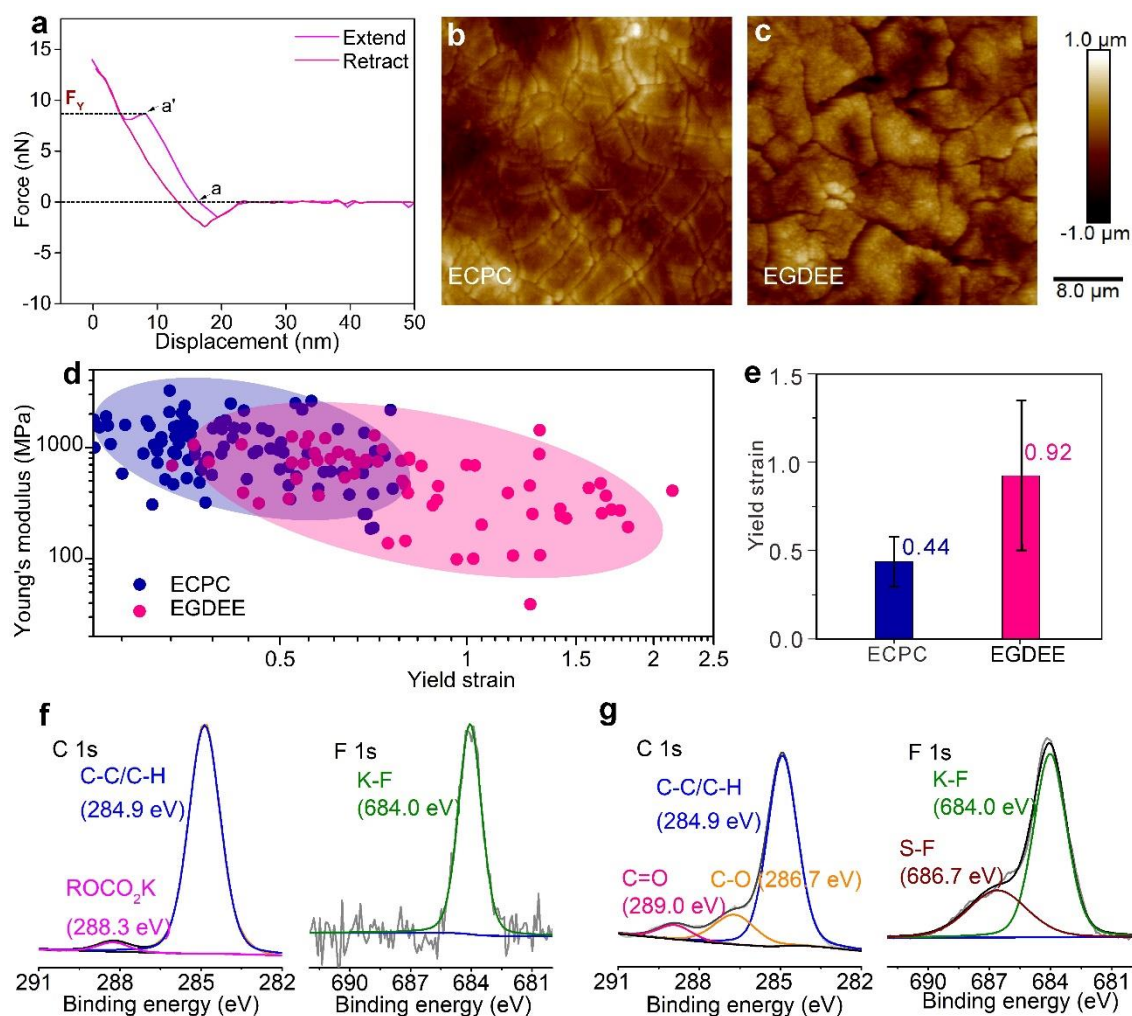


Figure 5.20 AFM and XPS characterizations. (a) Characteristic force curves obtained from the AFM tests on electrodeposited Sb electrodes. AFM topography images in (b) 1 M KFSI/ECPC and (c) 1 M KFSI/EGDEE. (d) Distributions of Young's modulus and yield strain of SEIs. (e) Histogram with an error bar of yield strain. XPS spectra of Sb electrodes after cycling 3 times in (f) 1 M KFSI/ECPC and (g) 1 M KFSI/EGDEE electrolytes.

The chemical composition of SEI formed in the two electrolytes is examined by XPS to explore the origin of such a stark difference in the mechanical properties. Figure 5.20f and g show C-C/C-H, C-O, C=O, and K-F bonds in deconvoluted C1s and F1s spectra, illustrating both organic and inorganic components are involved in SEIs. The C-C/C-H bonds (284.9 eV) are mainly from the hydrocarbonyl group in ECPC or EGDEE-derived SEIs.<sup>244</sup> The alkyl carbonates species (ROCO<sub>2</sub>K) are found in ECPC-developed SEI, signifying by the peak at 288.3 eV in

C1s spectrum (Figure 5.20f),<sup>245</sup> which is consistent with EEL spectra result (Figure 5.14k). An additional C-O type bond at 286.7 eV in C1s is detected in EGDEE-derived SEI, which can be assigned to polymer-like species of  $[\text{CH}_2\text{CH}_2\text{O}]_n$ .<sup>246-247</sup> Apart from the C-O bond, the C=O bond at 289.0 eV corresponds to ethyl formate, stemming from the deep decomposition of EGDEE.<sup>248-249</sup> These oligomers are characteristic of their high elasticity for increasing the maximum yield strain of the resulted SEI.<sup>250</sup> Other inorganic components that originated from the decomposition of KFSI salt such as KF are also observed (F1s spectra in Figure 5.20f and g).<sup>251</sup> Compared to the SEI formed in ECPC-based electrolyte, The one in EGDEE counterpart has overwhelming rich fluorine content (6.67 at.% vs. 0.72 at.%). which has been proven beneficial to improving the chemical stability of SEIs and charge transfer due to the large ratio of ionic-to-electronic conductivity.<sup>252</sup>

#### 5.2.4 Full cell demonstration

One concern regarding the adoption of ether-based electrolytes is the poor stability against oxidation at a high voltage, which may bring difficulties in full cell assembly. To assess the full cell performance in 1 M KFSI/EGDEE electrolyte, we synthesize  $\text{K}_x\text{MnFe}(\text{CN})_6$  cathode, which has been considered promising in K-ion batteries due to the advantages in the cost.<sup>18</sup> The synthesized  $\text{K}_x\text{MnFe}(\text{CN})_6$  shows an initial charge capacity of about  $130 \text{ mAh g}^{-1}$ . Therefore, the cathode to anode mass ratio of 6: 1 is adopted with a slight capacity excess in the anode side for preventing the K plating (Figure 5.21a). The full cells deliver a capacity of  $69.4 \text{ mAh g}^{-1}$  with an average potential of 2.8 V at a current density of  $10 \text{ mA g}^{-1}$  (based on the total mass of cathode and anode) (Figure 5.21b). The value could be increased to  $87.5 \text{ mAh g}^{-1}$  by eliminating SEI-induced capacity loss through pre-cycling of Sb. Correspondingly, an attractive energy density of about 194 and  $256 \text{ Wh kg}^{-1}$  is obtained for the cells without and with Sb pre-cycling, respectively (Figure 5.21d).

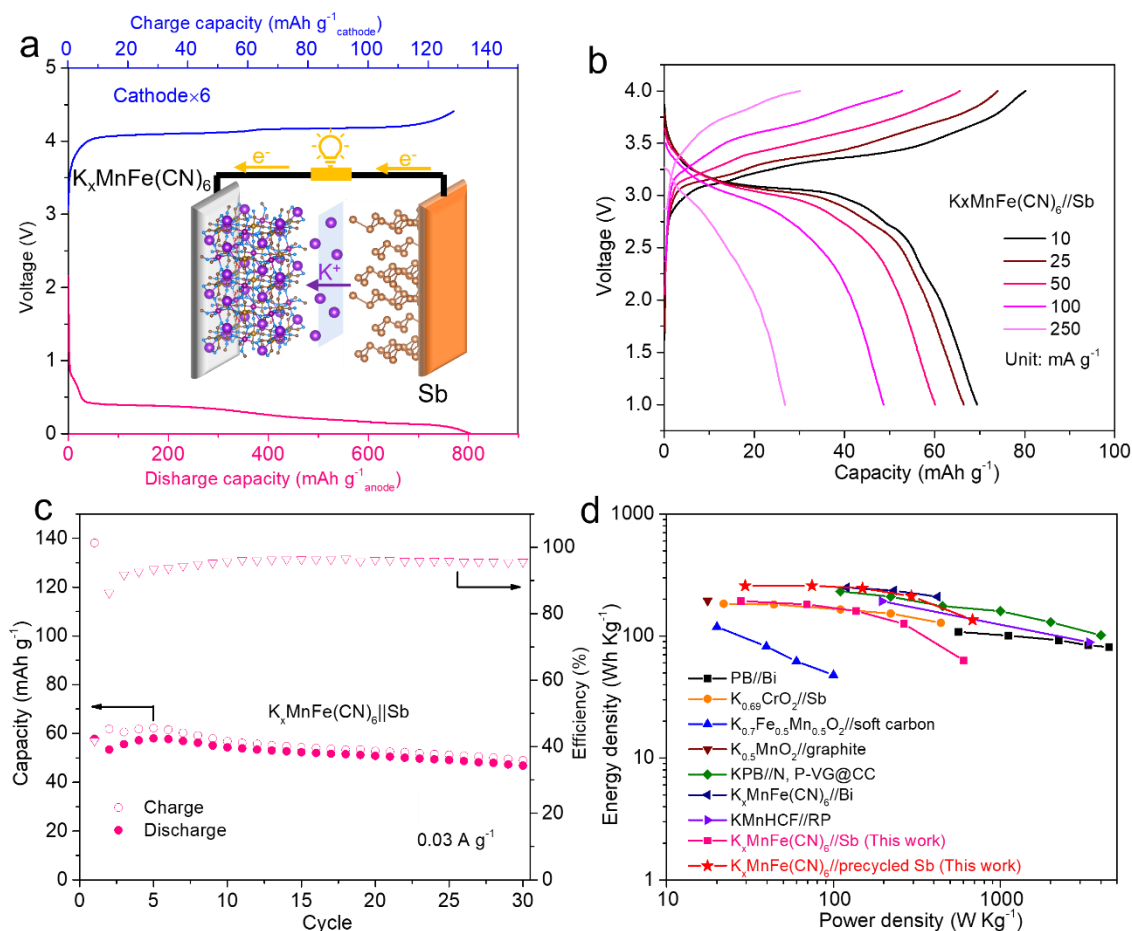


Figure 5.21 (a) Illustration of the full cell operation by adopting respectively the first charge and discharge curves of half Sb and  $K_xMnFe(CN)_6$  cells (inset: Schematic configuration of the PIBs full cell). (b) rate performance and (c) cyclic performance of  $K_xMnFe(CN)_6//Sb$  full cell (d) Ragone plot. (The value is based on the active material mass of anode and cathode).

### 5.2.5 Extending SEI construction to microsized Sn anodes in SIBs

The EGDEE and THF electrolyte solvents show large potentials for stabilizing anode materials. We further extend these two electrolyte solvents to the application of microsized Sn anodes in SIBs. The Sn electrodes are made by ball milling commercial Sn powder (10  $\mu\text{m}$ , Sigma), binder and carbon additives. The SEM image proves the morphologies of micro-sized Sn electrodes with an average particle size of 1.02  $\mu\text{m}$  (Figure 5.22a). The electrode shows excellent reversibility in the first cycle, delivering a capacity of  $738 \text{ mAh g}^{-1}$  in the typical carbonate electrolyte of 1 M  $\text{NaPF}_6/\text{PC-FEC}$  (Figure 5.22b). A 3 vol.% of FEC additive is incorporated to inhibit the Na corrosion in the counter electrode side.<sup>253</sup> The capacity degrades rapidly in the

subsequent cycling, owing to the large volume expansion as widely observed previously (Figure 5.22c).<sup>254</sup> Delightedly, the micro-sized Sn electrodes exhibit significantly improved stability in two ether-based electrolytes, *i.e.*, 1 M NaPF<sub>6</sub>/EGDDE and 1 M NaPF<sub>6</sub>/THF. Figure 5.22b displays the first discharge-charge curves under 0.05 A g<sup>-1</sup> in 1 M NaPF<sub>6</sub>/EGDDE and NaPF<sub>6</sub>/THF, showing a high initial reversible capacity of 720 and 778 mAh g<sup>-1</sup>, respectively. High ICE of 83.5%, 86.3% and 86.1% are achieved in 1M NaPF<sub>6</sub>/PC-FEC, 1M NaPF<sub>6</sub>/EGDDE and 1M NaPF<sub>6</sub>/THF, respectively. These high ICE are ascribed to the large particles of the Sn electrodes, which dramatically reduce the active interfaces with the electrolyte. Sn electrodes exhibit stable cycling with approximately 91% and 100% capacity retention after 100 cycles in 1M NaPF<sub>6</sub>/EGDDE and 1M NaPF<sub>6</sub>/THF. The high average CEs over 99.3% in ether-based electrolytes indicate negligible parasitic reactions between the electrodes and the electrolytes after several initial cycles. In comparison, the CE continuously decreases to 84.6% in 1M NaPF<sub>6</sub>/PC-FEC, suggesting that the bulk materials constantly break and produce new SEI during the cyclic measurements.

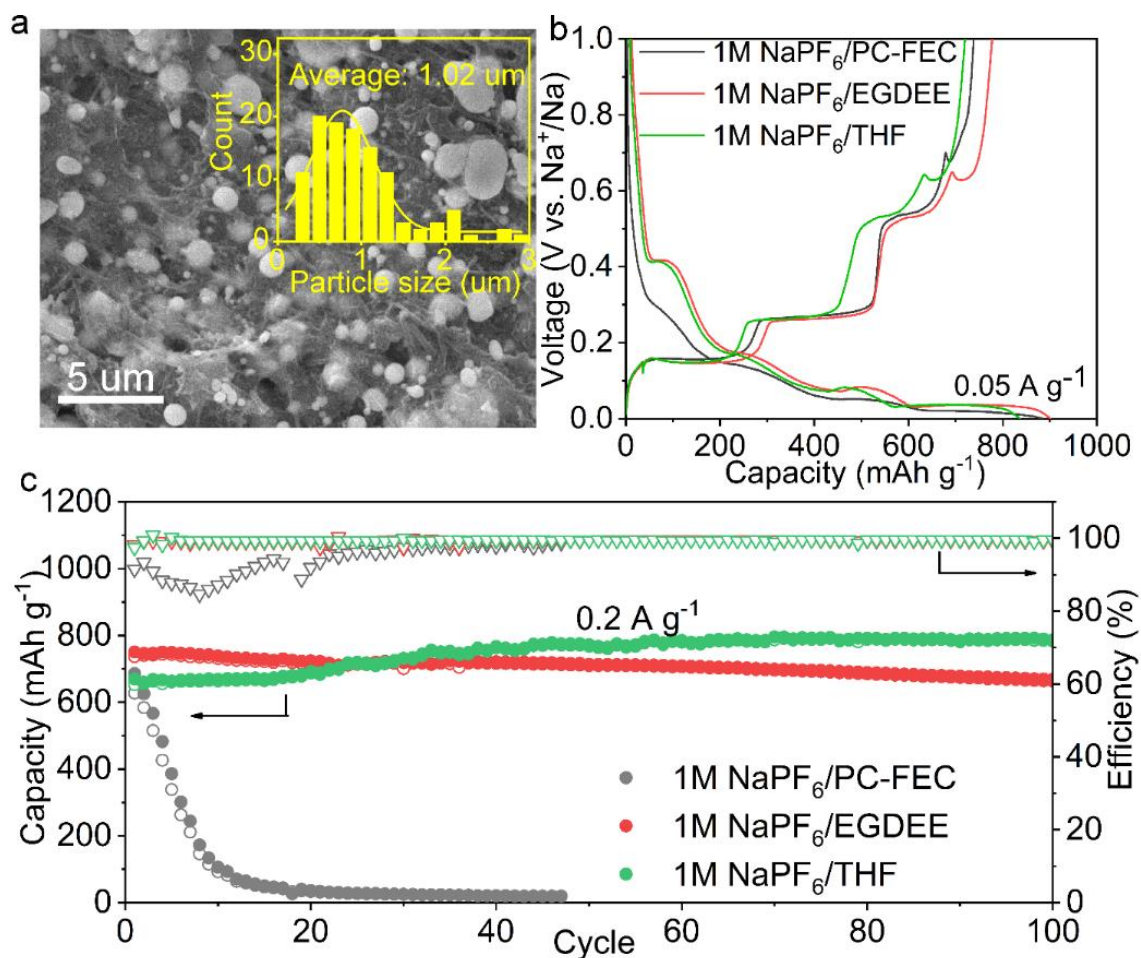


Figure 5.22 (a) SEM image and inset) particle size distribution of Sn electrode. (b) The galvanostatic discharge-charge profiles of the first cycle in 1M NaPF<sub>6</sub>/PC-FEC, 1M NaPF<sub>6</sub>/EGDDE and NaPF<sub>6</sub>/THF electrolytes under 0.05 A g<sup>-1</sup>. (c) Cycling performance under 0.2 A g<sup>-1</sup>.

Apart from the stable cycling, the electrode also delivers decent rate capability in ether-based electrolytes (Figure 5.23). After long-term cycling, the morphologies of Sn electrodes are collected by SEM to investigate the structural integrity (Figure 5.24). Obvious cracks are observed in the electrode cycled under all three electrolytes due to repeated expansion/contraction. Thick SEI layers that wrap the Sn particles could be discerned for the electrode tested in 1 M NaPF<sub>6</sub>/PC-FEC, as reflected by the apparent boundary between SEI and Sn particles (Figure 5.24c). The observation indicates the copious electrolyte decomposition that results in continuous SEI growth, which agrees well with the low CE. In contrast to it, the surface of active particles after cycling in EGDDE and THF-based electrolytes is smooth and

uniform under the resolution of SEM (Figure 5.24d-i), due potentially to the formation of thin and conformal SEI layer as will be confirmed by the HRTEM. We examine the electrodes' EIS after constructing SEIs through pre-cycling three times. The equivalent circuit fitted results indicate that both the SEIs ( $R_{SEI}$ ) and charge transfer ( $R_{ct}$ ) resistance are much lower in EGDEE and THF electrolytes than in carbonate counterparts (Figure 5.25).

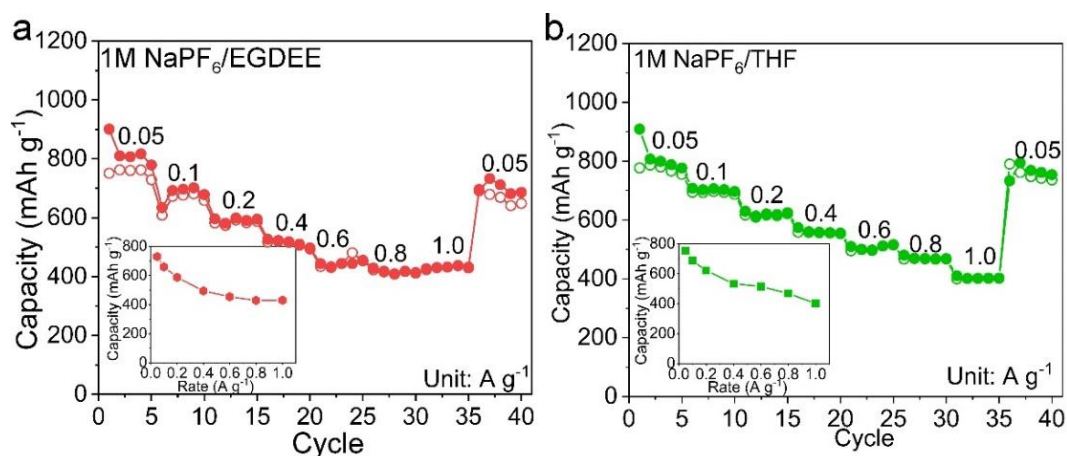


Figure 5.23 Rate performance of Sn electrodes in (a) 1 M NaPF<sub>6</sub>/EGDDE and (b) 1 M NaPF<sub>6</sub>/THF.

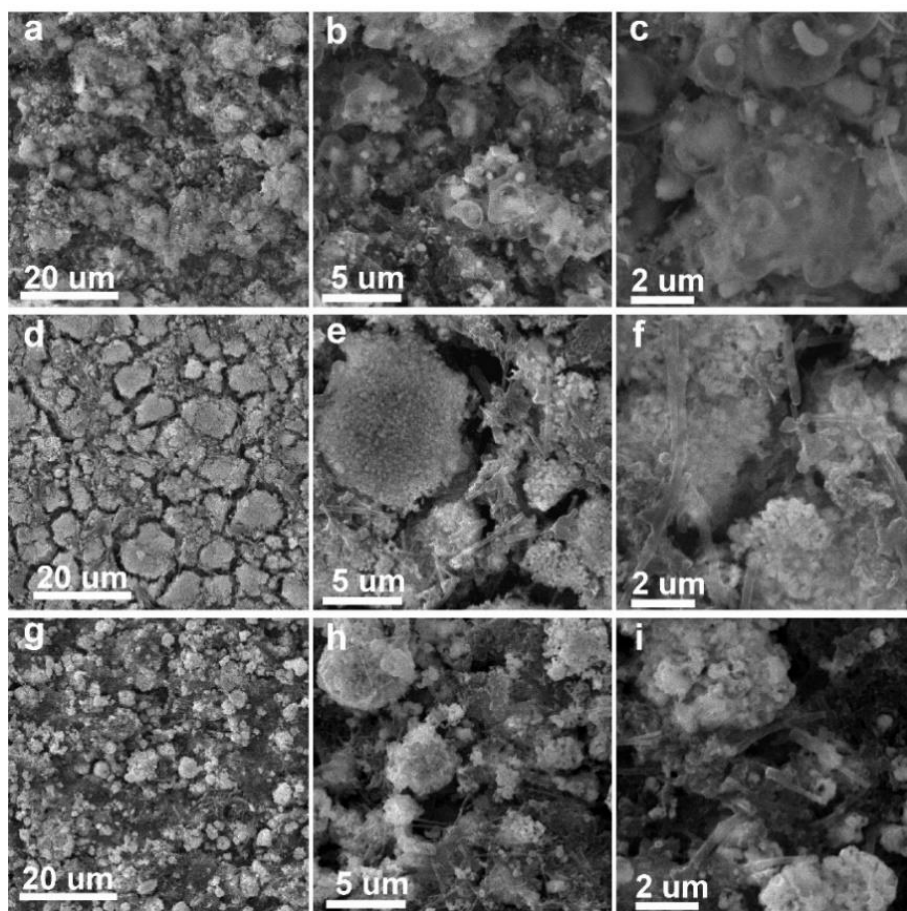


Figure 5.24 SEM images of Sn electrodes: (a-c) in 1 M  $\text{NaPF}_6/\text{PC-FEC}$ ; (d-f) in 1 M  $\text{NaPF}_6/\text{EGDDE}$  and (g-i) in 1 M  $\text{NaPF}_6/\text{THF}$  after 100 cycles.

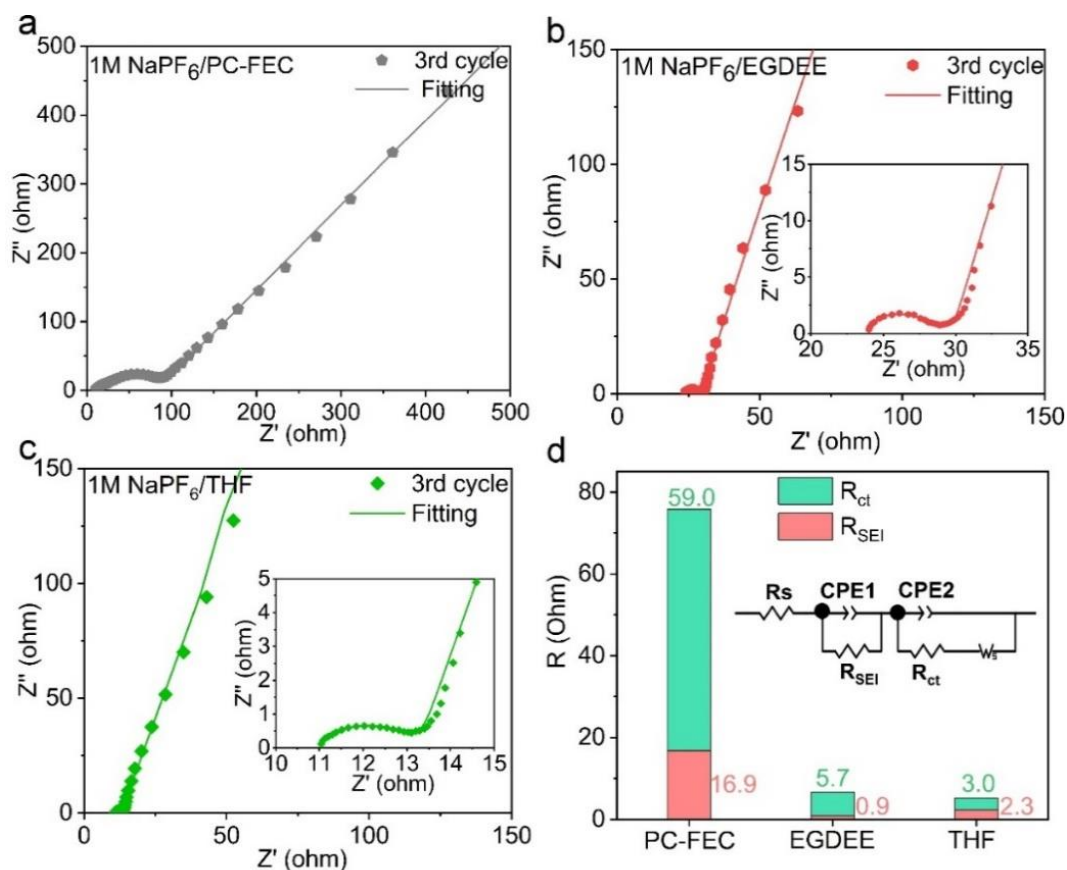


Figure 5.25 Nyquist plots of the Sn electrodes cycled three times in (a) 1 M NaPF<sub>6</sub>/PC-FEC, (b) 1 M NaPF<sub>6</sub>/EGDDE and (c) 1 M NaPF<sub>6</sub>/THF; d) the fitted impedance in these three electrolytes (d inset: the equivalent circuit used for EIS fitting).

The above results demonstrate the essential roles of SEIs in stabilizing micro-sized Sn anode. The nanostructures of SEIs in the three electrolytes are resolved by TEM to explore the underlying mechanism. In Figure 5.26a and b, a heterogeneous SEI with a thickness of about 25.2 nm is formed in 1 M NaPF<sub>6</sub>/PC-FEC electrolyte. Some tiny crystals present in the SEI and their lattice structure is analyzed by the HRTEM (Figure 5.26c). One pair of crossed lattices of 2.6 Å and 1.6 Å can be assigned to Na<sub>2</sub>CO<sub>3</sub> species on the (11-2) and (-422) planes (COD#9009418), respectively. The d-spacing of 2.3 Å might be the (002) plane of NaF (PDF#73-1922). Turning to the SEI formed in 1 M NaPF<sub>6</sub>/EGDDE electrolyte (Figure 5.26e-g), it exhibits ultrathin (about 3.4 nm) and amorphous morphologies without showing any crystalline particles. The stable SEI layer formed in the first cycle effectively prevents the continuous electrolyte decomposition, avoiding the over-growth of SEI and resulting in the

small thickness. Meanwhile, the thin SEI restricts the crystallization of the inorganic species.<sup>255-256</sup> The SEI established in 1 M NaPF<sub>6</sub>/THF shows similar nanostructures to that in 1 M NaPF<sub>6</sub>/EGDDE, where thin and amorphous SEI uniformly adheres to the Sn particles (Figure 5.26i-k). The Na<sub>x</sub>Sn recovers to Sn upon charging to 1 V, and the particle preserves the high crystallinity after cycling. The nanostructures of SEIs in both linear and cyclic ether-based electrolytes differ significantly from the one in classic carbonate electrolyte, as illustrated by Figure 5.26d, h and l. In general, the SEI could be treated as a composite with the inorganic species distributed among the organic matrixes. The relatively large inorganic particles with high crystallinity are presented in the SEI in the carbonate electrolyte, which may deteriorate the mechanical resilience, as will be explored by AFM test with eliminating the substrate's interference. Furthermore, the thick SEI is detrimental to the Na ion transfer and undermines the rate capability.

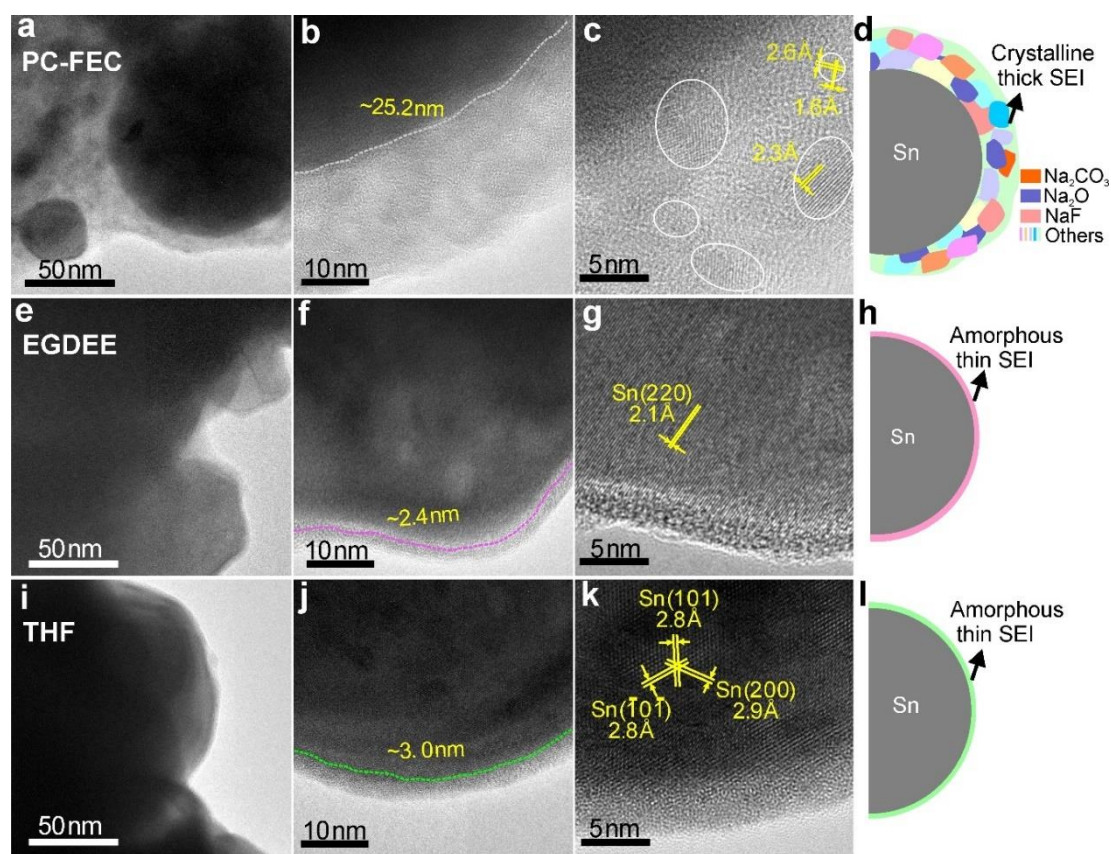


Figure 5.26 TEM/HRTEM characterization and SEI illustrations of Sn electrodes after 3 cycles in (a-d) 1 M NaPF<sub>6</sub>/PC-FEC, (e-h) 1 M NaPF<sub>6</sub>/EGDDE and (i-l) 1 M NaPF<sub>6</sub>/THF electrolytes.

XPS is conducted to compare the chemical compositions of the SEIs constructed in the three electrolytes. Similar species are detected in the three SEIs but with massive differences in the relative amounts. In C1s spectra of all the electrolytes (Figure 5.27a), the deconvoluted peaks located at 284.5, 285.4, 286.1, and 287.4 eV can be assigned to organic carbonates of C-C/C-H, C-O, O-C-O, and C=O species, which are mainly originated from solvent reduction, including the polymerization of PC, FEC, EGDEE and THF.<sup>250, 257</sup> In particular, the Na<sub>2</sub>CO<sub>3</sub> species involved with the NaPF<sub>6</sub> salt decompositions are defined at 289.5 eV.<sup>258</sup> As for the O1s spectra presented in Figure 5.27b, the peaks at 532.3 and 533.3 eV can be ascribed to the organic ingredients of O-C=O and C-O, consistent with that in C1s spectra.<sup>259</sup> Additionally, Na-O bonding at 531.5 eV is derived from the sodium alkyl carbonates (R-OCO<sub>2</sub>Na), Na<sub>2</sub>CO<sub>3</sub> or Na<sub>2</sub>O species.<sup>260</sup> We also examine the detailed F1s spectra considering the pivotal roles of F-related species. Two pronounced peaks of Na-F (684.9 eV) and P-F (687.7 eV) bonding (Figure 5.27c) correspond respectively to the salt decomposition products of NaF and Na<sub>x</sub>PF<sub>y</sub> (or Na<sub>x</sub>PO<sub>y</sub>F).<sup>261</sup> Moreover, Na<sub>2</sub>CO<sub>3</sub> and Na-O components are enriched in carbonate electrolyte-derived SEI, which agrees with the TEM observations. However, much higher Na-F species could be found under ether-based SEI. The F-rich SEI is reported to possess excellent mechanical and electrochemical stability for maintaining the structural integrity.<sup>55, 262</sup>

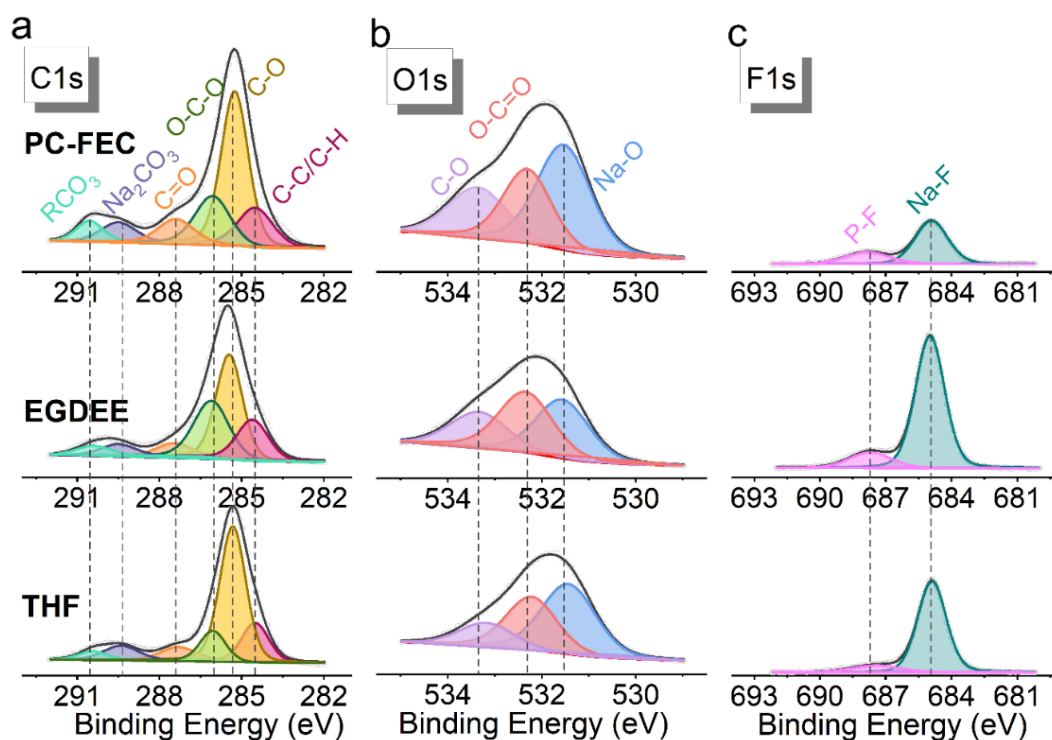


Figure 5.27 XPS measurements of (a) C1s, (b) O1s and (c) F1s for cycled Sn electrodes in corresponding electrolytes.

We employed AFM to probe the mechanical properties of SEIs formed in different electrolytes. To exclude the potential interferences from the binder and conductive carbon, neat Sn electrodes are prepared by magnetron sputtering. Similarly, the electrodes are pre-cycled in the three electrolytes to build SEIs for AFM tests. A two-step AFM test is conducted to explore the elastic and plastic deformation behaviour of SEIs. Figure 5.28a presents the typical force curves of the same point obtained from the first and second steps of AFM test, respectively.  $E$  is calculated from the first test that is conducted in the elastic deformation region, while the  $\epsilon_Y$  of SEIs is determined in the second test where a large force is applied to break the SEI deliberately. According to most recent studies,<sup>118</sup> the  $E$  and  $\epsilon_Y$  are calculated by eliminating the substrate's effects to increase the accuracy. The results show that the SEI formed in 1M NaPF<sub>6</sub>/PC-FEC has a high average  $E$  of 280.5 MPa, compared to 244.7 MPa and 183.4 MPa for the ones constructed in EGDEE and THF-derived electrolytes, respectively. The observation does not come as a surprise considering the better crystallinity of inorganic species in the SEI built in 1M NaPF<sub>6</sub>/PC-FEC. The high crystalline inorganic particles would have much higher Young's

modulus than the amorphous components.<sup>263</sup> Nevertheless, the SEI in ether-based electrolytes shows excellent elasticity, evidenced by the large  $\epsilon_Y$  of 0.38 and 0.41 for the ones formed respectively in 1 M NaPF<sub>6</sub>/EGDEE and 1 M NaPF<sub>6</sub>/THF, compared to 0.32 for the SEI in carbonate electrolyte. Both high values of  $E$  and  $\epsilon_Y$  are beneficial to the mechanical stability of SEI subject to expansion. The recent study suggests the maximum elastic deformation energy ( $U \propto E \cdot \epsilon_Y^5$ ) reveals the combining effects of  $E$  and  $\epsilon_Y$  in resisting the structure deformation (Equation 2-3). The  $U$  distribution and the average value are given in Figure 5.28c. The  $U$  value is 56.3 and 72.0 pJ for the SEIs in EGDEE and THF-based electrolytes, respectively, outperforming the 35.8 pJ for the one in NaPF<sub>6</sub>/PC-FEC. The results indicate that, although having a small thickness, the SEIs in the two ether-based electrolytes have better mechanical stability. A stable SEI prevents continuous SEI formation and encapsulates the fragmented particles, thus benefiting the cyclic stability of Sn electrodes.

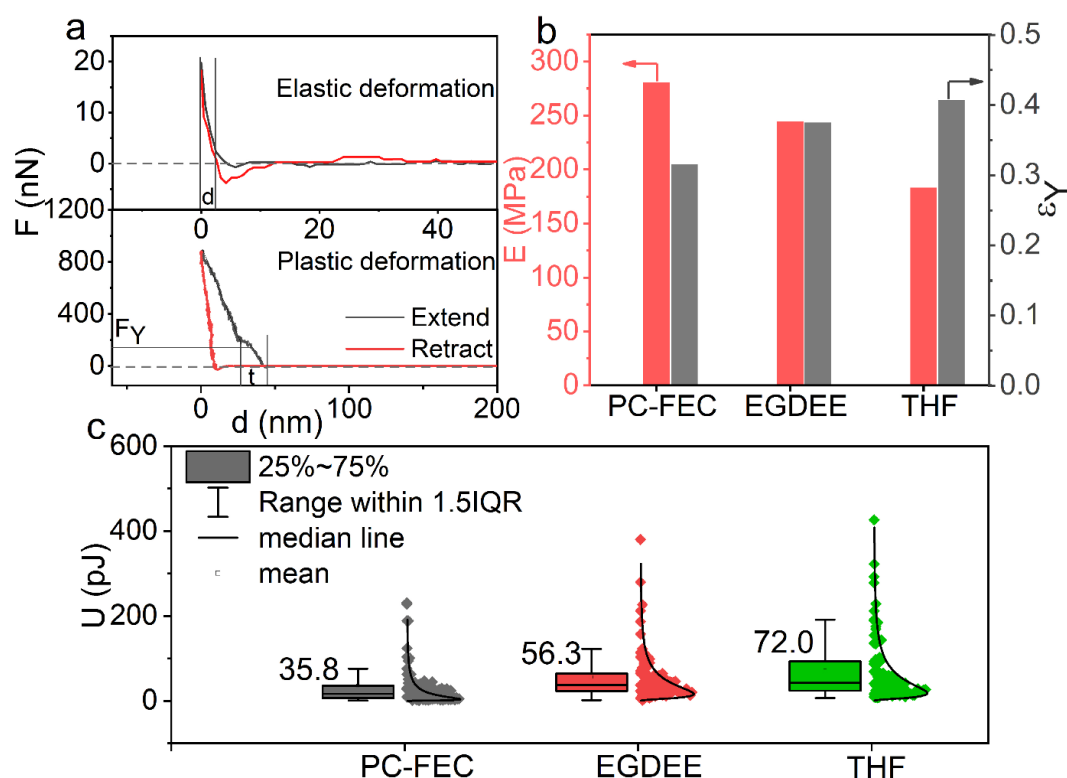


Figure 5.28 Mechanical properties of SEIs. (a) Characteristic force curves obtained from the AFM tests on magnetron sputtered Sn electrodes; (b) average Young's modulus and yield strain  $\epsilon_Y$  and (c)  $U$  for SEIs formed in the three electrolytes. Sample size = 108, 91 and 87 for PC-FEC, EGDEE and THF, respectively.

### 5.3 Summary

The phase transformation and morphology evolution of microsized Sb anodes during K ions insertion/extraction are thoroughly investigated to resolve the poor cyclic stability. The unique intercalation-assisted alloying reaction pathway partly prevents the structural collapse from rapid volume expansion. Combining with electrolyte regulation, we achieve an outstanding capacity for Sb microparticles, which is well maintained in the long-term cycles. We demonstrate that such stability originates from the construction of elastic SEI, which effectively encapsulates the particles during electrode expansion and contraction. The XPS analysis suggests the abundance of oligomer-like species and small amount inorganic species mainly account for the improved maximum elastic strain in the ether-derived SEI. Move over, the construction of SEI can be further extended to stabilizing Sn microparticles in SIBs. Except for larger  $\epsilon_Y$ , AFM tests also prove the SEIs in the ether electrolytes have higher maximum elastic deformation energy than the counterpart in the conventional electrolyte, offering superb mechanical stability. These findings elaborate the structural insights to design elastic SEIs for stabilizing microsized alloy anodes, so as to boost the energy densities of today's alkali-metal ion batteries. We are fully aware that the two reported candidates cannot completely address the challenges towards the practical application of ether-based electrolytes. For instance, the high vapor pressure of THF makes it hard to be used in real cells because of safety issues. Nevertheless, the results presented here indicate the great opportunity in building robust SEIs through ether solvent, which contains a large family of candidates besides widely adopted methyl glyme groups. The disclosed microstructure-mechanical stability correlation would benefit the screening of potential ether candidates and the rational design of SEI for stabilizing alloys anodes.

## Chapter 6

# Robust solid electrolyte interphases in localized high concentration electrolytes boosting black phosphorus anode for potassium ion batteries

Black phosphorus (BP) shows superior capacity towards K ion storage, yet it suffers from poor reversibility and fast capacity degradation. Herein, BP-graphite (BP/G) composite with a high BP loading of 80 wt.% is synthesized and stabilized *via* the utilization of a localized high concentration electrolyte (LHCE), *i.e.*, potassium bis(fluorosulfonyl)imide (KFSI) in trimethyl phosphate (TMP) with a fluorinated ether as the diluent. We reveal the benefits of high concentration electrolytes rely on the formation of inorganic component rich solid electrolyte interphase (SEI), which effectively passivate the electrode from copious parasite reactions. Furthermore, the diluent increases the electrolyte's ionic conductivity for achieving attractive rate capability and homogenizes the element distribution in the SEI. The latter essentially improves SEI's maximum elastic deformation energy for accommodating the volume change, resulting in excellent cyclic performance. This work promotes the application of advanced potassium-ion batteries (KIBs) by adopting high-capacity BP anodes, on the one hand. On the other hand, it unravels the beneficial roles of LHCE in building robust SEI for stabilizing alloy anodes.

### 6.1 Introduction

Phosphorus (P) has been predicted to be one of the highest-capacity anodes for alloying up to 1.33 K ion per P atom, corresponding to 1154 mAh g<sup>-1</sup> capacity.<sup>234</sup> Three types of P allotropes exist in nature, *i.e.*, red phosphorus (RP), white phosphorus (WP), and black phosphorus

(BP).<sup>264</sup> WP is precluded as a potential anode because of the safety issues associated with the self-ignition under ambient temperature. The non-toxic and safe RP is widely studied as anode materials for alkali metal ion storage.<sup>110, 265-268</sup> However, the poor electronic conductivity and large volume expansion (301% for forming  $K_4P_3$ ) hinder its development in PIBs. The low electronic conductivity of  $10^{-14} \text{ S cm}^{-1}$  makes bare RP hardly directly employed as electrodes.<sup>269</sup> The combination with conductive carbon is an effective strategy to modify its intrinsic poor electronic conductivity.<sup>104, 270-271</sup> Taking advantage of low sublimation temperature ( $\sim 419^\circ\text{C}$ ), the RP could be encapsulated into the pores of carbon materials through vaporization condensation conversion method, which enhances the conductivity and buffers the large volume change of P in the carbon matrix.<sup>111, 272</sup> The drawback is that WP will be produced during condensation. Thus, the composites need to be washed by toxic carbon disulfide ( $\text{CS}_2$ ) solvent to remove WP residual.<sup>273</sup> Besides, the large specific surface area of the carbon host will cause severe electrolyte decompositions in the first cycle with a low initial Coulombic efficiency (ICE).

BP is a two-dimensional layered material with an interlayer distance of  $5.2 \text{ \AA}$  and possesses the best thermal stability and electronic conductivity of  $0.2\text{-}3.3 \times 10^2 \text{ S cm}^{-1}$  among all the P allotropes.<sup>274</sup> Chemical vapour deposition (CVD) is extensively used to synthesize BP with superior crystallinity, but the high cost and low BP yielding of CVD discourage the wide application in the battery.<sup>275-276</sup> Mechanical ball milling is recognized as a practical approach to fabricate BP and its composite with carbon (BP/C) at a large scale.<sup>277-278</sup> Unfortunately, due to the difficulties in controlling the morphologies during ball milling processes, the particle size is relatively large and non-uniform, ranging from hundreds of nanometres to tens of micrometers.<sup>279</sup> Although the large particles reduce the active surface with electrolytes and benefit the high ICE, the ball-milled BP/C composites usually show rapid capacity decay in PIBs because of the particle pulverization during cycling.<sup>87-88, 280</sup>

High concentration electrolytes (HCE, usually  $> 3 \text{ M}$ ) show promising potentials in improving the cyclic stabilities of anode materials,<sup>35, 76, 91</sup> attributing to the new interfacial chemistry induced by compressed solvation sheaths.<sup>281</sup> The modified ion solvation structures help build a

salt anion-derived solid electrolyte interphase (SEI) to suppress continuous electrolyte decompositions.<sup>60</sup> To resolve the high viscosity of HCE, a localized high concentration electrolyte (LHCE) is proposed and has been popularly adopted in Li/Na batteries.<sup>235, 282-285</sup> Such a LHCE relies on fluorinated ethers as nonsolvent to dilute the HCE without changing its ion solvation structures.<sup>286</sup> The LHCEs are rarely researched for PIBs, probably due to the phase separation of fluorinated ethers and carbonate solvents in high concentration K electrolytes, although it is not a problem in Li electrolytes.<sup>287-288</sup> Recently, Qin *et al.* report a LHCE based on KFSI/monoglyme (DME) system, which enables excellent cyclability of graphite anode by toughening the SEI on graphite,<sup>289</sup> but the direct extension to alloy anodes has not been successful. In this work, we deviate from DME solvent and focus on trimethyl phosphate (TMP)-based electrolytes considering its non-flammability with a high flash point of 150 °C (compared to 5 °C for DME). It also possesses excellent oxidative stability to be compatible with high-voltage cathodes for practical applications. Furthermore, the high dielectric constant of 21.6 allows the preparation of highly concentrated electrolytes up to 6.6 M with a KFSI salt.<sup>61, 290</sup> We demonstrate that a LHCE based on KFSI/TMP system with a 1,1,2,2-tetrafluoroethyl-2,2,2-trifluoroethyl ether (HFE) diluent realizes the stable cycling of BP-graphite (BP/G) anode with a high BP loading of 80 wt.%. The BP/G electrodes show high reversible capacities of 618 mAh g<sup>-1</sup> under 0.1 A g<sup>-1</sup> and outstanding long-term cyclic stability with 342 mAh g<sup>-1</sup> after 300 cycles under 0.3 A g<sup>-1</sup> in LHCE.

## 6.2 Results and discussion

### 6.2.1 Physical characterizations

Commercial RP is purified by washing in boiling water, which is adopted to synthesize BP through high-energy ball milling (HEBM). The X-ray diffraction (XRD) in Figure 6.1a shows that the purified RP presents a medium-range order structure as manifested by the broad peak at about 15 ° and confirmed in transmission electron microscopy (TEM, Figure 6.2).<sup>291</sup> RP is completely transformed to orthorhombic BP (PDF#73-1358) after HEBM. Raman spectra also identify the successful synthesis of BP. The Raman peaks at 347, 381-405, and 462 cm<sup>-1</sup> (Figure 6.1b) match B<sub>1</sub> (fundamental mode), A<sub>1</sub> (symmetric stretch mode) and E<sub>1</sub> (degenerate mode) vibrations in RP.<sup>292</sup> In comparison, there are three peaks at 362, 434, and 462 cm<sup>-1</sup> after ball milling, corresponding to A<sub>g</sub><sup>1</sup> (out-of-plane mode), B<sub>2g</sub>, and A<sub>g</sub><sup>2</sup> (in-plane mode) of BP,

respectively.<sup>293</sup> The BP exhibits a large particle size up to several micrometers (Figure 6.1c). The d-spacing of 0.52 nm in high-resolution TEM (HRTEM) is indexed to the (020) plane of BP. The BP is further mixed with graphite to prepare a BP/G composite through planetary ball milling. There are no sharp peaks except two humps at about 23° and 35° in the XRD pattern of BP/G, indicating the long-term ball milling decreases the crystallinity of the BP. In the Raman spectrum of BP/G composite, the BP peaks between 350-500 cm<sup>-1</sup> become invisible, and only the D (1340 cm<sup>-1</sup>) and G (1586 cm<sup>-1</sup>) bands of graphite are detected. The D band originates from A<sub>1g</sub> ring breathing mode, which is absent in perfect graphite, and G band arises from E<sub>2g</sub> vibration mode of sp<sup>2</sup> carbon atoms.<sup>294</sup> The increase of D band (I<sub>D</sub>/I<sub>G</sub>=1.04) implies that significant defects are introduced in BP/G composite. The morphologies of BP/G composite are examined by TEM and scanning electron microscope (SEM) (Figure 6.1d, Figure 6.10a and b). It maintains the microparticle characteristic and exhibits the uniform elemental distribution of P and C in energy-dispersive X-ray spectroscopy (EDS) mappings (Figure 6.3a). Moreover, the chemical structures of BP/G are studied by X-ray photoelectron spectroscopy (XPS). As shown in Figure 6.3b, P-C bonding is found in both C1s (283.5 eV) and P2p spectra (130.3 eV), which would help reduce the energy barriers of ion migrations for fast alloying reactions.<sup>104, 295</sup>

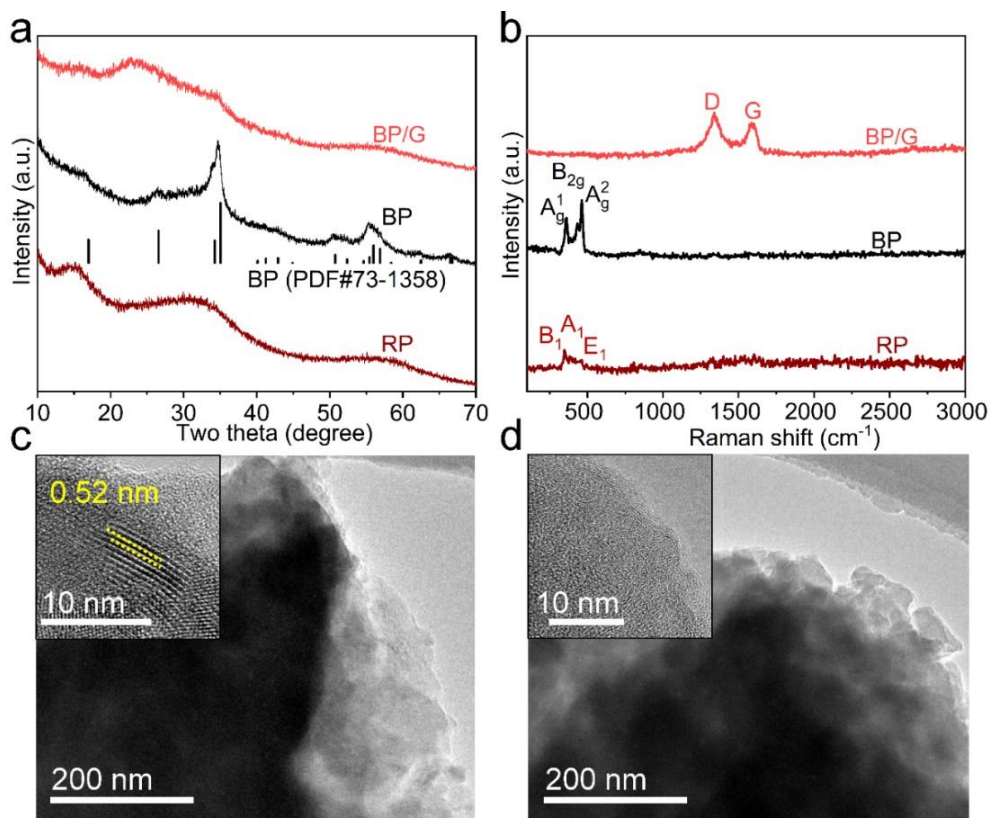


Figure 6.1 Sample preparation. (a) XRD patterns and (b) Raman spectra of RP, BP, and BP/G composite; TEM images of (c) BP and (d) BP/G composite.

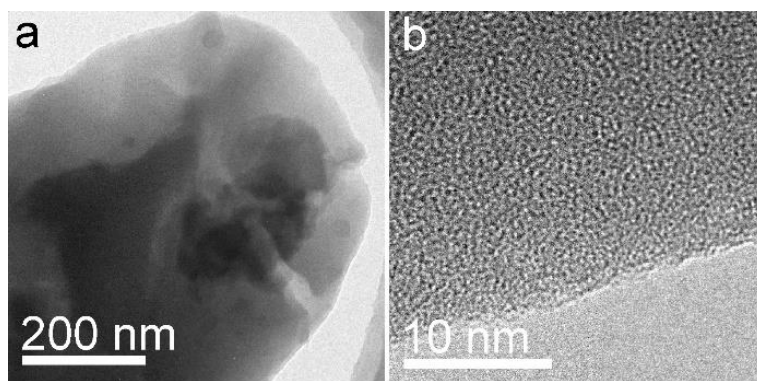


Figure 6.2 The TEM and HRTEM images of purified RP.

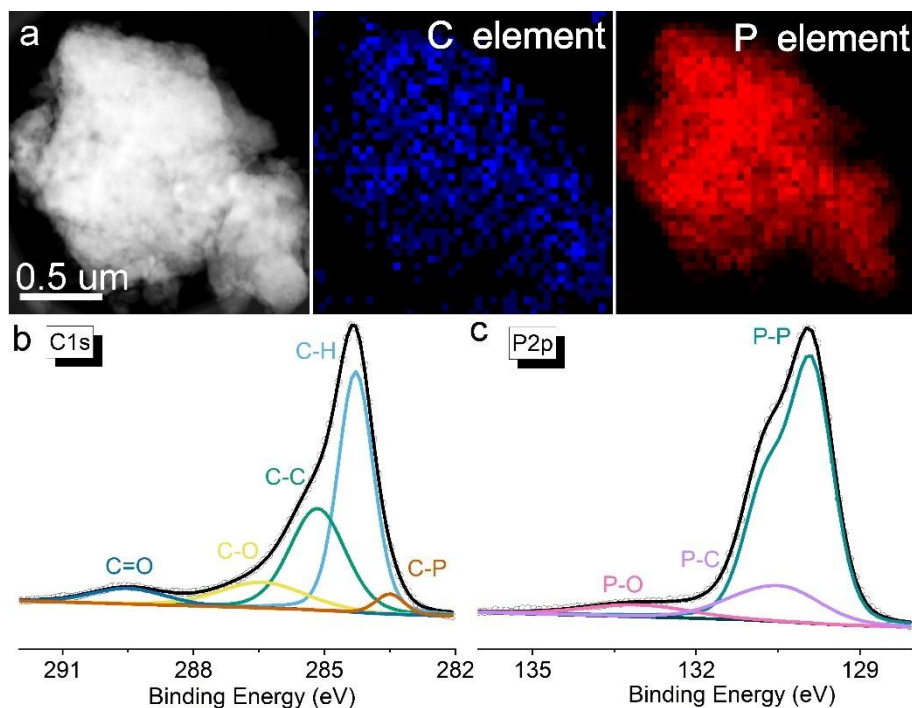


Figure 6.3 (a) The EDS mapping of C and P elements and (b) XPS spectra for BP/G composite.

### 6.2.2 Solvation structures of electrolytes

Three alkylphosphates electrolytes with different formulations are prepared for examining the electrochemical performance of BP/G, namely NCE (1 M KFSI/TMP), HCE (5 M KFSI/TMP), and LHCE (KFSI/TMP/HFE=1:1.7:2 by mol.). The ionic conductivities of the electrolytes are compared in Figure 6.4. Increasing the concentration significantly reduces the ionic conductivity from 5.31 for NCE to 1.82  $\text{mS cm}^{-1}$  for HCE because of the increased ion-pairing.<sup>63</sup> After adding HFE diluent in LHCE, the value is enhanced to 3.08  $\text{mS cm}^{-1}$ . The solvation structures of the electrolytes are investigated by Raman spectroscopy. In Figure 6.5a, two distinct peaks at 737 and 751  $\text{cm}^{-1}$  are presented in TMP solvent, which can be ascribed to asymmetric P-O-C stretching of free TMP molecular.<sup>61</sup> The free stretching peaks persist in NCE, although the intensity is weakened. In contrast, they are disappeared in HCE and LHCE, implying that all TMP molecules participate in K solvation in high concentration electrolytes.<sup>60</sup> In Figure 6.5b, a prominent peak at 1216  $\text{cm}^{-1}$  is observed in NCE, which comes from the S=O stretching in FSI<sup>-</sup> anion. This peak shifts to the high frequency of 1221  $\text{cm}^{-1}$  in HCE and LHCE owing to the enhanced coordination between K<sup>+</sup> and FSI<sup>-</sup>. Besides, the vibration band of HFE

between  $840\text{-}870\text{ cm}^{-1}$  does not show apparent shifts in LHCE (Figure 6.5c) since HFE molecules have minimal interaction with K ions.<sup>296</sup>

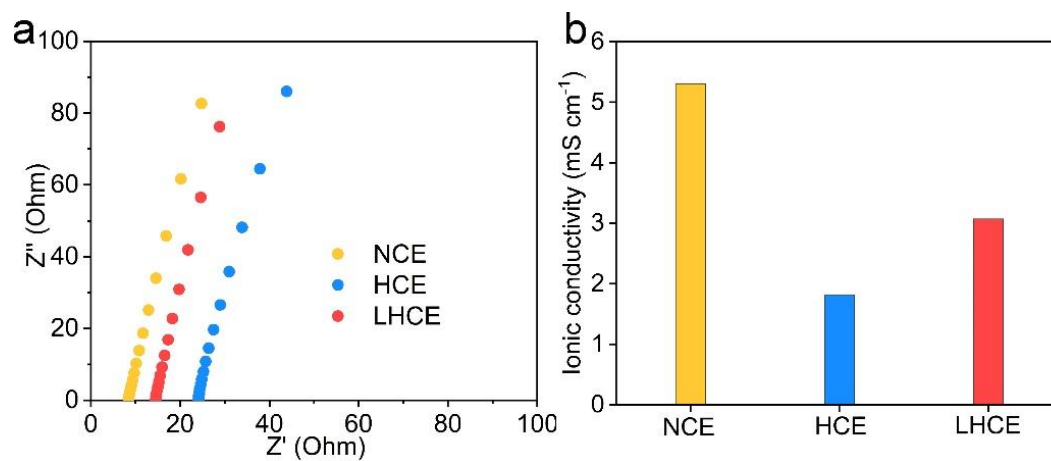


Figure 6.4 (a) Electrochemistry impedance spectra and (b) the calculated ionic conductivities of NCE, HCE and LHCE.

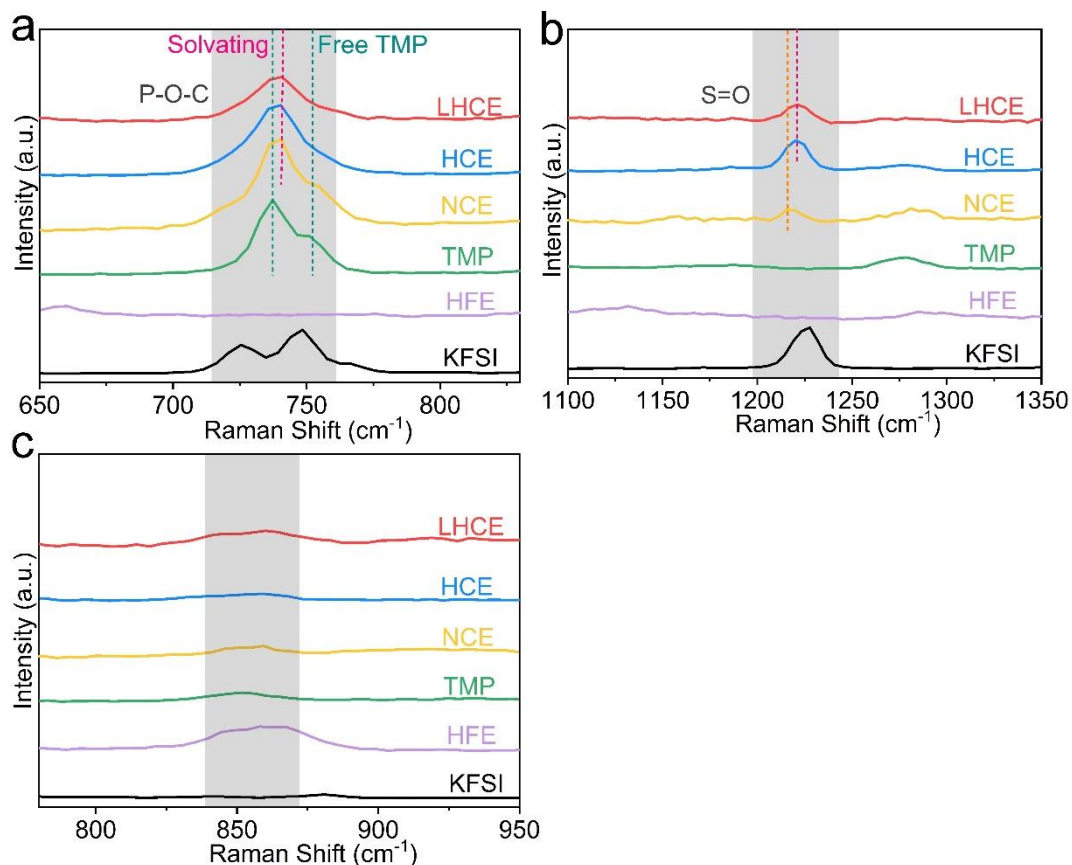


Figure 6.5 Electrolyte solvation structures. (a-c) Raman spectra of NCE, HCE, LHCE, KFSI, TMP and HFE.

### 6.2.3 K-P alloying mechanism

The cyclic voltammetry (CV) curves are first scrutinized to study the faradaic response of BP/G electrodes in the electrolytes mentioned above (Figure 6.6a). A broad peak at 0.5-1.2 V is shown in the first cycle under all the electrolytes due to the formation of SEI. In NCE, the CV curves do not reveal evident peaks after the first cycle as a reflection of the poor reversibility of the electrode. As for HCE and LHCE, two pronounced reduction peaks at 0.8-1.0 V and 0.25-0.27 V are observed in the cathodic sweep, which is associated with the formation of  $K_xP$  ( $x < 1.33$ ) and  $K_4P_3$ , respectively.<sup>106</sup> Correspondingly, two oxidation peaks at about 0.8 V and 1.7 V appear in anodic scan due to the reversible de-alloying process. Raman spectroscopy is then performed to elucidate the K ion storage mechanisms of BP/G composite. No distinct peak, except for graphite peaks, is detected at a fully discharged state in NCE, while three new Raman peaks at 392, 474, and 950  $\text{cm}^{-1}$  emerge in HCE (Figure 6.7a and b). Combined with the CV

curves in NCE and HCE, it can decipher that the BP/G composite is not alloyed with K in NCE but reacts successfully in HCE and LHCE. The *ex situ* Raman spectra for LHCE are shown in Figure 6.6b. In the state of discharging to 0.8 V, a broad peak at about  $440\text{ cm}^{-1}$  is found, possibly relating to the formation of  $\text{KP}_2$ .<sup>297</sup> When discharging from 0.2 V to 0 V, three distinct peaks in similar positions as those in HCE show high intensities, which is assigned to the  $\text{K}_4\text{P}_3$  phase.<sup>106</sup>

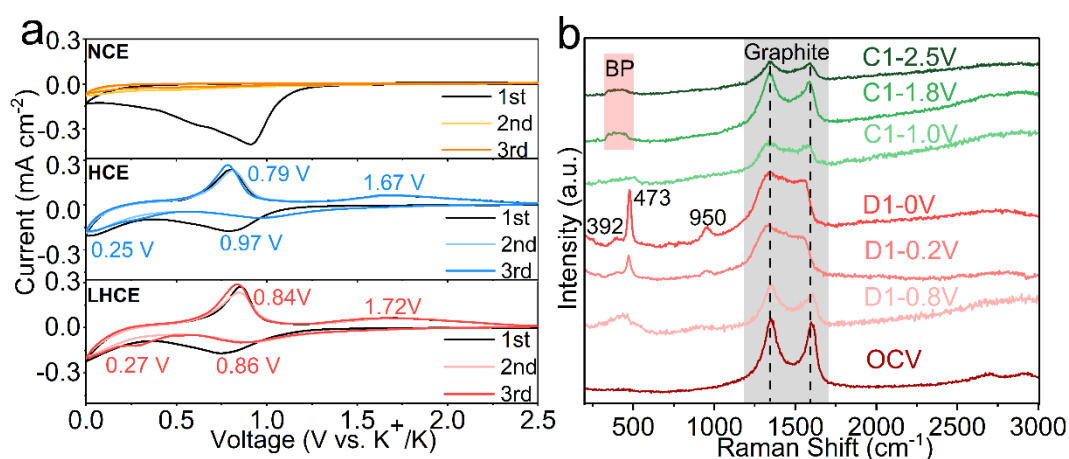


Figure 6.6 (a) CV curves of BP/G electrodes in NCE, HCE and LHCE at the scan rate of  $0.1\text{ mV s}^{-1}$ ; (b) *Ex situ* Raman characterization of BP/G electrodes under different states in LHCE (note: D1-0.8V represents 0.8 V in the first discharge process).

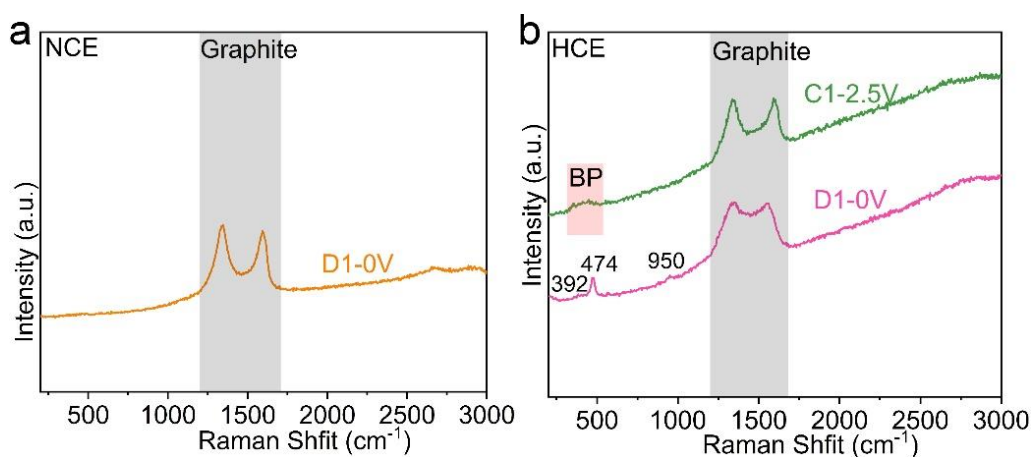


Figure 6.7 Raman spectra of BP/G electrode (a) at first fully discharged state (D1-0V) in NCE; (b) at first fully discharged (D1-0V) and first fully charged (C1-2.5V) states in HCE.

To confirm the final potassiated products, the  $K_4P_3$  is chemically synthesized by HEBM using K metal and BP powder with a stoichiometric ratio of 4:3. As observed in Figure 6.8, a group of  $K_4P_3$  peaks are well-defined, consistent with the peaks at a fully discharged state. Upon charge (Figure 6.6b), the sharp peak at  $473\text{ cm}^{-1}$  is disappeared and turns to a weak peak after charging to 1.0 V. Broad peaks located at between  $350$  and  $500\text{ cm}^{-1}$  arise when charging to above 1.8 V, evidencing the potassiated phases recovered to BP. Similarly, the BP peaks are detected when charging back to 2.5 V in HCE electrolyte as well (Figure 6.7b). The observations demonstrate the highly reversible alloying and de-alloying processes of  $4K+3P\leftrightarrow K_4P_3$  in high concentration electrolytes.

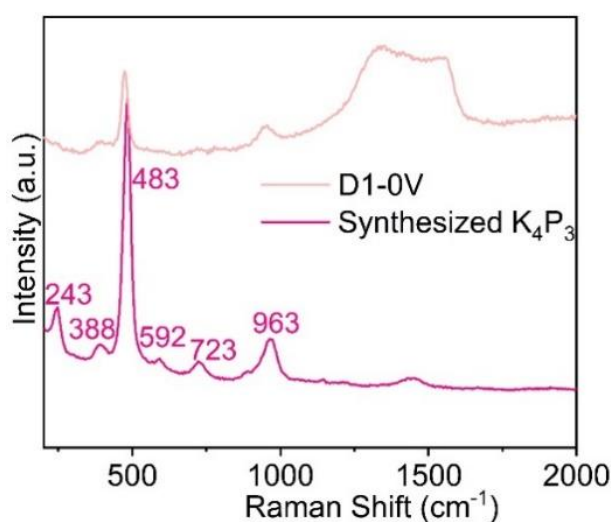


Figure 6.8 Comparison of Raman spectra of HEBM synthesized  $K_4P_3$  and first fully discharged (D1-0 V) BP/G electrodes in LHCE.

#### 6.2.4 Electrochemical performance evaluation

The electrochemical performances of BP/G composite in PIBs are evaluated in coin cells, and the specific capacities are calculated based on the total mass of BP/G composite. As shown in Figure 6.9a, the BP/G electrode shows a large discharge capacity and minor charge capacity with an extremely low ICE of 3.7% in NCE. We speculate that the electrolyte decomposition dominates the process owing to the failure of forming an effective protective SEI layer. As observed in SEM images (Figure 6.10c and d), a thick layer consisting of electrolyte reduction

products are coated on the surface of the electrode after only three cycles in NCE, compared to neat electrode surface under HCE (Figure 6.10e and f) and LHCE (Figure 6.10g and h). The restricted alloy reaction is also evidenced by the absence of  $K_xP$  phases in the Raman spectra since nearly all the discharge capacity arises from electrolyte reduction. In sharp contrast, a high reversible capacity of  $536 \text{ mAh g}^{-1}$  with ICE of 69.5% is achieved in HCE (Figure 6.9b).

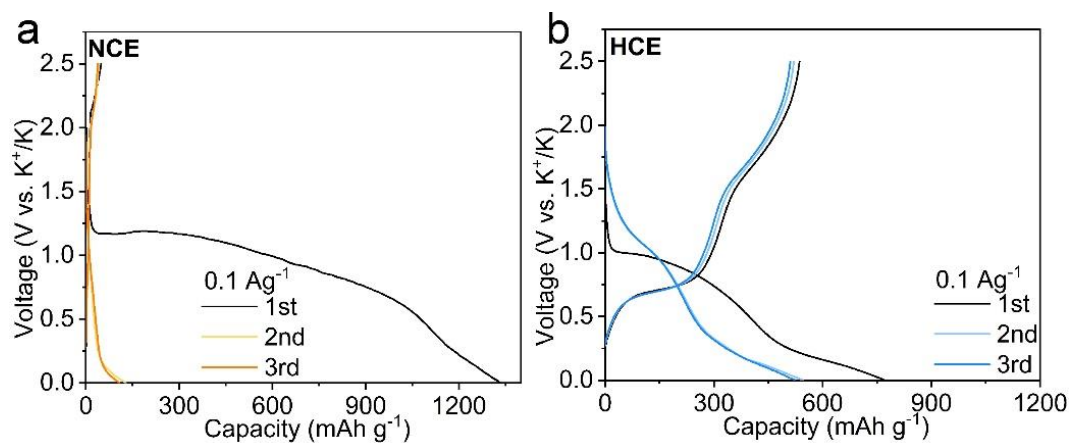


Figure 6.9 The selected galvanostatic discharge-charge profiles of BP/G electrodes under  $0.1 \text{ A g}^{-1}$  in (a) NCE and (b) HCE.

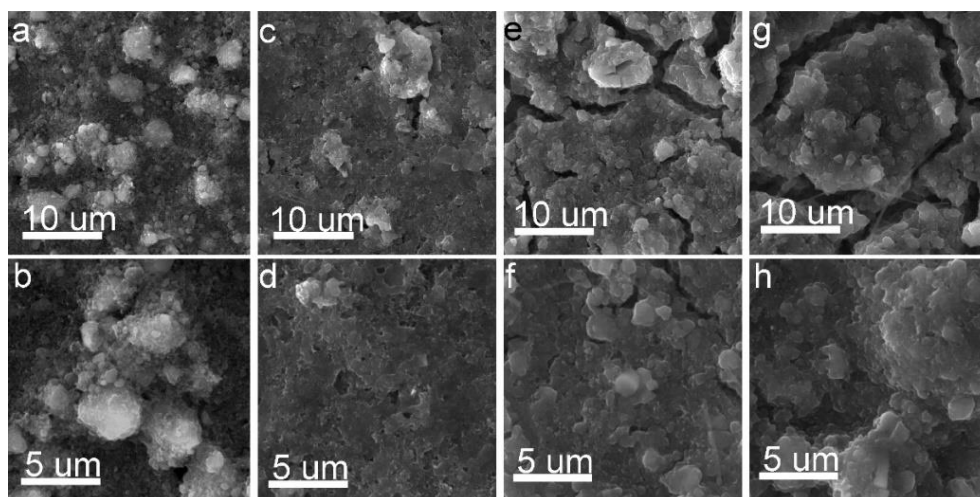


Figure 6.10 SEM images of BP/G electrode: (a-b) pristine; cycled three times in (c-d) NCE, (e-f) HCE and (g-h) LHCE.

Moreover, the performance can be further enhanced by adopting LHCE. The voltage profiles consist of two charge plateaus at around 0.70 V and 1.61 V, contributing to an accumulated capacity of  $668 \text{ mAh g}^{-1}$  with 70.8% ICE (Figure 6.11a). The improved specific capacity can be attributed to the higher ionic conductivity of LHCE than HCE, as discussed before. To quantify the K ion storage capacity of BP in BP/G composite, the ball-milled graphite electrodes are tested in LHCE (Figure 6.12a and b), which shows a low charge capacity of  $83 \text{ mAh g}^{-1}$  under  $0.1 \text{ A g}^{-1}$ . It can be calculated that about  $814 \text{ mAh g}^{-1}$  is contributed by BP, equivalent to 0.94 K ion per P atom participated in the alloying reaction. It is worth mentioning that the ball-milled BP electrodes without graphite cannot deliver such high specific capacity even in LHCE (Figure 6.12c and d). It emphasizes the synergistic effect of BP and graphite in achieving a high capacity and stable performance. The well overlapped discharge-charge curves of BP/G electrode in HCE and LHCE suggest stable cyclic performances. BP/G electrode presents a capacity of  $618 \text{ mAh g}^{-1}$  with 92.7% retention after 70 cycles in LHCE under  $0.1 \text{ A g}^{-1}$  (Figure 6.11b), which outperforms the  $399 \text{ mAh g}^{-1}$  in HCE and is among the highest values achieved in P-based anodes (Table 6.1).

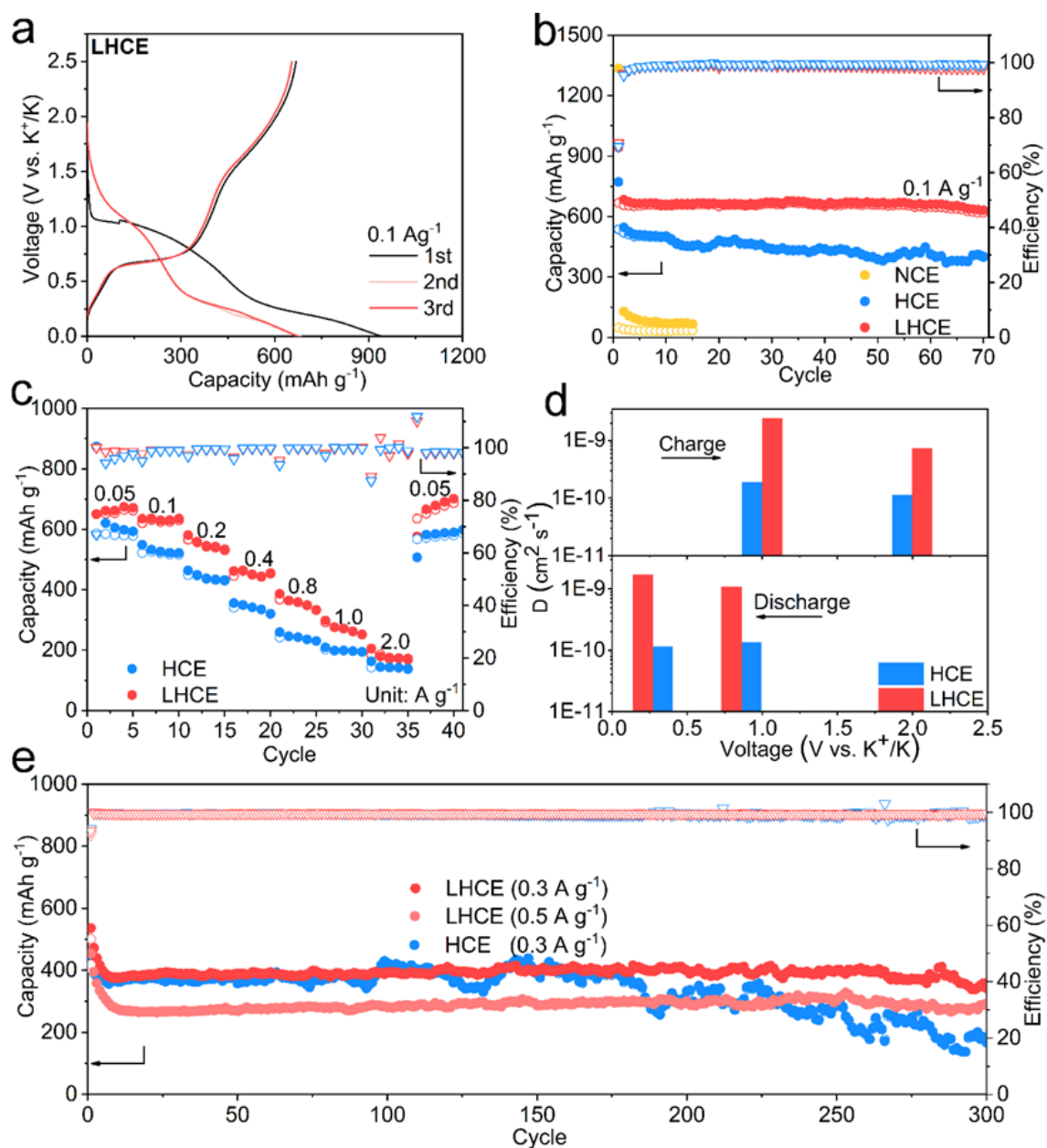


Figure 6.11 The electrochemical performances of BP/G. (a) Voltage profiles under  $0.1 \text{ A g}^{-1}$  in LHCE; (b) Cyclic performance under  $0.1 \text{ A g}^{-1}$  in NCE, HCE, and LHCE; (c) rate capability in HCE and LHCE; (d) Diffusion constant values derived from the CV profiles (Figure 6.13); (e) Long-term cyclic performances in corresponding electrolytes.

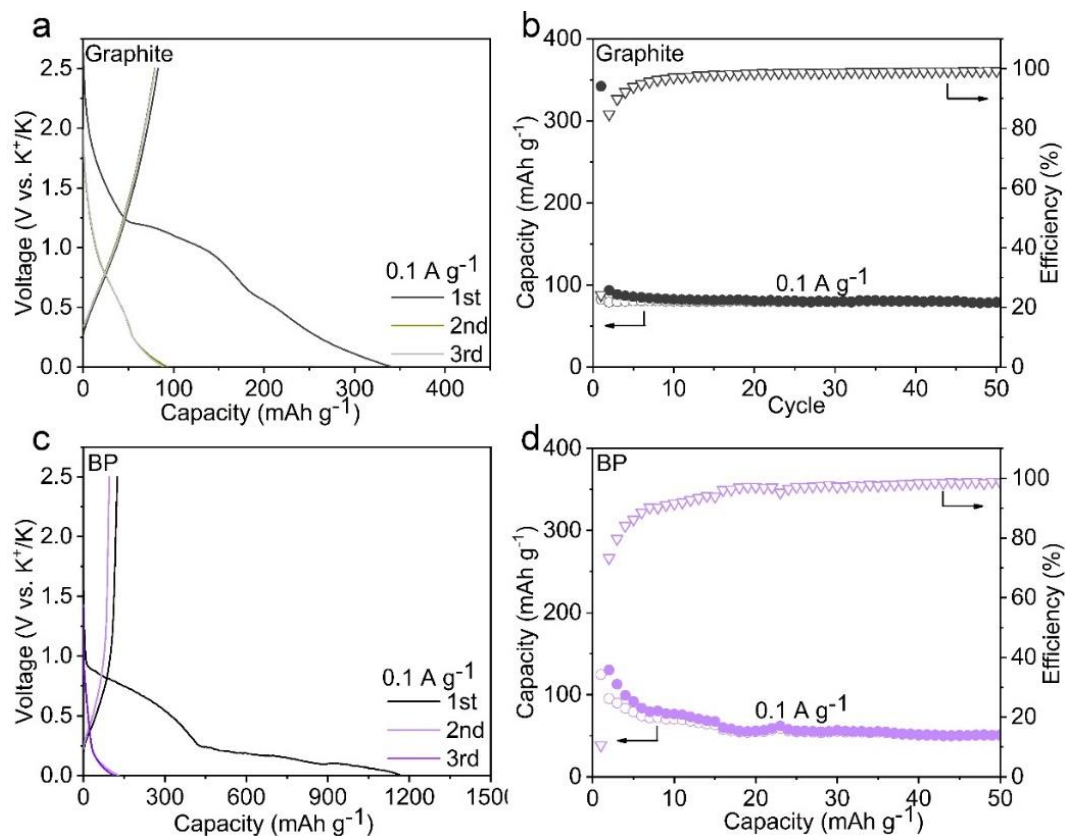


Figure 6.12 The selected galvanostatic discharge-charge profiles and corresponding cyclic performances of (a-b) ball milled graphite and (c-d) ball milled BP electrodes under  $0.1 \text{ A g}^{-1}$  in LHCE.

Table 6.1 The electrochemical performance of reported RP or BP composites in PIBs.

Electrodes	Electrolytes	ICE	Current density ( $\text{mA g}^{-1}$ )	Capacity ( $\text{mAh g}^{-1}$ ) (cycle number)	Ref.
BP/G <sup>a</sup>	KFSI/TMP/HFE=1:1.7:2 by mol.	70.78%	100	618.4 (70)	This work
			300	341.8 (300)	
BP/G <sup>b</sup>			125	773 (70)	
			375	427.3 (300)	
BP-C 7:3 <sup>c</sup>	0.6M (1:1)	KPF <sub>6</sub> /ECDEC 67%	50	30 (100)	<sup>87</sup>

P <sub>2</sub> @NSGCNT <sup>b</sup>	1M KPF <sub>6</sub> /ECDEC (1:1)	67.4%	100	514 (200)	270
			2000	319 (1000)	
H-P@NCNS/NCNT <sup>c</sup>	1M KFSI/DME	73%	500	561 (100)	268
BP-G <sup>b</sup>	1M KPF <sub>6</sub> /ECDEC (1:1)	~64%	250	600 (50)	88
RP/MoS <sub>2</sub> (2: 1) <sup>c</sup>	0.8M KPF <sub>6</sub> /ECDEC (1:1)	25.9%	1000	118 (500)	298
P@RGO <sup>c</sup>	0.8M KPF <sub>6</sub> /ECDEC (1:1)	52.6%	100	366.6 (50)	299
P-CP2 <sup>a</sup>	1M KFSI/ECDEC (1:1)	58.8%	200	512 (200)	111
P@TBMC-2.4 <sup>a</sup>	0.6M KPF <sub>6</sub> /ECPC (1:1)	63.5%	500	244 (200)	272
P@CN <sup>b</sup>	0.8M KPF <sub>6</sub> /ECDEC (1:1)	59%	100	427.4 (40)	271
P50@ZCRod-0.025 <sup>a</sup>	2.4M KFSI/EC EMC (1:1)	78.5%	100	401.8 (75)	300
Red P@N-PHCNFs <sup>c</sup>	0.7M KFSI/ECDEC (1:1)	34.8%	100	650 (100)	106
			1000	533 (200)	
RP/C <sup>b</sup>	1M KTFSI/ECDEC (1:1)	68.26%	1000	~300 (60)	104

<sup>a</sup>The capacities are calculated by the total weight of active P and carbon; <sup>b</sup>The capacities are calculated by the weight of P; <sup>c</sup>The capacity calculation methods are not mentioned.

Compared to HCE, much higher rate capacities are obtained in LHCE at increasing current density from 0.05 to 2.0 A g<sup>-1</sup> (Figure 6.11c). The CV scans at different rates (Figure 6.13) are carried out to calculate the K ion diffusion coefficient according to the Randles-Sevcik equation. The results show the values in LHCE are about an order of magnitude higher than those in HCE (Figure 6.11d), indicating faster ion transfer in the former electrolyte.

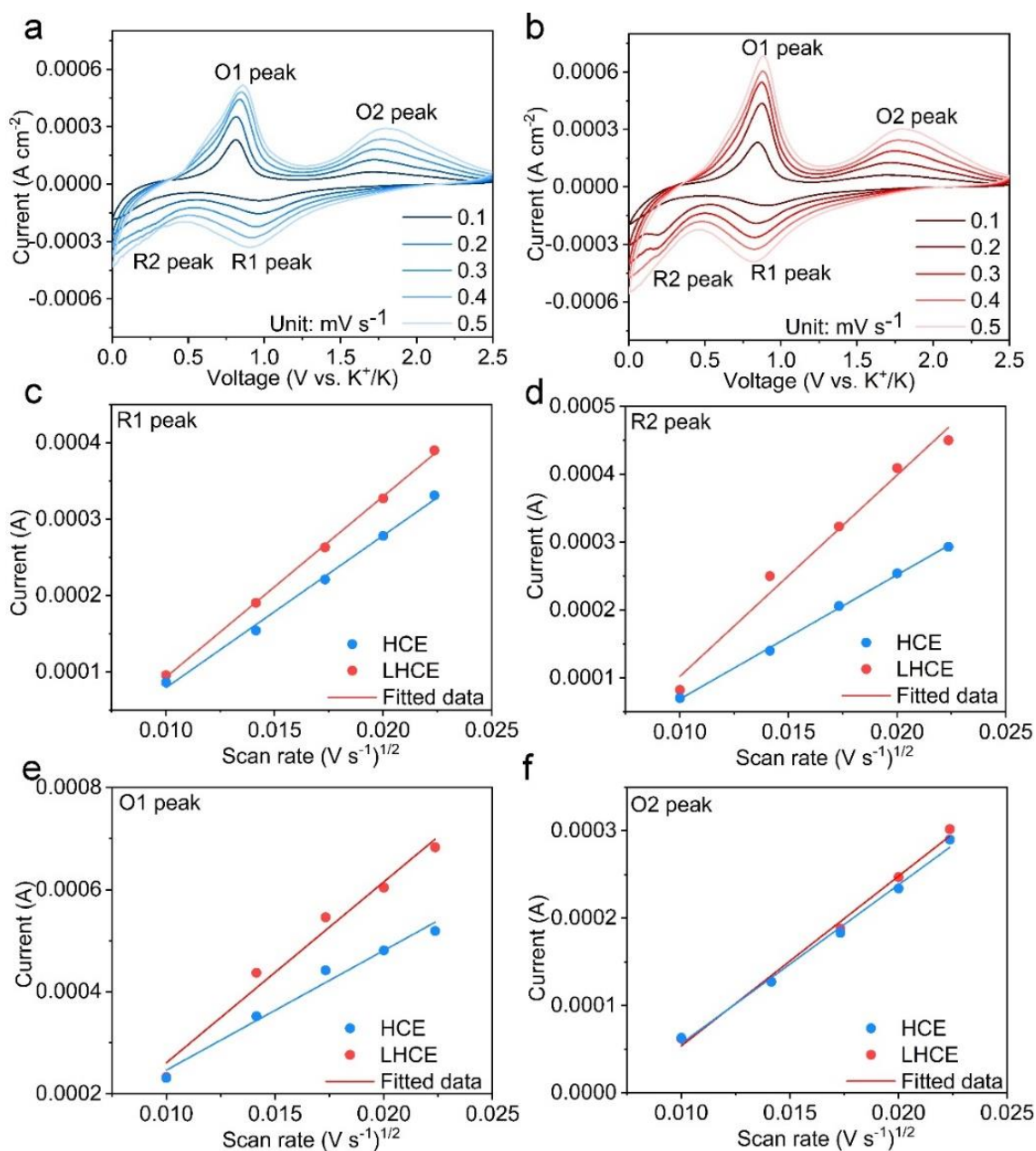


Figure 6.13 CV rate curves of BP/G electrodes in (a) HCE and (b) LHCE; Fitting results of peak current  $i_p$  (A) vs. the square root of scan rate  $v^{1/2}$  (V s<sup>-1</sup>)<sup>1/2</sup> for (c) R1, (d) R2, (e) O1 and (f) O2 peaks (R for reduction and O for oxidation).

The electrochemical impedance spectroscopy (EIS) is performed to further study the kinetics behavior of the interphase formed in HCE and LHCE. As shown in Figure 6.14 and Table 6.2, close resistances of charge transfer ( $R_{ct}$ ) in HCE (5197  $\Omega$ ) and LHCE (5106  $\Omega$ ) are obtained for the cells at OCV state, and the values separately decrease to 628.2 and 627.4  $\Omega$  after building

SEI. Nevertheless, the SEI ( $R_{SEI}$ ) resistance in LHCE is much smaller than the one in HCE (134.6 vs. 756.2  $\Omega$ ), confirming the faster charge transfer kinetics in the designed LHCE. Furthermore, the long-term cycling of BP/G composite is conducted to evaluate the electrochemical stability (Figure 6.11e). Outstanding cyclic performances are obtained when LHCE is employed, achieving a high reversible capacity of 342 and 291  $\text{mAh g}^{-1}$  over 300 cycles under 0.3 and 0.5  $\text{A g}^{-1}$ , respectively. In contrast, there is apparent capacity degradation and fluctuation in the HCE after 200 cycles, dropping to 168  $\text{mAh g}^{-1}$  in the 300th cycle under 0.3  $\text{A g}^{-1}$ .

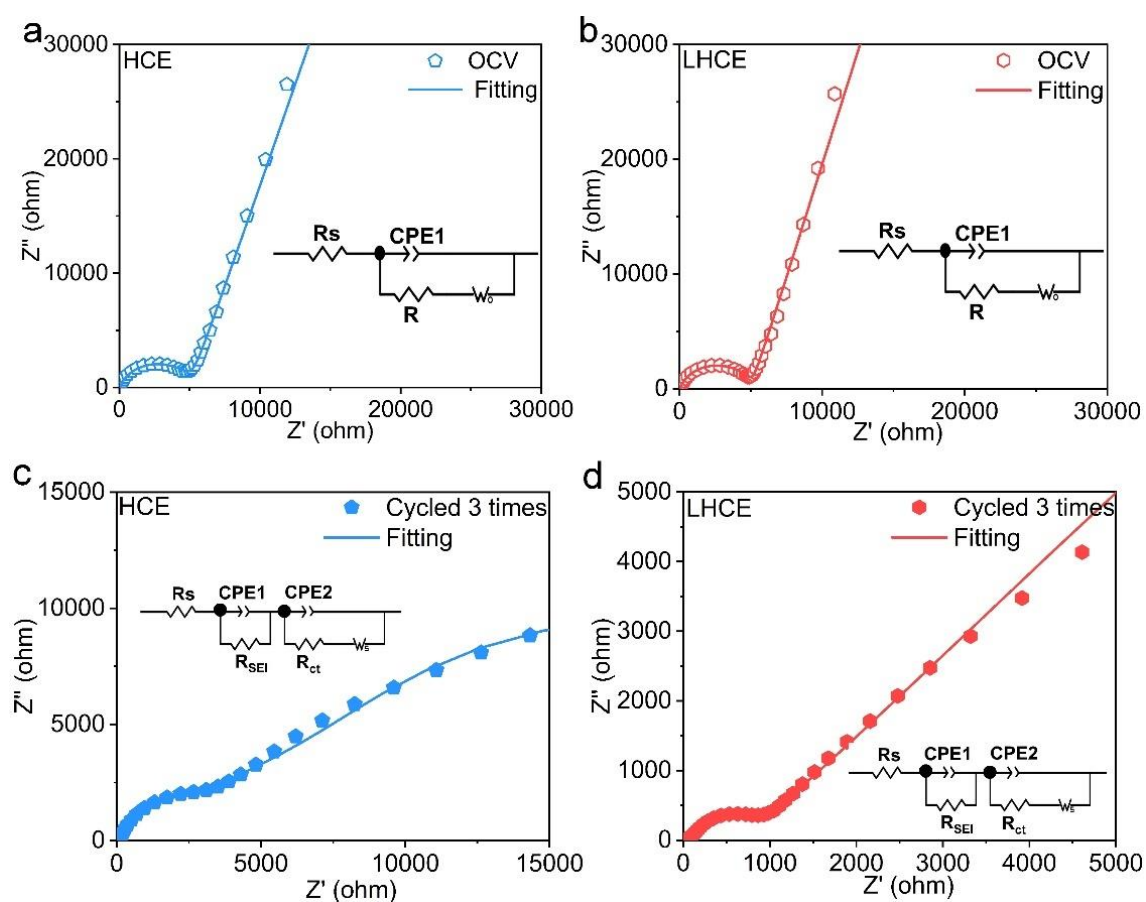


Figure 6.14 The Nyquist plots of the BP/G electrodes at OCV state in (a) HCE and (b) LHCE; cycled three times in (c) HCE and (d) LHCE.

Table 6.2 Cell resistance ( $R_s$ ) and charge transfer resistance ( $R_{ct}$ ) resistance of SEI of BP/G electrodes from equivalent circuit fitting of experimental data in Figure 6.14.

State	Electrolytes	$R_s$	$R_{SEI}$	$R_{ct}$
OCV	HCE	40.08	-	5197
	LHCE	40.99	-	5106
3rd	HCE	46.81	756.2	628.2
	LHCE	40.05	134.6	627.4

The well-designed LHCE can be further extended to improve the stability of RP/G in PIBs and BP/G in SIBs. The performance of RP/G composites is evaluated in the as-developed LHCE electrolyte (Figure 6.15), which shows decent cyclic stability and confirms the benefits of LHCE. Nevertheless, the performance is inferior to the BP/G with LHCE in PIBs owing to the better conductivity of BP than RP. These results highlight the advantages of BP/G composite anode and the proposed electrolyte. Na-LHCE for SIBs, *i.e.*, NaFSI/TMP/HFE with a molar ratio of 1: 1.7: 2 was also prepared, following the same formulation as the K counterpart but replacing the KFSI by NaFSI. It is a delight to find that the Na-LHCE could also benefit the BP/G for Na ion storage, thus partly demonstrate the general advantages of such an electrolyte formulation. However, it needs to further optimization in the electrolyte formulation for specific application in SIBs.

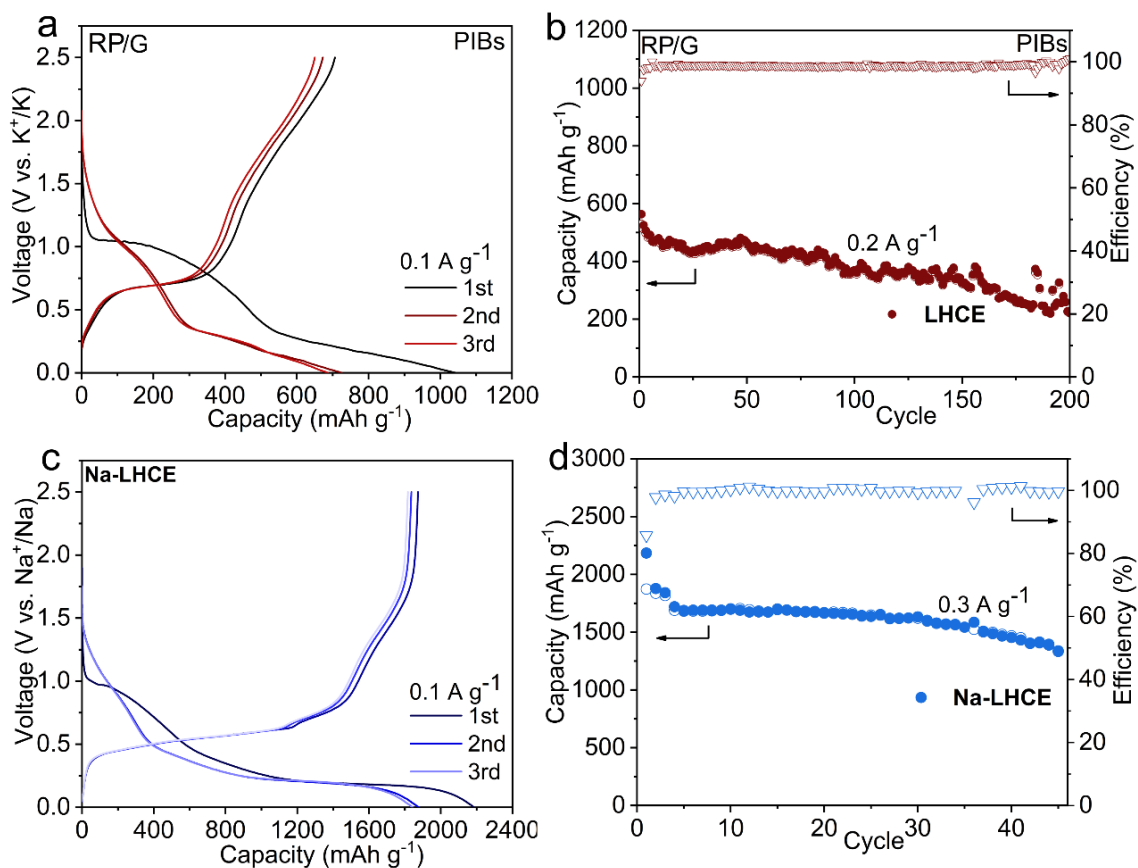


Figure 6.15 The selected galvanostatic discharge-charge profiles and corresponding cyclic performances of (a) and (b) RP/G in PIBs and (c) and (d) BP/G in SIBs.

### 6.2.5 Full cell demonstration

Furthermore, the full cell performance in LHCE is demonstrated using the BP/G anode and a Prussian blue  $K_xMnFe(CN)_6$  ( $0 \leq x \leq 2$ ) cathode. The structure of  $K_xMnFe(CN)_6$  has a monoclinic phase (ICSD#151697) (Figure 6.16a). The  $K_xMnFe(CN)_6$  half cell shows two discharge plateaus at about 4.0 and 3.9 V, leading to a cumulative capacity of  $122 \text{ mAh g}^{-1}$  (Figure 6.16b and c). The full cell delivers a considerable capacity of  $82 \text{ mAh g}^{-1}$  (based on the total mass of anode and cathode) with a decent rate capability at a current density up to  $0.5 \text{ A g}^{-1}$  (Figure 6.16d and e). A capacity of  $77 \text{ mAh g}^{-1}$  can be recovered and stabilized with a working potential of 3.01 V when the current density decreases to  $0.025 \text{ A g}^{-1}$ , giving rise to an energy density of  $233 \text{ Wh kg}^{-1}$ . This value is lower than the theoretical prediction due to the K ion consumption in the SEI formation, which may be resolved through pre-potassiation techniques, similar to

that adopted in LIBs and SIBs.<sup>132, 301</sup> Overall, these results indicate that the LHCE is fully compatible with the cathode.

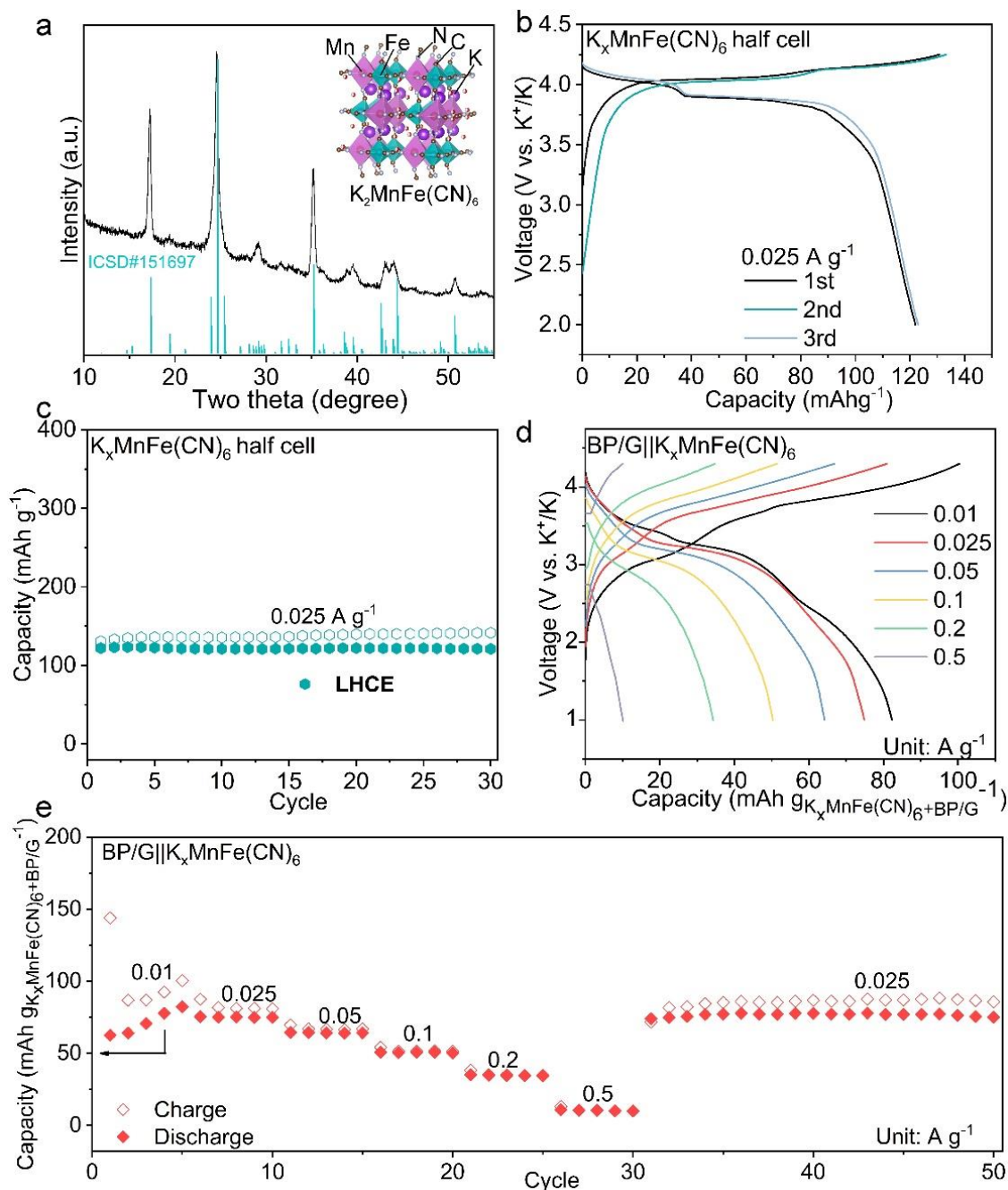


Figure 6.16 (a) The XRD pattern of  $K_xMnFe(CN)_6$  (inset: the crystal structure); (b) the selected galvanostatic discharge-charge profiles and (c) cyclic performance for  $K_xMnFe(CN)_6$  half cell in LHCE; (d) and (e) full cell performances of BP/G|| $K_xMnFe(CN)_6$  in LHCE.

### 6.2.6 Chemical compositions, nanostructure and mechanical properties of SEIs

To explore the underlying mechanism behind the electrolyte-induced enhancement, the SEI chemical compositions of the BP/G electrodes after cycling three times are investigated by XPS. As presented in the C1s and P2p spectra (Figure 6.17a-c), the SEIs consist of C-C (284.8 eV), C-OH (285.7 eV), C-O (286.7 eV), and P-O (around 133.3 eV) organic species, which are originated from the TMP decomposition. Other inorganic components are probed in F1s and S2p spectra, including K-F (683.6 eV), S-F (687.1 eV), (S=O)-N (168.3 eV), K<sub>2</sub>SO<sub>3</sub> (166.1 eV) and K<sub>2</sub>S (161.8 eV) species.<sup>63, 302</sup> In particular, the atomic concentrations of P and S elements presents significant differences in the three electrolytes. The SEI forming in NCE has the highest P content among the three but lower S content than those in HCE and LHCE (Figure 6.17d). The P and S elements in the SEI are mainly derived from the decomposition of TMP solvent and KFSI salt, respectively. That means the solvent decomposition is dominated in the low concentrated electrolyte, and more FSI<sup>-</sup> anion reduction occurs in the high concentration counterpart. The preference for FSI<sup>-</sup> anion decomposition is attributed to the lowest unoccupied molecular orbital (LUMO) shifting from solvent to anion due to the modified solvation structures of high concentration electrolytes.<sup>286</sup> Compared to the SEI in HCE, higher S content is found in the one under LHCE because HFE additive allows more FSI<sup>-</sup> anions to participate in the K ion solvation sheath, which leads to anion-derived SEI.<sup>303-304</sup> Further exploring the deconvoluted spectra (Figure 6.17d), it shows that the SEI in LHCE has more rich (S=O)-N species but less amount of classic inorganic components such as KF (1.64 vs. 3.23%), K<sub>2</sub>S (0.04% vs. 0.16%), and K<sub>2</sub>SO<sub>3</sub> (0.25% vs. 0.71%) than those in HCE counterparts.

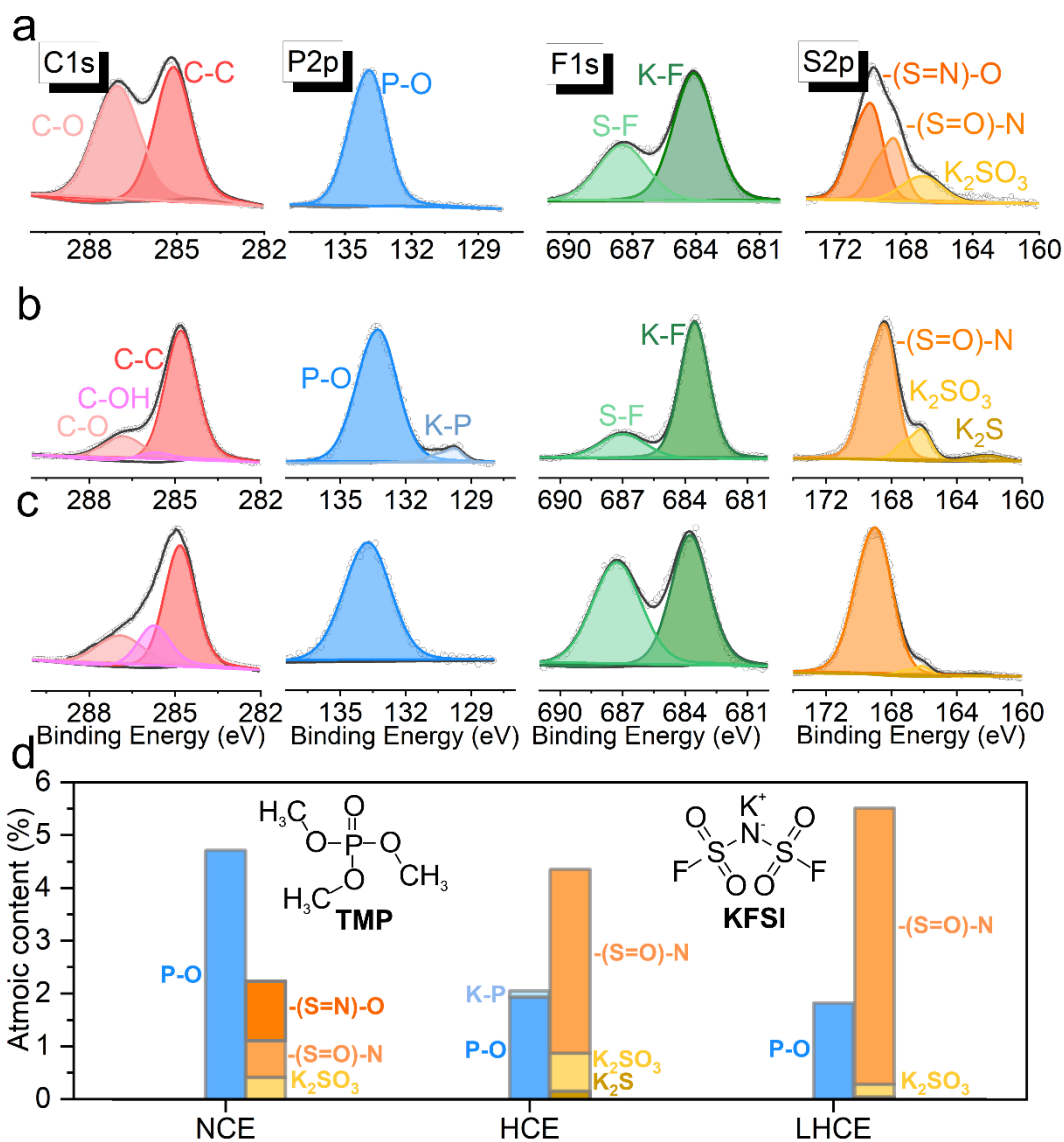


Figure 6.17 XPS Characterizations of BP/G electrodes after three cycles. C1s, P2p, F1s, and S2p spectra (a) in NCE; (b) HCE; (c) LHCE and (d) the atomic percentage of P and S elements in corresponding electrolytes.

The nanostructures of the SEIs are studied by TEM and EDS mappings to examine the morphology and elemental distribution. In NCE (Figure 6.18), the discontinuous SEI with rough and ruptured morphology is observed on the particle surface, which cannot successfully protect the electrode, leading to the overwhelming electrolyte decomposition in the first discharge. The SEI with a thickness of 17.7 and 9.4 nm is formed in HCE (Figure 6.19a and b)

and LHCE (Figure 6.19d and e), respectively. The C, O, S, F, K, and P elements show more uniform distributions in the LHCE than HCE (Figure 6.19c and f).

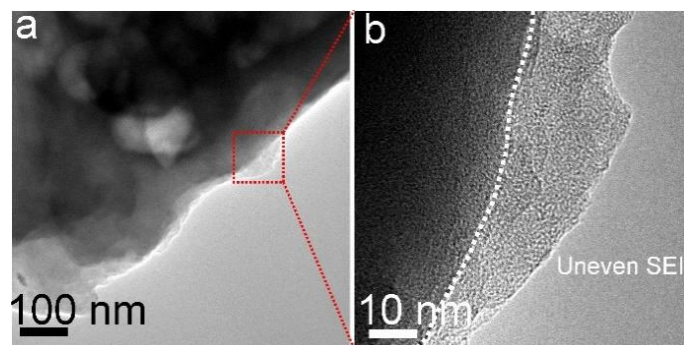


Figure 6.18 (a-b) The TEM images of BP/G after cycling three times in NCE.

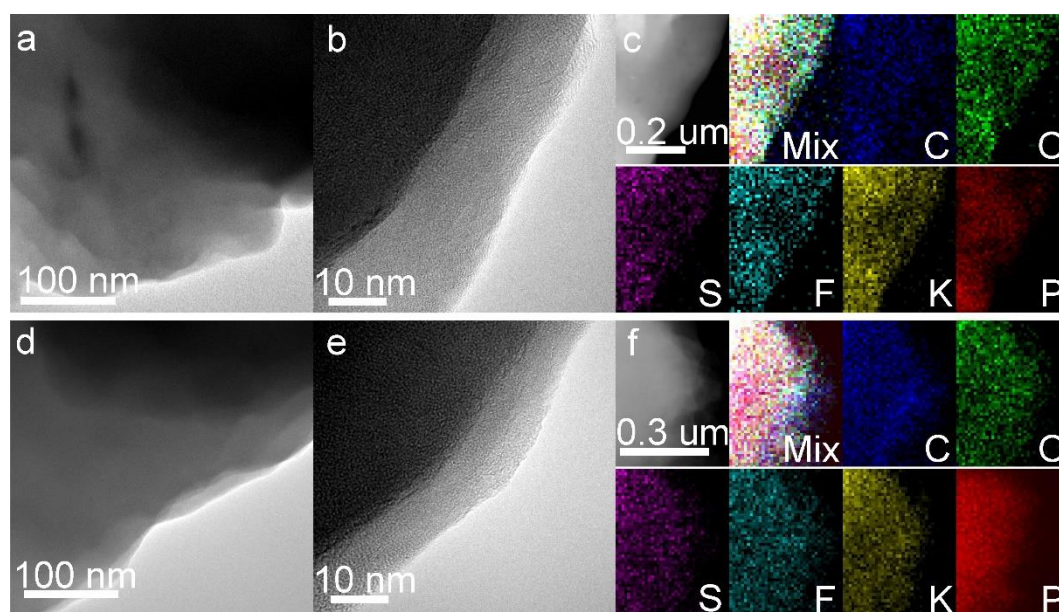


Figure 6.19 The TEM, STEM images and EDS mapping of BP/G after cycling three times in (a-c) HCE; (d-f) LHCE.

Meanwhile, the electrodes after long-term cycling are also characterized to understand the discrepancy in electrochemical cyclic stability. The thickness of the SEIs slightly increases to 22.3 nm for HCE and 12.2 nm for LHCE after 300 cycles (Figure 6.20a and c). It again confirms

the robustness of SEI subject to the deformation, successfully passivating the electrode surface to prevent the continuous SEI growth. Such stable SEI is crucial in protecting the integrity of active particles and suppressing the parasitic reactions of electrolytes. More importantly, the SEI formed in LHCE maintains excellent structural homogeneity (Figure 6.20d), while the segregation phenomenon becomes more severe for the SEI in HCE, as evidenced in the elements mixed image (Figure 6.20b).

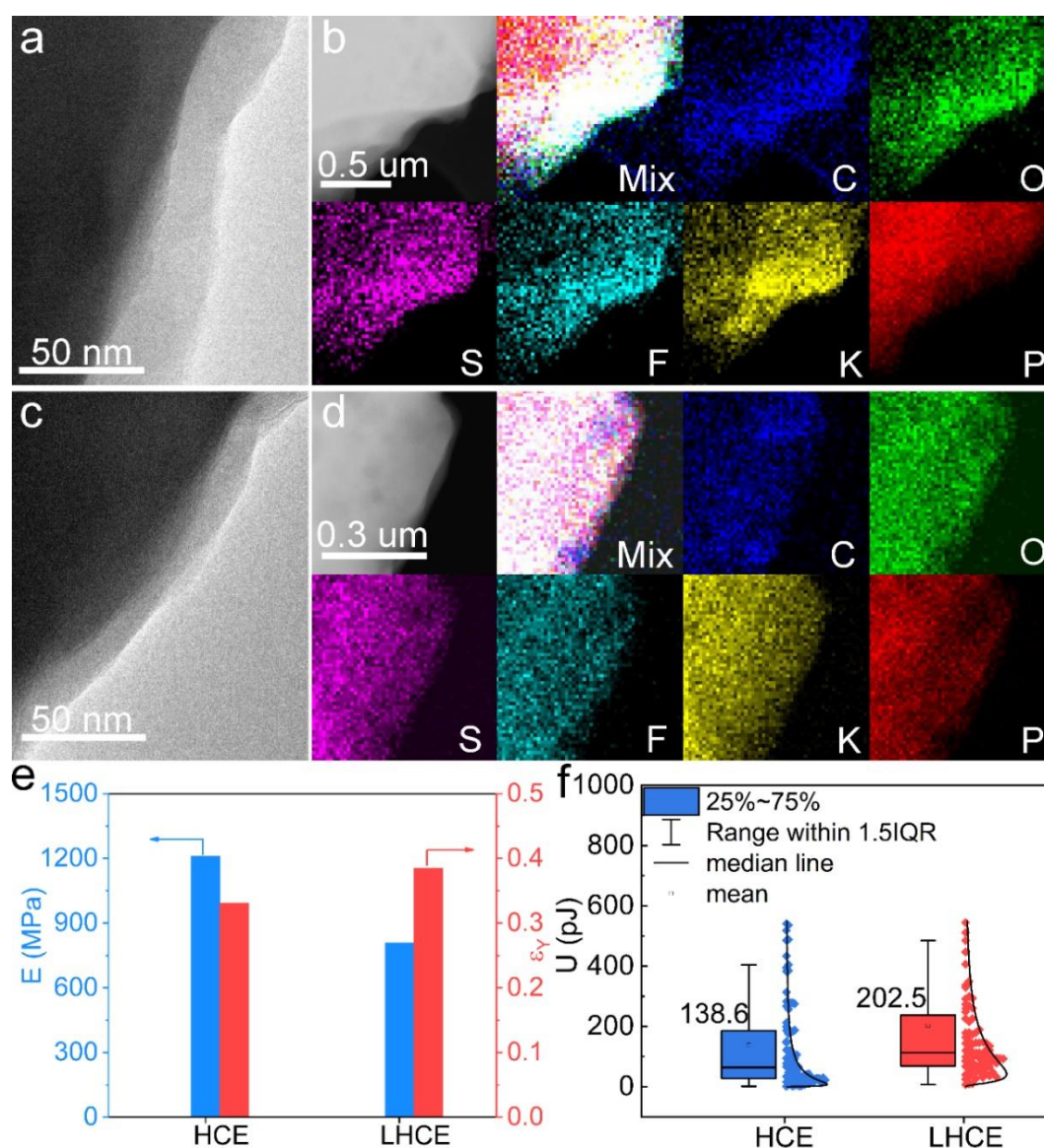


Figure 6.20 Morphologies and mechanical properties of the SEIs. The TEM, STEM images and EDS mapping after long-term cycling (300 cycles) in (a, b) HCE and (c, d) LHCE; e) Young's

modulus ( $E$ ) and elastic strain limit ( $\epsilon_Y$ ), and f) the maximum elastic deformation energy ( $U$ ) of SEIs formed in these two electrolytes.

The elemental segregation in the SEI formed under HCE may explain the inferior stability compared to LHCE. To examine the speculation, the mechanical properties of SEIs in HCE and LHCE are probed by atomic force microscopy (AFM) with eliminating the substrate's interferences. Young's modulus ( $E$ ) and elastic strain limit ( $\epsilon_Y$ ) are the most widely used parameters for evaluating the SEI's mechanical stability, and the maximum elastic deformation energy reflects their combined effect.<sup>118</sup> Elastic deformation is performed to determine the  $E$  in the 1<sup>st</sup> step AFM tests, while the SEI is intentionally fractured by applying a large indentation force in the 2<sup>nd</sup> step to calculate  $\epsilon_Y$ . At least 90 points are measured to increase the accuracy of the test. A larger  $E$  of 1210 MPa is attained for the SEI build in HCE than the counterpart (810 MPa) in LHCE (Figure 6.20e). The reason lies in the presence of abundant KF (29 GPa),  $K_2SO_3$  (45 GPa), and  $K_2S$  (19 GPa) components with high stiffness in HCE. Nevertheless, the SEI in LHCE shows higher  $\epsilon_Y$  than the one in HCE, attributed to the homogenous composition with reduced stress concentration. Combined the effects of  $E$  and  $\epsilon_Y$ , the parameter  $U$  (proportional to  $E \cdot \epsilon_Y^5$ ), is used to appraise the mechanical stability of SEI. The SEI formed in LHCE shows a large  $U$  of 202.5 pJ, almost two times higher than that in HCE (Figure 6.20f). The results indicate the better mechanical properties of the SEI in LHCE for accommodating the deformation to realize long lifespan BP/G electrode.

### 6.3 Summary

We prepare the BP/G electrode as advanced anodes in PIBs via a facile two-step ball milling approach. HEBM is adopted to transfer the RP into BP, which is mixed with graphite to obtain BP/G composite with a high BP loading of 80 wt.%. The electrode fails to deliver a decent reversible capacity in a standard concentration TMP-based electrolyte (1M). Increasing the concentration to 5 M essentially boosts the reversibility, albeit the rate capability remains poor due to low ionic conductivity. Therefore, LHCE (KFSI/TMP/HFE with a molar ratio of 1: 1.7: 2) is designed to resolve the long-term stability and rate performance. The electrode presents a high reversible and stable capacity of 342 mAh  $g^{-1}$  over 300 cycles under 0.3 A  $g^{-1}$  with the

---

assistance of LHCE. Such an improvement roots in the enhanced ionic conductivity and the building of a robust SEI. We summarize the essential roles of SEI in governing the electrochemical behavior as follows:

- i) The absence of an effective SEI in NCE leads to negligible reversible capacity because of the copious electrotype decomposition.
- ii) The electrode shows a high reversible capacity in HCE but suffers from capacity degradation in long-term cycles. The inhomogeneous SEI with apparent elemental segregation reduces the yield strain.
- iii) The building of an inorganic component rich SEI with uniform elemental distribution boosts the BP/G performance in the LHCE. On the one hand, the conformal SEI layer effectively prevents parasite reactions on the electrode surface. On the other hand, the homogenous SEI renders superb mechanical stability for accommodating deformation, as reflected by the large maximum elastic deformation energy.

Lastly, we demonstrate that the electrolyte is fully compatible with the cathode, thus promoting the application of advanced PIBs with high-capacity BP anodes.

## Chapter 7

### Conclusions and future work

This chapter summarizes the main results of this thesis and discusses the remaining issues for future studies.

#### 7.1 Conclusions

Several anode materials are explored to understand the K ion insertion chemistry and design high-performance anodes for boosting the energy density of potassium ion batteries (PIBs). The phase transition and structural evolution of MoS<sub>2</sub>, Sb, and P are systematically studied through complementary experimental investigation and theoretical simulations. Furthermore, robust SEIs are built via developing novel electrolyte formulation, realizing stable cycling of high-capacity anodes. The nanostructure and mechanical properties of the solid electrolyte interphases (SEIs) are probed to establish a structure-property correlation for guiding SEI design in advanced anodes. Four major findings drawn from this thesis are highlighted in the following:

(1) The *in situ* insertion behavior of Li, Na and K ions into MoS<sub>2</sub>/nanofiber are compared by real time TEM. The results show the largest volume expansion of about 140% occurs in K ion incorporation, but most layered compounds are preserved owing to a large ratio of intercalation reaction during K ions uptake. However, layered MoS<sub>2</sub> mostly collapses upon Li and Na insertion because of the dominated conversion reaction. The phase transition processes of MoS<sub>2</sub> toward K ion insertion are then explored by *in situ* XRD, which reveals a pathway of MoS<sub>2</sub>→K<sub>0.4</sub>MoS<sub>2</sub>→K<sub>0.5</sub>MoS<sub>2</sub>→K<sub>1.0</sub>MoS<sub>2</sub>. The layered K<sub>1.0</sub>MoS<sub>2</sub> phase is found in the fully discharged state, suggesting the intercalation reaction occurs even being discharged to 0 V. Such a layered compound supports the frame structure against collapse, enabling the stable cyclic performance of micro-sized MoS<sub>2</sub>.

(2) To stabilize Sb microparticles, novel ether-based electrolytes (1 M KFSI/EGDDE and 1 M KFSI/THF) are designed to replace the conventional carbonate electrolytes. The microsized Sb anode presents a high reversible capacity of 573 mAh g<sup>-1</sup> under 0.1 A g<sup>-1</sup> over 180 cycles and decent rate performance of 225 mAh g<sup>-1</sup> under 3.3 A g<sup>-1</sup> in 1 M KFSI/EGDDE. The phase transformation during K-Sb alloy/de-alloy is disclosed as Sb → K<sub>1</sub>Sb → cubic K<sub>3</sub>Sb and hexagonal K<sub>3</sub>Sb. A thinner and amorphous SEI with abundant oligomer-like species is built in ether base electrolyte. The nanoindentation tests reveal that the elastic strain limit of ether-derived SEI is twice that in the carbonate-based electrolyte, which helps to constrain the particles from pulverization and reinforce the electrochemical stabilities.

(3) The concept of ether-derived SEI is extended to the Sn microsized particles in SIBs. The Sn anode shows a high reversible capacity of 669 (in 1 M NaPF<sub>6</sub>/EGDDE) and 786 mAh g<sup>-1</sup> (in 1 M NaPF<sub>6</sub>/THF) after 100 cycles under 0.2 A g<sup>-1</sup>. The improved cyclic stability is closely related to the SEIs. The SEI presents an ultrathin (~3 nm) thickness with high maximum elastic deformation energy in the ether-based electrolyte. In contrast, many inorganic particles with high crystallinity are shown in the SEI in the carbonate-based electrolyte, reducing the capability of accommodating the deformation. In addition, the small thickness of SEI facilitates the fast Na ion transfer for rate performance.

(4) Black phosphorus and graphite (BP/G) composite with a high BP loading of 80 wt.% is synthesized by ball milling. A nonflammable trimethyl phosphate (TMP)-based electrolyte is developed for stabilizing the composite anode. It shows negligible reversible capacity in normal concentration (1 M) electrolyte due to the absence of effective SEI. In comparison, a considerable capacity of 399 mAh g<sup>-1</sup> under 0.1 A g<sup>-1</sup> is observed in high concentrate (5 M) electrolyte. Furthermore, a fluorinated ether diluent is incorporated to prepare a localized high concentration electrolyte (LHCE) to reduce viscosity. In LHCE, BP/G electrode presents a high capacity of 618 mAh g<sup>-1</sup> over 70 cycles under 0.1 A g<sup>-1</sup> and a stable capacity of 342 mAh g<sup>-1</sup> over 300 cycles under 0.3 A g<sup>-1</sup>.

## 7.2 Future work

Upon completion of this thesis, there are still great challenges for the practical application of high-capacity anodes in PIBs. The major issues are summarized in the following, which may be adopted in future studies:

### (1) Low ICE

Although the micro-sized active materials are used to reduce the active interfaces with the electrolyte, the ICEs are still lower than 80% (Figure 7.1a). Apart from SEI formation, the low ICEs can also be caused by parasite reactions, such as the trapping of K ions. A low ICE will significantly consume the K ions provided by the cathode in the full cells, remarkably decreasing the energy density. On the one hand, the electrode and electrolyte should be optimized to further increase the ICE. On the other hand, facile pre-potassium methods are required to compensate for the K ions loss in the first cycle, which are widely adopted in LIBs technologies.

### (2) General approach of SEI formation

Building robust SEIs in classic electrolytes and general electrodes. The SEI is mainly generated by the electrochemical reductions of solvent and salt. Ether-based electrolytes have shown significant advantages over classic carbonate counterparts in building mechanically stable SEI for alloy and metal anodes. However, the ether solvent suffers from oxidative stability at the cathode side, limiting its application in full cells. It remains unclear how to build such a SEI in carbonate electrolytes. The resolved structure-property correlation of SEI in this thesis may provide some guidance. Furthermore, the SEI could also be affected by the surface functionalities of the electrode materials, which are largely ignored in previous studies. For instance, the EGDEE-based electrolyte (1 M KFSI in EGDEE) is only effective for the Sb material. Fast decays are observed in the same electrolyte formula when changing to Sn, Bi and Si anodes (Figure 7.1b). The possible reasons can be summarized as follows: Firstly, electrochemical potentials of the electrodes may have big influences on the electrolyte's decomposition. Secondly, the phase and morphologies of anode materials can also alter the electrochemical reductions of the electrolytes. Thirdly, the surface properties of the anodes can also affect the products electrolytes reductions. The electrolytes decomposition pathways can be regarded as catalytic reactions using anode as catalyst, which will form various SEIs with

different anode materials, making more challenging to find a general electrolytes formulation for the anodes. Such information is somehow lacked currently, which is essential to generalize the SEI strategy to other anodes.

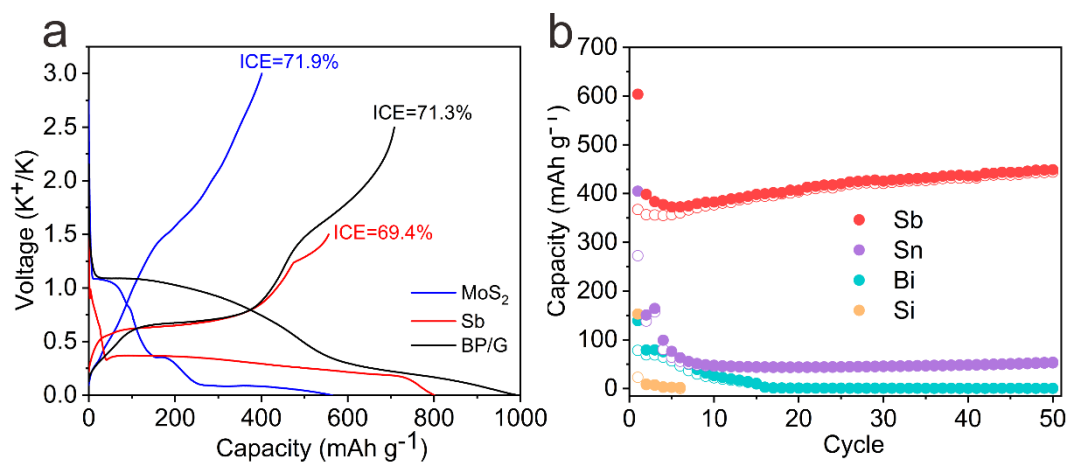


Figure 7.1 (a) The first charge and discharge curves for MoS<sub>2</sub>, Sb and BP/G in PIBs. (b) Cyclic performances of microsized Sb, Sn, Bi, Si electrodes under 0.1 A g<sup>-1</sup> in 1 M KFSI/EGDDE for PIBs.

---

## Reference

1. Tarascon, J.-M.; Armand, M., Issues and challenges facing rechargeable lithium batteries. *Mater. Sustain. Energy* **2011**, 171-179.
2. Larcher, D.; Tarascon, J. M., Towards greener and more sustainable batteries for electrical energy storage. *Nat. Chem.* **2015**, 7 (1), 19-29.
3. Goodenough, J. B.; Kim, Y., Challenges for rechargeable Li batteries. *Chem. Mater.* **2010**, 22 (3), 587-603.
4. Whittingham, M. S., Lithium batteries and cathode materials. *Chem. Rev.* **2004**, 104 (10), 4271-4302.
5. Hirsh, H. S.; Li, Y.; Tan, D. H.; Zhang, M.; Zhao, E.; Meng, Y. S., Sodium-ion batteries paving the way for grid energy storage. *Adv. Energy Mater.* **2020**, 10 (32), 2001274.
6. Pramudita, J. C.; Sehwat, D.; Goonetilleke, D.; Sharma, N., An initial review of the status of electrode materials for potassium-ion batteries. *Adv. Energy Mater.* **2017**, 7 (24), 1602911.
7. Huie, M. M.; Bock, D. C.; Takeuchi, E. S.; Marschilok, A. C.; Takeuchi, K. J., Cathode materials for magnesium and magnesium-ion based batteries. *Coord. Chem. Rev.* **2015**, 287, 15-27.
8. Lin, M.-C.; Gong, M.; Lu, B.; Wu, Y.; Wang, D.-Y.; Guan, M.; Angell, M.; Chen, C.; Yang, J.; Hwang, B.-J., An ultrafast rechargeable aluminium-ion battery. *Nature* **2015**, 520 (7547), 324-328.
9. Fang, G.; Zhou, J.; Pan, A.; Liang, S., Recent advances in aqueous zinc-ion batteries. *ACS Energy Lett.* **2018**, 3 (10), 2480-2501.
10. Kim, S.; Yin, L.; Lee, M. H.; Parajuli, P.; Blanc, L.; Fister, T. T.; Park, H.; Kwon, B. J.; Ingram, B. J.; Zapol, P., High-voltage phosphate cathodes for rechargeable Ca-ion batteries. *ACS Energy Lett.* **2020**, 5 (10), 3203-3211.
11. Hwang, J. Y.; Myung, S. T.; Sun, Y. K., Recent progress in rechargeable potassium batteries. *Adv. Funct. Mater.* **2018**, 28 (43), 1802938.
12. Wu, Z.; Zou, J.; Chen, S.; Niu, X.; Liu, J.; Wang, L., Potassium-ion battery cathodes: Past, present, and prospects. *J. Power Sources* **2021**, 484, 229307.

13. Dhir, S.; Wheeler, S.; Capone, I.; Pasta, M., Outlook on K-ion batteries. *Chem* **2020**.
14. Moon, H.; Mandai, T.; Tataru, R.; Ueno, K.; Yamazaki, A.; Yoshida, K.; Seki, S.; Dokko, K.; Watanabe, M., Solvent activity in electrolyte solutions controls electrochemical reactions in Li-ion and Li-sulfur batteries. *J. Phys. Chem. C* **2015**, *119* (8), 3957-3970.
15. Zhou, M.; Bai, P.; Ji, X.; Yang, J.; Wang, C.; Xu, Y., Electrolytes and Interphases in Potassium Ion Batteries. *Adv. Mater.* **2021**, *33* (7), 2003741.
16. Eftekhari, A.; Jian, Z.; Ji, X., Potassium Secondary Batteries. *ACS Appl. Mater. Interfaces* **2017**, *9* (5), 4404-4419.
17. Eftekhari, A., Potassium secondary cell based on Prussian blue cathode. *J. Power Sources* **2004**, *126* (1-2), 221-228.
18. Xue, L.; Li, Y.; Gao, H.; Zhou, W.; Lü, X.; Kaveevivitchai, W.; Manthiram, A.; Goodenough, J. B., Low-cost high-energy potassium cathode. *J. Am. Chem. Soc.* **2017**, *139* (6), 2164-2167.
19. Deng, L.; Qu, J.; Niu, X.; Liu, J.; Zhang, J.; Hong, Y.; Feng, M.; Wang, J.; Hu, M.; Zeng, L., Defect-free potassium manganese hexacyanoferrate cathode material for high-performance potassium-ion batteries. *Nat. Commun.* **2021**, *12* (1), 1-9.
20. Kim, H.; Kim, J. C.; Bo, S. H.; Shi, T.; Kwon, D. H.; Ceder, G., K-ion batteries based on a P2-type  $K_{0.6}CoO_2$  cathode. *Adv. Energy Mater.* **2017**, *7* (17), 1700098.
21. Vaalma, C.; Giffin, G. A.; Buchholz, D.; Passerini, S., Non-Aqueous K-Ion Battery Based on Layered  $K_{0.3}MnO_2$  and Hard Carbon/Carbon Black. *J. Electrochem. Soc.* **2016**, *163* (7), A1295-A1299.
22. Kim, H.; Seo, D. H.; Kim, J. C.; Bo, S. H.; Liu, L.; Shi, T.; Ceder, G., Investigation of Potassium Storage in Layered P3-Type  $K_{0.5}MnO_2$  Cathode. *Adv. Mater.* **2017**, *29* (37).
23. Kim, H.; Seo, D.-H.; Urban, A.; Lee, J.; Kwon, D.-H.; Bo, S.-H.; Shi, T.; Papp, J. K.; McCloskey, B. D.; Ceder, G., Stoichiometric layered potassium transition metal oxide for rechargeable potassium batteries. *Chem. Mater.* **2018**, *30* (18), 6532-6539.
24. Liao, J.; Hu, Q.; Yu, Y.; Wang, H.; Tang, Z.; Wen, Z.; Chen, C., A potassium-rich iron hexacyanoferrate/dipotassium terephthalate@carbon nanotube composite used for K-ion full-cells with an optimized electrolyte. *J. Mater. Chem. A* **2017**, *5* (36), 19017-19024.
25. Han, J.; Li, G.-N.; Liu, F.; Wang, M.; Zhang, Y.; Hu, L.; Dai, C.; Xu, M., Investigation of  $K_3V_2(PO_4)_3/C$  nanocomposites as high-potential cathode materials for potassium-ion batteries. *Chem. Commun.* **2017**, *53* (11), 1805-1808.

- 
26. Jin, T.; Li, H.; Zhu, K.; Wang, P.-F.; Liu, P.; Jiao, L., Polyanion-type cathode materials for sodium-ion batteries. *Chem. Soc. Rev.* **2020**, *49* (8), 2342-2377.
27. Lin, X.; Huang, J.; Tan, H.; Huang, J.-Q.; Zhang, B.,  $K_3V_2(PO_4)_2F_3$  as a robust cathode for potassium-ion batteries. *Energy Storage Mater.* **2019**, *16*, 97-101.
28. Chihara, K.; Katogi, A.; Kubota, K.; Komaba, S.,  $KVPO_4F$  and  $KVOPO_4$  toward 4 volt-class potassium-ion batteries. *Chem. Commun.* **2017**, *53* (37), 5208-5211.
29. Chen, Y.; Luo, W.; Carter, M.; Zhou, L.; Dai, J.; Fu, K.; Lacey, S.; Li, T.; Wan, J.; Han, X., Organic electrode for non-aqueous potassium-ion batteries. *Nano Energy* **2015**, *18*, 205-211.
30. Li, C.; Xue, J.; Huang, A.; Ma, J.; Qing, F.; Zhou, A.; Wang, Z.; Wang, Y.; Li, J., Poly(N-vinylcarbazole) as an advanced organic cathode for potassium-ion-based dual-ion battery. *Electrochim. Acta* **2019**, *297*, 850-855.
31. Tan, H.; Zhai, D.; Kang, F.; Zhang, B., Synergistic  $PF_6^-$  and  $FSI^-$  intercalation enables stable graphite cathode for potassium-based dual ion battery. *Carbon* **2021**, *178*, 363-370.
32. Deng, T.; Fan, X.; Chen, J.; Chen, L.; Luo, C.; Zhou, X.; Yang, J.; Zheng, S.; Wang, C., Layered P2-type  $K_{0.65}Fe_{0.5}Mn_{0.5}O_2$  microspheres as superior cathode for high-energy potassium-ion batteries. *Adv. Funct. Mater.* **2018**, *28* (28), 1800219.
33. Bie, X.; Kubota, K.; Hosaka, T.; Chihara, K.; Komaba, S., A novel K-ion battery: hexacyanoferrate (II)/graphite cell. *J. Mater. Chem. A* **2017**, *5* (9), 4325-4330.
34. Chong, S.; Yang, J.; Sun, L.; Guo, S.; Liu, Y.; Liu, H. K., Potassium nickel iron hexacyanoferrate as ultra-long-life cathode material for potassium-ion batteries with high energy density. *ACS Nano* **2020**, *14* (8), 9807-9818.
35. Li, X.; Ou, X.; Tang, Y., 6.0 V high-voltage and concentrated electrolyte toward high energy density K-based dual-graphite battery. *Adv. Energy Mater.* **2020**, *10* (41), 2002567.
36. Kim, H.; Kim, J. C.; Bo, S. H.; Shi, T.; Kwon, D. H.; Ceder, G., K-ion batteries based on a P2-type  $K_{0.6}CoO_2$  cathode. *Adv. Energy Mater.* **2017**, *7* (17), 1700098.
37. Kim, H.; Seo, D. H.; Bianchini, M.; Clément, R. J.; Kim, H.; Kim, J. C.; Tian, Y.; Shi, T.; Yoon, W. S.; Ceder, G., A new strategy for high-voltage cathodes for K-ion batteries: stoichiometric  $KVPO_4F$ . *Adv. Energy Mater.* **2018**, *8* (26), 1801591.
38. Zhang, C.; Xu, Y.; Zhou, M.; Liang, L.; Dong, H.; Wu, M.; Yang, Y.; Lei, Y., Potassium Prussian blue nanoparticles: a low-cost cathode material for potassium-ion batteries. *Adv. Funct. Mater.* **2017**, *27* (4), 1604307.

39. Deng, L.; Niu, X.; Ma, G.; Yang, Z.; Zeng, L.; Zhu, Y.; Guo, L., Layered potassium vanadate  $K_{0.5}V_2O_5$  as a cathode material for nonaqueous potassium ion batteries. *Adv. Funct. Mater.* **2018**, *28* (49), 1800670.
40. Kim, H.; Seo, D. H.; Kim, J. C.; Bo, S. H.; Liu, L.; Shi, T.; Ceder, G., Investigation of potassium storage in layered P3-type  $K_{0.5}MnO_2$  cathode. *Adv. Mater.* **2017**, *29* (37), 1702480.
41. Dong, J.; Lei, Y.; Han, D.; Wang, H.; Zhai, D.; Li, B.; Kang, F., Utilizing an autogenously protective atmosphere to synthesize a Prussian white cathode with ultrahigh capacity-retention for potassium-ion batteries. *Chem. Commun.* **2019**, *55* (83), 12555-12558.
42. Xiao, Z.; Meng, J.; Xia, F.; Wu, J.; Liu, F.; Zhang, X.; Xu, L.; Lin, X.; Mai, L.,  $K^+$  modulated  $K^+$ /vacancy disordered layered oxide for high-rate and high-capacity potassium-ion batteries. *Energy Environ. Sci.* **2020**, *13* (9), 3129-3137.
43. Vaalma, C.; Giffin, G. A.; Buchholz, D.; Passerini, S., Non-aqueous K-ion battery based on layered  $K_{0.3}MnO_2$  and hard carbon/carbon black. *J. Electrochem. Soc.* **2016**, *163* (7), A1295.
44. Masese, T.; Yoshii, K.; Yamaguchi, Y.; Okumura, T.; Huang, Z.-D.; Kato, M.; Kubota, K.; Furutani, J.; Oriyasa, Y.; Senoh, H., Rechargeable potassium-ion batteries with honeycomb-layered tellurates as high voltage cathodes and fast potassium-ion conductors. *Nat. Commun.* **2018**, *9* (1), 1-12.
45. Naveen, N.; Park, W. B.; Singh, S. P.; Han, S. C.; Ahn, D.; Sohn, K. S.; Pyo, M.,  $KCrS_2$  cathode with considerable cyclability and high rate performance: the first  $K^+$  stoichiometric layered compound for potassium-ion batteries. *Small* **2018**, *14* (49), 1803495.
46. Wang, W.; Ji, B.; Yao, W.; Zhang, X.; Zheng, Y.; Zhou, X.; Kidkhunthod, P.; He, H.; Tang, Y., A novel low-cost and environment-friendly cathode with large channels and high structure stability for potassium-ion storage. *Science China Materials* **2021**, *64* (5), 1047-1057.
47. Park, W. B.; Han, S. C.; Park, C.; Hong, S. U.; Han, U.; Singh, S. P.; Jung, Y. H.; Ahn, D.; Sohn, K. S.; Pyo, M.,  $KVP_2O_7$  as a robust high-energy cathode for potassium-ion batteries: pinpointed by a full screening of the inorganic registry under specific search conditions. *Adv. Energy Mater.* **2018**, *8* (13), 1703099.
48. Obrezkov, F. A.; Ramezankhani, V.; Zhidkov, I.; Traven, V. F.; Kurmaev, E. Z.; Stevenson, K. J.; Troshin, P. A., High-energy and high-power-density potassium ion batteries using dihydrophenazine-based polymer as active cathode material. *J. Phys. Chem. Lett.* **2019**, *10* (18), 5440-5445.

- 
49. Zhang, C.; Xu, Y.; He, K.; Dong, Y.; Zhao, H.; Medenbach, L.; Wu, Y.; Balducci, A.; Hannappel, T.; Lei, Y., Polyimide@ketjenblack composite: A porous organic cathode for fast rechargeable potassium-ion batteries. *Small* **2020**, *16* (38), 2002953.
50. Ponrouch, A.; Marchante, E.; Courty, M.; Tarascon, J.-M.; Palacin, M. R., In search of an optimized electrolyte for Na-ion batteries. *Energy Environ. Sci.* **2012**, *5* (9), 8572-8583.
51. Xu, K., Nonaqueous liquid electrolytes for lithium-based rechargeable batteries. *Chem. Rev.* **2004**, *104* (10), 4303-4418.
52. Zhang, Q.; Mao, J.; Pang, W. K.; Zheng, T.; Sencadas, V.; Chen, Y.; Liu, Y.; Guo, Z., Boosting the potassium storage performance of alloy-based anode materials via electrolyte salt chemistry. *Adv. Energy Mater.* **2018**, *8* (15), 1703288.
53. Yan, G.; Alves-Dalla-Corte, D.; Yin, W.; Madern, N.; Gachot, G.; Tarascon, J.-M., Assessment of the electrochemical stability of carbonate-based electrolytes in Na-ion batteries. *J. Electrochem. Soc.* **2018**, *165* (7), A1222.
54. Zhang, H.; Eshetu, G. G.; Judez, X.; Li, C.; Rodriguez-Martínez, L. M.; Armand, M., Electrolyte additives for lithium metal anodes and rechargeable lithium metal batteries: progress and perspectives. *Angew. Chem. Int. Ed.* **2018**, *57* (46), 15002-15027.
55. Chen, J.; Fan, X.; Li, Q.; Yang, H.; Khoshi, M. R.; Xu, Y.; Hwang, S.; Chen, L.; Ji, X.; Yang, C.; Huixin He; Chongmin Wang; Eric Garfunkel; Dong Su; Oleg Borodin; Wang, C., Electrolyte design for LiF-rich solid-electrolyte interfaces to enable high-performance micro-sized alloy anodes for batteries. *Nat. Energy* **2020**, *5* (5), 386-397.
56. Feng, J. K.; Ai, X. P.; Cao, Y. L.; Yang, H. X., Possible use of non-flammable phosphonate ethers as pure electrolyte solvent for lithium batteries. *J. Power Sources* **2008**, *177* (1), 194-198.
57. Xu, K., Li-ion battery electrolytes. *Nat. Energy* **2021**, *6* (7), 763-763.
58. Zheng, J.; Yang, Y.; Fan, X.; Ji, G.; Ji, X.; Wang, H.; Hou, S.; Zachariah, M. R.; Wang, C., Extremely stable antimony-carbon composite anodes for potassium-ion batteries. *Energy Environ. Sci.* **2019**, *12* (2), 615-623.
59. Huang, J.; Lin, X.; Tan, H.; Zhang, B., Bismuth microparticles as advanced anodes for potassium-ion battery. *Adv. Energy Mater.* **2018**, *8* (19), 1703496.
60. Liu, S.; Mao, J.; Zhang, L.; Pang, W. K.; Du, A.; Guo, Z., Manipulating the Solvation Structure of Nonflammable Electrolyte and Interface to Enable Unprecedented Stability of

- Graphite Anodes beyond 2 Years for Safe Potassium-Ion Batteries. *Adv. Mater.* **2021**, *33* (1), 2006313.
61. Ou, X.; Li, J.; Tong, X.; Zhang, G.; Tang, Y., Highly Concentrated and Nonflammable Electrolyte for High Energy Density K-Based Dual-Ion Battery. *ACS Appl. Energy Mater.* **2020**, *3* (10), 10202-10208.
62. Xu, K.; Angell, C. A., Sulfone-based electrolytes for lithium-ion batteries. *J. Electrochem. Soc.* **2002**, *149* (7), A920.
63. Zeng, G.; Xiong, S.; Qian, Y.; Ci, L.; Feng, J., Non-Flammable Phosphate Electrolyte with High Salt-to-Solvent Ratios for Safe Potassium-Ion Battery. *J. Electrochem. Soc.* **2019**, *166* (6), A1217-A1222.
64. Jian, Z.; Luo, W.; Ji, X., Carbon electrodes for K-ion batteries. *J. Am. Chem. Soc.* **2015**, *137* (36), 11566-11569.
65. Fan, L.; Ma, R.; Zhang, Q.; Jia, X.; Lu, B., Graphite anode for a potassium-ion battery with unprecedented performance. *Angew. Chem.* **2019**, *131* (31), 10610-10615.
66. Lin, X.; Huang, J.; Zhang, B., Correlation between the microstructure of carbon materials and their potassium ion storage performance. *Carbon* **2019**, *143*, 138-146.
67. Zhang, J.; Lai, L.; Wang, H.; Chen, M.; Shen, Z. X., Energy storage mechanisms of anode materials for potassium ion batteries. *Mater. Today Energy* **2021**, 100747.
68. Wu, H.; Cui, Y., Designing nanostructured Si anodes for high energy lithium ion batteries. *Nano Today* **2012**, *7* (5), 414-429.
69. Derrien, G.; Hassoun, J.; Panero, S.; Scrosati, B., Nanostructured Sn-C composite as an advanced anode material in high-performance Lithium-ion batteries. *Adv. Mater.* **2007**, *19* (17), 2336-2340.
70. Qian, J.; Chen, Y.; Wu, L.; Cao, Y.; Ai, X.; Yang, H., High capacity Na-storage and superior cyclability of nanocomposite Sb/C anode for Na-ion batteries. *Chem. Commun.* **2012**, *48* (56), 7070-7072.
71. Tran, T. T.; Obrovac, M., Alloy negative electrodes for high energy density metal-ion cells. *J. Electrochem. Soc.* **2011**, *158* (12), A1411.
72. Sultana, I.; Rahman, M. M.; Chen, Y.; Glushenkov, A. M., Potassium-ion battery anode materials operating through the alloying-dealloying reaction mechanism. *Adv. Funct. Mater.* **2018**, *28* (5), 1703857.

73. Yu, S.; Kim, S. O.; Kim, H. S.; Choi, W., Computational screening of anode materials for potassium - ion batteries. *Int. J. Energy Res.* **2019**, *43* (13), 7646-7654.
74. Han, Y.; Li, T.; Li, Y.; Tian, J.; Yi, Z.; Lin, N.; Qian, Y., Stabilizing antimony nanocrystals within ultrathin carbon nanosheets for high-performance K-ion storage. *Energy Storage Mater.* **2019**, *20*, 46-54.
75. Lei, K.; Wang, C.; Liu, L.; Luo, Y.; Mu, C.; Li, F.; Chen, J., A Porous Network of Bismuth Used as the Anode Material for High-Energy-Density Potassium-Ion Batteries. *Angew. Chem., Int. Ed. Engl.* **2018**, *57* (17), 4687-4691.
76. Zhou, L.; Cao, Z.; Zhang, J.; Cheng, H.; Liu, G.; Park, G. T.; Cavallo, L.; Wang, L.; Alshareef, H. N.; Sun, Y. K., Electrolyte-Mediated Stabilization of High-Capacity Micro-Sized Antimony Anodes for Potassium-Ion Batteries. *Adv. Mater.* **2021**, *33* (8), 2005993.
77. Xiong, P.; Wu, J.; Zhou, M.; Xu, Y., Bismuth-antimony alloy nanoparticle@porous carbon nanosheet composite anode for high-performance potassium-ion batteries. *ACS Nano* **2019**, *14* (1), 1018-1026.
78. Wang, Z.; Dong, K.; Wang, D.; Luo, S.; Liu, Y.; Wang, Q.; Zhang, Y.; Hao, A.; Shi, C.; Zhao, N., A nanosized SnSb alloy confined in N-doped 3D porous carbon coupled with ether-based electrolytes toward high-performance potassium-ion batteries. *J. Mater. Chem. A* **2019**, *7* (23), 14309-14318.
79. Palacin, M. R., Recent advances in rechargeable battery materials: a chemist's perspective. *Chem. Soc. Rev.* **2009**, *38* (9), 2565-2575.
80. Adekoya, D.; Chen, H.; Hoh, H. Y.; Gould, T.; Balogun, M.-S. J. T.; Lai, C.; Zhao, H.; Zhang, S., Hierarchical Co<sub>3</sub>O<sub>4</sub>@N-doped carbon composite as an advanced anode material for ultrastable potassium storage. *ACS Nano* **2020**, *14* (4), 5027-5035.
81. Li, J.; Zhuang, N.; Xie, J.; Li, X.; Zhuo, W.; Wang, H.; Na, J. B.; Li, X.; Yamauchi, Y.; Mai, W., K-ion storage enhancement in Sb<sub>2</sub>O<sub>3</sub>/reduced graphene oxide using ether-based electrolyte. *Adv. Energy Mater.* **2020**, *10* (5), 1903455.
82. Yao, K.; Xu, Z.; Ma, M.; Li, J.; Lu, F.; Huang, J., Densified metallic MoS<sub>2</sub>/graphene enabling fast potassium-ion storage with superior gravimetric and volumetric capacities. *Adv. Funct. Mater.* **2020**, *30* (24), 2001484.
83. Liu, Y.; Tai, Z.; Zhang, J.; Pang, W. K.; Zhang, Q.; Feng, H.; Konstantinov, K.; Guo, Z.; Liu, H. K., Boosting potassium-ion batteries by few-layered composite anodes prepared via solution-triggered one-step shear exfoliation. *Nat. Commun.* **2018**, *9* (1), 1-10.

- 
84. Cheng, Y.; Yao, Z.; Zhang, Q.; Chen, J.; Ye, W.; Zhou, S.; Liu, H.; Wang, M. S., In situ atomic-scale observation of reversible potassium storage in  $\text{Sb}_2\text{S}_3$ @carbon nanowire anodes. *Adv. Funct. Mater.* **2020**, *30* (52), 2005417.
85. Liu, Y.; Deng, Q.; Li, Y.; Li, Y.; Zhong, W.; Hu, J.; Ji, X.; Yang, C.; Lin, Z.; Huang, K., CoSe@N-doped carbon nanotubes as a potassium-ion battery anode with high initial coulombic efficiency and superior capacity retention. *ACS Nano* **2021**, *15* (1), 1121-1132.
86. Wang, S.; Xiong, P.; Guo, X.; Zhang, J.; Gao, X.; Zhang, F.; Tang, X.; Notten, P. H.; Wang, G., A stable conversion and alloying anode for potassium-ion batteries: a combined strategy of encapsulation and confinement. *Adv. Funct. Mater.* **2020**, *30* (27), 2001588.
87. Sultana, I.; Rahman, M. M.; Ramireddy, T.; Chen, Y.; Glushenkov, A. M., High capacity potassium-ion battery anodes based on black phosphorus. *J. Mater. Chem. A* **2017**, *5* (45), 23506-23512.
88. Jin, H.; Wang, H.; Qi, Z.; Bin, D. S.; Zhang, T.; Wan, Y.; Chen, J.; Chuang, C.; Lu, Y. R.; Chan, T. S., A Black Phosphorus-Graphite Composite Anode for Li-/Na-/K-Ion Batteries. *Angew. Chem.* **2020**, *132* (6), 2338-2342.
89. Zhang, W.; Mao, J.; Li, S.; Chen, Z.; Guo, Z., Phosphorus-based alloy materials for advanced potassium-ion battery anode. *J. Am. Chem. Soc.* **2017**, *139* (9), 3316-3319.
90. Yang, F.; Gao, H.; Hao, J.; Zhang, S.; Li, P.; Liu, Y.; Chen, J.; Guo, Z., Yolk-shell structured FeP@C nanoboxes as advanced anode materials for rechargeable lithium-/potassium-ion batteries. *Adv. Funct. Mater.* **2019**, *29* (16), 1808291.
91. Yang, F.; Hao, J.; Long, J.; Liu, S.; Zheng, T.; Lie, W.; Chen, J.; Guo, Z., Achieving High-Performance Metal Phosphide Anode for Potassium Ion Batteries via Concentrated Electrolyte Chemistry. *Adv. Energy Mater.* **2021**, *11* (6), 2003346.
92. Tan, H.; Du, X.; Huang, J.-Q.; Zhang, B.,  $\text{KVPO}_4\text{F}$  as a novel insertion-type anode for potassium ion batteries. *Chem. Commun.* **2019**, *55* (75), 11311-11314.
93. Wang, J.; Wang, B.; Lu, B., Nature of novel 2D van der Waals heterostructures for superior potassium ion batteries. *Adv. Energy Mater.* **2020**, *10* (24), 2000884.
94. Sun, N.; Zhu, Q.; Anasori, B.; Zhang, P.; Liu, H.; Gogotsi, Y.; Xu, B., MXene-bonded flexible hard carbon film as anode for stable Na/K-ion storage. *Adv. Funct. Mater.* **2019**, *29* (51), 1906282.

- 
95. Tan, H.; Du, X.; Zhou, R.; Hou, Z.; Zhang, B., Rational design of microstructure and interphase enables high-capacity and long-life carbon anodes for potassium ion batteries. *Carbon* **2021**, *176*, 383-389.
96. Wang, W.; Zhou, J.; Wang, Z.; Zhao, L.; Li, P.; Yang, Y.; Yang, C.; Huang, H.; Guo, S., Short-range order in mesoporous carbon boosts potassium-ion battery performance. *Adv. Energy Mater.* **2018**, *8* (5), 1701648.
97. Xu, Y.; Zhang, C.; Zhou, M.; Fu, Q.; Zhao, C.; Wu, M.; Lei, Y., Highly nitrogen doped carbon nanofibers with superior rate capability and cyclability for potassium ion batteries. *Nat. Commun.* **2018**, *9* (1), 1-11.
98. Wang, Y.; Wang, Z.; Chen, Y.; Zhang, H.; Yousaf, M.; Wu, H.; Zou, M.; Cao, A.; Han, R. P., Hyperporous sponge interconnected by hierarchical carbon nanotubes as a high-performance potassium-ion battery anode. *Adv. Mater.* **2018**, *30* (32), 1802074.
99. Zhao, R.; Di, H.; Wang, C.; Hui, X.; Zhao, D.; Wang, R.; Zhang, L.; Yin, L., Encapsulating Ultrafine Sb Nanoparticles in Na<sup>+</sup> Pre-Intercalated 3D Porous Ti<sub>3</sub>C<sub>2</sub>T<sub>x</sub> MXene Nanostructures for Enhanced Potassium Storage Performance. *ACS Nano* **2020**, *14* (10), 13938-13951.
100. Chen, K. T.; Tuan, H. Y., Bi-Sb Nanocrystals Embedded in Phosphorus as High-Performance Potassium Ion Battery Electrodes. *ACS Nano* **2020**, *14* (9), 11648-11661.
101. An, Y.; Tian, Y.; Ci, L.; Xiong, S.; Feng, J.; Qian, Y., Micron-sized nanoporous antimony with tunable porosity for high-performance potassium-ion batteries. *ACS Nano* **2018**, *12* (12), 12932-12940.
102. Tian, H.; Yu, X.; Shao, H.; Dong, L.; Chen, Y.; Fang, X.; Wang, C.; Han, W.; Wang, G., Unlocking few-layered ternary chalcogenides for high-performance potassium-ion storage. *Adv. Energy Mater.* **2019**, *9* (29), 1901560.
103. Wang, S.; Xiong, P.; Guo, X.; Zhang, J.; Gao, X.; Zhang, F.; Tang, X.; Notten, P. H.; Wang, G., A stable conversion and alloying anode for potassium-ion batteries: combined strategy of encapsulation and confinement. *Adv. Funct. Mater.* **2020**, *30* (27), 2001588.
104. Chang, W. C.; Wu, J. H.; Chen, K. T.; Tuan, H. Y., Red phosphorus potassium-ion battery anodes. *Adv. Sci.* **2019**, *6* (9), 1801354.
105. Zhang, W.; Wu, Z.; Zhang, J.; Liu, G.; Yang, N.-H.; Liu, R.-S.; Pang, W. K.; Li, W.; Guo, Z., Unraveling the effect of salt chemistry on long-durability high-phosphorus-concentration anode for potassium ion batteries. *Nano Energy* **2018**, *53*, 967-974.

106. Wu, Y.; Hu, S.; Xu, R.; Wang, J.; Peng, Z.; Zhang, Q.; Yu, Y., Boosting potassium-ion battery performance by encapsulating red phosphorus in free-standing nitrogen-doped porous hollow carbon nanofibers. *Nano Lett.* **2019**, *19* (2), 1351-1358.
107. Yang, C.; Lv, F.; Zhang, Y.; Wen, J.; Dong, K.; Su, H.; Lai, F.; Qian, G.; Wang, W.; Hilger, A., Confined Fe<sub>2</sub>VO<sub>4</sub>⊂nitrogen-doped carbon nanowires with internal void space for high-rate and ultrastable potassium-ion storage. *Adv. Energy Mater.* **2019**, *9* (46), 1902674.
108. Li, Y.; Zhang, Q.; Yuan, Y.; Liu, H.; Yang, C.; Lin, Z.; Lu, J., Surface amorphization of vanadium dioxide (B) for K-ion battery. *Adv. Energy Mater.* **2020**, *10* (23), 2000717.
109. Ge, X.; Liu, S.; Qiao, M.; Du, Y.; Li, Y.; Bao, J.; Zhou, X., Enabling Superior Electrochemical Properties for Highly Efficient Potassium Storage by Impregnating Ultrafine Sb Nanocrystals within Nanochannel-Containing Carbon Nanofibers. *Angew. Chem., Int. Ed. Engl.* **2019**, *58* (41), 14578-14583.
110. Fang, K.; Liu, D.; Xiang, X.; Zhu, X.; Tang, H.; Qu, D.; Xie, Z.; Li, J.; Qu, D., Air-stable red phosphorus anode for potassium/sodium-ion batteries enabled through dual-protection design. *Nano Energy* **2020**, *69*, 104451.
111. Xiao, W.; Li, X.; Cao, B.; Huang, G.; Xie, C.; Qin, J.; Yang, H.; Wang, J.; Sun, X., Constructing high-rate and long-life phosphorus/carbon anodes for potassium-ion batteries through rational nanoconfinement. *Nano Energy* **2021**, *83*, 105772.
112. Zhang, S.; Chowdari, B.; Wen, Z.; Jin, J.; Yang, J., Constructing highly oriented configuration by few-layer MoS<sub>2</sub>: toward high-performance lithium-ion batteries and hydrogen evolution reactions. *ACS Nano* **2015**, *9* (12), 12464-12472.
113. Wan, F.; Guo, J.-Z.; Zhang, X.-H.; Zhang, J.-P.; Sun, H.-Z.; Yan, Q.; Han, D.-X.; Niu, L.; Wu, X.-L., In situ binding Sb nanospheres on graphene via oxygen bonds as superior anode for ultrafast sodium-ion batteries. *ACS Appl. Mater. Interfaces* **2016**, *8* (12), 7790-7799.
114. Zhang, Y.; Li, G.; Wu, Y.; Zhang, B.; Song, W.; Zhang, L., Antimony nanowire arrays fabricated by pulsed electrodeposition in anodic alumina membranes. *Adv. Mater.* **2002**, *14* (17), 1227-1230.
115. Smith, J. B.; Hagaman, D.; Ji, H. F., Growth of 2D black phosphorus film from chemical vapor deposition. *Nanotechnology* **2016**, *27* (21), 215602.
116. Johnson, K. L.; Johnson, K. L., *Contact mechanics*. Cambridge university press: 1987.
117. Gao, Y.; Shi, S.-Q.; Zhang, T.-Y., Adhesion contact deformation in nanobridge tests. *Nanoscale* **2017**, *9* (18), 6033-6040.

- 
118. Gao, Y.; Du, X.; Hou, Z.; Shen, X.; Mai, Y.-W.; Tarascon, J.-M.; Zhang, B., Unraveling the mechanical origin of stable solid electrolyte interphase. *Joule* **2021**, *5* (7), 1860-1872.
119. Blöchl, P. E., Projector augmented-wave method. *Phys. Rev. B* **1994**, *50* (24), 17953-17979.
120. Kresse, G.; Furthmüller, J., Efficient iterative schemes for ab initio total-energy calculations using a plane-wave basis set. *Phys. Rev. B* **1996**, *54* (16), 11169.
121. Perdew, J. P.; Burke, K.; Ernzerhof, M., Generalized gradient approximation made simple. *Phys. Rev. Lett.* **1996**, *77* (18), 3865.
122. Klimes, J.; Bowler, D. R.; Michaelides, A., Chemical accuracy for the van der Waals density functional. *J. Condens. Matter Phys.* **2010**, *22* (2), 022201.
123. Xiao, Y.; Miara, L. J.; Wang, Y.; Ceder, G., Computational Screening of Cathode Coatings for Solid-State Batteries. *Joule* **2019**, *3* (5), 1252-1275.
124. Tan, H.; Lin, X.; Huang, J.; Huang, J.; Shi, M.; Du, X.; Zhang, B., The underestimated charge storage capability of carbon cathodes for advanced alkali metal-ion capacitors. *Nanoscale* **2019**, *11* (24), 11445-11450.
125. Xu, J.; Dou, Y.; Wei, Z.; Ma, J.; Deng, Y.; Li, Y.; Liu, H.; Dou, S., Recent progress in graphite intercalation compounds for rechargeable metal (Li, Na, K, Al)-ion batteries. *Adv. Sci.* **2017**, *4* (10), 1700146.
126. Wei, Z. X.; Wang, D. X.; Li, M. L.; Gao, Y.; Wang, C. Z.; Chen, G.; Du, F., Fabrication of Hierarchical Potassium Titanium Phosphate Spheroids: A Host Material for Sodium-Ion and Potassium-Ion Storage. *Adv. Energy Mater.* **2018**, *8* (27), 1801102.
127. Ni, D.; Sun, W.; Wang, Z.; Bai, Y.; Lei, H.; Lai, X.; Sun, K., Heteroatom-Doped Mesoporous Hollow Carbon Spheres for Fast Sodium Storage with an Ultralong Cycle Life. *Adv. Energy Mater.* **2019**, *9* (19), 1900036.
128. Ji, L.; Gu, M.; Shao, Y.; Li, X.; Engelhard, M. H.; Arey, B. W.; Wang, W.; Nie, Z.; Xiao, J.; Wang, C.; Zhang, J. G.; Liu, J., Controlling SEI formation on SnSb-porous carbon nanofibers for improved Na ion storage. *Adv. Mater.* **2014**, *26* (18), 2901-2908.
129. Lin, X.; Du, X.; Tsui, P. S.; Huang, J.-Q.; Tan, H.; Zhang, B., Exploring room- and low-temperature performance of hard carbon material in half and full Na-ion batteries. *Electrochim. Acta* **2019**, *316*, 60-68.
130. Jian, Z. L.; Xing, Z. Y.; Bommier, C.; Li, Z. F.; Ji, X. L., Hard Carbon Microspheres: Potassium-Ion Anode Versus Sodium-Ion Anode. *Adv. Energy Mater.* **2016**, *6* (3), 1501874.

- 
131. Liu, Z.; Hu, Y.-Y.; Dunstan, M. T.; Huo, H.; Hao, X.; Zou, H.; Zhong, G.; Yang, Y.; Grey, C. P., Local Structure and Dynamics in the Na Ion Battery Positive Electrode Material  $\text{Na}_3\text{V}_2(\text{PO}_4)_2\text{F}_3$ . *Chem. Mater.* **2014**, *26* (8), 2513-2521.
132. Zhang, B.; Dugas, R.; Rouse, G.; Rozier, P.; Abakumov, A. M.; Tarascon, J. M., Insertion compounds and composites made by ball milling for advanced sodium-ion batteries. *Nat. Commun.* **2016**, *7*, 10308.
133. Mizushima, K.; Jones, P.; Wiseman, P.; Goodenough, J. B.,  $\text{Li}_x\text{CoO}_2$  ( $0 < x < 1$ ): A new cathode material for batteries of high energy density. *Mater. Res. Bull.* **1980**, *15* (6), 783-789.
134. Yabuuchi, N.; Kubota, K.; Dahbi, M.; Komaba, S., Research development on sodium-ion batteries. *Chem. Rev.* **2014**, *114* (23), 11636-11682.
135. Darwiche, A.; Marino, C.; Sougrati, M. T.; Fraise, B.; Stievano, L.; Monconduit, L., Better cycling performances of bulk Sb in Na-ion batteries compared to Li-ion systems: an unexpected electrochemical mechanism. *J. Am. Chem. Soc.* **2012**, *134* (51), 20805-20811.
136. Kim, H.; Kim, J. C.; Bianchini, M.; Seo, D. H.; Rodriguez-Garcia, J.; Ceder, G., Recent progress and perspective in electrode materials for K-ion batteries. *Adv. Energy Mater.* **2018**, *8* (9), 1702384.
137. Xie, F.; Zhang, L.; Chen, B.; Chao, D.; Gu, Q.; Johannessen, B.; Jaroniec, M.; Qiao, S.-Z., Revealing the origin of improved reversible capacity of dual-shell bismuth boxes anode for potassium-ion batteries. *Matter* **2019**, *1* (6), 1681-1693.
138. Wang, T.; Chen, S.; Pang, H.; Xue, H.; Yu, Y.,  $\text{MoS}_2$ -Based Nanocomposites for Electrochemical Energy Storage. *Adv. Sci.* **2017**, *4* (2), 1600289.
139. Wang, J.; Liu, J.; Chao, D.; Yan, J.; Lin, J.; Shen, Z. X., Self-assembly of honeycomb-like  $\text{MoS}_2$  nanoarchitectures anchored into graphene foam for enhanced lithium-ion storage. *Adv. Mater.* **2014**, *26* (42), 7162-7169.
140. David, L.; Bhandavat, R.; Singh, G.,  $\text{MoS}_2$ /Graphene Composite Paper for Sodium-Ion Battery Electrodes. *ACS Nano* **2014**, *8* (2), 1759-1770.
141. Wang, Y.; Yu, L.; Lou, X. W., Synthesis of Highly Uniform Molybdenum-Glycerate Spheres and Their Conversion into Hierarchical  $\text{MoS}_2$  Hollow Nanospheres for Lithium-Ion Batteries. *Angew. Chem., Int. Ed. Engl.* **2016**, *55* (26), 7423-7426.
142. Fang, Y.; Luan, D.; Chen, Y.; Gao, S.; Lou, X. W. D., Rationally Designed Three-Layered  $\text{Cu}_2\text{S}@ \text{Carbon}@ \text{MoS}_2$  Hierarchical Nanoboxes for Efficient Sodium Storage. *Angew. Chem., Int. Ed. Engl.* **2020**, *59* (18), 7178-7183.

143. Han, M.; Lin, Z.; Yu, J., Ultrathin MoS<sub>2</sub> nanosheets homogenously embedded in a N,O-codoped carbon matrix for high-performance lithium and sodium storage. *J. Mater. Chem. A* **2019**, *7* (9), 4804-4812.
144. Li, Z.; Jiang, K.; Khan, F.; Goswami, A.; Liu, J.; Passian, A.; Thundat, T., Anomalous interfacial stress generation during sodium intercalation/extraction in MoS<sub>2</sub> thin-film anodes. *Sci. Adv.* **2019**, *5* (1), eaav2820.
145. Zhang, L.; Sun, D.; Kang, J.; Feng, J.; Bechtel, H. A.; Wang, L. W.; Cairns, E. J.; Guo, J., Electrochemical Reaction Mechanism of the MoS<sub>2</sub> Electrode in a Lithium-Ion Cell Revealed by in Situ and Operando X-ray Absorption Spectroscopy. *Nano Lett.* **2018**, *18* (2), 1466-1475.
146. Du, X.; Huang, J.; Guo, X.; Lin, X.; Huang, J.-Q.; Tan, H.; Zhu, Y.; Zhang, B., Preserved Layered Structure Enables Stable Cyclic Performance of MoS<sub>2</sub> upon Potassium Insertion. *Chem. Mater.* **2019**, *31* (21), 8801-8809.
147. Wang, X.; Shen, X.; Wang, Z.; Yu, R.; Chen, L., Atomic-scale clarification of structural transition of MoS<sub>2</sub> upon sodium intercalation. *ACS Nano* **2014**, *8* (11), 11394-11400.
148. Veerasubramani, G. K.; Park, M.-S.; Nagaraju, G.; Kim, D.-W., Unraveling the Na-ion storage performance of a vertically aligned interlayer-expanded two-dimensional MoS<sub>2</sub>@C@MoS<sub>2</sub> heterostructure. *J. Mater. Chem. A* **2019**, *7* (42), 24557-24568.
149. Fang, Y.; Yu, X. Y.; Lou, X. W., Bullet-like Cu<sub>9</sub>S<sub>5</sub> Hollow Particles Coated with Nitrogen-Doped Carbon for Sodium-Ion Batteries. *Angew. Chem. Int. Ed.* **2019**, *131* (23), 7826-7830.
150. Wang, L.; Xu, Z.; Wang, W.; Bai, X., Atomic mechanism of dynamic electrochemical lithiation processes of MoS<sub>2</sub> nanosheets. *J. Am. Chem. Soc.* **2014**, *136* (18), 6693-6697.
151. Li, F. X.; Zou, J. L.; Cao, L. J.; Li, Z. Q.; Gu, S.; Liu, Y.; Zhang, J. Q.; Liu, H. T.; Lu, Z. G., In Situ Study of K<sup>+</sup> Electrochemical Intercalating into MoS<sub>2</sub> Flakes. *J. Phys. Chem. C* **2019**, *123* (8), 5067-5072.
152. Gao, P.; Wang, L.; Zhang, Y.; Huang, Y.; Liu, K., Atomic-Scale Probing of the Dynamics of Sodium Transport and Intercalation-Induced Phase Transformations in MoS<sub>2</sub>. *ACS Nano* **2015**, *9* (11), 11296-301.
153. Andersen, A.; Kathmann, S. M.; Lilga, M. A.; Albrecht, K. O.; Hallen, R. T.; Mei, D., First-Principles Characterization of Potassium Intercalation in Hexagonal 2H-MoS<sub>2</sub>. *J. Phys. Chem. C* **2012**, *116* (2), 1826-1832.

154. Leng, K.; Chen, Z.; Zhao, X.; Tang, W.; Tian, B.; Nai, C. T.; Zhou, W.; Loh, K. P., Phase Restructuring in Transition Metal Dichalcogenides for Highly Stable Energy Storage. *ACS Nano* **2016**, 9208-9215.
155. Zhu, Z.; Tang, Y.; Leow, W. R.; Xia, H.; Lv, Z.; Wei, J.; Ge, X.; Cao, S.; Zhang, Y.; Zhang, W.; Zhang, H.; Xi, S.; Du, Y.; Chen, X., Approaching the Lithiation Limit of MoS<sub>2</sub> While Maintaining Its Layered Crystalline Structure to Improve Lithium Storage. *Angew. Chem., Int. Ed. Engl.* **2019**, 58 (11), 3521-3526.
156. Chen, B.; Lu, H.; Zhou, J.; Ye, C.; Shi, C.; Zhao, N.; Qiao, S.-Z., Porous MoS<sub>2</sub>/Carbon Spheres Anchored on 3D Interconnected Multiwall Carbon Nanotube Networks for Ultrafast Na Storage. *Adv. Energy Mater.* **2018**, 8 (15), 1702909.
157. Hao, S.; Shen, X.; Tian, M.; Yu, R. C.; Wang, Z. X.; Chen, L. Q., Reversible conversion of MoS<sub>2</sub> upon sodium extraction. *Nano Energy* **2017**, 41, 217-224.
158. Fan, Z.; Zhang, L.; Baumann, D.; Mei, L.; Yao, Y.; Duan, X.; Shi, Y.; Huang, J.; Huang, Y.; Duan, X., In Situ Transmission Electron Microscopy for Energy Materials and Devices. *Adv. Mater.* **2019**, 31 (33), 1900608.
159. Wang, W.; Jiang, B.; Qian, C.; Lv, F.; Feng, J.; Zhou, J.; Wang, K.; Yang, C.; Yang, Y.; Guo, S., Pistachio-Shuck-Like MoSe<sub>2</sub>/C Core/Shell Nanostructures for High-Performance Potassium-Ion Storage. *Adv. Mater.* **2018**, 30 (30), 1801812.
160. Huang, H.; Cui, J.; Liu, G.; Bi, R.; Zhang, L., Carbon-Coated MoSe<sub>2</sub>/MXene Hybrid Nanosheets for Superior Potassium Storage. *ACS Nano* **2019**, 13 (3), 3448-3456.
161. Li, H. L.; Yu, K.; Fu, H.; Guo, B. J.; Lei, X.; Zhu, Z. Q., MoS<sub>2</sub>/Graphene Hybrid Nanoflowers with Enhanced Electrochemical Performances as Anode for Lithium-Ion Batteries. *J. Phys. Chem. C* **2015**, 119 (14), 7959-7968.
162. Ge, J.; Fan, L.; Wang, J.; Zhang, Q.; Liu, Z.; Zhang, E.; Liu, Q.; Yu, X.; Lu, B., MoSe<sub>2</sub>/N-doped carbon as anodes for potassium-ion batteries. *Adv. Energy Mater.* **2018**, 8 (29), 1801477.
163. Jia, B.; Zhao, Y.; Qin, M.; Wang, W.; Liu, Z.; Lao, C.-Y.; Yu, Q.; Liu, Y.; Wu, H.; Zhang, Z.; Qu, X., Multirole organic-induced scalable synthesis of a mesoporous MoS<sub>2</sub>-monolayer/carbon composite for high-performance lithium and potassium storage. *J. Mater. Chem. A* **2018**, 6 (24), 11147-11153.

164. Xie, K.; Yuan, K.; Li, X.; Lu, W.; Shen, C.; Liang, C.; Vajtai, R.; Ajayan, P.; Wei, B., Superior Potassium Ion Storage via Vertical MoS<sub>2</sub> "Nano-Rose" with Expanded Interlayers on Graphene. *Small* **2017**, *13* (42), 1701471.
165. Tian, B.; Tang, W.; Leng, K.; Chen, Z.; Tan, S. J. R.; Peng, C.; Ning, G.-H.; Fu, W.; Su, C.; Zheng, G. W.; Loh, K. P., Phase Transformations in TiS<sub>2</sub> during K Intercalation. *ACS Energy Lett.* **2017**, *2* (8), 1835-1840.
166. Yang, C.; Feng, J.; Lv, F.; Zhou, J.; Lin, C.; Wang, K.; Zhang, Y.; Yang, Y.; Wang, W.; Li, J.; Guo, S., Metallic Graphene-Like VSe<sub>2</sub> Ultrathin Nanosheets: Superior Potassium-Ion Storage and Their Working Mechanism. *Adv. Mater.* **2018**, *30* (27), e1800036.
167. Mao, M.; Cui, C.; Wu, M.; Zhang, M.; Gao, T.; Fan, X.; Chen, J.; Wang, T.; Ma, J.; Wang, C., Flexible ReS<sub>2</sub> nanosheets/N-doped carbon nanofibers-based paper as a universal anode for alkali (Li, Na, K) ion battery. *Nano Energy* **2018**, *45*, 346-352.
168. Wang, Y.; Wang, Z.; Chen, Y.; Zhang, H.; Yousaf, M.; Wu, H.; Zou, M.; Cao, A.; Han, R. P. S., Hyperporous Sponge Interconnected by Hierarchical Carbon Nanotubes as a High-Performance Potassium-Ion Battery Anode. *Adv. Mater.* **2018**, *30* (32), e1802074.
169. Liu, L.; Chen, Y.; Xie, Y.; Tao, P.; Li, Q.; Yan, C., Understanding of the Ultrastable K-Ion Storage of Carbonaceous Anode. *Adv. Funct. Mater.* **2018**, *28* (29), 1801989.
170. Bin, D. S.; Lin, X. J.; Sun, Y. G.; Xu, Y. S.; Zhang, K.; Cao, A. M.; Wan, L. J., Engineering Hollow Carbon Architecture for High-Performance K-Ion Battery Anode. *J. Am. Chem. Soc.* **2018**, *140* (23), 7127-7134.
171. Cao, B.; Zhang, Q.; Liu, H.; Xu, B.; Zhang, S.; Zhou, T.; Mao, J.; Pang, W. K.; Guo, Z.; Li, A.; Zhou, J.; Chen, X.; Song, H., Graphitic Carbon Nanocage as a Stable and High Power Anode for Potassium-Ion Batteries. *Adv. Energy Mater.* **2018**, *8* (25), 1801149.
172. Chen, Z.; Yin, D.; Zhang, M., Sandwich-like MoS<sub>2</sub>@SnO<sub>2</sub>@C with high capacity and stability for Sodium/Potassium ion batteries. *Small* **2018**, *14* (17), 1703818.
173. Zhang, J.; Wang, D.-W.; Lv, W.; Zhang, S.; Liang, Q.; Zheng, D.; Kang, F.; Yang, Q.-H., Achieving superb sodium storage performance on carbon anodes through an ether-derived solid electrolyte interphase. *Energy Environ. Sci.* **2017**, *10* (1), 370-376.
174. Soto, F. A.; Yan, P.; Engelhard, M. H.; Marzouk, A.; Wang, C.; Xu, G.; Chen, Z.; Amine, K.; Liu, J.; Sprenkle, V. L.; El-Mellouhi, F.; Balbuena, P. B.; Li, X., Tuning the Solid Electrolyte Interphase for Selective Li- and Na-Ion Storage in Hard Carbon. *Adv. Mater.* **2017**, *29* (18), 1606860.

175. Li, K.; Zhang, J.; Lin, D.; Wang, D. W.; Li, B.; Lv, W.; Sun, S.; He, Y. B.; Kang, F.; Yang, Q. H.; Zhou, L.; Zhang, T. Y., Evolution of the electrochemical interface in sodium ion batteries with ether electrolytes. *Nat. Commun.* **2019**, *10* (1), 725.
176. Huang, J.; Guo, X.; Du, X.; Lin, X.; Huang, J.-Q.; Tan, H.; Zhu, Y.; Zhang, B., Nanostructures of solid electrolyte interphases and their consequences for micro-sized Sn anodes in sodium ion batteries. *Energy Environ. Sci.* **2019**, *12* (5), 1550-1557.
177. Zhang, B.; Rousse, G.; Foix, D.; Dugas, R.; Corte, D. A.; Tarascon, J. M., Micro-sized Sn as Advanced Anodes in Glyme-Based Electrolyte for Na-Ion Batteries. *Adv. Mater.* **2016**, *28* (44), 9824-9830.
178. Wang, C.; Wang, L.; Li, F.; Cheng, F.; Chen, J., Bulk Bismuth as a High-Capacity and Ultralong Cycle-Life Anode for Sodium-Ion Batteries by Coupling with Glyme-Based Electrolytes. *Adv. Mater.* **2017**, *29* (35), 1702212.
179. Zhang, J.; Wang, D.-W.; Lv, W.; Qin, L.; Niu, S.; Zhang, S.; Cao, T.; Kang, F.; Yang, Q.-H., Ethers Illuminate Sodium-Based Battery Chemistry: Uniqueness, Surprise, and Challenges. *Adv. Energy Mater.* **2018**, *8* (26), 1801361.
180. Yang, E.; Ji, H.; Jung, Y., Two-Dimensional Transition Metal Dichalcogenide Monolayers as Promising Sodium Ion Battery Anodes. *J. Phys. Chem. C* **2015**, *119* (47), 26374-26380.
181. Wang, H.; Wang, X.; Wang, L.; Wang, J.; Jiang, D.; Li, G.; Zhang, Y.; Zhong, H.; Jiang, Y., Phase Transition Mechanism and Electrochemical Properties of Nanocrystalline MoSe<sub>2</sub> as Anode Materials for the High Performance Lithium-Ion Battery. *J. Phys. Chem. C* **2015**, *119* (19), 10197-10205.
182. Chong, S.; Sun, L.; Shu, C.; Guo, S.; Liu, Y.; Wang, W.; Liu, H. K., Chemical bonding boosts nano-rose-like MoS<sub>2</sub> anchored on reduced graphene oxide for superior potassium-ion storage. *Nano Energy* **2019**, *63*, 103868.
183. Ren, X.; Zhao, Q.; McCulloch, W. D.; Wu, Y., MoS<sub>2</sub> as a long-life host material for potassium ion intercalation. *Nano Res.* **2017**, *10* (4), 1313-1321.
184. Xiao, N.; McCulloch, W. D.; Wu, Y., Reversible Dendrite-Free Potassium Plating and Stripping Electrochemistry for Potassium Secondary Batteries. *J. Am. Chem. Soc.* **2017**, *139* (28), 9475-9478.

185. Li, Y.; Liang, Y.; Robles Hernandez, F. C.; Deog Yoo, H.; An, Q.; Yao, Y., Enhancing sodium-ion battery performance with interlayer-expanded MoS<sub>2</sub>-PEO nanocomposites. *Nano Energy* **2015**, *15*, 453-461.
186. Jia, B.; Yu, Q.; Zhao, Y.; Qin, M.; Wang, W.; Liu, Z.; Lao, C. Y.; Liu, Y.; Wu, H.; Zhang, Z., Bamboo-like hollow tubes with MoS<sub>2</sub>/N-doped-C interfaces boost potassium-ion storage. *Adv. Funct. Mater.* **2018**, *28* (40), 1803409.
187. Xu, Y.; Bahmani, F.; Zhou, M.; Li, Y.; Zhang, C.; Liang, F.; Kazemi, S. H.; Kaiser, U.; Meng, G.; Lei, Y., Enhancing potassium-ion battery performance by defect and interlayer engineering. *Nanoscale Horiz.* **2019**, *4* (1), 202-207.
188. Dong, Y.; Xu, Y.; Li, W.; Fu, Q.; Wu, M.; Manske, E.; Kröger, J.; Lei, Y., Insights into the crystallinity of layer-structured transition metal dichalcogenides on potassium ion battery performance: a case study of molybdenum disulfide. *Small* **2019**, *15* (15), 1900497.
189. Luo, Y.; Han, J.; Ma, Q.; Zhan, R.; Zhang, Y.; Xu, Q.; Xu, M., Exploration of NbSe<sub>2</sub> flakes as reversible host materials for sodium-ion and potassium-ion batteries. *ChemistrySelect* **2018**, *3* (34), 9807-9811.
190. Zhang, R.; Tsai, I. L.; Chapman, J.; Khestanova, E.; Waters, J.; Grigorieva, I. V., Superconductivity in Potassium-Doped Metallic Polymorphs of MoS<sub>2</sub>. *Nano Lett.* **2016**, *16* (1), 629-636.
191. Xie, X.; Makaryan, T.; Zhao, M.; Van Aken, K. L.; Gogotsi, Y.; Wang, G. J. A. E. M., MoS<sub>2</sub> Nanosheets Vertically Aligned on Carbon Paper: A Freestanding Electrode for Highly Reversible Sodium-Ion Batteries. *Adv. Energy Mater.* **2016**, *6* (5), 1502161.
192. George, C.; Morris, A. J.; Modarres, M. H.; De Volder, M., Structural Evolution of Electrochemically Lithiated MoS<sub>2</sub> Nanosheets and the Role of Carbon Additive in Li-Ion Batteries. *Chem. Mater.* **2016**, *28* (20), 7304-7310.
193. Acerce, M.; Voiry, D.; Chhowalla, M., Metallic 1T phase MoS<sub>2</sub> nanosheets as supercapacitor electrode materials. *Nat. Nanotechnol.* **2015**, *10* (4), 313-318.
194. Jiao, Y.; Hafez, A. M.; Cao, D.; Mukhopadhyay, A.; Ma, Y.; Zhu, H., Metallic MoS<sub>2</sub> for High Performance Energy Storage and Energy Conversion. *Small* **2018**, *14* (36), e1800640.
195. Shu, H.; Li, F.; Hu, C.; Liang, P.; Cao, D.; Chen, X., The capacity fading mechanism and improvement of cycling stability in MoS<sub>2</sub>-based anode materials for lithium-ion batteries. *Nanoscale* **2016**, *8* (5), 2918-2926.

196. Sun, D.; Huang, D.; Wang, H.; Xu, G.-L.; Zhang, X.; Zhang, R.; Tang, Y.; Abd El-Hady, D.; Alshitari, W.; Saad Al-Bogami, A.; Amine, K.; Shao, M., 1T MoS<sub>2</sub> nanosheets with extraordinary sodium storage properties via thermal-driven ion intercalation assisted exfoliation of bulky MoS<sub>2</sub>. *Nano Energy* **2019**, *61*, 361-369.
197. Zhao, Q.; Hu, Y.; Zhang, K.; Chen, J., Potassium-sulfur batteries: a new member of room-temperature rechargeable metal-sulfur batteries. *Inorg. Chem.* **2014**, *53* (17), 9000-9005.
198. Stephenson, T.; Li, Z.; Olsen, B.; Mitlin, D., Lithium ion battery applications of molybdenum disulfide (MoS<sub>2</sub>) nanocomposites. *Energy Environ. Sci.* **2014**, *7* (1), 209-231.
199. Joensen, P.; Frindt, R.; Morrison, S. R., Single-layer MoS<sub>2</sub>. *Mater. Res. Bull.* **1986**, *21* (4), 457-461.
200. Park, C.-M.; Kim, J.-H.; Kim, H.; Sohn, H.-J., Li-alloy based anode materials for Li secondary batteries. *Chem. Soc. Rev.* **2010**, *39* (8), 3115-3141.
201. Peled, E., The electrochemical behavior of alkali and alkaline earth metals in nonaqueous battery systems-the solid electrolyte interphase model. *J. Electrochem. Soc.* **1979**, *126* (12), 2047.
202. Pinson, M. B.; Bazant, M. Z., Theory of SEI formation in rechargeable batteries: capacity fade, accelerated aging and lifetime prediction. *J. Electrochem. Soc.* **2012**, *160* (2), A243.
203. Winter, M., The solid electrolyte interphase-the most important and the least understood solid electrolyte in rechargeable Li batteries. *Z. Phys. Chem.* **2009**, *223* (10-11), 1395-1406.
204. Ge, P.; Li, S.; Xu, L.; Zou, K.; Gao, X.; Cao, X.; Zou, G.; Hou, H.; Ji, X., Hierarchical hollow-microsphere metal-selenide@carbon composites with rational surface engineering for advanced sodium storage. *Adv. Energy Mater.* **2019**, *9* (1), 1803035.
205. Cui, C.; Xu, J.; Zhang, Y.; Wei, Z.; Mao, M.; Lian, X.; Wang, S.; Yang, C.; Fan, X.; Ma, J., Antimony nanorod encapsulated in cross-linked carbon for high-performance sodium ion battery anodes. *Nano Lett.* **2018**, *19* (1), 538-544.
206. Wang, J.; Fan, L.; Liu, Z.; Chen, S.; Zhang, Q.; Wang, L.; Yang, H.; Yu, X.; Lu, B., In situ alloying strategy for exceptional potassium ion batteries. *ACS Nano* **2019**, *13* (3), 3703-3713.
207. Bian, X.; Dong, Y.; Zhao, D.; Ma, X.; Qiu, M.; Xu, J.; Jiao, L.; Cheng, F.; Zhang, N., Microsized antimony as a stable anode in fluoroethylene carbonate containing electrolytes for

- rechargeable lithium-/sodium-ion batteries. *ACS Appl. Mater. Interfaces* **2019**, *12* (3), 3554-3562.
208. Zhou, J.; Chen, J.; Chen, M.; Wang, J.; Liu, X.; Wei, B.; Wang, Z.; Li, J.; Gu, L.; Zhang, Q., Few-Layer Bismuthene with Anisotropic Expansion for High-Areal-Capacity Sodium-Ion Batteries. *Adv. Mater.* **2019**, *31* (12), 1807874.
209. Zhao, X.; Wang, J.; Yu, R.; Wang, D., Construction of multishelled binary metal oxides via coabsorption of positive and negative ions as a superior cathode for sodium-ion batteries. *J. Am. Chem. Soc.* **2018**, *140* (49), 17114-17119.
210. Wu, H.; Chan, G.; Choi, J. W.; Ryu, I.; Yao, Y.; McDowell, M. T.; Lee, S. W.; Jackson, A.; Yang, Y.; Hu, L.; Cui, Y., Stable cycling of double-walled silicon nanotube battery anodes through solid-electrolyte interphase control. *Nat. Nanotechnol.* **2012**, *7* (5), 310-315.
211. Huang, Y.; Fang, Y.; Lu, X. F.; Luan, D.; Lou, X. W., Co<sub>3</sub>O<sub>4</sub> Hollow Nanoparticles Embedded in Mesoporous Walls of Carbon Nanoboxes for Efficient Lithium Storage. *Angew. Chem.* **2020**, *132* (45), 20086-20090.
212. Li, Z.; Fang, Y.; Zhang, J.; Lou, X. W., Necklace-Like Structures Composed of Fe<sub>3</sub>N@C Yolk-Shell Particles as an Advanced Anode for Sodium-Ion Batteries. *Adv. Mater.* **2018**, *30* (30), 1800525.
213. Yang, K.; Tang, J.; Liu, Y.; Kong, M.; Zhou, B.; Shang, Y.; Zhang, W.-H., Controllable Synthesis of Peapod-like Sb@C and Corn-like C@Sb Nanotubes for Sodium Storage. *ACS Nano* **2020**, *14* (5), 5728-5737.
214. Yang, H.; Chen, L.-W.; He, F.; Zhang, J.; Feng, Y.; Zhao, L.; Wang, B.; He, L.; Zhang, Q.; Yu, Y., Optimizing the Void Size of Yolk-Shell Bi@Void@C Nanospheres for High-Power-Density Sodium-Ion Batteries. *Nano Lett.* **2019**, *20* (1), 758-767.
215. Zhang, Y.; Wang, G.; Wang, L.; Tang, L.; Zhu, M.; Wu, C.; Dou, S.-X.; Wu, M., Graphene-encapsulated CuP<sub>2</sub>: a promising anode material with high reversible capacity and superior rate-performance for sodium-ion batteries. *Nano Lett.* **2019**, *19* (4), 2575-2582.
216. Liu, J.; Yu, L.; Wu, C.; Wen, Y.; Yin, K.; Chiang, F.-K.; Hu, R.; Liu, J.; Sun, L.; Gu, L., New nanoconfined galvanic replacement synthesis of hollow Sb@C yolk-shell spheres constituting a stable anode for high-rate Li/Na-ion batteries. *Nano Lett.* **2017**, *17* (3), 2034-2042.
217. Fang, Y.; Yu, X. Y.; Lou, X. W., Formation of Polypyrrole-Coated Sb<sub>2</sub>Se<sub>3</sub> Microclips with Enhanced Sodium-Storage Properties. *Angew. Chem.* **2018**, *130* (31), 10007-10011.

218. Wu, J.; Zhang, Q.; Liu, S.; Long, J.; Wu, Z.; Zhang, W.; Pang, W. K.; Sencadas, V.; Song, R.; Song, W., Synergy of binders and electrolytes in enabling micro-sized alloy anodes for high performance potassium-ion batteries. *Nano Energy* **2020**, *77*, 105118.
219. Zhou, L.; Cao, Z.; Wahyudi, W.; Zhang, J.; Hwang, J.-Y.; Cheng, Y.; Wang, L.; Cavallo, L.; Anthopoulos, T.; Sun, Y.-K.; Alshareef, H. N.; Ming, J., Electrolyte engineering enables high stability and capacity alloying anodes for sodium and potassium ion batteries. *ACS Energy Lett.* **2020**, *5* (3), 766-776.
220. Tian, Y.; An, Y.; Xiong, S.; Feng, J.; Qian, Y., A general method for constructing robust, flexible and freestanding MXene@metal anodes for high-performance potassium-ion batteries. *J. Mater. Chem. A* **2019**, *7* (16), 9716-9725.
221. Tao, H.; Zhou, M.; Wang, R.; Wang, K.; Cheng, S.; Jiang, K., TiS<sub>2</sub> as an Advanced Conversion Electrode for Sodium-Ion Batteries with Ultra-High Capacity and Long-Cycle Life. *Adv. Sci.* **2018**, *5* (11), 1801021.
222. Yang, H.; Xu, R.; Yao, Y.; Ye, S.; Zhou, X.; Yu, Y., Multicore-shell Bi@N-doped carbon nanospheres for high power density and long cycle life sodium-and potassium-ion anodes. *Adv. Funct. Mater.* **2019**, *29* (13), 1809195.
223. Fan, X.; Gao, T.; Luo, C.; Wang, F.; Hu, J.; Wang, C., Superior reversible tin phosphide-carbon spheres for sodium ion battery anode. *Nano energy* **2017**, *38*, 350-357.
224. Wang, X.; He, J.; Zhou, B.; Zhang, Y.; Wu, J.; Hu, R.; Liu, L.; Song, J.; Qu, J., Bandgap-Tunable Preparation of Smooth and Large Two-Dimensional Antimonene. *Angew. Chem.* **2018**, *130* (28), 8804-8809.
225. Ou, X.; Cao, L.; Liang, X.; Zheng, F.; Zheng, H.-S.; Yang, X.; Wang, J.-H.; Yang, C.; Liu, M., Fabrication of SnS<sub>2</sub>/Mn<sub>2</sub>SnS<sub>4</sub>/carbon heterostructures for sodium-ion batteries with high initial coulombic efficiency and cycling stability. *ACS Nano* **2019**, *13* (3), 3666-3676.
226. Cao, L.; Gao, X.; Zhang, B.; Ou, X.; Zhang, J.; Luo, W.-B., Bimetallic sulfide Sb<sub>2</sub>S<sub>3</sub>@FeS<sub>2</sub> hollow nanorods as high-performance anode materials for sodium-ion batteries. *ACS Nano* **2020**, *14* (3), 3610-3620.
227. Yi, Z.; Qian, Y.; Tian, J.; Shen, K.; Lin, N.; Qian, Y., Self-templating growth of Sb<sub>2</sub>Se<sub>3</sub>@C microtube: a convention-alloying-type anode material for enhanced K-ion batteries. *J. Mater. Chem. A* **2019**, *7* (19), 12283-12291.

228. Cao, L.; Zhang, B.; Xia, H.; Wang, C.; Luo, B.; Fan, X.; Zhang, J.; Ou, X., Hierarchical chrysanthemum-like MoS<sub>2</sub>/Sb heterostructure encapsulated into N-doped graphene framework for superior potassium-ion storage. *Chem. Eng. J.* **2020**, *387*, 124060.
229. Ko, Y. N.; Choi, S. H.; Kim, H.; Kim, H. J., One-Pot Formation of Sb-Carbon Microspheres with Graphene Sheets: Potassium-Ion Storage Properties and Discharge Mechanisms. *ACS Appl. Mater. Interfaces* **2019**, *11* (31), 27973-27981.
230. Cao, K.; Liu, H.; Jia, Y.; Zhang, Z.; Jiang, Y.; Liu, X.; Huang, K. J.; Jiao, L., Flexible Antimony@Carbon Integrated Anode for High-Performance Potassium-Ion Battery. *Adv. Mater. Technol.* **2020**, 2000199.
231. Luo, W.; Li, F.; Zhang, W.; Han, K.; Gaumet, J.-J.; Schaefer, H.-E.; Mai, L., Encapsulating segment-like antimony nanorod in hollow carbon tube as long-lifespan, high-rate anodes for rechargeable K-ion batteries. *Nano Res.* **2019**, *12* (5), 1025-1031.
232. Ding, H.; Wang, J.; Fan, L.; Liu, Z.; Jia, X.; Yu, X.; Lu, B., Sn-Sb compounds with novel structure for stable potassium storage. *Chem. Eng. J.* **2020**, 125147.
233. He, X.-D.; Liao, J.-Y.; Wang, S.; Wang, J.-R.; Liu, Z.-H.; Ding, X.; Hu, Q.; Wen, Z.-Y.; Chen, C.-H., From nanomelting to nanobeads: nanostructured Sb<sub>x</sub>Bi<sub>1-x</sub> alloys anchored in three-dimensional carbon frameworks as a high-performance anode for potassium-ion batteries. *J. Mater. Chem. A* **2019**, *7* (47), 27041-27047.
234. Yu, S.; Kim, S. O.; Kim, H. S.; Choi, W., Computational screening of anode materials for potassium-ion batteries. *Int. J. Energy Res.* **2019**, *43* (13), 7646-7654.
235. Zheng, J.; Chen, S.; Zhao, W.; Song, J.; Engelhard, M. H.; Zhang, J.-G., Extremely Stable Sodium Metal Batteries Enabled by Localized High-Concentration Electrolytes. *ACS Energy Lett.* **2018**, *3* (2), 315-321.
236. Sangster, J.; Pelton, A., The K-Sb (potassium-antimony) system. *J. Ph. Equilibria* **1993**, *14* (4), 510-514.
237. Mayo, M.; Morris, A. J., Structure prediction of Li-Sn and Li-Sb intermetallics for lithium-ion batteries anodes. *Chem. Mater.* **2017**, *29* (14), 5787-5795.
238. Gabaudan, V.; Berthelot, R.; Stievano, L.; Monconduit, L., Inside the Alloy Mechanism of Sb and Bi Electrodes for K-Ion Batteries. *J. Phys. Chem. C* **2018**, *122* (32), 18266-18273.
239. Gao, Y.; Tian, W.; Huo, C.; Zhang, K.; Guo, S.; Zhang, S.; Song, X.; Jiang, L.; Huo, K.; Zeng, H., Tailoring natural layered  $\beta$ -phase antimony into few layer antimonene for Li storage with high rate capabilities. *J. Mater. Chem. A* **2019**, *7* (7), 3238-3243.

240. Tian, W.; Zhang, S.; Huo, C.; Zhu, D.; Li, Q.; Wang, L.; Ren, X.; Xie, L.; Guo, S.; Chu, P. K.; Zeng, H.; Huo, K., Few-layer antimonene: anisotropic expansion and reversible crystalline-phase evolution enable large-capacity and long-life Na-ion batteries. *ACS Nano* **2018**, *12* (2), 1887-1893.
241. Wang, H.; Zhai, D.; Kang, F., Solid Electrolyte Interphase (SEI) in Potassium Ion Batteries. *Energy Environ. Sci.* **2020**, *13*, 4583-4608.
242. Li, Y., Li, Y., Pei, A., Yan, K., Sun, Y., Wu, C.L., Joubert, L.M., Chin, R., Koh, A.L., Yu, Y. and Perrino, J., , Atomic structure of sensitive battery materials and interfaces revealed by cryo-electron microscopy. *Science* **2017**, *58*(6362), 506-510.
243. Hertz, H., On the contact of elastic solids. *Z. Reine Angew. Mathematik* **1881**, *92*, 156-171.
244. Bryngelsson, H.; Stjerndahl, M.; Gustafsson, T.; Edström, K., How dynamic is the SEI? *J. Power Sources* **2007**, *174* (2), 970-975.
245. Chattopadhyay, S.; Lipson, A. L.; Karmel, H. J.; Emery, J. D.; Fister, T. T.; Fenter, P. A.; Hersam, M. C.; Bedzyk, M. J., In situ X-ray study of the solid electrolyte interphase (SEI) formation on graphene as a model Li-ion battery anode. *Chem. Mater.* **2012**, *24* (15), 3038-3043.
246. Bar - Tow, D.; Peled, E.; Burstein, L., A study of highly oriented pyrolytic graphite as a model for the graphite anode in Li-Ion batteries. *J. Electrochem. Soc.* **1999**, *146* (3), 824.
247. Andersson, A.; Edström, K., Chemical composition and morphology of the elevated temperature SEI on graphite. *J. Electrochem. Soc.* **2001**, *148* (10), A1100.
248. Aurbach, D.; Pollak, E.; Elazari, R.; Salitra, G.; Kelley, C. S.; Affinito, J., On the surface chemical aspects of very high energy density, rechargeable Li-sulfur batteries. *J. Electrochem. Soc.* **2009**, *156* (8), A694.
249. Lodovico, L.; Varzi, A.; Passerini, S., Radical decomposition of ether-based electrolytes for Li-S batteries. *J. Electrochem. Soc.* **2017**, *164* (9), A1812.
250. Aurbach, D., Review of selected electrode-solution interactions which determine the performance of Li and Li ion batteries. *J. Power Sources* **2000**, *89* (2), 206-218.
251. Deng, L.; Zhang, Y.; Wang, R.; Feng, M.; Niu, X.; Tan, L.; Zhu, Y., Influence of KPF<sub>6</sub> and KFSI on the Performance of Anode Materials for Potassium-Ion Batteries: A Case Study of MoS<sub>2</sub>. *ACS Appl. Mater. Interfaces* **2019**, *11* (25), 22449-22456.

252. Zhang, Q.; Pan, J.; Lu, P.; Liu, Z.; Verbrugge, M. W.; Sheldon, B. W.; Cheng, Y.-T.; Qi, Y.; Xiao, X., Synergetic effects of inorganic components in solid electrolyte interphase on high cycle efficiency of lithium ion batteries. *Nano Lett.* **2016**, *16* (3), 2011-2016.
253. Komaba, S.; Ishikawa, T.; Yabuuchi, N.; Murata, W.; Ito, A.; Ohsawa, Y., Fluorinated ethylene carbonate as electrolyte additive for rechargeable Na batteries. *ACS Appl. Mater. Interfaces* **2011**, *3* (11), 4165-4168.
254. Xie, H.; Kalisvaart, W. P.; Olsen, B. C.; Lubner, E. J.; Mitlin, D.; Buriak, J. M., Sn-Bi-Sb alloys as anode materials for sodium ion batteries. *J. Mater. Chem. A* **2017**, *5* (20), 9661-9670.
255. Cao, X.; Ren, X.; Zou, L.; Engelhard, M. H.; Huang, W.; Wang, H.; Matthews, B. E.; Lee, H.; Niu, C.; Arey, B. W., Monolithic solid-electrolyte interphases formed in fluorinated orthoformate-based electrolytes minimize Li depletion and pulverization. *Nat. Energy* **2019**, *4* (9), 796-805.
256. Yu, Z.; Wang, H.; Kong, X.; Huang, W.; Tsao, Y.; Mackanic, D. G.; Wang, K.; Wang, X.; Huang, W.; Choudhury, S.; Zheng, Y.; Amanchukwu, C. V.; Hung, S. T.; Ma, Y.; Lomeli, E. G.; Qin, J.; Cui, Y.; Bao, Z., Molecular design for electrolyte solvents enabling energy-dense and long-cycling lithium metal batteries. *Nat. Energy* **2020**, *5* (7), 526-533.
257. Aurbach, D.; Granot, E., The study of electrolyte solutions based on solvents from the “glyme” family (linear polyethers) for secondary Li battery systems. *Electrochim. Acta* **1997**, *42* (4), 697-718.
258. Gelius, U.; Heden, P.; Hedman, J.; Lindberg, B.; Manne, R.; Nordberg, R.; Nordling, C.; Siegbahn, K., Molecular spectroscopy by means of ESCA III. Carbon compounds. *Phys. Scr.* **1970**, *2* (1-2), 70.
259. Muñoz-Márquez, M. A.; Zarrabeitia, M.; Castillo-Martínez, E.; Eguía-Barrio, A.; Rojo, T. f.; Casas-Cabanas, M., Composition and evolution of the solid-electrolyte interphase in Na<sub>2</sub>Ti<sub>3</sub>O<sub>7</sub> electrodes for Na-ion batteries: XPS and Auger parameter analysis. *ACS Appl. Mater. Interfaces* **2015**, *7* (14), 7801-7808.
260. Ma, M.; Cai, H.; Xu, C.; Huang, R.; Wang, S.; Pan, H.; Hu, Y. S., Engineering Solid Electrolyte Interface at Nano-Scale for High-Performance Hard Carbon in Sodium-Ion Batteries. *Adv. Funct. Mater.* **2021**, 2100278.

261. Zhang, X.; Hao, F.; Cao, Y.; Xie, Y.; Yuan, S.; Dong, X.; Xia, Y., Dendrite-Free and Long-Cycling Sodium Metal Batteries Enabled by Sodium-Ether Cointercalated Graphite Anode. *Adv. Funct. Mater.* **2021**, *31* (15), 2009778.
262. Wang, Y.; Liu, F.; Fan, G.; Qiu, X.; Liu, J.; Yan, Z.; Zhang, K.; Cheng, F.; Chen, J., Electroless Formation of a Fluorinated Li/Na Hybrid Interphase for Robust Lithium Anodes. *J. Am. Chem. Soc.* **2021**, *143* (7), 2829-2837.
263. Shin, H.; Park, J.; Han, S.; Sastry, A. M.; Lu, W., Component-/structure-dependent elasticity of solid electrolyte interphase layer in Li-ion batteries: experimental and computational studies. *J. Power Sources* **2015**, *277*, 169-179.
264. Wu, Y.; Huang, H. B.; Feng, Y.; Wu, Z. S.; Yu, Y., The promise and challenge of phosphorus-based composites as anode materials for potassium-ion batteries. *Adv. Mater.* **2019**, *31* (50), 1901414.
265. Zhu, J.; Liu, Z.; Wang, W.; Yue, L.; Li, W.; Zhang, H.; Zhao, L.; Zheng, H.; Wang, J.; Li, Y., Green, Template-Less Synthesis of Honeycomb-like Porous Micron-Sized Red Phosphorus for High-Performance Lithium Storage. *ACS Nano* **2021**, *15* (1), 1880-1892.
266. Zhu, Y.; Wen, Y.; Fan, X.; Gao, T.; Han, F.; Luo, C.; Liou, S.-C.; Wang, C., Red phosphorus-single-walled carbon nanotube composite as a superior anode for sodium ion batteries. *ACS Nano* **2015**, *9* (3), 3254-3264.
267. Liu, Y.; Liu, Q.; Jian, C.; Cui, D.; Chen, M.; Li, Z.; Li, T.; Nilges, T.; He, K.; Jia, Z., Red-phosphorus-impregnated carbon nanofibers for sodium-ion batteries and liquefaction of red phosphorus. *Nat. Commun.* **2020**, *11* (1), 1-8.
268. Qin, G.; Liu, Y.; Liu, F.; Sun, X.; Hou, L.; Liu, B.; Yuan, C., Magnetic Field Assisted Construction of Hollow Red P Nanospheres Confined in Hierarchical N-Doped Carbon Nanosheets/Nanotubes 3D Framework for Efficient Potassium Storage. *Adv. Energy Mater.* **2021**, *11* (4), 2003429.
269. Zhou, J.; Shi, Q.; Ullah, S.; Yang, X.; Bachmatiuk, A.; Yang, R.; Rummeli, M. H., Phosphorus-Based Composites as Anode Materials for Advanced Alkali Metal Ion Batteries. *Adv. Funct. Mater.* **2020**, *30* (49), 2004648.
270. Ruan, J.; Mo, F.; Long, Z.; Song, Y.; Fang, F.; Sun, D.; Zheng, S., Tailor-Made Gives the Best Fits: Superior Na/K-Ion Storage Performance in Exclusively Confined Red Phosphorus System. *ACS Nano* **2020**, *14* (9), 12222-12233.

271. Xiong, P.; Bai, P.; Tu, S.; Cheng, M.; Zhang, J.; Sun, J.; Xu, Y., Red Phosphorus Nanoparticle@3D Interconnected Carbon Nanosheet Framework Composite for Potassium-Ion Battery Anodes. *Small* **2018**, *14* (33), 1802140.
272. Liu, D.; Huang, X.; Qu, D.; Zheng, D.; Wang, G.; Harris, J.; Si, J.; Ding, T.; Chen, J.; Qu, D., Confined phosphorus in carbon nanotube-backboned mesoporous carbon as superior anode material for sodium/potassium-ion batteries. *Nano Energy* **2018**, *52*, 1-10.
273. Zhang, S.; Liu, C.; Wang, H.; Wang, H.; Sun, J.; Zhang, Y.; Han, X.; Cao, Y.; Liu, S.; Sun, J., A Covalent P-C Bond Stabilizes Red Phosphorus in an Engineered Carbon Host for High-Performance Lithium-Ion Battery Anodes. *ACS Nano* **2021**, *15* (2), 3365-3375.
274. Gusmao, R.; Sofer, Z.; Pumera, M., Black phosphorus rediscovered: from bulk material to monolayers. *Angew. Chem. Int. Ed.* **2017**, *56* (28), 8052-8072.
275. Ren, X.; Lian, P.; Xie, D.; Yang, Y.; Mei, Y.; Huang, X.; Wang, Z.; Yin, X., Properties, preparation and application of black phosphorus/phosphorene for energy storage: a review. *J. Mater. Sci.* **2017**, *52* (17), 10364-10386.
276. Liu, H.; Du, Y.; Deng, Y.; Peide, D. Y., Semiconducting black phosphorus: synthesis, transport properties and electronic applications. *Chem. Soc. Rev.* **2015**, *44* (9), 2732-2743.
277. Xu, G.-L.; Chen, Z.; Zhong, G.-M.; Liu, Y.; Yang, Y.; Ma, T.; Ren, Y.; Zuo, X.; Wu, X.-H.; Zhang, X., Nanostructured black phosphorus/Ketjenblack-multiwalled carbon nanotubes composite as high performance anode material for sodium-ion batteries. *Nano Lett.* **2016**, *16* (6), 3955-3965.
278. Jin, H.; Xin, S.; Chuang, C.; Li, W.; Wang, H.; Zhu, J.; Xie, H.; Zhang, T.; Wan, Y.; Qi, Z.; Yan, W.; Lu, Y.-R.; Chan, T.-S.; Wu, X.; Goodenough, J. B.; Ji, H.; Duan, X., Black phosphorus composites with engineered interfaces for high-rate high-capacity lithium storage. *Science* **2020**, *370* (6513), 192-197.
279. Ferrara, C.; Vigo, E.; Albin, B.; Galinetto, P.; Milanese, C.; Tealdi, C.; Quartarone, E.; Passerini, S.; Mustarelli, P., Efficiency and quality issues in the production of black phosphorus by mechanochemical synthesis: a multi-technique approach. *ACS Appl. Energy Mater.* **2019**, *2* (4), 2794-2802.
280. Capone, I.; Aspinall, J.; Darnbrough, E.; Zhao, Y.; Wi, T.-U.; Lee, H.-W.; Pasta, M., Electrochemo-Mechanical Properties of Red Phosphorus Anodes in Lithium, Sodium, and Potassium Ion Batteries. *Matter* **2020**, *3* (6), 2012-2028.

281. Li, M.; Wang, C.; Chen, Z.; Xu, K.; Lu, J., New concepts in electrolytes. *Chem. Rev.* **2020**, *120* (14), 6783-6819.
282. Jiang, L. L.; Yan, C.; Yao, Y. X.; Cai, W.; Huang, J. Q.; Zhang, Q., Inhibiting Solvent Co-Intercalation in a Graphite Anode by a Localized High-Concentration Electrolyte in Fast-Charging Batteries. *Angew. Chem., Int. Ed. Engl.* **2021**, *60* (7), 3402-3406.
283. Ren, X.; Zou, L.; Cao, X.; Engelhard, M. H.; Liu, W.; Burton, S. D.; Lee, H.; Niu, C.; Matthews, B. E.; Zhu, Z.; Wang, C.; Arey, B. W.; Xiao, J.; Liu, J.; Zhang, J.-G.; Xu, W., Enabling High-Voltage Lithium-Metal Batteries under Practical Conditions. *Joule* **2019**, *3* (7), 1662-1676.
284. Jia, H.; Zou, L.; Gao, P.; Cao, X.; Zhao, W.; He, Y.; Engelhard, M. H.; Burton, S. D.; Wang, H.; Ren, X.; Li, Q.; Yi, R.; Zhang, X.; Wang, C.; Xu, Z.; Li, X.; Zhang, J. G.; Xu, W., High-Performance Silicon Anodes Enabled By Nonflammable Localized High-Concentration Electrolytes. *Adv. Energy Mater.* **2019**, *9* (31), 1900784.
285. Jin, Y.; Xu, Y.; Le, P. M. L.; Vo, T. D.; Zhou, Q.; Qi, X.; Engelhard, M. H.; Matthews, B. E.; Jia, H.; Nie, Z.; Niu, C.; Wang, C.; Hu, Y.; Pan, H.; Zhang, J.-G., Highly Reversible Sodium Ion Batteries Enabled by Stable Electrolyte-Electrode Interphases. *ACS Energy Lett.* **2020**, *5* (10), 3212-3220.
286. Cao, X.; Jia, H.; Xu, W.; Zhang, J.-G., Localized High-Concentration Electrolytes for Lithium Batteries. *J. Electrochem. Soc.* **2021**, *168* (1), 010522.
287. Perez Beltran, S.; Cao, X.; Zhang, J.-G.; Balbuena, P. B., Localized High Concentration Electrolytes for High Voltage Lithium-Metal Batteries: Correlation between the Electrolyte Composition and Its Reductive/Oxidative Stability. *Chem. Mater.* **2020**, *32* (14), 5973-5984.
288. Piao, N.; Ji, X.; Xu, H.; Fan, X.; Chen, L.; Liu, S.; Garaga, M. N.; Greenbaum, S. G.; Wang, L.; Wang, C.; He, X., Countersolvent Electrolytes for Lithium-Metal Batteries. *Adv. Energy Mater.* **2020**, *10* (10), 1903568.
289. Qin, L.; Xiao, N.; Zheng, J.; Lei, Y.; Zhai, D.; Wu, Y., Localized High-Concentration Electrolytes Boost Potassium Storage in High-Loading Graphite. *Adv. Energy Mater.* **2019**, *9* (44), 1902618.
290. Liu, X.; Zheng, X.; Dai, Y.; Wu, W.; Huang, Y.; Fu, H.; Huang, Y.; Luo, W., Fluoride-Rich Solid-Electrolyte-Interface Enabling Stable Sodium Metal Batteries in High-Safe Electrolytes. *Adv. Funct. Mater.* **2021**, 2103522.

291. Zaug, J. M.; Soper, A. K.; Clark, S. M., Pressure-dependent structures of amorphous red phosphorus and the origin of the first sharp diffraction peaks. *Nat. Mater.* **2008**, *7* (11), 890-899.
292. Liu, F.; Shi, R.; Wang, Z.; Weng, Y.; Che, C. M.; Chen, Y., Direct Z-Scheme Hetero-phase Junction of Black/Red Phosphorus for Photocatalytic Water Splitting. *Angew. Chem., Int. Ed. Engl.* **2019**, *58* (34), 11791-11795.
293. Chhetry, A.; Sharma, S.; Barman, S. C.; Yoon, H.; Ko, S.; Park, C.; Yoon, S.; Kim, H.; Park, J. Y., Black Phosphorus@Laser-Engraved Graphene Heterostructure-Based Temperature-Strain Hybridized Sensor for Electronic-Skin Applications. *Adv. Funct. Mater.* **2020**, *31* (10), 2007661.
294. Xing, T.; Li, L. H.; Hou, L.; Hu, X.; Zhou, S.; Peter, R.; Petravic, M.; Chen, Y., Disorder in ball-milled graphite revealed by Raman spectroscopy. *Carbon* **2013**, *57*, 515-519.
295. Sun, J.; Zheng, G.; Lee, H.-W.; Liu, N.; Wang, H.; Yao, H.; Yang, W.; Cui, Y., Formation of stable phosphorus-carbon bond for enhanced performance in black phosphorus nanoparticle-graphite composite battery anodes. *Nano Lett.* **2014**, *14* (8), 4573-4580.
296. Ren, X.; Chen, S.; Lee, H.; Mei, D.; Engelhard, M. H.; Burton, S. D.; Zhao, W.; Zheng, J.; Li, Q.; Ding, M. S.; Schroeder, M.; Alvarado, J.; Xu, K.; Meng, Y. S.; Liu, J.; Zhang, J.-G.; Xu, W., Localized High-Concentration Sulfone Electrolytes for High-Efficiency Lithium-Metal Batteries. *Chem* **2018**, *4* (8), 1877-1892.
297. Abellan, G.; Neiss, C.; Lloret, V.; Wild, S.; Chacon-Torres, J. C.; Werbach, K.; Fedi, F.; Shiozawa, H.; Gorling, A.; Peterlik, H.; Pichler, T.; Hauke, F.; Hirsch, A., Exploring the Formation of Black Phosphorus Intercalation Compounds with Alkali Metals. *Angew. Chem., Int. Ed. Engl.* **2017**, *56* (48), 15267-15273.
298. Gao, Y.; Ru, Q.; Liu, Y.; Cheng, S.; Wei, L.; Ling, F. C. C.; Chen, F.; Hou, X., Mosaic Red Phosphorus/MoS<sub>2</sub> Hybrid as an Anode to Boost Potassium-Ion Storage. *ChemElectroChem* **2019**, *6* (17), 4689-4695.
299. Wang, H.; Wang, L.; Wang, L.; Xing, Z.; Wu, X.; Zhao, W.; Qi, X.; Ju, Z.; Zhuang, Q., Phosphorus Particles Embedded in Reduced Graphene Oxide Matrix to Enhance Capacity and Rate Capability for Capacitive Potassium - Ion Storage. *Chem. Eur. J.* **2018**, *24* (52), 13897-13902.

- 
300. Sui, X.; Huang, X.; Pu, H.; Wang, Y.; Chen, J., Tailoring MOF-derived porous carbon nanorods confined red phosphorous for superior potassium-ion storage. *Nano Energy* **2021**, *83*, 105797.
301. Zhan, R.; Wang, X.; Chen, Z.; Seh, Z. W.; Wang, L.; Sun, Y., Promises and challenges of the practical implementation of prelithiation in lithium-ion batteries. *Adv. Energy Mater.* **2021**, *11* (35), 2101565.
302. Jiang, X.; Liu, X.; Zeng, Z.; Xiao, L.; Ai, X.; Yang, H.; Cao, Y., A Nonflammable Na<sup>+</sup>-Based Dual-Carbon Battery with Low-Cost, High Voltage, and Long Cycle Life. *Adv. Energy Mater.* **2018**, *8* (36), 1802176.
303. Ding, J. F.; Xu, R.; Yao, N.; Chen, X.; Xiao, Y.; Yao, Y. X.; Yan, C.; Xie, J.; Huang, J. Q., Non-Solvating and Low-Dielectricity Cosolvent for Anion-Derived Solid Electrolyte Interphases in Lithium Metal Batteries. *Angew. Chem., Int. Ed. Engl.* **2021**, *60* (20), 11442-11447.
304. Yan, C.; Jiang, L. L.; Yao, Y. X.; Lu, Y.; Huang, J. Q.; Zhang, Q., Nucleation and Growth Mechanism of Anion-Derived Solid Electrolyte Interphase in Rechargeable Batteries. *Angew. Chem., Int. Ed. Engl.* **2021**, *60* (15), 8521-8525.